Title
Long-Term Properties and Combinations of Stochastic Hull Girder Loads on Ships

Author
Petricic, Martin

Publication Date
2012

Peer reviewed|Thesis/dissertation

Long-Term Properties and Combinations of Stochastic Hull Girder Loads on Ships

by

Martin Petričić

A dissertation submitted in partial satisfaction of the
requirements for the degree of
Doctor of Philosophy

in

Engineering – Mechanical Engineering

in the

Graduate Division

of the

University of California, Berkeley

Committee in charge:

Professor Alaa E. Mansour, Chair
Professor Tarek I. Zohdi
Professor David R. Brillinger

Fall 2012

Long-Term Properties and Combinations of Stochastic Hull Girder Loads on Ships

Abstract

Long-Term Properties and Combinations of Stochastic Hull Girder Loads on Ships

by

Martin Petričić

Doctor of Philosophy in Engineering – Mechanical Engineering

University of California, Berkeley

Professor Alaa E. Mansour, Chair

This dissertation presents a novel simulation-based method which provides a consistent and rational framework for long-term hull girder load combination analysis. During its lifetime, which is typically a period of 20 to 25 years (long-term), a ship structure will be subjected to many different dynamic loads. Most of them are caused by very harsh and constantly changing ocean environment and they are random. Therefore, methods of classical statistics and time series analysis have to be applied in order to analyze the structural response to these loads. Many of currently available methods rely on the assumption of weak stationarity of the wave elevation process. This assumption usually holds for a period of up to three hours (short-term) and these methods cannot be used to analyze long-term statistical properties of the loads and their combinations. Long-term methods that can handle the non-stationarity of the wave elevation process often involve many assumptions and require the knowledge of short-term probability density functions of loads or their linear and nonlinear combinations as well as the joint probability density functions of multiple random variables having an impact on these loads.

The method presented in this dissertation is based on efficient multi-voyage simulations of properly correlated hull-girder loads. It relies on a comprehensive statistical model from which nine relevant variables that have an impact on the hull-girder load spectral densities can be simulated or sampled using the rejection sampling technique. These nine variables are: significant wave height, zero crossing wave period, prevailing wind and wave direction, ship's relative heading with respect to waves, ship's location, season of the year, ship's speed, voluntary and involuntary speed reductions in severe sea states and the ship's loading condition. The rejection sampling can significantly decrease the number of sea state and operational profile combinations that have to be considered in the long-term analysis. Non-stationary wave elevations during the ship's entire life are treated as a sequence of different short-term weakly stationary Gaussian stochastic processes, each of which is two hours long. Hull girder sectional loads during each short-term period are efficiently simulated from the load spectral densities taking into account their relative phase differences. Multi-voyage long time series of various load combinations, including the nonlinear ones, are obtained and

their correlation structure and other statistical properties are examined. Nonlinearities in the vertical bending moment (VBM) and the hydroelastic response of the ship in the form of springing and whipping are also included in the simulation. Slamming events are determined from the linear motion analysis and the subsequent whipping response of the structure is simulated in time domain using a combination of trapezoidal and finite element methods to numerically solve dynamic Timoshenko beam problem. Nonlinearities have a significant effect on the simulation time. However, neglecting the super and subharmonics of small amplitudes significantly reduces simulation time while retaining reasonable accuracy. This makes it possible to use simulation even at the initial stages of ship design process.

Although some assumptions are necessary when calculating the loads on a ship structure, the main advantages of the simulation method are that it doesn't make assumptions about the statistical nature of these loads, and it enables nonlinear combinations of linear and nonlinear loads even when their theoretical short-term probability distributions don't exist.

Three different ship types; container ship, tanker and bulk carrier, navigating in the North Atlantic, North Pacific, and between Europe and Asia are used to demonstrate the capabilities of the simulation method in three different areas of hull-girder structural analysis: load combinations, extreme value, and fatigue analysis. Correlation structure between all six sectional loads is examined as well as some linear and nonlinear load combinations. The effect of ship route, damping ratio, slamming extent, hydroelasticity, and nonlinearities on the long-term exceedance probabilities of the VBM are also examined. Finally, the fatigue behavior of a selected container ship is studied on all three routes. The total fatigue damage caused by the vertical bending stresses is separated into damage caused by low- and high-frequency VBM components. The high-frequency part is further divided into the damage caused by linear springing, nonlinearities (including nonlinear springing), and whipping.

Linear springing does not have a significant effect on the long-term exceedance probabilities of the VBM, but has a significant effect on the fatigue life of the structure. Nonlinearities, on the other hand, have a significant effect on the exceedance probabilities of the VBM and its extreme values as well as on the fatigue life of the structure. Damping ratio has a relatively significant effect on the nonlinear component of the VBM, but does not significantly affect the long-term exceedance probabilities of the total VBM since the damping effects are only pronounced in moderate sea states with steep waves. Nonlinearities are also largest in these sea states.

Whipping alone has a relatively small effect on the exceedance probabilities of the VBM and also on the fatigue life of the post-Panamax container ship analyzed in this work. This is attributed to the lack of strong positive correlation in time between whipping peaks and the peaks of the global VBM. More research is needed on studying the phase relationship between these peaks for different ship types, sizes and routes.

Simulation method results agree very well with the full-scale measurements taken on board ships in service in terms of linear and nonlinear VBM exceedance probabilities and fatigue life predictions. For ships studied in this work, the simulation outperforms some existing and commonly used long-term methods in terms of accuracy.

To my wife, Dunja, who supported me every step of the way, even when that meant moving to the "other side of the World".

Contents

List of Figures

List of Tables

Acknowledgments

First and foremost, I would like to acknowledge the help and support I have received from my mentor, Professor Alaa Mansour. I am extremely grateful for all the knowledge, wisdom and kindness that I have received from him during my graduate studies at UC Berkeley. As a researcher, educator, and a human being, I couldn't have imagined a better mentor than Professor Mansour. I sincerely cherish his invaluable pieces of advice, his guidance, constant encouragement, and support.

I would also like to thank my dissertation committee members, Professor David Brillinger and Professor Tarek Zohdi for their helpful comments and suggestions. In addition, I am thankful to Professor Zohdi for letting me use the computer resources at his Computational Materials Research Laboratory. This greatly accelerated my research.

I have spent the first three years of my graduate studies at UC Berkeley with the support of Fulbright Science and Technology Fellowship. I am very grateful to the US Department of State and entire Fulbright organization for their personal and financial support without which this work would not have been possible.

My gratitude also goes to my colleague and friend, Debanjan Mukherjee, who assisted me in setting up the workstations at the Computational Materials Research Laboratory and providing me with the technical support necessary to run the simulations. I also appreciate his sincere and kind words of encouragement and support when times were tough.

I also have to thank Dr. Jelena Vidić-Perunović for providing me with important results from program SOST. Her pieces of advice and assistance are very much appreciated.

Finally, I am thankful to my family. Their love, support and understanding have been my constant inspiration and driving strength.

Chapter 1

Introduction

1.1 Hull Girder Load Classification

During the ship's lifetime, which is typically a period of twenty five years, its hull structure will be subjected to various stochastic and dynamic loads. There are many ways to categorize these loads, but a very natural one can be obtained by looking at a long time record of, e.g., normal stresses in a longitudinal structural member of the ship's hull structure. A simple Fourier transformation of such a signal would reveal that its variance is mainly distributed around three frequency bands. The first one is very close to zero, the second one is close to the wave encounter frequency (around 0.5 rad/s), while the third one is in the range of high frequencies (usually above 2.5 rad/s). Hence, the stationarity and load frequency become the basis for load categorization as follows:

1. QUASI-STATC LOADS
    - Still water loads
    - Thermal loads
2. LOW-FREQUENCY DYNAMIC LOADS
    - Wave-induced loads
3. HIGH-FREQUENCY DYNAMIC LOADS
    - Loads due to springing of the ship
    - Whipping loads due to slamming
    - Hydrodynamic loads induced by propulsive devices
    - Hydrodynamic loads caused by the interaction of appendages with the water flow around the ship
    - Low speed machinery-induced vibrational loads

Still water loads arise from the ship's weight (including cargo) and buoyancy distributions when the ship is floating in still water. They can be accurately determined from the loading condition of the ship and will change only slightly during the ship's voyage as the fuel and provisions are consumed. From one voyage to the next, they will have an almost step change in magnitude as the cargo or ballast are discharged in the port and the new cargo or ballast are loaded onto the ship. Still water loads are very significant part of the total load acting on the hull girder. However, due to their quasi-static nature, they can simply be superimposed to the other stochastic dynamic loads during the course of one voyage. Wang and Moan [111] presented a probabilistic method for combining the still-water and wave bending moments over the entire life of the ship structure. A considerable reduction of the total design bending moment was found when the load coincidence was properly considered instead of combining the maximum values of each load. Thermal loads arise due to variations in ambient temperature and differences in water and air temperatures. In some cases, the cargo carried on board the ship can induce these loads. This is the case with the natural gas carriers (LNG) or reefer ships carrying refrigerated cargo. Thermal loads change very slowly in time and are, thus, considered as quasi-static. For most commercial vessels thermal loads can be ignored. Quasi-static loads are not the topic of this dissertation.

Low-frequency loads result mainly from the rigid body motion of the vessel in waves. Their central frequency is close in magnitude to the wave encounter frequency for wave lengths equal to the ship length [69]. The most important subcategory of these loads consists of wave-induced hull girder sectional forces and moments. Ship motion coupled with the changing wave profile causes a change in weight and buoyancy distributions, which in turn causes a change in the sectional forces and moments compared to the still water loads. The difference between the total sectional loads at a particular cross-section of the hull and the still water sectional loads is equal to the wave-induced sectional loads. In low sea states, the amplitude of these loads is considered to be linearly proportional to the wave amplitude. However, in higher sea states some sectional loads, like the vertical bending moment, can be affected by nonlinearities in waves themselves, or nonlinearities in hydrodynamic forces and hull geometry.

High-frequency loads are associated with the hydroelastic behavior of the ship. Hydroelasticity describes the coupling between the elastic vibrations and the hydrodynamic loading of the hull girder. There are three main types of these loads. The first one is caused primarily by short waves whose encounter frequency is close to the lower natural frequencies of the hull and can, therefore, induce a significant resonant steady-state response known as *springing*. Linear springing occurs when the encounter frequency of the waves is equal to the natural frequency of the two-node flexural vibration mode. Nonlinear springing occurs when the sum of encounter frequencies of the component harmonics in the bi-harmonic wave equals the two-node mode frequency. Higher flexural modes can also be excited, but due to their high natural frequency this is not very likely. Springing is observed on very slender ship structures with a high length to breadth ratio. Some of the Great Lakes cargo vessels have been known to suffer from springing. Springing also affects large container ships. The second type of high-frequency loads is called *whipping* and is caused by the *slamming* phe-

nomenon. Slamming usually occurs in rough seas when the ship's bow or stern emerge from the water and impact the water surface upon reentry with a high relative speed. This creates a very large pressure acting on the shell plating of the hull for a fraction of a second causing transient loads that reverberate throughout the entire structure of the ship. These transient stochastic whipping loads can be observed as the rapidly varying part superimposed to the slowly varying wave-induced loads. Sometimes it can be very difficult to distinguish between springing and whipping while looking at the time series of e.g. vertical bending moment. This is especially the case when the structural and hydrodynamic damping of the hull is small leading to slowly decaying whipping loads. The third type of high-frequency loads is caused by the low speed machinery (e.g, main engine), propulsive devices (e.g, propeller), or by vortex induced vibrations (VIV) of the hull appendages. Because these loads are cyclic and can be determined very accurately, they are considered as deterministic. Also, in most cases they are much less significant compared to the other hull girder loads. Machinery-induced vibrations will not be considered in this dissertation.

Apart from the loads mentioned in the previous three paragraphs, there is a number of other loads that can arise in somewhat special circumstances, such as: underwater explosion, grounding, collision with other ships, fire, navigation through icy waters, operating the cargo-handling equipment, mooring, and landing of aircrafts or helicopters. Wind loads can also be significant for some ship types. Most of the loads mentioned in this paragraph occur only a small number of times during the ship's lifetime, if at all, compared to the other loads.

When designing a ship structure, engineers need to find a realistic estimate of the total combined load to which the structure will be subjected. The estimate that is too conservative will subsequently result in an over-designed, heavier structure that has a smaller payload. On the other hand, if the estimate of the total combined load is lower than its true value, the resulting ship structure might be unfit for service, expensive to maintain or unsafe to operate. If all the loads acting on the ship structure were deterministic and static (or quasi-static), then simple addition of the load effects at a certain point in the structure would be sufficient to obtain the total combined load effect. That value could then be used in the design of that particular structural member. However, due to stochastic and dynamic nature of the ocean waves during the ship's lifetime, both the low- and high-frequency loads will also be stochastic and dynamic. In order to properly combine these loads, methods of time series analysis and classical statistics have to be used.

Currently available statistical and deterministic methods for combining extreme loads on ship structures can be classified into two main categories:

- Short-term methods
- Long-term methods

Short-term denotes a time interval of up to three hours during which the sea state, represented by the significant wave height, zero crossing period and the prevailing wind and wave direction (H_S, T_0, β), does not change. Wave elevations in a stationary sea state

can be represented by a weakly stationary Gaussian process. Measurements of the wave surface in deep water have offered no evidence to reject this hypothesis. On the other hand, long-term load combinations correspond span across the entire lifetime of the ship. Here, the stationarity of input (wave elevations) is not satisfied since the ship encounters many different sea states at many different operational profiles (speed, heading, location, season of the year, loading condition). Short-term load combinations in the extreme design sea state and for a certain loading condition can be used for the structural strength evaluations, especially the limit state calculations. However, they are not sufficient for the structural reliability analysis and fatigue calculations where all the loads encountered by the ship during its lifetime need to be taken into account. An overview of currently available methods for short- and long-term load combination is given in Section 2.1. In case of a linear combination of loads in the short-term sense, there exists an exact analytical method for load combination developed by Mansour [70]. However, this method is not capable of analyzing the nonlinear combination of loads and it is limited to weakly stationary load processes.

A number of long-term methods have been developed in the last two decades. While lifting the load stationarity requirement, these methods are still mainly limited to linear combination of loads. In order to achieve computational efficiency, many of them rely on significant simplifications that have an adverse effect on their accuracy. Additionally, they don't provide a reliable framework for including the hydroelastic response of the hull girder in the form of springing and whipping, or for including the nonlinear effects on the vertical bending moment. Although some of the more simple methods have been calibrated against the more complex ones, a calibration against the full-scale measurements taken on board vessels in service is still missing. A need for developing a more rational and consistent approach to long-term load combination problem is identified in the present study.

1.2 Objectives and Scope of the Present Study

The main objective of this dissertation is to present a novel method for analyzing long-term hull girder load combinations. The method is capable of efficiently simulating properly correlated hull girder load time series over multiple transcontinental voyages. These time records can then be combined in an arbitrary fashion and their statistical properties can be analyzed. The applications of this method in three different areas of hull girder structural analysis will be presented; load combinations, extreme value analysis, and fatigue calculations. A possible application of the simulation method in reliability analysis is also indicated. The main objectives of this study were to:

1. present the novel method for analyzing the long-term hull girder load combinations and their extreme values;

2. demonstrate how the nonlinear effects on the vertical bending moment and the hydroelastic response of the hull girder can be accounted for in a rational and computationally efficient manner;

3. show the applicability of the method to fatigue analysis;
4. discuss the methods's accuracy, computational efficiency and versatility when compared with currently available statistical methods and full-scale measurements;
5. discuss the advantages and disadvantages of the method and suggest steps for future work.

This dissertation is divided into five chapters. Each subsequent chapter builds upon the results of the previous one by adding new capabilities to the method.

Chapter 2 gives an overview of currently available short- and long-term statistical methods for load combination analysis and a theoretical development of the proposed novel simulation method. It also demonstrates how the method is used to find the long-term correlation coefficients between various hull girder loads as well as the long-term exceedance probabilities of their combinations. The loads are simulated in time domain from the load spectral densities that are obtained by using modified linear strip theory. Only linear loads are considered in Chapter 2.

Chapters 3 and 4 build upon the results of Chapter 2 by adding new capabilities to the simulation method. Chapter 3 introduces high-frequency springing loads as well as the nonlinearities in the vertical bending moment by using the quadratic strip theory developed by Jensen and Pedersen [51]. It analyzes the effect of springing and nonlinearities on the long-term statistical properties of the vertical bending moment. Chapter 4 introduces whipping vertical bending moment. Whipping is simulated in time domain using a combination of implicit trapezoidal and finite element methods to solve a system of two coupled partial differential equations of the dynamic Timoshenko free-free beam model. The slamming instances are determined from the simulated ship motion taking into account all six degrees of freedom. The vertical force per unit length on the ship's bow is approximated using two-dimensional boundary element method (see Zhao and Faltinsen [119] and Jensen et al. [52]) on a wedge impacting the water surface. After adding low- and high-frequency loads together (both linear and nonlinear parts), a final comparison with the full-scale measurements and the Jensen's simplified method is performed.

Chapter 4 also describes how the method can be used to find the cumulative fatigue damage of an arbitrary structural detail. The percent damage caused by low- and high-frequency loads is analyzed separately and compared to the full-scale measurements.

Chapter 5 gives conclusions, discusses advantages and disadvantages of the simulation method and also gives recommendations for future work.

Chapter 2

Low-Frequency Wave-Induced Hull Girder Loads

2.1 Overview of the Current Load Combination Methods

This section presents an overview of the current load combination methods suitable for analyzing cumulative effects of different low-frequency hull girder loads on ship structures. Overview of the load combination methods that are suitable for combining low-frequency with high-frequency loads due to springing and slamming will be presented in Chapters 3 and 4, respectively.

A number of methods to combine the extreme load values can be found in the literature. Some of them depend on the knowledge of linear relationship between two individual loads which is represented by the correlation coefficient ρ. It is important to distinguish between the short- and long-term load combinations.

All the wave-induced load effects on the ship structure have a common cause - the wave elevations. This commonality of input causes the load effects on the ship structure to have a higher level of correlation than is the case with some other engineering structures like the buildings on land.

2.1.1 Short-Term Load Combination

2.1.1.1 Mansour's K Factor Method

Mansour [70] studied the short-term combinations of two and three extreme loads of the form

$$f_c = f_1 + Kf_2 \qquad f_1 > f_2 \tag{2.1}$$

for the two load case, or

$$f_c = f_1 + K_2 f_2 + K_3 f_3 \qquad f_1 > f_2 > f_3 \tag{2.2}$$

for the three load case. f_1, f_2, and f_3 are the characteristic design values of individual loads and f_c is the characteristic value of the combined load. Characteristic value can be defined as, e.g., the expected extreme load value in N peaks, the most probable extreme load value in N peaks or the extreme load value with a certain probability of exceedance in N peaks. K, K_2 and K_3 are the load combination factors that depend, among other things, on the degree of correlation between individual load components. Mansour considered a ship traveling in oblique irregular seas as a multiple linear system (filter) with the ocean waves representing a common input. The output, which can be a time series of any measurable quantity (e.g., motion, velocity, acceleration, sectional load or stress), is given by the convolution integral in the time domain

$$y(t) = \sum_{i=1}^{n} a_i \int_0^{\infty} h_{1,i}(\tau) x(t-\tau) d\tau \tag{2.3}$$

where $h_{1,i}(\cdot)$ are the first order impulse response functions (or kernels) of the individual load components, $x(\cdot)$ is the common input, i.e., a time history of wave elevation, a_i are the constants to ensure the uniformity of units and direction, e.g., to convert loads to stresses in the same direction, and n is the number of individual load components. Using system linearity, the summation and integration signs can be interchanged in this case and a composite linear impulse response function can be written as

$$h_{1,c}(t) = \sum_{i=1}^{n} a_i h_{1,i}(t) \tag{2.4}$$

In the frequency domain, the linear frequency response (transfer) function $H_{1,i}(\omega)$ for each load component can be obtained as the Fourier transform of $h_{1,i}(t)$

$$H_{1,i}(\omega) = \int_0^{\infty} h_{1,i}(t) e^{-j\omega t} dt \tag{2.5}$$

and the composite linear frequency response function can be obtained as

$$H_{1,c}(\omega) = \int_0^{\infty} h_{1,c}(t) e^{-j\omega t} dt \tag{2.6}$$

Again, using linearity, one can write

$$H_{1,c}(\omega) = \sum_{i=1}^{n} a_i H_{1,i}(\omega) \tag{2.7}$$

The relationship between the input (wave elevation) one-sided spectral density $S_x(\omega)$ and the output (response) one-sided spectral density $S_y(\omega)$ is given by the well-known equation

from linear filter theory (see, e.g., [99])

$$\begin{aligned} S_y(\omega) =& \left|H_{1,c}(\omega)\right|^2 S_x(\omega) = H_{1,c}(\omega)H^*_{1,c}(\omega)S_x(\omega) \\ =& S_x(\omega)\sum_{i=1}^{n}\sum_{j=1}^{n} a_i a_j H_{1,i}(\omega)H^*_{1,j}(\omega) \\ =& S_x(\omega)\sum_{i=1}^{n} a_i^2 \left|H_{1,i}(\omega)\right|^2 + S_x(\omega)\sum_{\substack{i=1\\ i\neq j}}^{n}\sum_{j=1}^{n} a_i a_j H_{1,i}(\omega)H^*_{1,j}(\omega) \end{aligned} \tag{2.8}$$

where $H^*_{1,c}(\omega)$ is the complex conjugate of $H_{1,c}(\omega)$. The first term in Eqn. (2.8) is the sum of individual response spectra, each modified by a factor of a_i^2. The second term, which can be either positive or negative, reflects the amount of correlation between individual load components.

The total variance of the combined response can be calculated as the zeroth moment of the one-sided spectral density

$$\begin{aligned} \sigma_c^2 =& m_0 = \int_0^\infty S_y(\omega)d\omega \\ =& \sum_{i=1}^{n} a_i^2 \int_0^\infty \left|H_{1,i}(\omega)\right|^2 S_x(\omega)d\omega + \sum_{\substack{i=1\\ i\neq j}}^{n}\sum_{j=1}^{n} a_i a_j \int_0^\infty H_{1,i}(\omega)H^*_{1,j}(\omega)S_x(\omega)d\omega \end{aligned} \tag{2.9}$$

In order to obtain the correlation coefficients between different load components, Eqn. (2.9) can be written in a different form using a sum of correlated random variables

$$\sigma_c^2 = \sum_{i=1}^{n} a_i^2\sigma_i^2 + \sum_{\substack{i=1\\ i\neq j}}^{n}\sum_{j=1}^{n} a_i a_j \rho_{ij}\sigma_i\sigma_j \tag{2.10}$$

where σ_i^2 are the variances of the individual load components and ρ_{ij} are the correlation coefficients between them. Comparing Eqn. (2.9) with Eqn. (2.10) yields the expression for individual load variances

$$\sigma_i^2 = \int_0^\infty \left|H_{1,i}(\omega)\right|^2 S_x(\omega)d\omega \tag{2.11}$$

and the expression for the correlation coefficients between them

$$\rho_{ij} = \frac{1}{\sigma_1\sigma_2}\int_0^\infty \Re\left[H_{1,i}(\omega)H^*_{1,j}(\omega)\right] S_x(\omega)d\omega \tag{2.12}$$

The linear filter analysis in the frequency domain described thus far using the one-sided wave spectral density (referred to as spectrum throughout this dissertation) assumes that

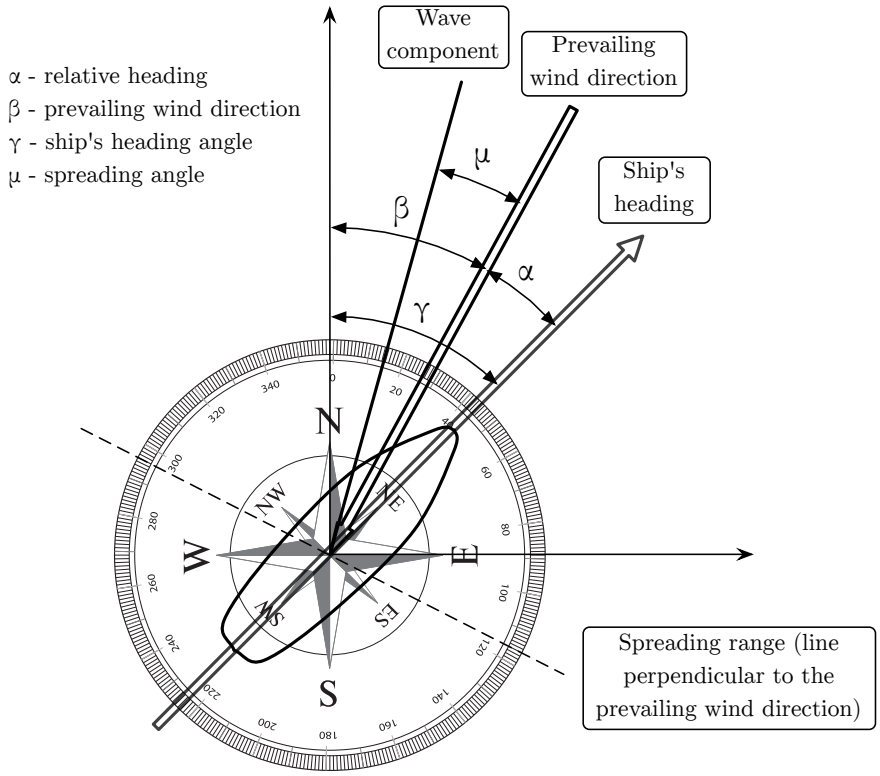

Figure 2.1: Notation of relevant angles for short-crested waves.

the wave energy is traveling in a specific direction, commonly considered the same direction as the wind. In this respect, the wave spectrum may be considered as a *uni-directional spectrum* or the *long-crested spectrum*, denoted $S(\omega)$. In reality, however, for wind-generated waves the wave energy usually spreads over various directions, though the major part of the energy may propagate in the prevailing wind direction. The wave spectrum representing energy in a specific direction is called the *directional spectrum* or the *short-crested spectrum*, denoted $S(\omega, \mu)$, where μ is the wave spreading angle, i.e., μ is the angle between the wave component under consideration and the prevailing wind direction β. The above results can also be generalized to the case of short-crested waves. If α denotes the angle between the ship velocity vector and the prevailing wind direction (see Figure 2.1), then

$$\sigma_i^2 = \int_{-\frac{\pi}{2}}^{\frac{\pi}{2}} \int_0^{\infty} |H_{1,i}(\omega, \alpha - \mu)|^2 \, S_x(\omega, \mu) d\omega d\mu \tag{2.13}$$

and

$$\rho_{ij} = \frac{1}{\sigma_1 \sigma_2} \int_{-\frac{\pi}{2}}^{\frac{\pi}{2}} \int_0^{\infty} \Re \left[H_{1,i}(\omega, \alpha - \mu) H_{1,j}^*(\omega, \alpha - \mu) \right] S_x(\omega, \mu) d\omega d\mu \tag{2.14}$$

The characteristic design values f_1, f_2, and f_3 from Eqns. (2.1) and (2.2) are usually determined from extreme value theory. If the most probable extreme values are used as

characteristic values, and if the wave elevations are represented with a stationary Gaussian process, then it can be shown, [70], that there is an exact theoretical expression that relates the load combination factors (K factors) from Eqns. (2.1) and (2.2) to the correlation coefficients from Eqn. (2.12) or Eqn. (2.14). For the two load case this relationship becomes

$$K = \frac{m_r}{r}\left[m_c\left(1 + r^2 + 2\rho_{12}r\right)^{1/2} - 1\right] \tag{2.15}$$

where

$$m_r = \sqrt{\frac{\ln\left[\left(1-\epsilon_1^2\right)^{1/2} N_1\right]}{\ln\left[\left(1-\epsilon_2^2\right)^{1/2} N_2\right]}} \tag{2.16a}$$

$$m_c = \sqrt{\frac{\ln\left[\left(1-\epsilon_c^2\right)^{1/2} N_c\right]}{\ln\left[\left(1-\epsilon_1^2\right)^{1/2} N_1\right]}} \tag{2.16b}$$

$r = \frac{\sigma_2}{\sigma_1}$, ρ_{12} is the short-term correlation coefficient between two individual loads, r is the ratio between the standard deviations of individual loads, ϵ_1 and ϵ_2 are the bandwidths of the corresponding response spectra, and N_1, N_2 and N_c are the numbers of peaks of the individual loads and the combined load, respectively. If the individual and combined load processes are narrow-banded and have similar central frequency, m_r and m_c can be taken as unity. This is usually the case when combining stresses resulting from vertical and horizontal bending moments. For the three load case, K factors can be calculated similarly (see [70]).

It can be shown, [70], that the combination factor K is always greater than or equal to the correlation coefficient between the two loads with equality being established only for $K = \rho_{12} = 1$, i.e., for perfectly correlated loads. Since the correlation coefficient represents the overall linear relationship between the two loads and K represents the linear relationship between the extreme values of these loads, it is evident that the load values are more correlated at the extreme value level than overall. This is a very important consideration in the structural strength analysis. It is also shown in [70] that the three widely used load combination methods; the *Peak Coincidence method* (PC), the *Square Root of the Sum of Squares method* (SRSS) [77], and the *Turkstra's Rule* (TR) [107] are just special versions of the K factor method described previously.

2.1.1.2 Peak Coincidence (PC) Method

The PC method assumes perfect correlation between the loads in which case $K = \rho_{12} = 1$ and

$$f_c = f_1 + f_2 \tag{2.17}$$

2.1.1.3 Square Root of the Sum of Squares (SRSS) Method

The SRSS method [77], on the other hand, assumes no correlation between the loads ($\rho_{12} = 0$) and $m_r = m_c = 1$. In that case it can also be shown that $r = \frac{\sigma_2}{\sigma_1} \cong \frac{f_2}{f_1}$, i.e., the ratio of the individual extreme loads is approximately equal to the ratio of their standard deviations. This yields the SRSS rule

$$\begin{aligned} f_c =& f_1 + K f_2 = f_1 + \frac{1}{r}\left[\left(\sqrt{1+r^2}\right) - 1\right] f_2 \\ =& f_1 + f_1\left(\sqrt{1+r^2} - 1\right) \\ =& f_1\sqrt{1+r^2} \\ =& \sqrt{f_1^2 + f_2^2} \end{aligned} \tag{2.18}$$

2.1.1.4 Turkstra's Rule (TR)

Turkstra [107] proposed that the maximum extreme load can be found by combining the maximum value of each individual load with the expected "point in time" values of the other loads, and then taking the maximum of these combinations. In the case of two loads this can be mathematically expressed as

$$f_c = \max\{f_1 + \mathbb{E}\left[x_2|f_1\right]; f_2 + \mathbb{E}\left[x_1|f_2\right]\} \tag{2.19}$$

where $\mathbb{E}\left[x_2|f_1\right]$ and $\mathbb{E}\left[x_1|f_2\right]$ denote the conditional expectations of "point in time" load values x_2 and x_1, given the occurrence of the maximum load values f_1 and f_2, respectively. If the loads are Gaussian random processes with zero mean, then the two conditional expectations become equal to $\rho_{12}\left(\frac{\sigma_2}{\sigma_1}\right) f_1$ and $\rho_{12}\left(\frac{\sigma_1}{\sigma_2}\right) f_2$, respectively. These expressions are based on the mean value of the conditional distribution of the two loads which is also Gaussian. If $m_r = m_c = 1$ which also means that $r = \frac{\sigma_2}{\sigma_1} \cong \frac{f_2}{f_1}$, as stated before, then the TR rule simplifies to

$$f_c = \max\{f_1 + \rho_{12}\left(\frac{\sigma_2}{\sigma_1}\right) f_1; f_2 + \rho_{12}\left(\frac{\sigma_1}{\sigma_2}\right) f_2\} = f_1 + \rho_{12} f_2 \quad \text{for} \quad f_1 > f_2 \tag{2.20}$$

that is, in this case $K = \rho_{12}$. This is also intuitively obvious, since the linear relationship between any two load values, including the case when one of them reaches its maximum value, is given by the correlation coefficient.

Figure 2.2 shows the dependence of the K factor on the values of the correlation coefficient ρ_{12} for various values of the variance ratio r. The plot is made for the case when $m_r = m_c = 1$. The figure also shows how the K factor method reduces to PC when $\rho_{12} = 1$, to SRSS when $\rho_{12} = 0$, and to TR when $\rho_{12} = K$. It can be observed that in the case when the loads are completely uncorrelated ($\rho_{12} = 0$), the K factor has a nonzero value depending on the

value of r. Thus, even though the loads are uncorrelated, the presence of the second load contributes to the combined load.

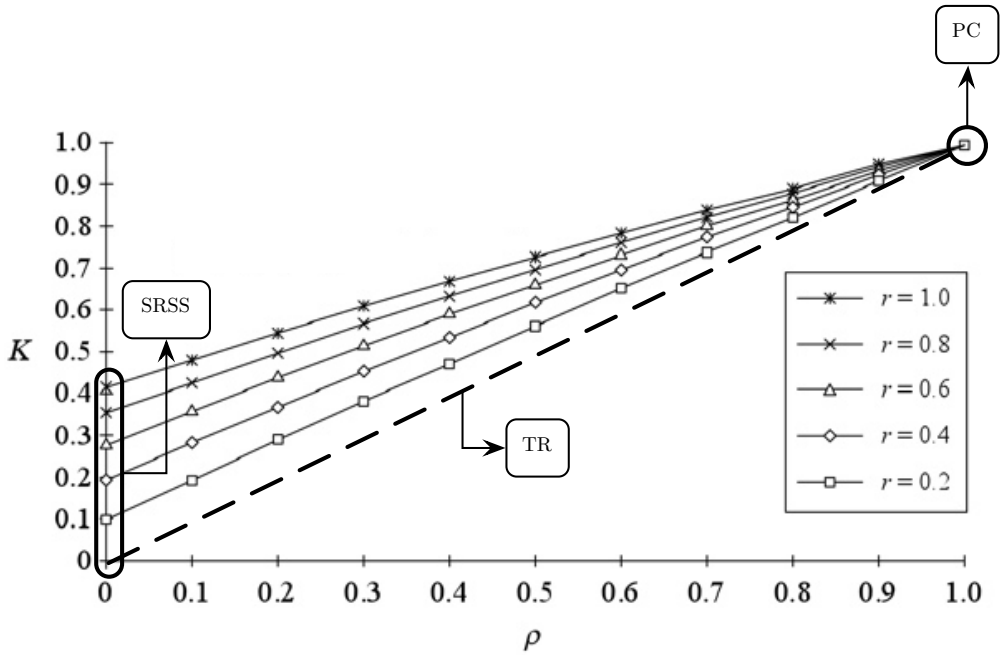

Figure 2.2: Load combination factors for two correlated wave loads when $m_r = m_c = 1$ (taken with modifications from [70]).

Obviously, the PC method overestimates the value of the combined extreme load because it assumes a perfect load correlation. In reality, extreme values of individual loads almost never reach their maximum values simultaneously. It is also clear from Figure 2.2 that the SRSS and the TR underestimate the combined load.

It is also worth mentioning that in the case where $m_r = m_c = 1$, Eqn. (2.1) can be re-casted into a more familiar form used by many classification societies

$$f_c = \sqrt{f_1^2 + 2\rho_{12} f_1 f_2 + f_2^2} \tag{2.21}$$

In this case the ratio of the individual extreme loads is equal to the ratio of their standard deviations. Hence, the expression for the load combination in Eqn. (2.21) has the same form as the expression for the standard deviation of the sum of two correlated random variables where the standard deviations are replaced by the corresponding extreme loads.

All the load combination methods mentioned so far, including the K factor method, apply only to the short-term load combination case in a single sea state when the assumption of stationarity holds.

2.1.2 Long-Term Load Combination

A difficulty that the long-term methods have to overcome is that the assumption of load stationarity is no longer satisfied over a time period longer than a couple of hours. Therefore, the statistical methods described in the previous section are no longer valid. Long-term methods break down the non-stationary wave input into a sequence of many short-term stationary ones. Then, the contribution of each short-term load effect is accounted for in the probabilistic manner. A number of such methods exist today with different levels of complexity, accuracy and computational efficiency. The following subsections present the overview of the most important long-term load combination methods. Some of them were primarily developed for the marine structures, while the others are more general and can also be used on civil engineering structures on land.

2.1.2.1 All Sea States Method

The so called All Sea States Method is, by far, the most commonly used long-term load combination method in the marine industry today. It was first proposed by Nordenström [83] and Fukuda [27]. More details about this method can also be found in, e.g., [15]. It consists of finding the long-term cumulative distribution function (CDF) of the combined response peaks (e.g., longitudinal stress peaks in the shear strake) by statistically combining many short-term CDFs as follows

$$\begin{aligned} F_{R_{LT}}(r) = & \int_{H_S}\int_{T_0}\int_{\alpha}\int_{V} F_{R_{ST}}\left(r|h_s,t_0,\alpha,v\right) \\ & \cdot f_{H_S,T_0,\alpha,V}\left(h_s,t_0,\alpha,v\right)\overline{w}dh_S dt_0 d\alpha dv \\ = & \int_{H_S}\int_{T_0}\int_{\alpha}\int_{V} F_{R_{ST}}\left(r|h_s,t_0,\alpha,v\right) f_{H_S,T_0}\left(h_s,t_0\right) \\ & \cdot f_{\alpha,V|H_S,T_0}\left(\alpha,v|h_s,t_0\right)\overline{w}dh_S dt_0 d\alpha dv \end{aligned} \tag{2.22}$$

where $F_{R_{LT}}(r)$ is the long-term CDF of the combined response peaks, $F_{R_{ST}}\left(r|h_s,t_0,\alpha,v\right)$ is the short-term conditional CDF of the combined response peaks given significant wave height, H_S, zero crossing period, T_0, speed, V, and relative heading, α. $f_{H_S,T_0,\alpha,V}\left(h_s,t_0,\alpha,v\right)$ is the joint probability density function (JPDF) of H_S, T_0, α, and V. $f_{H_S,T_0}\left(h_s,t_0\right)$ is the JPDF of H_S and T_0 only, and $f_{\alpha,V|H_S,T_0}\left(\alpha,v|h_s,t_0\right)$ is the conditional PDF of α and V given H_S and T_0. $\overline{w}$ is the weighting factor which expresses the relative rate of response peaks within each sea state (a combination of H_S and T_0). Each realization of random variables H_S, T_0, α, and V represents one of many short-term conditions which the ship encounters during its lifetime. The integration in Eqn. (2.22) has to be performed over the entire range of random variables involved. If expressions for all the terms in Eqn. (2.22) are known, then the integration can be performed either analytically or numerically yielding the desired long-term CDF of the combined response.

It can be quite difficult to obtain the analytical expressions for $f_{H_S,T_0,\alpha,V}(h_s, t_0, \alpha, v)$, and especially for $F_{R_{ST}}(r|h_s, t_0, \alpha, v)$ as a function of the random variables involved. The situation becomes even more difficult if we introduce new variables such as the area of the ocean, A, season, S, and the loading condition, LC. Therefore, the integral in Eqn. (2.22) has to be discretized into individual sea state (H_S, T_0) / operational profile (α, V, A, S, LC) combinations whose number can become quite large depending on the number of variables and their resolution. Hence, the integration is approximated with the summation over discretized random variables. Additionally, to facilitate the calculations in Eqn. (2.22), the independence of the relative heading and the sea states is usually assumed. This is, however, not true for the ships operating on a single route where the wind blows predominantly in one direction.

When using the All Sea States Method, it is often necessary to perform additional approximations like using a single deterministic value for the ships's speed and its heading and to ignore the spatial variations of wave statistical data along the ship's route. Even after the discretization has been performed, the knowledge of the short-term CDFs of the combined response, $F_{R_{ST}}$, is still needed for every sea state–operational profile combination. These can be difficult to obtain, especially in the case when the loads are nonlinear for which no theoretical distribution exists. Another difficult case arises when the response differs from Gaussian narrow-banded process like in the case of superimposed low- and high-frequency loads.

If the response is Gaussian and narrow-banded, then its short-term CDF exactly follows the Rayleigh distribution [69]

$$F_{R_{ST}}(r|h_s, t_0, \alpha, v) = 1 - e^{\frac{-r^2}{2m_0}} \tag{2.23}$$

where $m_0 = \sigma_c^2$ is the zeroth moment of the combined response spectrum and is equal to the variance of the combined response. It depends on the values of H_S, T_0, α, and V through the combined frequency response function. Today, the combined frequency response function can be calculated using the state-of-the-art seakeeping software, but only for sums of individual responses. Moreover, in reality, the combined response is rarely narrow-banded, even if the wave elevations are. This is also true for the case of ship springing where a second peak at higher frequencies in the vertical bending moment spectrum exists. In that case, the short-term CDF of the combined response should be represented with the Rice distribution [69]

$$F_{R_{ST}}(r|h_s, t_0, \alpha, v) = \Phi\left[\frac{r}{\epsilon\sqrt{m_0}}\right] - \sqrt{1-\epsilon^2}e^{\frac{-r^2}{2m_0}}\Phi\left[\frac{\sqrt{1-\epsilon^2}}{\epsilon}\frac{r}{\sqrt{m_0}}\right] \tag{2.24}$$

where

$$\epsilon = \sqrt{1 - \frac{m_2^2}{m_0 m_4}}$$

$$\Phi(u) = \int_{-\infty}^{u} \frac{1}{\sqrt{2\pi}} e^{\frac{-z^2}{2}} dz$$

$$m_n = \int_0^\infty \omega^n S(\omega) d\omega$$

ϵ is the bandwidth parameter, $\Phi(u)$ is the standard Gaussian CDF, and m_n is the n-th moment of the combined response spectrum. For a perfect narrow-banded process with $\epsilon = 0$ Rice distribution reduces to Rayleigh probability law. Since ϵ depends on the zeroth, second and fourth moment of the combined response spectrum, this numerical method becomes computationally very expensive. This is because for every sea state–operational profile combination, one needs to compute three moments of the combined load spectrum just to find the combined response CDF. Therefore, apart from being complex and computationally expensive, the All Sea States Method is not very suitable for nonlinear load combinations or combinations of non-Gaussian or non-narrow-banded responses. Also, this method does not provide any means of explicitly calculating the long-term correlation coefficients between individual nonlinear responses that are sometimes used in the design rules of the classification societies or in the reliability calculations. An implicit method of calculating the correlation coefficients that combines the All Sea Sates Method with Eqn. (2.21) is presented in [40]. However, the author of this dissertation cautions against using Eqn. (2.21) to implicitly calculate the long-term correlation coefficient when the extreme values of the individual and the combined responses are known. This is because Eqn. (2.21) is only valid in the short-term case when the responses are stationary random processes.

Although the All Sea States Method is extensively used today, its limitations decrease the designer's confidence in the results. Throughout the remainder of this section, some of the other long-term methods developed in recent years will be briefly discussed.

2.1.2.2 Contour Line Method

In order to reduce the number of necessary short-term sea states in the long-term analysis, Baarholm and Moan [10] suggested the use of the Contour Line Method. They have showed that the sufficiently accurate long-term extreme load values can be obtained by considering only a few short-term sea states (combinations of H_S and T_0) that lie along the contour line corresponding to the constant probability of exceedance. This exceedance probability is chosen to represent the sea states with a return period of D years, i.e., $p_e = 1/(DN_S)$ where N_S is the number of sea states encountered within a single year. The contour line can be calculated using the Inverse First Order Reliability Method (IFORM) [108]. It can be shown that the extreme combined load with the return period of D years can be reasonably well approximated using the maximum of the extreme combined loads with a certain probability of exceedance along the contour line, or

$$r_D = \max_{(H_S,T_0)_D} \{r_\alpha\} \tag{2.25}$$

where r_D is the extreme combined load with the return period of D years and r_α is the extreme combined load with the exceedance probability α. However, α needs to be calibrated for each ship type and then modified to account for different length of the ship. Baarholm

and Moan performed the calibration by comparing the estimated extreme loads from the Contour Line Method with the ones calculated using the All Sea States Method and achieved a discrepancy of less than 5%. Since the results from the All Sea States Method entail their own inaccuracies, the Contour Line Method adds another layer of uncertainty in the final results. Also, since only a limited number of sea states is considered, long-term probability density function of the combined load cannot be obtained. Only the extreme value of the combined load can be estimated using the calibration with more accurate methods. Contour Line Method makes the calculation of the extreme combined load much more computationally efficient compared to the All Sea States Method, but it ads more uncertainty in the final result and retains all the other difficulties present in the All Sea States Method.

2.1.2.3 Coefficient of Contribution Method

Apart from their work on the Contour Line Method, Baarholm and Moan also proposed another, slightly more accurate method called the Coefficient of Contribution Method [12] that is primarily aimed at estimating the long-term extreme nonlinear load values with the return period of D years. They have realized that the long-term extreme values can be estimated by considering only a few of the most important short-term sea states that are defined by their coefficients of contribution. These coefficients are determined as a ratio of short-term and long-term exceedance probabilities as follows

$$C_R\left(H_S, T_0\right) = \frac{1 - F_{R_{ST}}\left(r_D | h_s, t_0, \alpha, v\right) f_{H_S, T_0, \alpha, V}\left(h_s, t_0, \alpha, v\right) \overline{w} \Delta h_S \Delta t_0 \Delta \alpha \Delta v}{1 - F_{R_{LT}}(r_D)} \tag{2.26}$$

where all the symbols are defined as for Eqn. (2.22). In order to find the coefficients of contribution, one needs to perform the full (all sea states) long-term analysis to estimate the value of the extreme combined load, r_D. Baarholm and Moan showed that, in most cases, taking only one sea state with the largest coefficient of contribution yields the long-term extreme load value which is only 10 to 15% smaller than the value obtained by using the All Sea States Method. Taking eight more sea states surrounding the one with the largest coefficient of contribution decreases this discrepancy to only 2%. These results show that only a limited number of sea states is needed to estimate the long-term extreme loads, provided that the sea state with the largest coefficient of contribution is included in the analysis. Compared to the Contour line Method where the chosen sea states lie on the contour with a return period of D years, the Coefficient of Contribution Method choses only the sea states in the vicinity of the one with the largest coefficient of contribution. Since this method requires a full long-term analysis as the first step, there is no point in using it only for the estimation of long-term extreme values of linear loads and their sums. Instead, this procedure is used to find the extremes of the nonlinear loads using an iterative procedure to find the corresponding coefficients of contribution for the nonlinear loads in the vicinity of the largest coefficient of contribution from the linear analysis. A second long-term analysis is then performed, but now only for a few sea states with the largest nonlinear coefficients of contribution. This method significantly reduces a very long computation time needed to

obtain the short-term statistical properties of the nonlinear loads since it reduces the number of sea states for which these properties are needed. The accuracy of the nonlinear extreme load values cannot be guaranteed if the maximum nonlinear coefficient of contribution has not been found. Also, this method retains most of the drawbacks and simplifications of the All Sea States Method.

2.1.2.4 Load Coincidence Method

Wen [114], Wen and Pearce [116], Wen [113] and Wen and Pearce [115] extensively studied the effects of load combinations on structures, particularly nuclear ones. They have proposed the Load Coincidence Method which classifies the time varying loads as random processes with their scales of fluctuation being in the vicinity of the natural periods of the structure (micro-scale), or much larger (macro-scale), or both. A proposed model for the macro-scale process, which is both simple and flexible, is the pulse process in which the loading is characterized by a random occurrence time, random duration and, intensity. Micro-scale process can be modeled by a continuous random process conditional on the set of macro-scale parameters of the pulse process. The micro-scale random process is characterized by its mean function, auto-covariance function (or power spectral density) and probability structure (e.g., Gaussian). Mean value of the micro-process corresponds to the intensity of the pulse process. The Load Coincidence Method can consider various types of load coincidences and dependencies. There are two basic types of load dependences: within-load and between-load dependences. The within-load dependences can be between intensity and duration, occurrence dependences (clustering) and intensity dependences. The between-load dependences can be intensity dependences and clustering. Since all the global hull girder loads considered in this work are caused by the same random process, the ocean waves, all of these loads will have strong intensity dependences. However, six hull girder sectional loads (three forces and three moments) will always be occurring together since the ocean waves give rise to all six of these loads simultaneously. In that case the Load Coincidence Method effectively becomes equivalent to the All Sea States Method. The load Coincidence Method can be extended to consider the effects of nonlinear combinations of nonlinear loads with some arbitrary degree of coincidence. The short-term statistical properties of these nonlinear load combinations have to be known either from measurements or some other methods that use linearization techniques such as the one described by Baber and Wen [13].

2.1.2.5 Approach of the Ship Classification Societies

Classification societies are non-governmental institutions which specify and maintain technical standards for design, construction, operation, maintenance, and decommissioning of ships and other offshore structures. These technical standards are published in the classification society's Rules. All the major classification societies are members of the International Association of Classification Societies (IACS) whose purpose is to harmonize the rules of individual member societies. A recent major attempt at rule harmonization occurred in

2006 when the first unified set of rules were published for tankers and bulk carriers. These Common Structural Rules (CSR) for double hull oil tankers [44] and bulk carriers [43] have been revised a few times since 2006. Traditionally, this *rule book* approach to ship design is applied by engineers. It meets the requirements of easy to follow step-wise set of rules for ship design and it is backed up by the large collective technical expertise and experience of the classification societies. However, these rules do not yet provide means of quantifying the effect of a proposed design change on the subsequent safety of that design. Also, the rules are based on existing ship designs and will generally not be optimal for novel designs.

In terms of load combinations, the CSR require that the static and dynamic loads be simply added together. Although there are differences between the CSR for tankers and bulk carriers, the basic principles of combining the dynamic loads are the same. Several dynamic load cases with relevant simultaneously acting dynamic loads have to be considered. For each dynamic load case, the envelope (extreme) values of individual loads have to be multiplied with appropriate dynamic load combination factors (DLCF) to give the simultaneously acting dynamic loads. CSR specify the DLCFs for a number of load cases in head, beam, and oblique seas. The DLCFs have been determined from experience and simplified long-term analyses using, e.g., the All Sea States Method. The dynamic load cases together with the corresponding DLCFs have been determined in such a way that the "worst case scenario" that the ship will encounter during its entire lifetime is captured.

The complexity of novel ship designs and possible effects of structural dynamics and nonlinear loads suggest the use of direct calculations of loads and load combinations in these cases. Most classification societies provide guidelines on this *Dynamic Loading Approach* (DLA) which provides an enhanced structural analysis basis for assessing the adequacy and efficiency of structural design of the ship. Classification society American Bureau of Shipping (ABS) provides an optional classification notation, SafeHull-Dynamic Loading Approach (SH-DLA), for vessels that comply with the provisions of their guide for direct load calculations [5]. The results of the DLA analysis cannot be used to decrease the structural scantlings obtained from the direct application of the basic ABS rules for steel vessels [6]. However, if the DLA analysis indicates the need to increase any of the basic scantling, this increase has to be performed in order to meet the DLA criteria. For container ships longer than 350 meters, DLA is mandatory, not optional.

The DLA requires the development of load cases to be investigated using the Finite Element (FE) structural analysis. Each load case is defined by a combination of ship speed, loading condition, specified Dominant Load Parameter (DLP) and other instantaneous dynamic loads that accompany the DLP. Dominant Load Parameters refer to the load effects, arising from ship motion and wave loads, that may yield the maximum structural response for critical structural members. DLPs are specified for each ship type. For container ships, for example, DLPs are: maximum vertical and horizontal bending moments, maximum vertical acceleration, maximum torsional moment, and maximum roll angle. Loading conditions that have to be considered in the DLA are the ones typically found in the ship's Loading Manual. The long-term extreme values of each DLP is to be calculated using the All Sea Sates Method. Then, equivalent design wave (EDW) is determined for each specified DLP.

EDW is a regular wave that simulates the long-term extreme value of the DLP. Its amplitude is determined by dividing the long-term extreme value of the DLP with the maximum value of the response amplitude operator (RAO) of that DLP

$$a_w = \frac{LTR_j}{RAO_j^{max}} \tag{2.27}$$

where a_w is the equivalent wave amplitude of the j-th DLP, LTR_j is the long-term extreme value of the j-th DLP, and RAO_j^{max} is the maximum RAO amplitude of the j-th DLP and occurs for a specific wave frequency and heading. The instantaneous values of other dynamic loads that are accompanying the DLP can be found from the following equation

$$M_i = RAO_i a_w cos(\varepsilon_j - \varepsilon_i) \tag{2.28}$$

where M_i is the instantaneous i-th load component being considered (i.e. bending moment, shear force, external or internal pressure, or acceleration at selected points), RAO_i is the RAO amplitude of the i-th load component, a_w is the equivalent wave amplitude of the j-th DLP, ε_j is the RAO phase angle of the j-th DLP, and ε_i is the RAO phase angle of the i-th load component. It can be seen that this approach is equivalent to the Turkstra's Rule (see Section 2.1.1.4), but this time applied to the long-term extreme value of the DLP, instead of short-term. The Dynamic Loading Approach provides a more consistent and rational basis for calculating the combined dynamic load compared to the basic rules of the classification societies. However, it is still based on some approximations like using the Turkstra's Rule for short-term load combinations. It is important to mention that the speed of the vessel is assumed zero in the design wave conditions, except for container ships where it is assumed to be 5 knots.

Other classification societies use similar approach to load combination as the ABS. For example, Germaniscer Lloyd [29] also uses the approach based on dominant load parameters and equivalent design waves. This approach is explained in detail by Hughes and Paik in [42].

Some classification societies use Eqn. (2.21) to calculate the long-term load combinations of the global fatigue stress ranges, but instead of the short-term extreme load values and correlation coefficients, the corresponding long-term values are used. For example, DNV Classification Notes [21] give empirical expressions for the extreme global stress ranges due to vertical and horizontal bending moments. The long-term correlation coefficient is taken to be $\rho_{VBM,HBM} = 0.1$. This value was suggested by Hovem [40]. It has been calculated implicitly from Eqn. (2.21) using the long-term characteristic values of individual and combined responses ($f_1,\ f_2,\ f_c$) which were calculated using the ship motion software in design sea state(s). The ships used for these calculations where AFRAMAX and VLCC oil tankers. The obtained correlation coefficient is only valid for the long-crested waves. However, this single value for the correlation coefficient does not take into account the influences from factors such as ship type and size, area of navigation, and velocity/heading profile.

2.1.2.6 Miscelaneous Approaches

In 2002, Baarholm and Moan [11] used the Contour Line Method to combine the longitudinal stresses in the hull arising from vertical and horizontal bending moments. They showed that Eqn. (2.21) could be used even in the long-term case, provided that the appropriate correlation coefficient is used. Their analysis considered only headings from beam to head seas and relied on the assumption that the heading is independent of the sea state. However, this assumption is rarely valid. Preferably, the long-term correlation coefficient should be used in Eqn. (2.21), but Baarholm and Moan showed that the maximum short-term correlation coefficient along the contour line can also be used. This is a significant approximation and the accuracy of this approach relies on calibration with more accurate methods such as the All Sea States Method. This approach has also been validated for nonlinear loads, but only in head seas. Its applicability for nonlinear loads and multiple headings remains as a topic for further study [11].

Funaki et al. [28] proposed that the long-term correlation coefficient can be approximated using the phase difference between the dominant load and other loads at a wavelength for which the RAO of the dominant load reaches its maximum. This approach is similar to the Dynamic Load Approach (see Section 2.1.2.5). It disregards the load correlations at other frequencies and other sea states.

Kawabe and Shibazaki [55] used the correlation coefficient from [28] to combine the whole shapes of the wave-induced long-term response CDFs. Apart from the approximations made to calculate the correlation coefficient (one dominant sea state and frequency), this procedure relies on the assumption that all individual loads have to have the same dominant sea state (have to reach their maxima in the same sea state) which is not always true.

Shin et al. [98] proposed a method for combining the extreme loads that is based on Eqn. (2.21) rewritten in a slightly different form. It takes into account the correlations between different responses by weighting the short-term correlation coefficients with percent contributions to the combined stress that each response component makes at a certain probability of exceedance level. While the long-term correlation coefficient can be calculated by weighting the short-term moments involved in the calculation of the correlation coefficients, no mathematical proof is given for weighting the entire correlation coefficients.

While accurate and general methods exist for the short-term load combinations, current long-term methods rely on many assumptions, and hence, lack in generality. They all rely on knowing a priori the short-term statistical properties, e.g., JPDFs of load combinations which are difficult to obtain in cases when the loads are nonlinear, non-Gaussian, or not narrow-banded. In the case of nonlinear loads, no theoretical short-term probability distribution exists and the statistical properties have to be obtained through measurements or nonlinear time domain load simulations which are computationally too expensive for preliminary ship design stage. Finally, existing long-term methods don't provide means for nonlinear combination of either linear or nonlinear loads (e.g. von Mises stress).

Next section presents the novel method for analyzing long-term properties of loads and load combinations which simulates the environmental conditions and operational parame-

ters of the ship on a specific route and uses load transfer functions to efficiently simulate long-term time series of properly correlated loads. The method completely avoids the issue of knowing the short-term probability density functions of individual loads or their combinations, allowing it to be applied in cases when other methods have difficulties (e.g. nonlinear loads or nonlinear load combinations). The sampling procedure reduces the number of sea state–operational profile combinations compared to the All Sea States Method. In order to assess the applicability and accuracy of the novel method, its results will be compared with results from the long-term measurements on board a ship in service, and with results from the All Sea States Method. Only the All Sea States Method has been chosen for comparison purposes because it is most commonly in use today and almost all of the other long-term methods discussed in this section are derivatives or simplifications of the All Sea States Method. Chapter 2 focuses on linear low-frequency loads and their linear and nonlinear combinations, while Chapters 3 and 4 introduce nonlinear and high-frequency loads.

2.2 Simulation Procedure

2.2.1 Background

Wave-induced loads acting on a ship's hull are generated by a common stochastic process - the wave elevations. This commonality of input is an important source of their correlation. Wave elevations during the ship's lifetime are a non-stationary stochastic process. This creates difficulties in statistical analysis because many of the methods and theorems of classical statistics and time series analysis are only valid if the process is at least weakly stationary (has constant first and second moments over a period of time). In order to apply spectral analysis in the frequency domain, long-term wave elevations can be decomposed into a sequence of time periods during which the stationarity assumption is satisfied. Observations of the wave elevations at a certain area of the ocean have shown that there is no evidence against the assumption that the wave elevations are a weakly stationary Gaussian stochastic process over a period of up to three hours. Therefore, linear filter analysis in the frequency domain can be applied in order to obtain the wave loads that are acting on a ship structure during each short-term period. These results can be used to efficiently simulate the correlated load realizations in time domain for each short-term period and the long-term time series can be obtained by appending many short-term realizations.

In order to simulate the stochastic loads (outputs), a statistical model of the environment and the operational profile of the ship has to be developed first. For a ship navigating between two different ports with a constant loading condition pattern, the shortest time series, generated by the computer model (simulator), would have to be one year long to correctly account for all the randomness of the input process. Only then can the effects of seasonality in the wave elevations be accounted for. Therefore, every one-year record represents a different realization of the underlying stochastic process and they all have the same statistical properties. However, since the only additional randomness not included in a

single voyage simulation (both legs) comes from the seasonal changes in the wave elevation, these effects can be artificially incorporated into a single voyage which will be explained later in this section. Thus, time series of different loads obtained by simulating only one voyage, with seasonality effects included, can be used to obtain the unbiased estimate of the correlation coefficients between the individual loads according to the following expression

$$R = \frac{\sum_{i=1}^{n} (x_{1,i} - \bar{x}_1)(x_{2,i} - \bar{x}_2)}{\left[\sum_{j=1}^{n} (x_{1,j} - \bar{x}_1)^2 \sum_{k=1}^{n} (x_{2,k} - \bar{x}_2)^2\right]^{1/2}} \tag{2.29}$$

where R is the unbiased sample estimate of the true correlation coefficient ρ, n is the number of simulated load values in a single voyage, $x_{1,i}$ and $x_{2,i}$ are the individual load values of two different loads whose correlation is being estimated, and $\bar{x}_1$ and $\bar{x}_2$ are their mean values.

It can be proven, using *Slutsky's lemma* (see, e.g., [19]), that the unbiased estimates of the correlation coefficient $R_{1\ voyage}, R_{2\ voyages}, \ldots, R_{1\ year}, R_{2\ years}, \ldots, R_{25\ years}, \ldots$ all approach the true correlation coefficient ρ in probability as n increases. Here, the indices of the estimates R denote the lengths of each simulation. The proof is given in Appendix A.1. It relies on the fact that the simulated non-stationary time series of each individual load can be transformed into stationary by randomly permuting the simulated load values within each time series. If this is performed in such a way that the load value $x_{1,i}$ remains paired with the load value $x_{2,i}$, then the estimate of the correlation coefficient is unchanged. Of course, any autocorrelation within individual loads is removed, but that is of no significance. The randomized values of time series, for each load, can be taught of as realizations of a sequence of independent and identically distributed (iid) random variables. If all the randomness of the underlying input process is accurately represented in a one-voyage simulation, then simulating longer time series will only decrease the variability of the correlation coefficient estimate, but will not add any new information about the stochastic process itself. Randomizing simulated time series for 1 voyage, 2 voyages,..., 1 year, 2 years,..., 25 years,... produces stationary time series. Therefore, the estimates of the correlation coefficients are also stationary.

The foregoing analysis confirms that an estimates of the long-term correlation coefficients between the individual loads can be obtained from a single voyage simulation. Multiple simulations are needed only if the variability of the estimate R needs to be assessed.

2.2.2 Simulation Steps

The simulation procedure is demonstrated on six different ships: three container ships, two oil tankers and one iron ore bulk carrier. All six ships are used in Chapter 2 while only one tanker and one container ship are used in Chapter 3. Just one container ship from Chapter 3 is used to demonstrate the results of Chapter 4. This is done in order to limit the scope of nonlinear and high-frequency load calculations while retaining an increasing level of accuracy at each consecutive chapter, for demonstrative purposes. Figure 2.3 shows the ships used in each chapter. As can be seen, the 319 meters long container ship is used

in all the chapters to demonstrate the effects of nonlinear and high-frequency loads on the vertical bending moment. Container ship is selected because, from experience, these effects are largest for this ship type due to its fine hull form and high speed. Ships are referred to by their abbreviations given in brackets in Figure 2.3. Main ship particulars are given in Section 2.3.

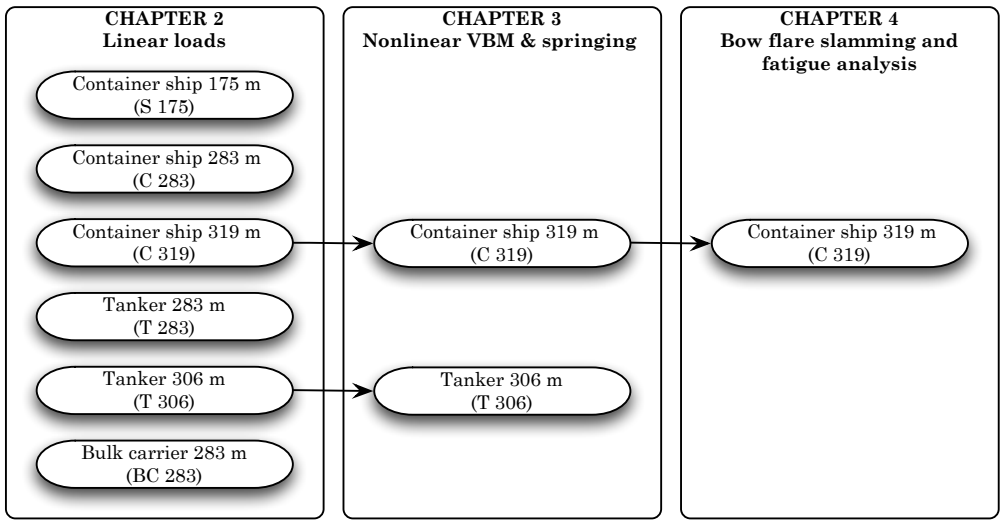

Figure 2.3: Ships used in each chapter.

All ships considered in this work are analyzed on three busy shipping routes: the North Atlantic (NA) route between Boston, MA and Southampton, UK, the North Pacific (NP) route between Long Beach, CA and Singapore and the Europe-Asia (EA) route between Barcelona and Singapore (see Figure 2.4).

2.2.2.1 STEP 1: Wave Climate Statistical Model

Wave climate statistical data for specific ocean areas along all three routes considered in this work are taken from the Global Wave Statistics Online Worldwide and European databases [16]. Global Wave Statistics (GWS) provides nearly worldwide coverage of wave climate in 104 sea areas, and an additional database providing smaller sea areas for the North European Continental Shelf. The data is based on 130 years of ship visual observations to provide a stable climatic average and it has been quality enhanced by the well established NMIMET process ([7], [39], [18] and [38]). Wave statistical data from the GWS database is organized into scatter tables (see Table 2.1) containing number of observations of each combination of the significant wave height, H_S, and zero crossing period, T_0, for a particular area of the ocean called the *Marsden Zone*, particular season, and particular wave direction. The observations are normalized by hundred thousand. Relative frequencies of wave directions are also given in separate tables.

Table 2.1: Scatter table for Marsden zone 9 in winter with waves from the north.

	T_0 [s]										
H_S [m]	< 4	4–5	5–6	6–7	7–8	8–9	9–10	10–11	11–12	12–13	> 13
>14					7	47	137	211	203	135	68
13–14					8	49	125	171	147	87	39
12–13				1	19	101	240	310	250	141	60
11–12				3	43	211	466	561	425	226	91
10–11				7	99	447	908	1014	718	357	136
9–10				20	234	958	1778	1827	1197	555	197
8–9			1	54	566	2071	3475	3254	1958	839	277
7–8			4	151	1388	4482	6712	5663	3095	1214	369
6–7			13	437	3428	9593	12610	9441	4622	1638	453
5–6			47	1289	8395	19870	22427	14605	6288	1980	491
4–5		1	181	3809	19832	38366	36054	19857	7330	2004	436
3–4		6	713	10891	42815	64338	48090	21493	6557	1505	279
2–3		40	2794	27768	74955	80509	44466	15109	3595	658	99
1–2		300	9449	49133	76067	50242	18049	4181	705	94	11
0–1	30	1436	9930	18899	12829	4003	716	86	8	1	

Most long-term methods use only one scatter table to represent the area of the ocean that spans the entire route of the ship, e.g, North Atlantic. This way a lot of statistical information is lost since there can be large differences in wave climate between different areas of the ocean along the ship's route. Additionally, seasonal variability, wave direction statistics, relative headings between the ship and the waves, and the amount of time that the ship spends in each area of the ocean cannot be accurately represented with the single scatter table. The simulation method, described in the following, relies on the development of comprehensive statistical model of the ocean for each area and season. It is first necessary to determine the Marsden Zones as defined in the GWS through which the ship is navigating on a particular route. For that purpose the ship's route is accurately plotted using the charting software Netpas Distance [82]. For example, on the Boston - Southampton route, the ship is traveling through areas 8, 9, 15, and 16 from the Worldwide database and areas 23, 24, and 25 from the European database. The letter database is used for parts of the ocean close to the North European Continental Shelf because it has a better resolution and accuracy than the Worldwide database. Distances in each ocean area is accurately calculated using the Netpas Distance software. The ship routes that are used in this work along with the associated Marsden Zones are shown on a World map in Figure 2.4.

The wave climate statistics for each Marsden Zone (called area in the remainder of this dissertation), except area 25, is given by a total of 32 scatter tables; for each season (winter, spring, summer, and autumn) and for each of the eight different prevailing wind/wave directions (N, NE, SE, S, SW, W, NW). Only 8 scatter tables are given for area 25 (collective scatter diagrams for all seasons), due to the lack of data for individual seasons. Therefore, a total of 744 scatter diagram are used to describe the wave climate statistics along all three

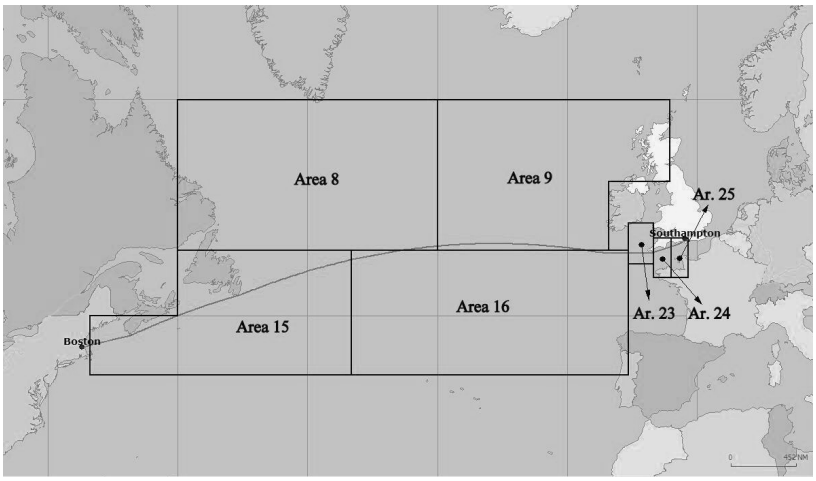

(a) North Atlantic route.

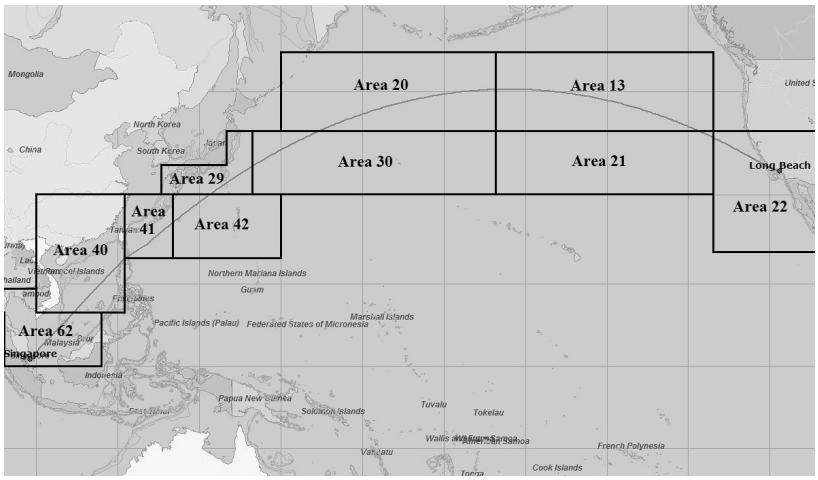

(b) North Pacific route.

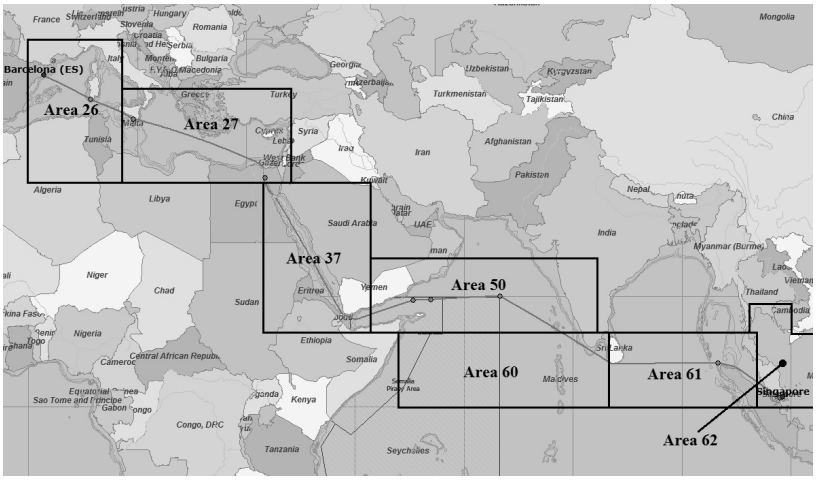

(c) Europe-Asia route.

Figure 2.4: Different shipping routes considered in this work.

routes.

Ochi [84] found that, for certain ocean area, A, season, S and wave direction, B, the conditional PDF of the significant wave height, $f_{H_S|A,S,B}\left(h_S|a,s,\beta\right)$ can be accurately represented by the gamma distribution over its entire domain. The conditional distribution, $f_{T_0|H_S,A,S,B}\left(t_0|h_S,a,s,\beta\right)$, of the average zero crossing period T_0 given H_S, A, S, and B can be described by the log-normal distribution. Therefore, the conditional JPDF of H_S and T_0, given A, S, and B is given by

$$\begin{aligned} f_{H_S,T_0|A,S,B}(h_S,t_0|a,s,\beta) =& f_{H_S|A,S,B}\left(h_S|a,s,\beta\right)\cdot f_{T_0|H_S,A,S,B}\left(t_0 \mid h_S,a,s,\beta\right) \\ =& \frac{c}{\Gamma(m)}\lambda^{cm}h_S^{cm-1}\exp\left[-\left(\lambda h_s\right)^c\right] \\ & \cdot\frac{1}{\sqrt{2\pi}\sigma\left(h_S\right)t_0}\exp\left\{-\frac{\left[\ln(t_0)-\mu\left(h_S\right)\right]^2}{2\left[\sigma\left(h_S\right)\right]^2}\right\} \end{aligned} \tag{2.30}$$

where c, m, and λ are the parameters of the gamma distribution and have to be estimated from the wave climate data. Parameters of the conditional log-normal distribution depend on the significant wave height

$$\begin{aligned} \mu\left(H_S\right) =& a_1+a_2H_S^{a_3} \\ \sigma\left(H_S\right) =& b_1+b_2\exp\left(b_3H_S\right) \end{aligned} \tag{2.31}$$

where the parameters $a_1,\ a_2,\ a_3,\ b_1,\ b_2$, and b_3 are also estimated from the wave climate data.

The JPDF in Eqn. (2.30) is fitted to the data in each of the 744 scatter diagrams by using the maximum likelihood estimation (MLE) to find the parameters $c,\ m,\ \lambda,\ a_1,\ a_2,\ a_3,\ b_1,\ b_2$, and b_3. The MLE is based on the assumption that the form of the JPDF is known, Eqn. (2.30)), apart from the uncertainty about its parameters. The first step in the MLE is to form the likelihood function

$$L(\theta)=\prod_{\substack{\text{All observations}\\ \text{of } H_S \text{ and } T_0}} f_{H_S,T_0|A,S,B}(h_S,t_0|a,s,\beta;\theta),\quad \theta\in\Theta \tag{2.32}$$

where $\theta=[c,\ m,\ \lambda,\ a_1,\ a_2,\ a_3,\ b_1,\ b_2,b_3]$ is the vector of unknown parameters and Θ is the parameter space (e.g., c,m,λ, and $\sigma(H_S)$ all greater than zero). The main idea of the MLE is that the likelihood function, $L(\theta)$, will be relatively larger for values of θ near that which generated the original data. Therefore, parameters are found by maximizing $L(\theta)$. This is performed in Matlab [76] using the nonlinear constrained optimization routine *fmincon*. Since the data in the scatter tables is right and left censored (see Table 2.1), the likelihood function needs to be modified as follows

$$L(\theta)=\prod_{\substack{\text{All observations}\\ \text{of } H_S \text{ and } T_0}}\int_{H_{S_L}}^{H_{S_U}}\int_{T_{0_L}}^{T_{0_U}} f_{H_S,T_0|A,S,B}(h_S,t_0|a,s,\beta;\theta)dh_sdt_0 \tag{2.33}$$

where H_{S_L}, H_{S_U}, T_{0_L}, and T_{0_U} are the lower and upper bounds of H_S and T_0 intervals, respectively.

After obtaining these nine parameters at eight different wind/wave directions for each area and season, a piecewise cubic Hermite polynomial is fitted to each parameter in order to get the explicit dependence of the conditional JPDF in Eqn. (2.30) on the wind/wave direction B. Finally, the conditional JPDF of H_S, T_0 and B, given a certain area and season, can be found from

$$f_{H_S,T_0,B|A,S}(h_S,t_0,\beta|a,s) = f_{H_S,T_0|A,S,B}(h_S,t_0|a,s,\beta) \cdot f_{B|A,S}(\beta|a,s) \tag{2.34}$$

The conditional PDF of wind/wave direction, given area and season, $f_{B|A,S}(\beta|a,s)$, is estimated from the prevailing wind direction data in the Global Wave Statistics database. Westerly wave directions are more likely then other wave directions on the NA route. For the NP and EA routes, bigger seasonal wind direction variations are present.

The foregoing analysis needs to be performed only once. When the explicit dependence of the nine parameters c, m, λ, a_1, a_2, a_3, b_1, b_2, and b_3 on wind/wave direction is found for each area and season, the model is saved on a computer for later use.

Given area and season, a triplet (H_S, T_0, B) can be sampled from the conditional JPDF in Eqn. (2.34) using the rejection sampling technique (for details see, e.g., Davison [19] or Appendix A.2). The idea is to first independently sample H_S, T_0, and B from uniform distributions. Then, each generated sample is accepted with a probability that is proportional to the value of the conditional JPDF in Eqn. (2.34) for that sample.

It is important to emphasize that the triplets sampled using rejection sampling are independent. In reality, the time series of H_S, T_0, and B have a non-zero autocorrelation function, at least for small lags. This means that the consecutive sea states are not independent. However, for the purpose of determining the estimates of the correlation coefficients or the long-term distributions of various loads and their combinations, the correct (realistic) sequence of sea states is irrelevant.

To correctly incorporate the seasonality effects in one voyage, the seasons are sampled randomly between winter, spring, summer, and autumn with the probabilities corresponding to the percent of time that the ship spends navigating in each of them. In this work equal probabilities are assumed. This way, each simulated voyage record will have correct proportions of data from each season.

2.2.2.2 STEP 2: Operational Profile and Voyage Simulation

Ship loading conditions are given in Table 2.2 depending on the ship type, route, and leg of the voyage. This is in accordance with the usual shipping patterns, i.e., oil and iron ore have a one way transportation pattern, while the container ships are almost always loaded with containers. For simplicity, changes in the loading condition due to the consumption of fuel and provisions are not taken into account. Such effects can easily be included by

Table 2.2: Loading conditions used in this work.

	NA		EA		NP	
	Eastern Leg	Western Leg	Eastern Leg	Western Leg	Eastern Leg	Western Leg
Container ship	Full load	Full load	Full load	Full load	Full load	Full load
Tanker	Ballast	Full load	Ballast	Full load	Full load	Ballast
Bulk Carrier	Ballast	Full load	Ballast	Full load	Full load	Ballast

Table 2.3: Velocity profiles for ship types used in this work.

(a) Container ship.

	H_S [m]				
α	≤4	4–6	6–9	9–12	>12
Head	100%	90%	78%	40%	25%
Bow	100%	90%	78%	60%	25%
Beam	100%	90%	60%	40%	25%
Quartering	100%	90%	78%	60%	25%
Following	100%	90%	78%	40%	25%

(b) Tanker and bulk carrier.

	H_S [m]				
α	≤4	4–6	6–9	9–12	>12
Head	100%	92%	75%	50%	25%
Bow	100%	92%	75%	67%	25%
Beam	100%	92%	67%	50%	25%
Quartering	100%	92%	78%	67%	25%
Following	100%	92%	78%	50%	25%

using transfer functions corresponding to the actual mass distribution of the ship at different stages of the voyage.

Since ships are mainly following the great circle route on a transcontinental voyage, their headings (North=0°) will constantly change. For simplicity, on the Boston - Southampton leg of the voyage an average heading of 70° is used in areas 15, 24 and 25 and 90° in areas 8, 9, 16 and 23. On the Southampton - Boston leg, corresponding headings modified by 180° are used. A similar procedure is performed for the other two routes. Involuntary and voluntary speed reductions depend on the significant wave height and the relative heading between the ship and waves. They are accounted for by specifying appropriate speed profiles. Involuntary speed reduction is usually small (around 1 knot) and it is caused by increased resistance and decreased propulsion efficiency in more severe sea states. Voluntary speed reduction can, on the other hand, be very significant. Ship's master will voluntary decrease the speed in very high sea states to prevent excessive motions and wave loads from endangering the vessel. Table 2.3 shows the speed profiles used in this work for different ship types. The speeds are given as a percentage of the vessel's design speed, V_d. These speed profiles are modifications of the ABS recommended speed profiles [4] and reflect the voluntary and involuntary speed reductions. It should be noted that other speed profiles can easily be specified and tailored to the specific vessel under consideration.

Weather routing is partially considered in this work by limiting the highest possible sampled significant wave height to 20 meters. This is similar to the procedure used by Jensen et al. [52] where the scatter diagram has been modified depending on the value of

the significant wave height. Changes in the ship's heading due to rough weather are not considered in this work. This is a very important topic and it is an object of an ongoing investigation.

Once the H_S, T_0, and β triplets are sampled from Eqn. (2.34), depending on the current position of the ship A and the randomly determined season S, the relative heading α that the ship makes with the prevailing wind/wave direction (β) can be calculated as $\alpha = \gamma - \beta$ where γ is the ship's fixed heading in that area and voyage leg (see Figure 2.1). Consequently, the ship's speed is automatically selected from Table 2.3. In this work, the stationarity assumption is taken to hold for a period of up to two hours. In that time period, linear low-frequency, wave-induced loads are simulated using the linear filter analysis (see Section 2.2.2.3) and the distance traveled by the ship is calculated. This procedure is then repeated until the ship reaches a new area, and from then on, until all the areas along the route are traversed and booth legs of the voyage are completed. Multiple routes can also be accounted for, provided that the percent of the ship's total lifetime spent on each route is known. For example, if the ship spends two thirds of its life on route A and one third on route B, then the shortest time series for finding the long-term statistical properties of loads and their combinations must be composed of two complete voyages on route A and one voyage on route B. Any longer time series would have to contain simulated load values from both routes in proportion to their lifetime probabilities.

2.2.2.3 STEP 3: Load Simulation Along the Route

All six sectional low-frequency wave-induced loads are simulated in this work; longitudinal force (LF), Q_x, horizontal shear force (HSF), Q_y, vertical shear force (VSF), Q_z, torsional moment (TM), M_x, vertical bending moment (VBM), M_y, and horizontal bending moment (HBM), M_z, all at amidship. Figure 2.5 shows the definition of sectional forces and moment in relation to the x-y-z coordinate system fixed to the ship. Other loads can be simulated using the same procedure described in this section, provided that their transfer functions are known.

The autocorrelation function, $R(h)$, of a stationary stochastic process measures the linear dependence between two points on the same time series separated by time lag h. If $R(h)$ satisfies the *absolute integrability assumption*

$$\int_{-\infty}^{\infty} |R(h)|\, dh < \infty \tag{2.35}$$

then the process has a spectral representation in the form of the real and even spectral density function of frequency $S(\omega)$. Ocean wave elevations are known to satisfy this assumption because they have a short span of dependence. In other words, two values on the wave elevations time series, separated by time lag h, quickly become uncorrelated as h increases. Thus, $R(h)$ quickly approaches zero. The weak memory of the time series is generally referred to as the *mixing condition* [17].

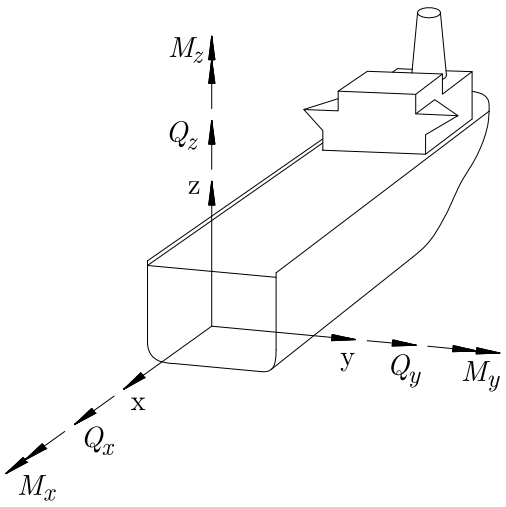

Figure 2.5: Sign convention for the sectional forces and moments.

Wave elevation stochastic process during each short-term period can be represented in the frequency domain by the Pierson-Moskowitz (PM) empirical spectral density function that depends on the significant wave height, H_S, and the zero crossing period, T_0

$$S_\eta(\omega) = 4\pi^3 \frac{H_S^2}{T_0^4} \omega^{-5} \exp\left[-\frac{16\pi^3}{T_0^4}\omega^{-4}\right] \tag{2.36}$$

The PM spectrum has been obtained using the Finite Fourier Transform (FFT) of many time series of the wave elevations measured in the North Atlantic during 1964. It is widely used in Naval Architecture and Ocean Engineering to represent the energy of fully developed seas such as in open-ocean waters. Its use is also recommended by IACS and its members. The cosine squared spreading function is used to account for the prevailing wind/wave direction and the short-crested nature of the ocean waves. This function spreads the ocean wave energy through a 180° angle relative to the prevailing wind/wave direction.

Load linear transfer functions (LTFs), both the amplitude and the phase part, are calculated using *SEAWAY* [53] software. It is a frequency-domain ship motion program based on the modified strip-theory which includes the effects of forward speed. The program is capable of modeling the effects of the bilge kiel on the rolling behavior of the ship. It also uses the *stochastic linearization* technique to deal with the effects of nonlinear frequency-dependent viscous roll damping. The method of Ikeda [45] is used for viscous roll damping in this work. The linear transfer functions are calculated for each loading condition, each relative heading angle (in ten degree increments), and for every speed specified in Table 2.3. For example, Figure 2.6 shows the linear VBM response amplitude operators (moduli of the linear transfer functions) calculated using SEAWAY for C 319 container ship in full load with forward speed $V = 6.35$ knots and for all relative headings α. These RAOs do not reflect the high-frequency springing response of the flexible ship.

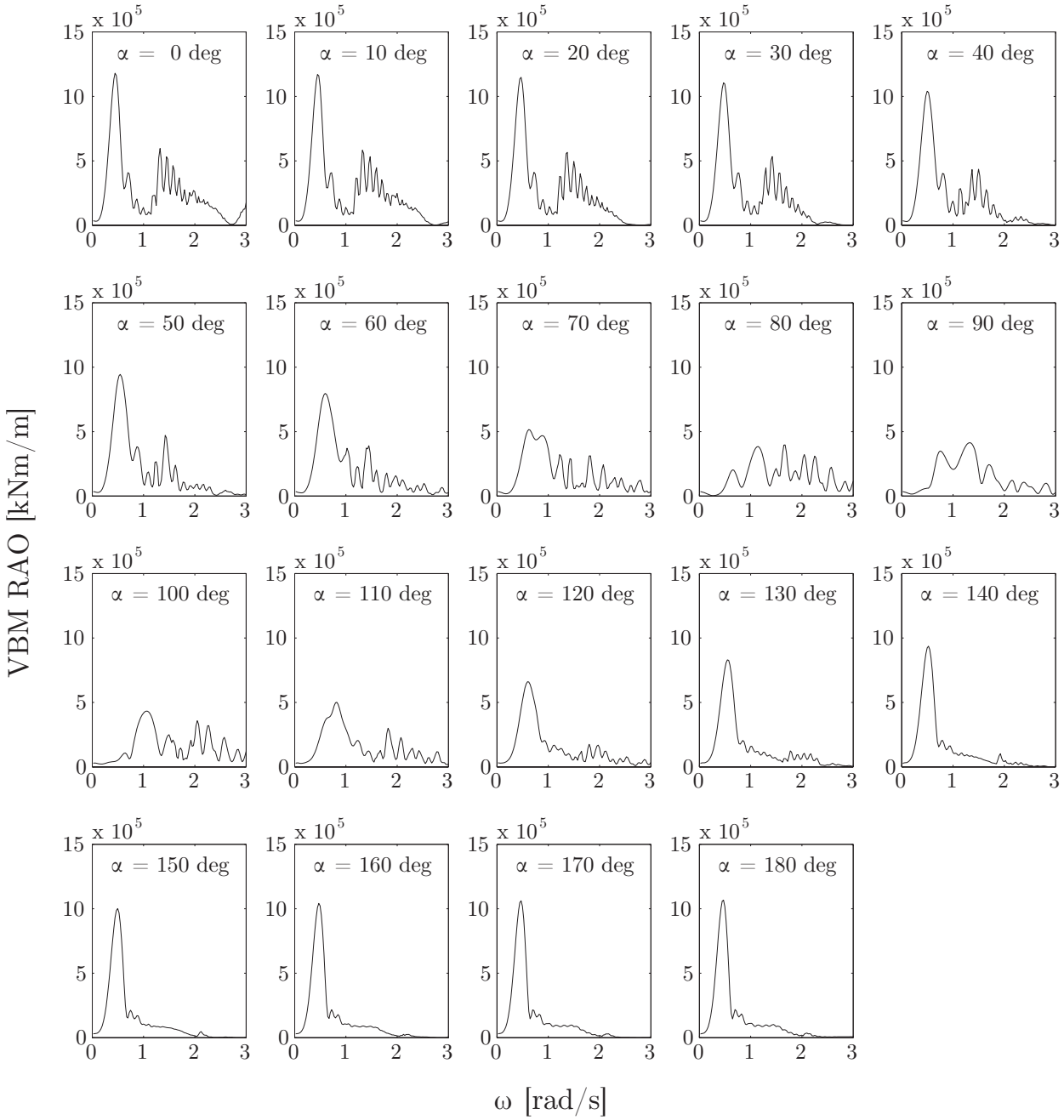

Figure 2.6: Linear VBM RAOs from SEAWAY for fully loaded C 319 container ship with $V = 6.35$ knots.

The output spectra for each individual load is calculated according to the well-know expression for linear filters

$$\begin{aligned} S_y(\omega_e) &= \int_{-\frac{\pi}{2}}^{\frac{\pi}{2}} S_y(\omega_e, \mu) d\mu \\ &= \int_{-\frac{\pi}{2}}^{\frac{\pi}{2}} \left|H_{1,y}\left(\omega_e, \alpha - \mu\right)\right|^2 S_\eta(\omega_e, \mu) d\mu \\ &= S_\eta(\omega_e) \int_{-\frac{\pi}{2}}^{\frac{\pi}{2}} \frac{2}{\pi} \cos^2(\mu) \left|H_{1,y}\left(\omega_e, \alpha - \mu\right)\right|^2 d\mu \end{aligned} \tag{2.37}$$

where index η denotes the input (ocean wave elevation), y denotes the output (any of the sectional forces and moments), $S(\omega_e)$ is the one-sided encounter spectral density of the input or the output, μ is the angle between the wave component under consideration and the prevailing wind direction, α is the relative angle between the ship velocity vector and the prevailing wind direction, and $\alpha - \mu$ is the angle between the ship velocity vector and the wave component under consideration (see Figure 2.1). ω_e is the encounter frequency of the waves that is measured on board a moving ship and can be calculated using

$$\omega_e = \omega + \frac{\omega^2}{g} V \cos(\alpha) \tag{2.38}$$

where ω is the absolute wave frequency, g is the gravitational acceleration and V is the speed of the ship. The integral in Eqn. (2.37) can be calculated numerically.

According to the spectral representation theorem (for details see, e.g., Shumway and Stoffer [99]) any zero-mean stationary time series can be taught of, approximately, as the random superposition of independent sines and cosines oscillating at various frequencies and appearing in proportion to their underlying variances. Therefore, the wave elevation time record taken on board a ship can be expressed as a Fourier integral and approximated with a finite sum of independent periodic components as follows

$$\begin{aligned} \eta(t) &= \int_{\omega_{e,MIN}}^{\omega_{e,MAX}} a_\eta\left(\omega_e\right) \cos\left(\omega_e t + \phi\right) d\omega_e \\ &\approx \sum_{i=1}^{N} a_{\eta,i} \cos\left(\omega_{e,i} t + \phi_i\right) \end{aligned} \tag{2.39}$$

where the summation is conducted over N equally spaced encounter frequencies between $\omega_{e,MIN}$ and $\omega_{e,MAX}$ of the wave spectrum, a_η is the amplitude of the wave component oscillating at frequency ω_e, and ϕ's are independent identically distributed random phase angles having a uniform distribution on the interval [-π, π]. This ensures the independence of

individual components. Also, wave elevation, $\eta(t)$, expressed as a sum in Eqn. (2.39) is approximately Gaussian stochastic process according to the Central Limit Theorem (see, e.g., [36]).

For simple gravity waves, the total energy per unit area is composed of kinetic and potential energy in equal proportions. It is proportional to the square of the wave amplitude and can be calculated as follows

$$E = \frac{1}{2}\rho g A_\eta^2 \tag{2.40}$$

where ρ is the sea water density, g is the gravitational constant and A_η is the wave amplitude. The amplitude of a wave component oscillating at a frequency which is within a very small frequency band, $\delta\omega$, can be obtained by equating the wave energy per unit area, E, and the unit spectral energy contained within that frequency band

$$\frac{1}{2}\rho g A_\eta^2 = \rho g S_\eta(\omega_0)\delta\omega \tag{2.41}$$

$$\Rightarrow A_\eta = \sqrt{2S_\eta(\omega_0)\delta\omega} \tag{2.42}$$

where ω_0 is the middle frequency of the frequency band $\delta\omega$. This is only valid in the limiting case when $\delta\omega \to 0$. However, the amplitude of any wave component, $a_{\eta,i}$, in the finite sum of periodic components in Eqn. (2.39) can be approximated for small $\Delta\omega_e$ as

$$a_{\eta,i} \approx \sqrt{2S_\eta\left(\omega_{e,i}\right)\Delta\omega_e} \tag{2.43}$$

where

$$\Delta\omega_e = \left(\omega_{e,MAX} - \omega_{e,MIN}\right)/N \tag{2.44}$$

For any linear filter, represented by its transfer function H_1, the periodic component of the output will have the same frequency as its corresponding input component. However, its phase will change by the phase part of the transfer function and its amplitude will change by a factor of $|H_1|$. Therefore, the output time series can be simulated as follows

$$Q_x(t) = \sum_{i=1}^{N} \sqrt{2S_{LF}\left(\omega_{e,i}\right)\Delta\omega_e} \cdot \cos\left(\omega_{e,i}t + \phi_i + \phi_{LF,i}\right) \tag{2.45a}$$

$$Q_y(t) = \sum_{i=1}^{N} \sqrt{2S_{HSF}\left(\omega_{e,i}\right)\Delta\omega_e} \cdot \cos\left(\omega_{e,i}t + \phi_i + \phi_{HSF,i}\right) \tag{2.45b}$$

$$Q_z(t) = \sum_{i=1}^{N} \sqrt{2S_{VSF}\left(\omega_{e,i}\right)\Delta\omega_e} \cdot \cos\left(\omega_{e,i}t + \phi_i + \phi_{VSF,i}\right) \tag{2.45c}$$

$$M_x(t) = \sum_{i=1}^{N} \sqrt{2S_{TM}\left(\omega_{e,i}\right)\Delta\omega_e} \cdot \cos\left(\omega_{e,i}t + \phi_i + \phi_{TM,i}\right) \tag{2.45d}$$

$$M_y(t) = \sum_{i=1}^{N} \sqrt{2S_{VBM}\left(\omega_{e,i}\right)\Delta\omega_e} \cdot \cos\left(\omega_{e,i}t + \phi_i + \phi_{VBM,i}\right) \tag{2.45e}$$

$$M_z(t) = \sum_{i=1}^{N} \sqrt{2S_{HBM}\left(\omega_{e,i}\right)\Delta\omega_e} \cdot \cos\left(\omega_{e,i}t + \phi_i + \phi_{HBM,i}\right) \tag{2.45f}$$

where S_{LF}, S_{HSF}, S_{VSF}, S_{TM}, S_{VBM}, and S_{HBM} are the one-sided spectral densities of the sectional loads calculated using Eqn. (2.37), ϕ is the random phase angle identical for all six loads, and ϕ_{LF}, ϕ_{HSF}, ϕ_{VSF}, ϕ_{TM}, ϕ_{VBM}, and ϕ_{HBM} are the input-output phase differences for each load. For example, the torsion input-output phase difference is given as

$$\phi_{TM} = \tan^{-1}\left\{\frac{\Im\left[H_{1,TM}(\omega_e)\right]}{\Re\left[H_{1,TM}(\omega_e)\right]}\right\} \tag{2.46}$$

As it can be seen in equation 2.45, all the loads retain the proper phase relationship with the common input. Therefore, the loads themselves are mutually properly correlated.

Since the encounter spectra can have singularities for certain combinations of the ship's speed and relative heading, the product $S_{Load}\left(\omega_{e,i}\right)\Delta\omega_e$ can be replaced by $S_{Load}\left(\omega_i\right)\Delta\omega$ for sufficiently small $\Delta\omega$. The encounter frequency ω_e and the absolute frequency ω are related by Eqn. (2.38). This is possible because the total variance of all periodic load components inside an infinitesimal encounter frequency band is equal to the total variance of all the load periodic components inside the corresponding infinitesimal absolute frequency band, i.e.

$$S_{Load}(\omega)d\omega = S_{Load}\left(\omega_e\right)d\omega_e \tag{2.47}$$

Having obtained the six load time series for the whole voyage or multiple voyages (with seasonality correctly represented), the estimates of the long-term correlation coefficients can be calculated using Eqn. (2.29). Long-term empirical probability distributions of the loads and their combinations can also be found.

An important consideration when simulating load values is how closely must two consecutive load values be spaced in time, in order to accurately represent the time series. According to the Shannon's Theorem (see, e.g., [68]), a continuous time series is completely described if the values are generated with the frequency that is at least twice as large as the maximum frequency, $\omega_{e,MAX}$, of a periodic component that is present in the series. $2\omega_{e,MAX}$ is called the *Nyquist frequency*. It has been found in this work that for all load encounter spectra, $\omega_{e,MAX} < \pi$ rad/s. Therefore, generating load values at the frequency of 2π rad/s or 1 Hz, is sufficient.

Another consideration is the number of encounter frequency intervals, N. This number must be sufficiently large to avoid any periodicities in the simulated time series and to ensure that the assumption of normality can be used according to the Central Limit Theorem. This can be checked by means of a normal q–q plot. $N = 200$ satisfies both of these criteria. Figure 2.7 shows a q–q plot of VBM data for the C 319 container ship navigating in a stationary sea state with $H_S = 4$ meters, $T_0 = 5.2$ seconds, $\alpha = 0$ degrees, and with forward

speed $V = 25.4$ knots. The plot shows no evidence to reject the hypothesis of normality of the stationary VBM during a single sea state.

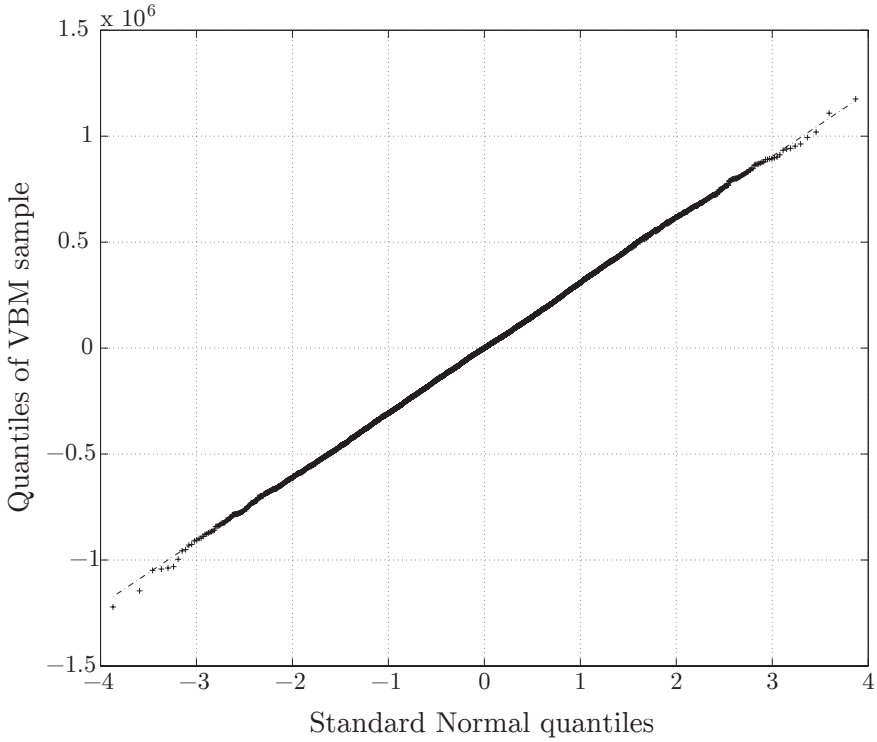

Figure 2.7: q–q plot of the simulated linear VBM data in a single sea state (C 319, $H_S = 4$ m, $T_0 = 5.2$ s, $\alpha = 0°$, $V = 25.4$ kn.

The simulation procedure described in this section is implemented into a computer program using Matlab [76]. In order to take advantage of the Matlab's efficient algorithms for operations on vectors and matrices, the cosine term in Eqns. (2.45) can be rewritten as a difference of the cosine and sine products. If a time series of a certain load, $r(t)$, is being generated from time t_1 to t_M, then the column vector of load values at each time instant is $\boldsymbol{r} = [r_1, r_2, \cdots, r_M]^{\mathrm{T}}$. Also, a column vector of time instants at which the load is being generated can be written as $\boldsymbol{t} = [t_1, t_2, \cdots, t_M]^{\mathrm{T}}$ and a row vector of mid-range encounter frequencies from all N frequency intervals can be written as $\boldsymbol{\omega_e} = [\omega_{e,1}, \omega_{e,2}, \cdots, \omega_{e,N}]$. Simulated load value at time instant t_i is then calculated using Eqn. (2.45)

$$r_i = r(t_i) = \sum_{j=1}^{N} a_{r,j} \cos\left(t_i \omega_{e,j} + \Phi_j\right) = \sum_{j=1}^{N} a_{r,j} \left[\cos\left(t_i \omega_{e,j}\right) \cos \Phi_j - \sin\left(t_i \omega_{e,j}\right) \sin \Phi_j\right] \quad (2.48)$$

where $a_{r,j} = \sqrt{2 S_r\left(\omega_{e,j}\right) \Delta\omega_e}$ is the amplitude of j-th component of the load r and $\Phi_j =$

$\phi_j + \phi_{r,j}$ is the sum of the phase angles from Eqn. (2.45). The total load vector is equal to

$$\boldsymbol{r} = \begin{pmatrix} r_1 \\ r_2 \\ \vdots \\ r_M \end{pmatrix} = \cos \begin{pmatrix} t_1\omega_{e,1} & t_1\omega_{e,2} & \cdots & t_1\omega_{e,N} \\ t_2\omega_{e,1} & t_2\omega_{e,2} & \cdots & t_2\omega_{e,N} \\ \vdots & \vdots & \ddots & \vdots \\ t_M\omega_{e,1} & t_M\omega_{e,2} & \cdots & t_M\omega_{e,N} \end{pmatrix} \begin{pmatrix} a_{r,1}\cos\Phi_1 \\ a_{r,2}\cos\Phi_2 \\ \vdots \\ a_{r,N}\cos\Phi_N \end{pmatrix} - \sin \begin{pmatrix} t_1\omega_{e,1} & t_1\omega_{e,2} & \cdots & t_1\omega_{e,N} \\ t_2\omega_{e,1} & t_2\omega_{e,2} & \cdots & t_2\omega_{e,N} \\ \vdots & \vdots & \ddots & \vdots \\ t_M\omega_{e,1} & t_M\omega_{e,2} & \cdots & t_M\omega_{e,N} \end{pmatrix} \begin{pmatrix} a_{r,1}\sin\Phi_1 \\ a_{r,2}\sin\Phi_2 \\ \vdots \\ a_{r,N}\sin\Phi_N \end{pmatrix} \tag{2.49}$$

The two very large (M × N) cosine and sine matrices from Eqn. (2.49) are pre-calculated once for every combination of ship speed and heading which are the variables that affect the encounter frequency. These results are stored in the computer's memory for even faster load simulation. The complete flowchart of the simulation procedure is given in Appendix A.3. The capabilities and accuracy of this method are presented in the next section.

2.3 Results

This section demonstrates the use and accuracy of the simulation method in determining the long-term correlation coefficients between all six low-frequency wave-induced sectional forces and moments. It also presents the long-term probabilities of exceedance of some important linear and nonlinear combinations of loads. The long-term exceedance probabilities of the VBM are compared with the long-term measurements taken on board a container ship in service on the EA route as well as with the results from the All Sea States Method.

2.3.1 Verification of the Wave Climate Statistical Model

The sampled triplets of variables describing each sea state, H_S, T_0, and β have to be in accordance with the actual observations. Figure 2.8a shows the contour plot of the sea state data from the GWS scatter table for area 9 (North Atlantic) in winter with waves coming from the north. The contours are drown based on the empirical histogram of H_S and T_0 from the scatter table. Figure 2.8b shows the contours of the fitted two dimensional JPDF of H_S and T_0 for the same area, season and wave direction. It can be seen that the fitted JPDF agrees quite well with the observed data. The statistical model for the distribution of H_S and T_0 given A, S and B (see Eqn. (2.30)) with its nine parameters determined using the MLE is sufficiently flexible to capture the distinct shape and scale of the observed data. Superimposed on the contour plot of Figure 2.8b are one thousand sampled sea states. It can be seen that the concentration of the sampled sea states is consistent with their probability

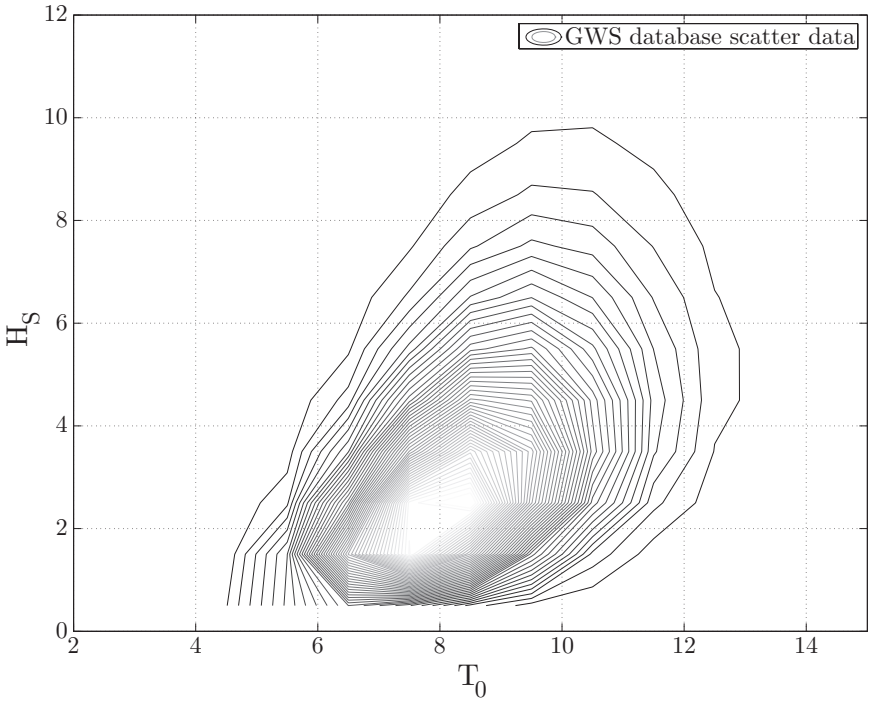

(a) Contour plot of the GWS scatter table data.

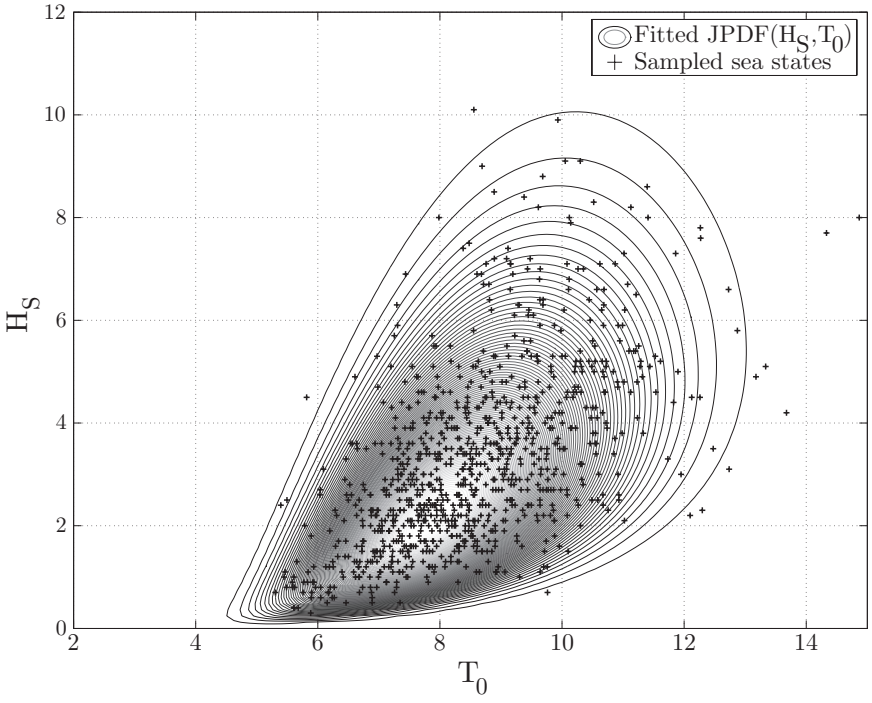

(b) Contour plot of the fitted JPDF(H_S, T_0) and sampled sea states.

Figure 2.8: Validation of sampling for area 9 in winter with waves from the north.

of occurrence which validates the rejection sampling technique that is used in this work. Figure 2.9 also shows the sampled sea states, but this time superimposed on the contour and the surface plot of the fitted JPDF.

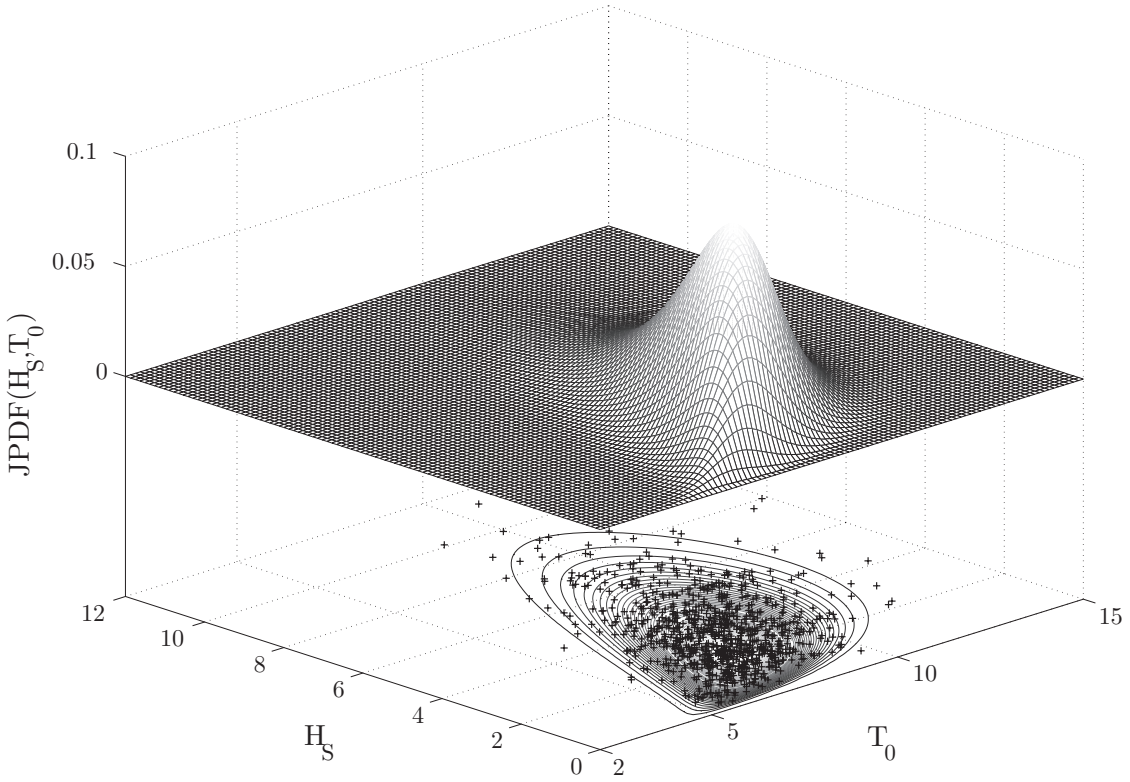

Figure 2.9: Sampled sea sates for area 9 in winter with waves from the north.

Table 2.4: Estimated parameters of $f_{H_S,T_0|A,S,B}(h_S, t_0|a, s, \beta)$ for area 9 in winter.

β	0°	45°	90°	135°	180°	225°	270°	315°	360°
c	0.967	0.943	0.958	1.012	1.108	0.943	0.849	0.899	0.967
m	3.533	3.384	3.422	3.517	3.773	3.644	3.936	3.603	3.533
λ	1.121	1.230	1.209	1.123	0.952	1.069	1.207	1.113	1.121
a_1	0.127	0.118	0.120	0.118	0.113	0.131	0.500	0.140	0.127
a_2	1.837	1.828	1.826	1.827	1.823	1.852	1.517	1.851	1.837
a_3	0.081	0.080	0.083	0.088	0.098	0.079	0.087	0.076	0.081
b_1	0.136	0.148	0.147	0.137	0.139	0.126	0.110	0.115	0.136
b_2	-0.010	-0.018	-0.020	0.017	-0.036	-0.014	0.006	0.065	-0.010
b_3	-0.691	-0.693	-0.693	-0.691	-0.690	-0.692	-0.443	-0.690	-0.691

Bivariate JPDF is used here only to validate the samples of H_S and T_0 since it is easy to plot such a distribution. Actual sampling, however, is done from the trivariate JPDF of

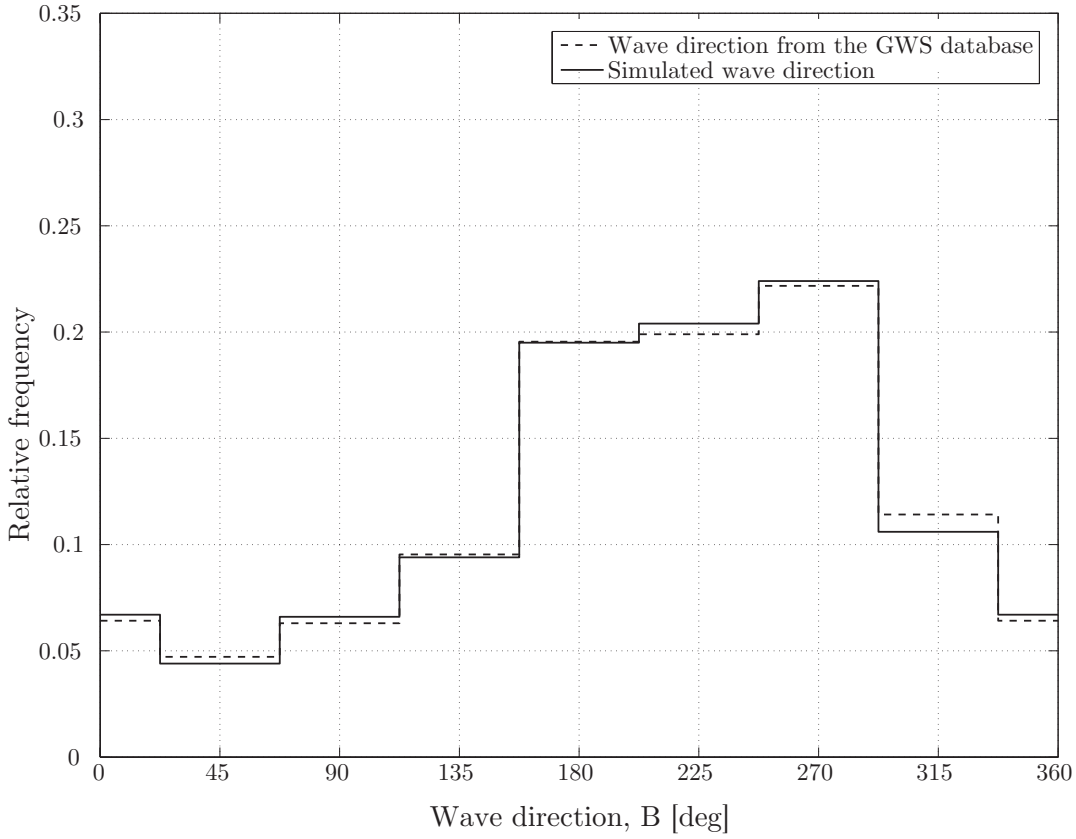

Figure 2.10: Relative frequencies of the wave directions for area 9 in winter.

H_S, T_0, and β (Eqn. (2.34)) which is obtained by performing a directional fit on all nine parameters of the bivariate JPDF, as explained in Section 2.2.2.1. Table 2.4 shows the estimated values of these nine parameters for area 9 in winter and for each wave direction available in the GWS database.

In order to verify the samples of the third random variable, β, triplets of H_S, T_0, and β have to be generated from the trivariate JPDF. Figure 2.10 shows the comparison of relative frequencies of wave directions from the GWS database and from one thousand generated sea state samples for area 9 in winter. The resolution of the sampled wave directions is 10 degrees, while the resolution of the directions from the GWS database is 45 degrees. In order to facilitate the comparison, the sampled directions have been grouped into 45 degree bins as well. As it can be seen, the relative frequencies of wave directions match really well and that is another validation of the developed statistical model of wave climate. A similar validation has also been performed for all areas and seasons considered in this work. It is important to note the dominance of waves coming from the west and the south in area 9. This is also true for most of the areas in the North Atlantic.

Figure 2.11 shows the simulated sea states for fifty voyages of C 319 container ship on

all three routes. It is evident that the North Atlantic is the harshest environment followed by the North Pacific and Euro-Asia. It can also be observed that the assumption of uniform relative heading distribution, which is used by many long-term methods, is not valid on any route. The dominance of following and bow seas can be observed on all routes. Dashed lines in Figure 2.11 represent the Ochi's wave breaking limit for plunging waves [87]. Tests conducted on irregular waves in wave tanks show that the waves with

$$H \geq 0.020gT^2 \tag{2.50}$$

will break. Here, H is the wave height, g is the acceleration of gravity, and T is the wave period. In other words, waves with a hight exceeding the criterion in Eqn. (2.50) cannot exist in nature. In order to limit the occurrence of physically impossible waves, all the simulated sea states in which

$$H_S \geq 0.020gT_0^2 \tag{2.51}$$

are rejected.

2.3.2 Long-Term Correlation Coefficients

Correlation coefficient is a statistical measure of the linear relationship between two random variables, in this case two hull girder sectional loads. Before any buckling and yielding occurs, hull girder stresses in a certain direction, arising from different loads, can simply be added together. In these cases the knowledge of the long-term correlation coefficient can be of great importance. This is especially true for the fatigue analysis of structural details which can fail at stress levels well below the yield stress of the material. That is why many classification societies use long-term correlation coefficients in their rules (see, e.g., DNV [21]).

Long-term correlation coefficients are also used in some long-term load combination methods such as the one described in Section 2.1.2.6 by Baarholm and Moan [11], as well as in the reliability analysis where these coefficients are needed for establishing the simplified joint probability density models of various loads. These models include Morgenstern, Nataf and Copula family of distributions (see Liu and Der Kiureghian [67]). A linear relationship between the vertical and horizontal bending moment is especially important for ship structures.

For all the foregoing reasons, it is important for any long-term load combination method to enable, among other things, an efficient calculation of this statistic. This section presents some of the basic results of the simulation method pertaining to the calculation of estimate of the long-term correlation coefficients between different hull girder sectional loads at amidship. For variation of the correlation coefficients along the length of the ship see Petričić and Mansour [90]. Full symmetric correlation matrices for all six sectional loads are given in Appendix A.4 for each of the six different ships considered in this work and for all three routes. A more detailed analysis of the accuracy of the correlation coefficient estimate is presented for 319 meter long container ship C 319 navigating on the North Atlantic route. This vessel is used throughout this work. Main particulars of all six ships are presented in Table 2.5. Special care has been taken to model the realistic ship forms with realistic

(a) North Atlantic: H_s vs. T_0.

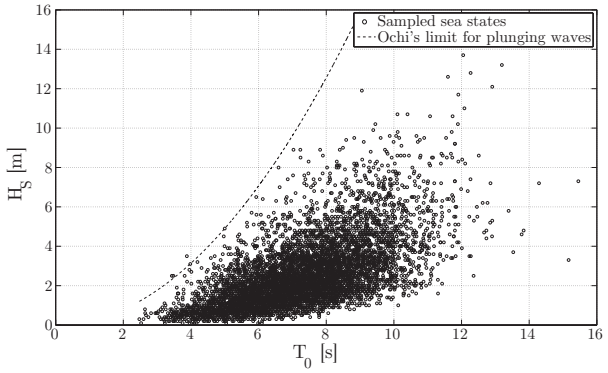

(b) North Atlantic: α.

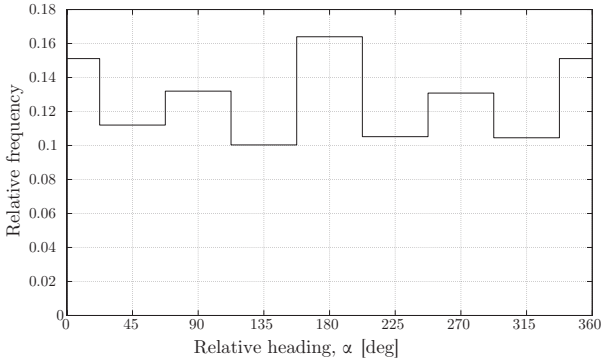

(c) North Pacific: H_s vs. T_0.

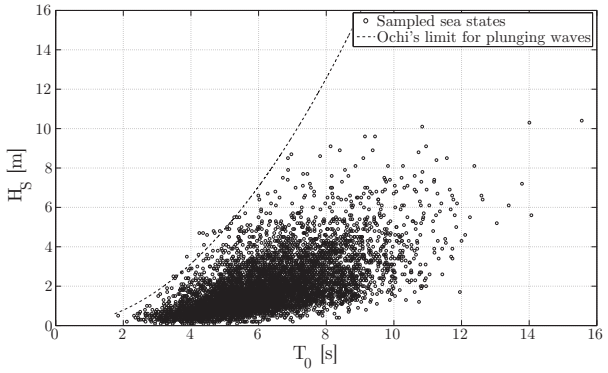

(d) North Pacific: α.

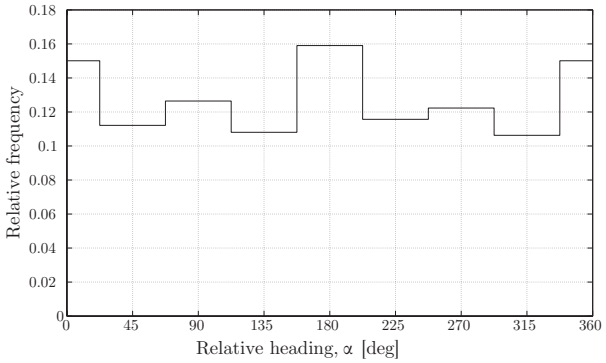

(e) Euro-Asia: H_s vs. T_0.

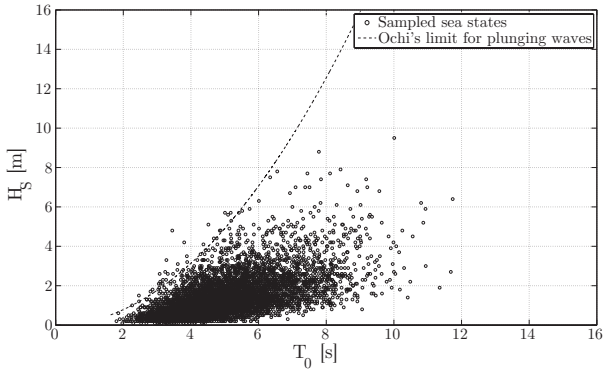

(f) Euro-Asia: α.

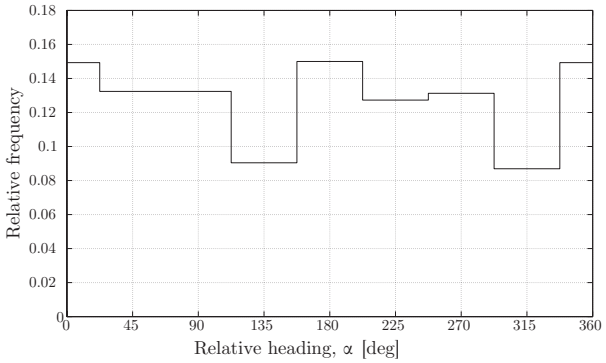

Figure 2.11: Sampled sea states during fifty voyages of C 319 container ship on all three routes.

loading conditions in the SEAWAY ship motion software. Hull forms of these ships are given in Appendix A.5.

Table 2.5: Ship main particulars.

	S 175	C 283	C 319	T 283	T 306	BC 283
L_{pp} [m]	175.00	283.30	319.00	282.89	306.00	283.00
B [m]	25.40	32.20	42.8	49.00	53.90	45.00
T (fl) [m]	9.50	11.26	14.5	15.00	19.00	16.00
T/trim (b) [m]	NA/NA	NA/NA	NA/NA	7.06/2.28	12.00/0.00	6.36/2.95
C_b (fl)	0.588	0.697	0.680	0.835	0.820	0.808
Δ (fl) [t]	24610	67874	135336	172007	263351	168743
Δ (b) [t]	NA	NA	NA	76146	160958	62450
r_x (fl/b) [m]	8.331/NA	13.672/NA	17.12/NA	17.15/19.60	18.87/21.56	15.75/18.00
r_y (fl/b) [m]	42.01/NA	69.10/NA	79.77/NA	70.74/70.74	76.52/76.52	70.76/70.77
r_z (fl/b) [m]	42.06/NA	69.18/NA	79.97/NA	71.23/71.56	77.10/77.77	71.11/71.42
GM (fl/b) [m]	1.00/NA	0.98/NA	2.43/NA	7.46/18.23	8.40/16.97	4.96/16.76
W_d [m^3]	12.54	47.18	52.62	NA	NA	NA
W_s [m^3]	22.69	85.00	87.38	NA	NA	NA
V_d [kn]	25.6	25.6	25.4	15.0	15.0	15.0
Type	Container	Container	Container	Tanker	Tanker	Bulk carrier

fl = full load
b = ballast
W_d = section modulus of the deck
W_s = section modulus of the side
r_x = mass radius of gyration about x axis
r_y = mass radius of gyration about y axis
r_z = mass radius of gyration about z axis
V_d = design speed

Figure 2.12 shows a scatter plot of the VBM versus the HBM for C 319 container ship navigating on the North Atlantic route. A fair amount of linear relationship exists between these two loads which leads to a relatively high estimate of the long-term correlation coefficient, as will be shown later in this section.

The effects of the number, N, of frequency bands inside the load spectra frequency range and the time resolution of each load series has been analyzed in this work. It has been found that neither N, nor the time resolution affect the correlation coefficient estimate. N has been varied from 50 to 500 and time step from 0.5 seconds to 100 seconds with almost no effect on the results. Even for lower values of N, there is no empirical evidence to reject the assumption of normality of the load time series in the Central Limit sense. Also, due to non-zero load components at very low encounter frequencies, the output time series has no periodicities during any of the short-term periods.

The effects of length of each of the load time series on the variability of the correlation coefficient estimate are shown in Table 2.6 for C 319 container ship on NA route. For simplicity, estimates are given for forces and moments separately. Full symmetric correlation matrix for this ship on NA route is given in Table 2.7 that includes mutual correlations between all forces and moments. As already mentioned, Appendix A.4 contains correlation

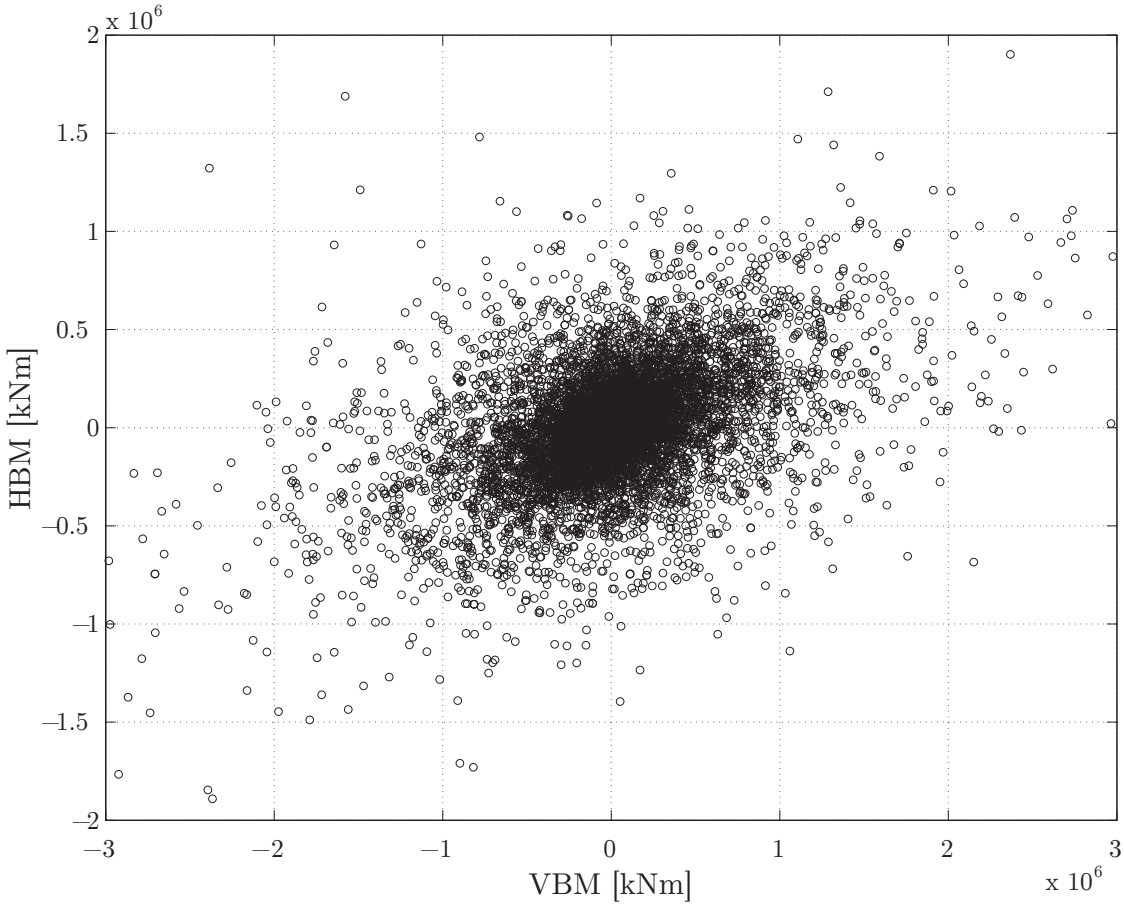

Figure 2.12: Scatter plot of VBM vs. HBM for C 319 container ship on NA route.

matrices for all six ships navigating on all three routes. Estimates of the long-term correlation coefficients given in those tables have a coefficient of variation of less than 0.05.

Each row of Table 2.6 presents the results of a total of 50 simulations, but with different length of the time series (1 voyage, 5 voyages, 10 voyages, 25 voyages, and 50 voyages). As it was stated in Section 2.2.1, and proven in Appendix A.1, the estimate of the correlation coefficient, R, approaches its true (population) value in probability as the length of the time series increases. This can be seen from the fact that the variability of the estimate, represented by the coefficient of variation (δ = ratio between the standard deviation and the mean value), decreases as the time series length increases. At the same time, the mean values of the correlation coefficient estimates (μ_R) do not change appreciably. Therefore, even fifty consecutive simulations of one voyage are sufficient to accurately estimate the true correlation coefficient using the mean value of its estimates. This simulation takes a couple of minutes on an ordinary personal computer. It can be noticed that the coefficient of variation of the estimate of the correlation coefficient between torsion and horizontal bending moment does not quite follow the decreasing trend as the length of the simulated time series increases.

This is due to the fact that the estimated value of the corresponding correlation coefficient between torsion and horizontal bending moment is very close to zero.

Table 2.6: Estimates of the correlation coefficient between various loads for C 319 container ship on NA route.

No. of sim.	Length of sim.	Q_x-Q_y		Q_x-Q_z		Q_y-Q_z		M_x-M_y		M_x-M_z		M_y-M_z	
		μ	δ	μ	δ	μ	δ	μ	δ	μ	δ	μ	δ
50	1 voy.	-0.17	-0.508	0.28	0.191	-0.18	-0.329	0.17	0.359	-0.01	-3.752	0.42	0.168
50	5 voy.	-0.17	-0.225	0.28	0.074	-0.17	-0.172	0.18	0.172	0.00	-6.970	0.42	0.069
50	10 voy.	-0.17	-0.170	0.28	0.050	-0.17	-0.107	0.18	0.123	0.00	13.104	0.42	0.048
50	25 voy.	-0.17	-0.095	0.28	0.032	-0.17	-0.055	0.18	0.070	0.00	2.991	0.42	0.030
50	50 voy.	-0.16	-0.071	0.28	0.026	-0.17	-0.044	0.18	0.046	0.00	3.252	0.42	0.019
50 (Bts.)	50 voy.	-0.18	NA	0.29	NA	-0.18	NA	0.16	NA	-0.02	NA	0.42	NA

μ = mean value of the correlation coefficient estimate

δ = coefficient of variation of the correlation coefficient estimate

Note: Simulation time for a single time series containing fifty voyages is four minutes on Intel® Core™ i7 processor, while the total simulation time for bootstrap (fifty resamplings of fifty voyages long time series) is twenty minutes on the same machine.

The last row in Table 2.6 corresponds to the resampling technique called the bootstrap. The multiple samples of load values are obtained by resampling values from only one time series of each load. Resampling is done randomly, with replacement, and simultaneously for all loads to retain the correlation. This is equivalent to generating alternative samples based on the empirical distributions of the loads, but it is much faster than the simulation procedure described thus far. Bootstrap method is a fast and accurate alternative for obtaining the mean value of the correlation coefficient estimate, yielding almost the same values as the multiple voyage simulations. However, if the variability of the correlation coefficient estimate is to be determined, then multiple voyage simulations have to be used. On its own, bootstrap does not provide any convergence guarantees since it is based on samples created by resampling of a single sample, not on truly different samples generated by multiple simulations.

As stated before, in the case of C 319 container ship on NA route there is a fair amount of positive correlation between the two most dominant hull girder sectional loads: the vertical and horizontal bending moments. This is the most important correlation coefficient in terms of its significance in the ship design process. Significant positive correlation exists between the longitudinal force and the vertical bending moment as well. This is expected, considering that both loads reach their maximum in seas with the same relative wave directions; in head and following seas (0° and 180°). Also, a large negative correlation exists between the horizontal shear force and torsion. On the other hand, torsion and horizontal bending moment appear to be uncorrelated. Finally, it is important to note that the sign of the correlation coefficient estimates depends on the sign convention of the sectional loads.

Table 2.7: Long-term correlation coefficient estimates for C 319 on NA route (C.O.V. < 0.05).

	Q_x	Q_y	Q_z	M_x	M_y	M_z
Q_x	1.00	-0.16	0.28	0.21	0.58	0.19
Q_y	-0.16	1.00	-0.17	-0.72	-0.07	0.11
Q_z	0.28	-0.17	1.00	0.10	0.08	-0.03
M_x	0.21	-0.72	0.10	1.00	0.18	0.00
M_y	0.58	-0.07	0.08	0.18	1.00	0.42
M_z	0.19	0.11	-0.03	0.00	0.42	1.00

Table 2.8 shows a comparison of the correlation coefficients between the VBM and the HBM and also between the VSF and the VBM for all six ships and all three routes. It is seen

Table 2.8: Comparison of some important long-term correlation coefficients.

		C 319	C 283	S 175	T 306	T 283	BC 283
M_y-M_z	NA	0.42	0.49	0.42	0.32	0.34	0.36
	NP	0.39	0.47	0.41	0.34	0.36	0.41
	EA	0.35	0.43	0.37	0.25	0.29	0.31
Q_z-M_y	NA	0.08	0.14	0.04	0.15	0.38	0.22
	NP	0.09	0.14	0.00	0.12	0.36	0.21
	EA	0.09	0.13	-0.09	0.06	0.30	0.12

that correlation coefficient estimates between the VBM and the HBM are larger for container ships than for the tankers and bulk carrier. In general, all correlation coefficients are lowest on the EA route, while they don't differ significantly between NA and NP routes. This is probably related to the distribution of relative headings on these routes, see Figure 2.11.

Literature review has revealed that there is very little published information on the values of the long-term correlation coefficients between different loads which could be used for comparison purposes.

Hovem [40] calculated the long-term correlation coefficient between stresses due to VBM and HBM, $\rho_{M_y-M_z}$, implicitly using the simplified short-term load combination model of Eqn. (2.21). She used the long-term extreme values of the individual loads and their sum instead of short-term ones. The loads were calculated using the All Sea States Method assuming long-crested narrow-banded waves, North Atlantic route, constant loading condition, and zero forward speed of the vessel. Stresses at various points on the ship's cross section have been calculated from the bending moments using the simple beam theory. Therefore, stresses due to VBM and HBM should have the same magnitude of correlation, regardless of the position on the cross section. Depending on the position of the stresses that are being evaluated with respect to neutral lines for vertical and horizontal bending, only the sign of the correlation can change. However, if the implicit method of calculating the correlation

coefficients is used, then their magnitudes may also vary, as can be seen in [40]. Hovem analyzed two tankers, one of which had main particulars and loading condition comparable to T 306 tanker analyzed in this work. The reported values of the long-term correlation coefficient between stresses due to VBM and HBM are shown in Table 2.9 for the side shell at waterline level (first value) and for bottom plating B/4 from the centerline (second value). As mentioned before, these two values differ only because of the simplified implicit calculation procedure used in [40]. Both values agree well with the one obtained in this work for the similar ship in long-crested seas. Based on the work by Hovem, the classification society DNV adopted an average value of $\rho_{M_y-M_z} = 0.1$ to be used in the fatigue analysis of all ship types in the absence of more precise values.

The International Ship Structures Congress (ISSC) [46] suggested the use of long-term correlation coefficients calculated by Kikuiri and Mathisen [56]. These two authors did a systematic long-term study on the Series 60 ships and calculated the values of the correlation coefficients between the VBM and the HBM and also between the VSF and the VBM for various ship lengths, block coefficients, and positions along the hull. Kikuiri and Mathisen used a method similar to that of Hovem with one (top) speed, narrow-banded waves assumption, and North Atlantic conditions. Their results can be compared with the simulation results by matching the length and block coefficient of the Series 60 vessel with the corresponding particulars of the C 319 and T 306 vessels used in this work. The long-term correlation coefficients between the VBM and the HBM from the simulation method for short-crested seas agree very well with the results of Kikuiri and Mathisen for both vessels (see Table 2.9), in spite the fact that C 319 and T 306 ships don't have exactly the same hull forms or loading conditions as the matching Series 60 vessels. In the long-crested sea, which is a simplification over the more realistic short-crested sea, the simulation results give larger values of the correlation coefficient. This is expected since there is less directional variability in the incoming waves, and subsequently less variability in the sectional loads.

The results for the correlation coefficients between the VSF and the VBM don't agree quiet as well, although, both methods predict that they are significantly lower than the correlation coefficients between the VBM and the HBM. This may be due to differences between the VSF transfer functions used by these methods, especially in the phase part. As can be seen in Tables 2.8, the value of the correlation coefficient between the VSF and the VBM is much more sensitive to ship type, size, and route than the value of correlation coefficient between the VBM and the HBM.

Literature survey performed during this work has not revealed any published values of the long-term correlation coefficients between sectional forces and moments which were calculated based on actual long-term measurements of loads on board ships in service. Although the long-term correlation coefficients calculated using the simulation method agree quite well with the other calculated long-term correlation coefficients found in the literature, the real validation of the simulation method (and other available methods) with respect to correlation coefficient calculations can only be done in direct comparison with the measured values. This remains an object of further study when such measurements become available.

Table 2.9: Comparison of long-term correlation coefficients from different sources.

		Simulation (L-C)	Simulation (S-C)	Hovem (L-C)	Kikuiri and Mathisen
M_y-M_z	C 319	0.53	0.42	NA	0.42
	T 306	0.43	0.32	0.38 / 0.47	0.33
Q_z-M_y	C 319	0.11	0.08	NA	0.14
	T 306	0.24	0.15	NA	0.21

L-C = long-crested waves
S-C = short-crested waves

2.3.3 Probability of Exceedance and Linear and Nonlinear Combinations of Linear Loads

It is of great importance for the ship designer to know the statistical properties of the loads to which the structure of the ship will be subjected during its lifetime, especially the long-term probability of exceedance of the load peaks. These probability distributions are used in the fatigue analysis of critical structural details, or they can be used to obtain the extreme value distributions of load peak values during a certain period of time. Long-term probabilities of exceedance can be determined for individual loads or for the combined load. If individual probability distributions are used, then the knowledge of the correlation between the loads is usually required (see previous section).

This section presents the results of the simulation method pertaining to the long-term probabilities of exceedance of the VBM, as well as to the probabilities of exceedance of stresses arising from the linear and nonlinear combinations of hull girder sectional loads. Again, the majority of the presented results are for the C 319 container ship. However, probabilities of exceedance of the VBM are given for C 283 container ships in order to compare them with the measurements taken over a period of three years on board a very similar ship trading on the Europe-Asia route. Nonlinear combination of loads is performed on the S 175 container ship.

Examples of correlated time series of the VBM and the HBM for one whole voyage of C 319 on NA route are shown in Figures 2.13a and 2.13b, respectively. There are more than 800,000 simulated load values in each of those series which are generated at one second intervals. No detail can be observed at such density of points in the graph. However, different sea states can be clearly distinguished. Figures 2.13c and 2.13d show only one hundred seconds long portions of the simulated time series of these loads around time T which corresponds to the largest generated value of the VBM. Black circular markers denote the positions of the local positive peaks. It is important to note that every local peak is identified and counted. For narrow-banded signals there is only one positive peak between

an up-crossing and a down-crossing of the zero load level. On the other hand, non-narrow-bended signals can have multiple positive (or negative) peaks between two crossings of the zero level, like in Figures 2.13c and 2.13d. In order to obtain the correct estimate of the cumulative distribution function of load peaks, it is, therefore, necessary to consider every up-crossing of a certain threshold level.

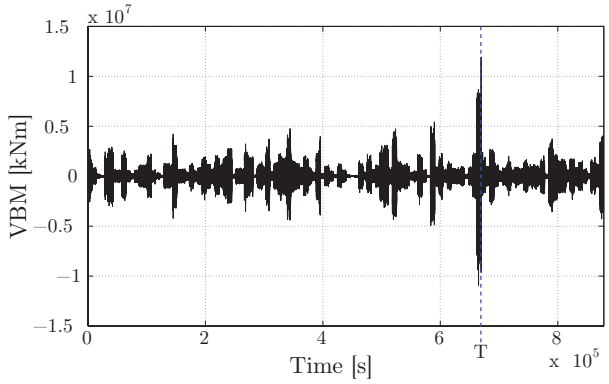

(a) Time series of the VBM for one voyage.

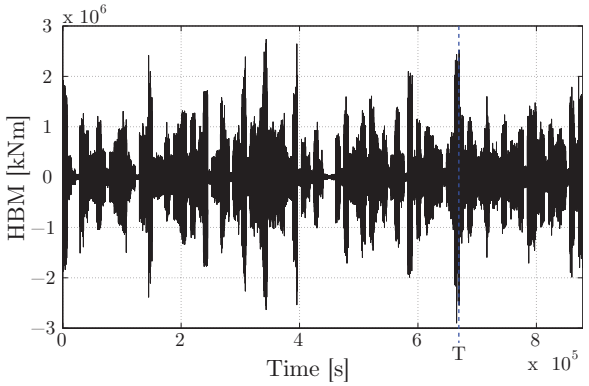

(b) Time series of the HBM for one voyage.

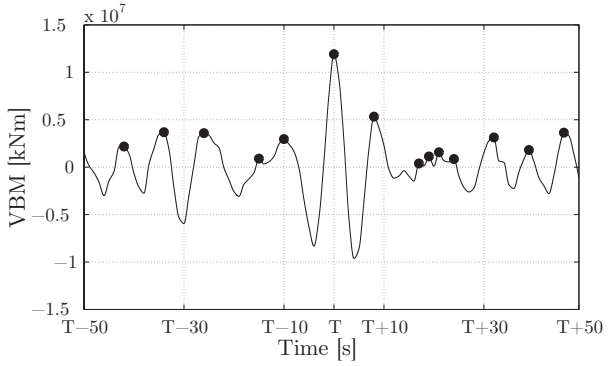

(c) Hundred seconds portion of the VBM time series.

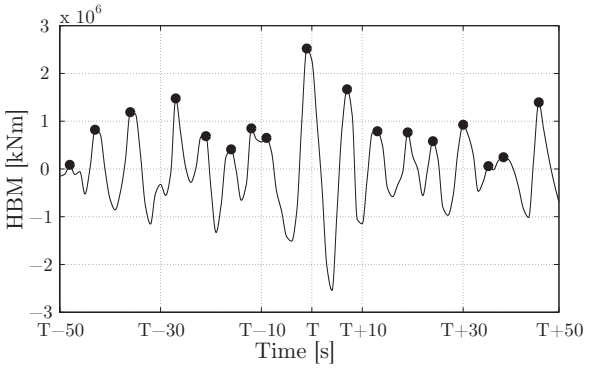

(d) Hundred seconds portion of the HBM time series.

Figure 2.13: Correlated time series of the VBM and the HBM for C 319 on NA route.

The estimate of the cumulative distribution function is called the empirical cumulative distribution function (ECDF). If $X_1, X_2, \ldots, X_n$ is a random sample of load values from the long-term cumulative distribution function F, and if $I_j(x)$ is the indicator random variable for the event $X_j \leq x$ such that $I_j(x)$ equals one if $X_j \leq x$ and zero otherwise, then the ECDF of the sample is

$$\widehat{F}(x) = n^{-1} \sum_{j=1}^{n} I_j(x) \tag{2.52}$$

The $I_j(x)$ are independent and each has the Bernoulli distribution with probability $\Pr[I_j(x) = 1] = F(x)$. Therefore $\widehat{F}(x)$ is an average of independent identically distributed variables and has mean $F(x)$ and variance $F(x)[1 - F(x)]/n$. Also, at a value x for which $0 < F(x) < 1$, we have

$$\widehat{F}(x) \xrightarrow{\mathrm{P}} F(x), \quad n^{1/2} \frac{\widehat{F}(x) - F(x)}{\{F(x)[1 - F(x)]\}^{1/2}} \xrightarrow{\mathrm{D}} Z, \quad \text{as } n \to \infty \tag{2.53}$$

where Z is a standard normal variate, $\xrightarrow{\mathrm{P}}$ denotes the convergence in probability and $\xrightarrow{\mathrm{D}}$ denotes the convergence in distribution. Therefore, the standard error of $\widehat{F}(x)$ is equal to

$$V^{1/2} = \sqrt{\widehat{F}(x)\left[1 - \widehat{F}(x)\right]/n} \tag{2.54}$$

and the 95% confidence intervals of $\widehat{F}(x)$ are given as

$$\widehat{F}(x) - 1.96 \cdot V^{1/2} \leq F(x) \leq \widehat{F}(x) + 1.96 \cdot V^{1/2} \tag{2.55}$$

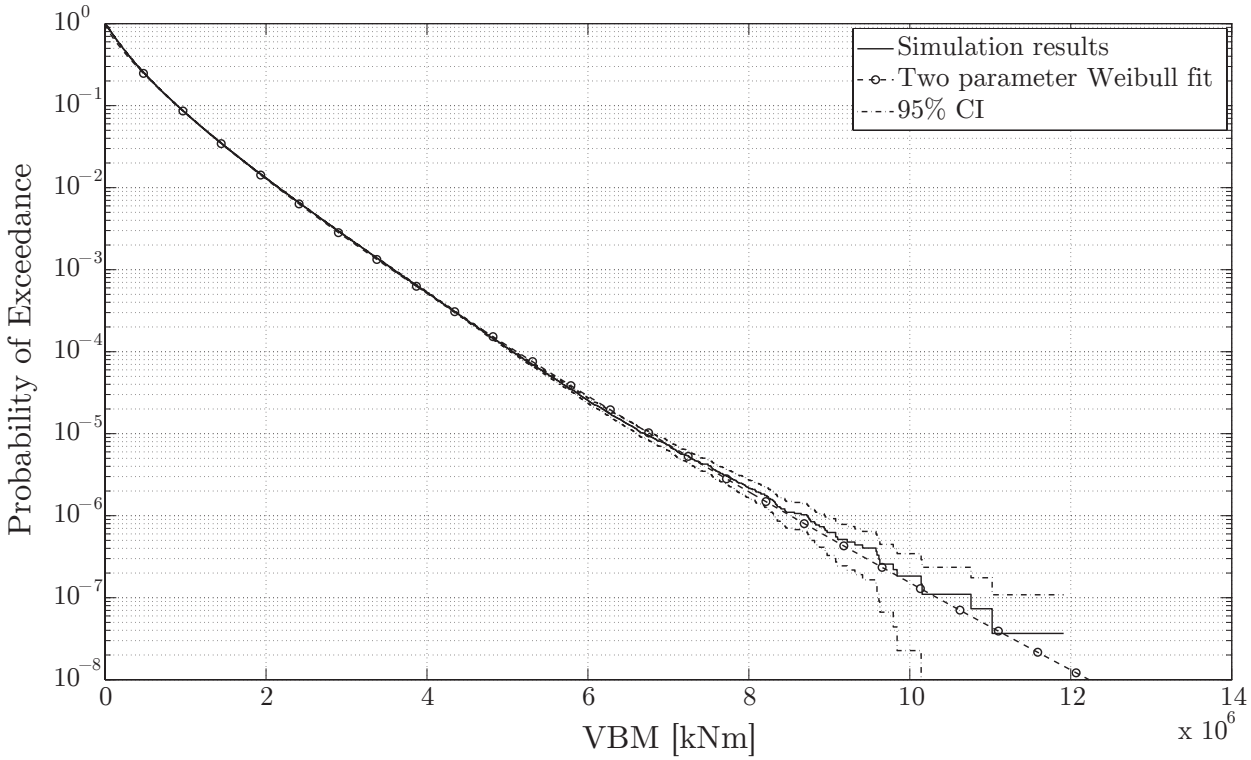

Figure 2.14: Probability of exceedance of VBM peaks based on two hundred voyages of C 319 container ship on NA route.

Figure 2.14 shows the plot of estimated probability of exceedance of the VBM peaks based on 200 voyages long time series for C 319 container ship navigating on NA route. Estimated probability of exceedance is equal to 1-ECDF. Also plotted are the 95% confidence intervals and the two parameter Weibull distribution fitted to the VBM peaks using the MLE. Weibull distribution is chosen based on at-sea measurements of the wave-induced bending moments carried out by Little et al. [66], Lewis and Zubaly [62] and Fain and Booth [23]. These measurements suggested that the wave-induced bending moments appear to follow the two parameter Weibull distribution. Many other researchers have also arrived at similar conclusions, including Frieze et al. [25]. The plot in Figure 2.14 also shows that the two parameter Weibull distribution appears to fit the simulated VBM peaks very well. The CDF of two parameter Weibull distribution is given as follows

$$F(x) = 1 - e^{-\left(\frac{x}{\lambda}\right)^k}, \quad x \geq 0 \tag{2.56}$$

where $\lambda > 0$ and $k > 0$ are the scale and shape parameters, respectively. Understandably, due to small number of generated load values with extremely small probabilities of exceedance (smaller than 10^{-5}), the confidence intervals become larger at those small probabilities. However, the Weibull probability plot of the ECDF in Figure 2.15 shows a very good agreement between the simulated data and the fitted Weibull distribution, especially in the right tail region for very large values of the VBM. As the right tail of the Weibull distribution is the only one that matters in the extreme value analysis, the not-so-god fit at the lowest values of the VBM is of no practical significance.

2.3.3.1 Sufficient Number of Simulated Voyages

The results presented in Figure 2.14 are based on the two hundred voyages long time series of the VBM. In order to assess the effect of the length of simulated time series on the parameters of the corresponding Weibull fits, the foregoing analysis is repeated for ten, twenty five, fifty, and hundred voyages. Figure 2.16 shows the Weibull fits of the VBM peaks from time series of different lengths. Table 2.10 presents the values of the Weibull scale and shape parameter estimates, as well as their confidence bounds and the values of the extreme VBM with a probability of exceedance of 10^{-8} which correspond to "once in 20 years" event. As it can be seen in Figure 2.16, the Weibull fits for ten and twenty five voyages lie little above the Weibull fits for fifty, hundred and two hundred voyages. The last three fits lie virtually on the same line showing convergence in distribution, and have almost the same value of the VBM at the probability level of 10^{-8}. Therefore, simulating time series that are fifty voyages long seems to be sufficient for estimating the long-term probabilities of exceedance of the load peaks. This is confirmed for all ship types and all routes.

2.3.3.2 Long-Term Effects of Ship Route

Figure 2.17 shows the effect of route on the long-term probabilities of exceedance of the VBM peaks for C 319 container ship. Plotted are the Weibull fits of the simulated VBM values

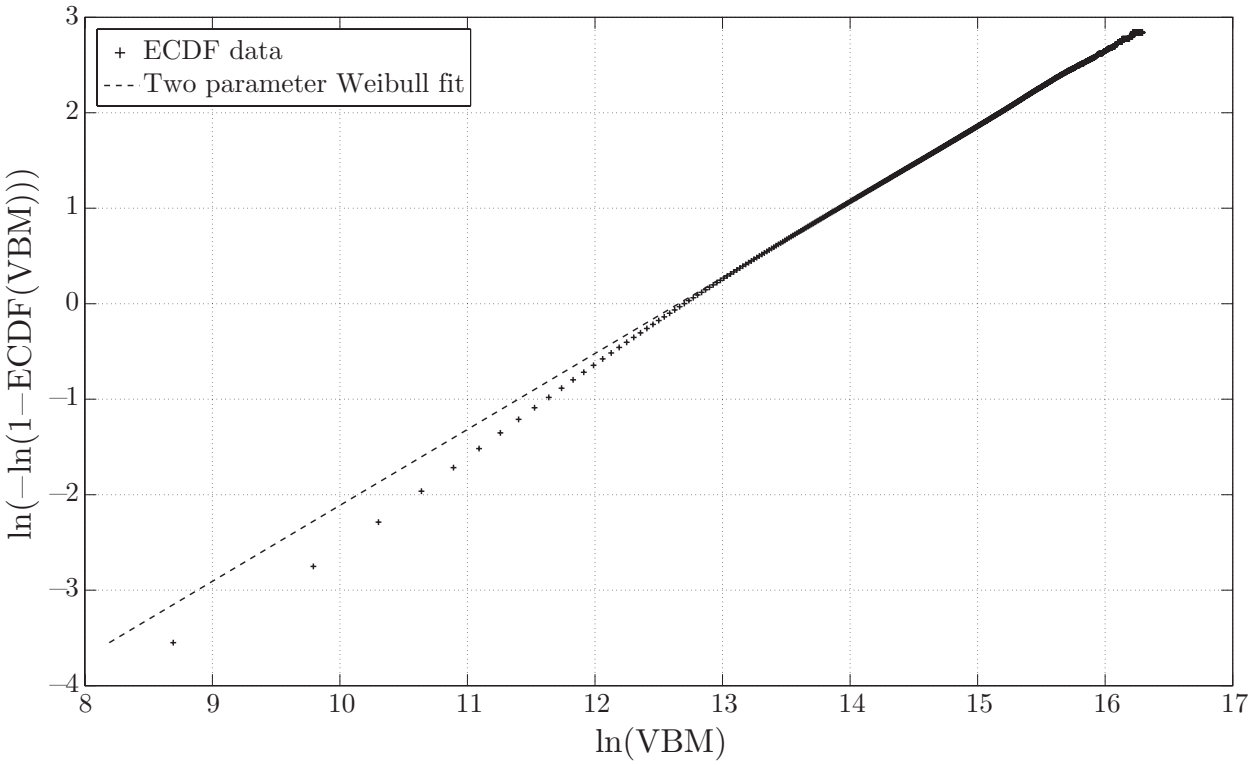

Figure 2.15: Weibull probability plot of the simulated VBM data for two hunderd voyages of C 319 container ship on NA route.

Table 2.10: Weibull parameter properties for different lengths of simulations.

Length of t. s.	λ [kNm]			k			VBM at Pr = 10^{-8}
[voyages]	$\widehat{\lambda}$	LCB	UCB	$\widehat{k}$	LCB	UCB	[kNm]
200	3.14E+05	3.13E+05	3.14E+05	0.795	0.795	0.796	1.223E+07
100	3.15E+05	3.15E+05	3.15E+05	0.796	0.795	0.796	1.226E+07
50	3.15E+05	3.14E+05	3.15E+05	0.795	0.794	0.795	1.230E+07
25	3.14E+05	3.14E+05	3.14E+05	0.791	0.790	0.791	1.252E+07
10	3.16E+05	3.16E+05	3.16E+05	0.791	0.790	0.791	1.258E+07

LCB = lower 95% confidence bound
UCB = upper 95% confidence bound
$\widehat{\lambda}$ = the estimate of the Weibull scale parameter λ
$\widehat{k}$ = the estimate of the Weibull shape parameter k

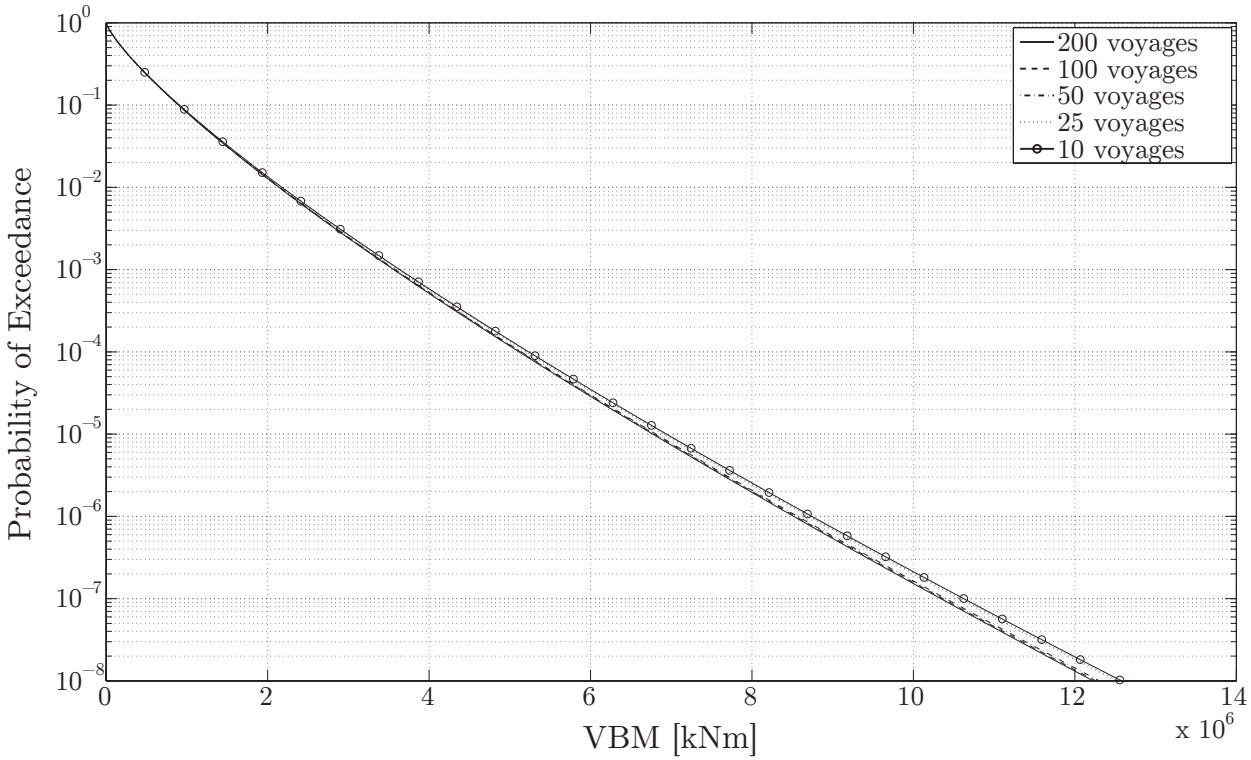

Figure 2.16: Weibull fits of the VBM peaks from time series of different lengths for C 319 container ship.

on all three routes considered in this work. As expected, there is a significant difference between different routes in terms of the probability of exceedance of the VBM peaks. The North Atlantic route produced the largest probabilities of exceedance. It is widely regarded as the harshest part of the oceans and commonly taken as the design ocean area for the ships that are designed for unrestricted navigation. The North Atlantic route is followed by the North Pacific route and then by the Europe Asia route which has the lowest probabilities of exceedance. This is also consistent with the ocean wave climate statistics. It is interesting to note that the extreme VBM value with the probability of exceedance of 10^{-8} on the EA route is 38.6% smaller than the corresponding value on the NA route.

The fourth line in Figure 2.17 represents the "Worldwide" route which consists of 200 voyages long time series of the VBM on the NA route concatenated with the time series of equal lengths from the NP and EA routes, respectively. It can be seen that the NP route has a dominating effect on the resulting "Worldwide" route at small values of the VBM, while the NA route has a dominating effect for extreme values of the VBM. These results show how time series from different routes can easily be concatenated, provided that the percentage of ship's lifetime spent on each route is known. In this example, equal proportions of time are assigned to each route. The simulation method can be tailored to the specific operation

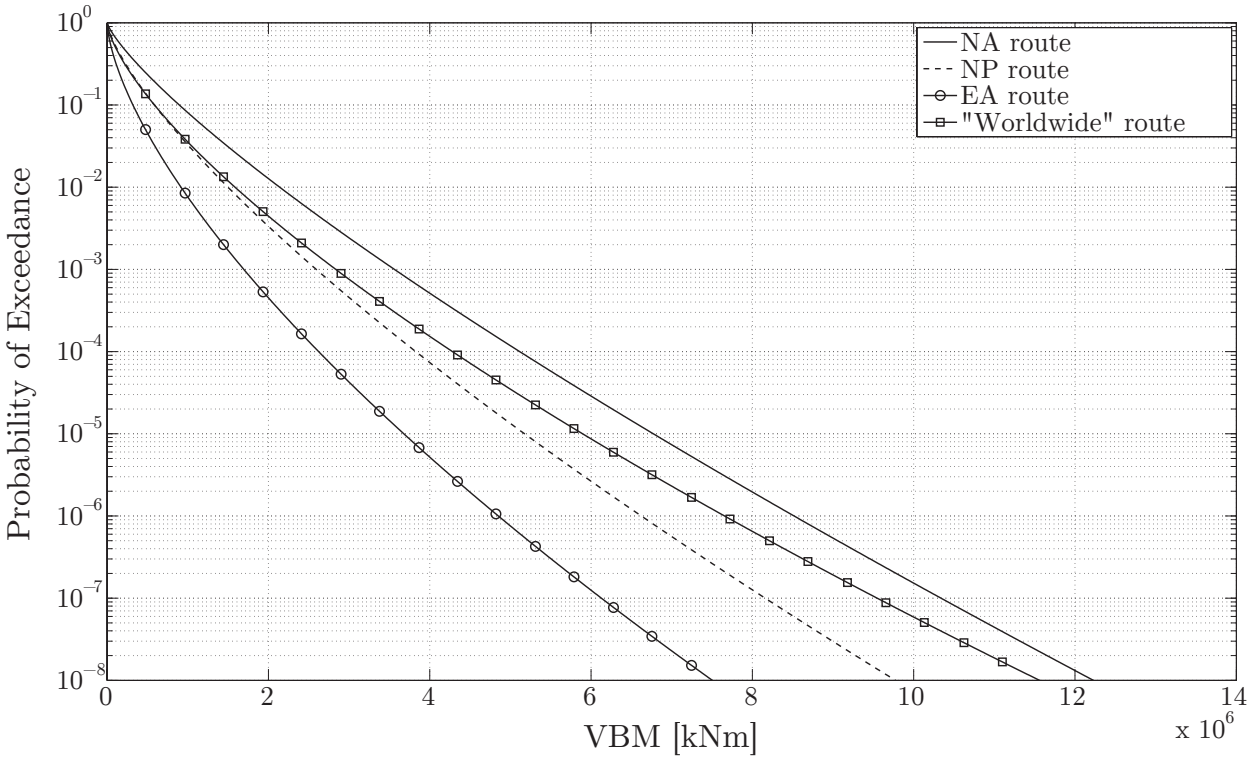

Figure 2.17: Weibull fits of the VBM peaks for C 319 container ship on different routes.

profile of the ship that is expected to navigate on multiple routes.

Table 2.11 presents the parameter properties of the Weibull fits to the simulated VBM peaks for all four routes. The values of the extreme VBM at 10^{-8} probability level are given as well.

Table 2.11: Weibull parameter properties for C 319 container ship on different routes.

	λ [kNm]			k			VBM at Pr = 10^{-8}
Route	$\widehat{\lambda}$	LCB	UCB	$\widehat{k}$	LCB	UCB	[kNm]
NA	3.14E+05	3.13E+05	3.14E+05	0.795	0.795	0.796	1.223E+07
NP	1.90E+05	1.89E+05	1.90E+05	0.739	0.738	0.740	9.774E+06
EA	9.04E+04	9.00E+04	9.07E+04	0.659	0.658	0.660	7.504E+06
"Worldwide"	1.78E+05	1.77E+05	1.78E+05	0.698	0.697	0.699	1.156E+07

LCB = lower 95% confidence bound
UCB = upper 95% confidence bound
$\widehat{\lambda}$ = the estimate of the Weibull scale parameter λ
$\widehat{k}$ = the estimate of the Weibull shape parameter k

2.3.3.3 Comparison With Full-Scale Measurements and All Sea States Method

A comprehensive literature survey has been conducted on full-scale long-term measurements of global hull girder sectional loads on ships. A number of studies have been identified, but few were reported in such detail that they could be used for accurate comparison with the results developed in this work. In most cases, data on ship main particulars and ship geometric characteristics was missing. In other instances there was no, or little information on the environmental and operating conditions under which the full-scale measurements were collected. Only one study by Okada et al. [88] has been identified where the measurements were collected in a way that enabled the authors to isolate the low frequency wave-induced loads such are the ones considered in this chapter. The authors have collected the full-scale measurements of stresses and deformations on a post-Panamax container ship navigating for 3 years between Europe and Japan. The main particulars of the ship ($L_{pp} \times B \times D \times T =$ 283.8 m $\times$ 42.8 m $\times$ 24.4 m $\times$ 14.0 m) are comparable with the particulars of the C 283 container ship analyzed in this work with the exception of beam. Both ships have very similar operational profiles and loading conditions.

In [88] the high-frequency components of the measured stresses due to springing and slamming were filtered using a low-pass filter, thus making possible the comparison with the results of this chapter. Okada et al. considered only the maximum peaks between two zero crossings, omitting other positive (or negative) peaks. They have effectively reduced the original signal to a narrow-banded one, where each up-crossing event if followed by a single peak, and discarded the information contained in other peaks. This procedure slightly alters the resulting ECDF of the stress peaks. The amount of alteration depends on the band of the original stress signal.

Comparison between simulation, All Sea States Method and the full-scale measurements with respect to the vertical bending stress amplitudes for C 283 container ship on the EA route is shown in Figure 2.18. Only the original output from each method is shown, without corresponding Weibull fits. This is done to facilitate the comparison and to avoid cluttering the plot. The simulation results agree very well with the full-scale measurements up to the probability level of 10^{-6}. Beyond this probability level there is some discrepancy, but this is quite expected since the confidence intervals of the estimated cumulative distribution functions are fairly wide in that region. Probability of exceedance of the largest data point in the measured or simulated data set does not accurately represent the true (population) probability of exceedance. For example, if the measurement time had been doubled and if the largest measured data point from the first half of the measurement had not been reached again (or exceeded), then the probability of exceedance of the largest measured data point would have been approximately twice as low. Finally, regarding the full-scale measurements, there is additional uncertainty about the accuracy of measuring large stresses.

On the other hand, the All Sea States Method significantly overestimates the exceedance probabilities in the entire stress range. It relies on the assumptions that the VBM is narrow-banded and that the relative headings of the ship are uniformly distributed and independent from other random variables. It employs a single scatter table of relative frequencies of sea

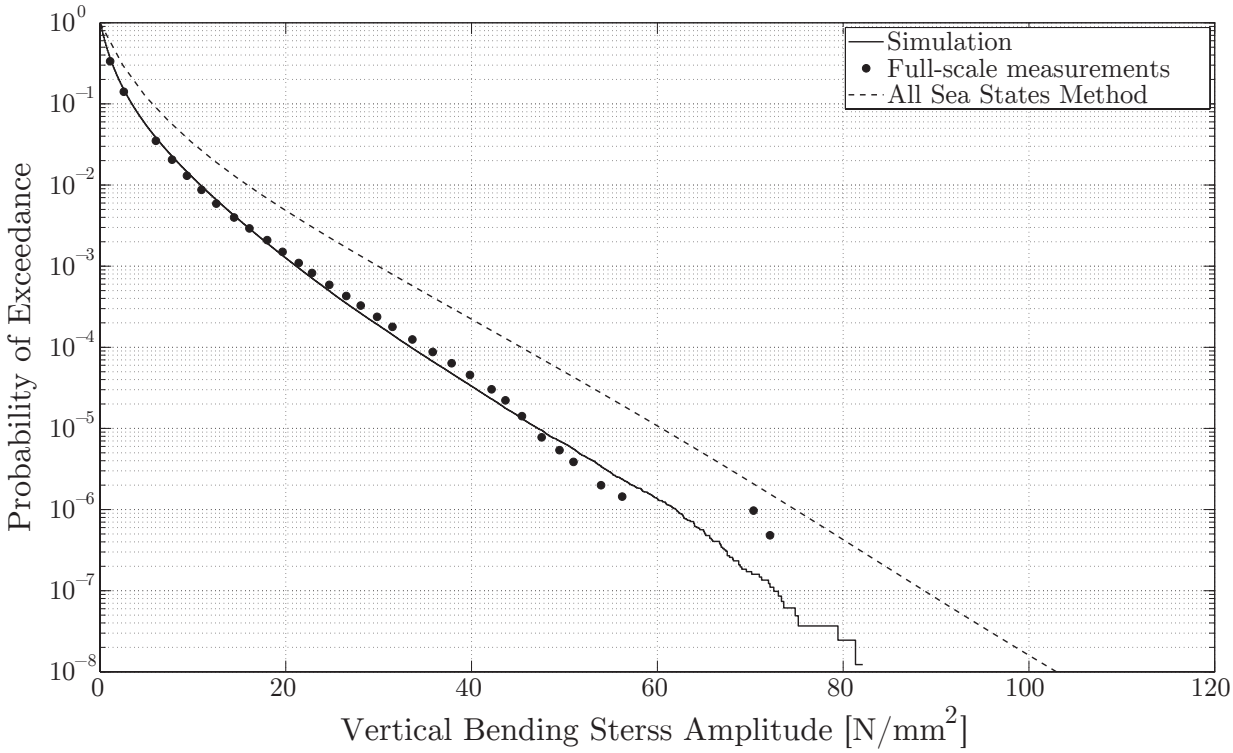

Figure 2.18: Comparison of simulation results with full-scale measurements and All Sea States Method for C 283 container ship on EA route.

states for the entire EA route, all seasons, and all wave directions, and uses the same velocity profile and linear transfer functions as the simulation method.

Simulation method avoids most of the assumptions of the All Sea States Method, and it is capable of representing the real ocean environment and ship operational conditions with much more detail and accuracy. Therefore, the results it produces match the full-scale measurements more closely. Naito et al. [80] also observed that the All Sea States Method significantly overestimates the exceedance probabilities of the longitudinal stresses due to VBM in the deck at amidship, compared with the full-scale measurements on a 261 meters long container ship on the NP route. They have developed a probability density function of the standard deviation of the ship response using two different approaches. First approach is based on considering the operational limitations of the ship through the use of critical standard deviations proposed by the classification societies or by various maritime institutions. The second approach is to use the full-scale measurements of the ship responses to find this distribution. The authors have showed how these PDFs can be used to calibrate the standard All Sea States Method. Not surprisingly, the calibration with the full-scale measurements seems to produce the best results. Guedes Soares and Moan [31] reported that the probabilities of exceedance of the stress due to the VBM are far more sensitive to the wave climate and operational profile of the ship than to the actual code used to calculate

the linear transfer functions. Their conclusion is consistent with the findings of this work where the same linear transfer functions were used in the All Sea States Method and the simulation method with quite different results.

It is also important to note that the computation times between the simulation and the All Sea States Method are comparable. Both methods can furnish the probabilities of exceedance for a single load in less then a minute on an ordinary personal computer.

A number of long-term full-scale measurement campaigns have started recently, mainly on board container ships (see [103], [1], [102], [64], [59], [58], [35], [74], [63]). However, the main purpose of these investigations was to assess the fatigue damage due to low- and high-frequency wave-induced loads. The probabilities of exceedance of neither the individual nor combined loads have been published in these reports. When and if these measurements become available, their comparison with the simulation results would be very beneficial for further validation of the simulation method.

2.3.3.4 Linear Combination of Linear Loads

An advantage of the simulation method is that any load combination can be obtained by directly combining point-in-time values of the corresponding loads. For example, combined longitudinal stress in the shear strake of the ship due to both the VBM and the HBM can be obtained by simply adding the two time series (divided by the corresponding section moduli). This way, long-term exceedance probabilities can be obtained for the combined stress peaks. Because of the positive correlation between the VBM and the HBM, the total longitudinal stress will not be symmetric with respect to the ship's centerline and can be expressed for each side of the ship as follows

$$\sigma_{SB}(t) = \frac{M_y(t)}{W_d} + \frac{M_z(t)}{W_s} \tag{2.57a}$$

$$\sigma_{PS}(t) = \frac{M_y(t)}{W_d} - \frac{M_z(t)}{W_s} \tag{2.57b}$$

This asymmetry of stresses can be observed in Figure 2.19 where the Weibull fits of the long-term probabilities of exceedance of the combined tensile stress peaks for the port side (PS) and the starboard side (SB) are shown for C 283 container ship on NA route and two hundred voyages. Whenever the bending moments are correlated, the combined stress ranges will be asymmetrical, thus leading to more fatigue damage on one side of the ship. In this case, the starboard side of the ship experiences significantly higher stresses than the port side which has approximately 26% lower extreme value of the tensile stress.

It should also be noted that the warping longitudinal stresses are approximately equal to zero at amidship due to vanishing of the warping bimoment (see Section 2.3.3.5). This means that the longitudinal stress due to VBM and HBM is also the total primary longitudinal stress in the hull at amidship.

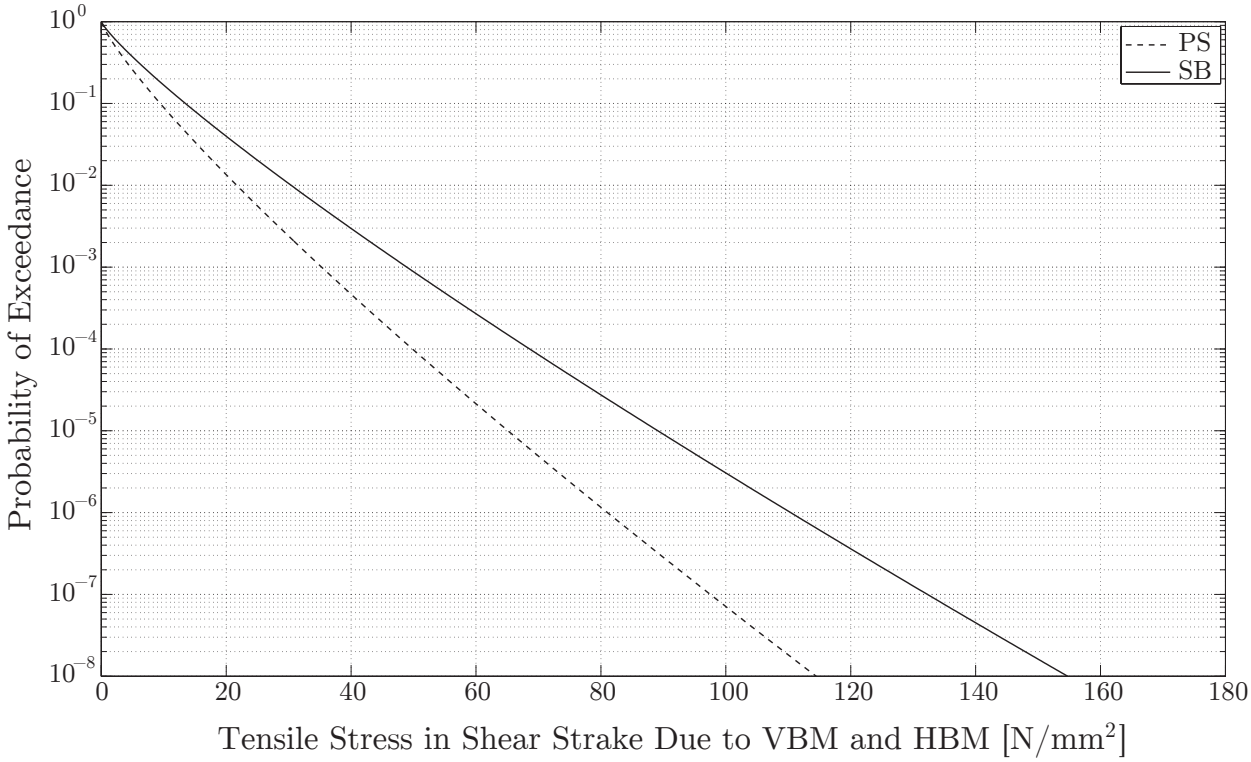

Figure 2.19: Tensile stress in the shear starke of the C 283 container ship on NA route due to combined VBM and HBM. SB: $\widehat{\lambda} = 5.058$, $\widehat{k} = 0.852$; PS: $\widehat{\lambda} = 3.467$, $\widehat{k} = 0.833$.

2.3.3.5 Nonlinear Combination of Linear Loads

Perhaps, one of the main advantages of the simulation method over other long-term methods is its ability to combine the loads in a nonlinear fashion by simply taking their point in time values and inserting them into the nonlinear expression. Many limit state functions that commonly arise during the reliability analysis of ship structures are nonlinear in nature, but perhaps the most common nonlinear load combination in structural mechanics comes in the form of equivalent tensile stress or the von Mises stress which is used to predict yielding of ductile materials under multi-axial loading conditions. Since the ships are thin-walled structures, the assumption of plain stress field can be used. In that case the von Mises stress is equal to

$$\sigma_{VM} = \sqrt{\sigma_x^2 + \sigma_y^2 - \sigma_x \sigma_y + 3\tau_{xy}^2} \tag{2.58}$$

where σ_x and σ_y are the normal stresses in the longitudinal x direction and transverse y direction, respectively. τ_{xy} is the shear stress.

The capabilities of the simulation method in performing this nonlinear load combination are demonstrated on the example of S 175 container ship. The dynamic von Mises stresses are computed on two positions of the side shell plating on the SB side of the vessel. The first

position is in the shear strake at deck level and the second position is 4850 mm below the first one. The longitudinal stresses reach their maximum at the first position, while the shear stresses reach their maximum at the second position. The total dynamic normal stress in the x direction, σ_x, is composed of normal stresses due to VBM and HBM (see Eqn. (2.57)) and the warping normal stress, σ_w, due to torsional moment M_x.

The total dynamic shear stress is a linear combination of shear stresses due to vertical shear force, Q_z, and shear stresses due to torsional moment M_x. The latter is composed of the Saint Venant shear stress, τ_s, due to rotation of the ship's cross section about the lengthwise torsional axes, and the warping shear stress, τ_w, due to longitudinal deformation in the x direction. Warping normal and shear stresses are consequences of the restrained axial deformation at the ends of the cargo space by the stiff structure such as the engine room or the forward peak. The shear stress due to horizontal shear force, normal stress due to longitudinal force and girth stress, σ_y, are usually small compared to the other stresses and can be neglected. The total dynamic plane stresses in the side shell of the S 175 container ship can be written as

$$\sigma_x = \sigma_{VBM} + \sigma_{HBM} + \sigma_w \tag{2.59a}$$

$$\sigma_y \approx 0 \tag{2.59b}$$

$$\tau_{xy} = \tau_{VSF} + \tau_{TM} = \tau_{VSF} + \tau_s + \tau_w \tag{2.59c}$$

where σ_{VBM}, σ_{HBM} and σ_w are the normal stresses due to VBM, HBM, and TM, respectively. τ_{VSF} and τ_{TM} are the shear stresses due to VSF and TM, respectively.

Similar to τ_{TM}, the torsional moment acting on the ship's structure can be decomposed into Saint Venant torsional moment, M_s, and warping moment M_w

$$M_x(x) = M_s(x) + M_w(x) = GI_d(x)\theta(x) - EI_{\Omega\Omega}(x)\frac{d^2\theta(x)}{dx^2} \tag{2.60}$$

where E and G are the Young's and shear moduli, respectively. θ is the derivative of the angular displacement ϕ. I_d is the Saint Venant torsional constant, also called the torsional modulus, $I_{\Omega\Omega}(x) = \int_A t(x,\zeta)\Omega^2(x,\zeta)d\zeta$ is the warping constant, also called the warping modulus or the sectorial moment of inertia, t is the thickness of plating, $\Omega(x,s) = \int_0^s r(x,\zeta)d\zeta$ is the sector coordinate, r is the perpendicular distance from the shear center to the tangent of the cross-section plating at arc length parameter s, and A denotes the entire cross section.

The problem of finding τ_{VSF} in a multicell structure is statically indeterminate. It can be found by making artificial "cuts" in the closed cells and imposing the no-slip condition at these cuts. This procedure leads to linear system of equations for finding shear flow, q, for each cell. The Saint Venant shear stress, τ_s, can be found by assuming a constant shear flow in each cell, imposing the moment equilibrium, and realizing that the angular displacement of each cell is equal to the angular displacement of the whole cross-section. Finally, the warping normal stress, σ_w, and the warping shear stress, τ_w, at a certain position along the

cross-section defined by s can be found using the following expressions

$$\sigma_w(x,s) = \frac{\Omega(x,s)M_\Omega(x)}{I_{\Omega\Omega}(x)} \tag{2.61a}$$

$$\tau_w(x,s) = -\frac{M_w(x)}{I_{\Omega\Omega}(x)t(x,s)}\int_0^s t(x,\zeta)\Omega(x,\zeta)d\zeta \tag{2.61b}$$

where $M_\Omega(x) = -EI_{\Omega\Omega}\theta'$ is the warping bimoment. More information on calculating σ_w, τ_{VSF}, τ_s and τ_w can be found in many standard textbooks on ship structural design such as [72], [42], [48] and [97]. These stresses can also be calculated using the finite element method. However, in this work a simplified procedure used by Jensen in [48] is employed.

Jensen analyzed a typical container ship with main particulars closely resembling those of the S 175 container ship used in this work. The assumption is that the entire cargo section of the ship is prismatic with constant cross-sections. The length, l, of the cargo space is 110 meters in the case of S 175 container ship and it extents equally on either side of the midship section. Another assumption is that the warping is completely restrained at the ends of the cargo space by the engine room and the forward peak. Then, for uniform distribution of the total torsional moment, M_x, the first derivative of the angular displacement and other torsional moments can be calculated using the following

$$\theta(x) = \frac{M_x}{GI_d}\left[1 - \frac{\cosh\left[\alpha\left(x - l/2\right)\right]}{\cosh\left(\alpha l/2\right)}\right] \tag{2.62a}$$

$$M_s(x) = M_x\left[1 - \frac{\cosh\left[\alpha\left(x - l/2\right)\right]}{\cosh\left(\alpha l/2\right)}\right] \tag{2.62b}$$

$$M_w(x) = M_x\frac{\cosh\left[\alpha\left(x - l/2\right)\right]}{\cosh\left(\alpha l/2\right)} \tag{2.62c}$$

$$M_\Omega(x) = M_x\frac{1}{\alpha}\frac{\sinh\left[\alpha\left(x - l/2\right)\right]}{\cosh\left(\alpha l/2\right)} \tag{2.62d}$$

where

$$\alpha l = \sqrt{\frac{GI_d}{EI_{\Omega\Omega}}}l \tag{2.63}$$

is a dimensionless constant consisting of material and geometric properties of the ship and x is a longitudinal coordinate with origin at the beginning of the cargo space. For S 175 container ship $\alpha l = 1.64$. The warping bimoment and, therefore, σ_w vanish at the midship section ($x = l/2$).

It can easily be shown that stresses σ_{VBM}, σ_{HBM}, σ_w, τ_{VSF}, τ_s, and τ_w all linearly depend on the sectional loads within the limits of small deflection theory. The stresses for the two positions on the SB side shell of S 175 container ship at amidship are given in Table 2.12.

Table 2.12: Stresses in the SB side shell of S 175 container ship at amidship.

Stress [N/mm^2]	Deck level	4850 mm below deck level
$\sigma_{VBM}(t) =$	$7.975 \cdot 10^{-5} M_y(t)$	$3.404 \cdot 10^{-5} M_y(t)$
$\sigma_{HBM}(t) =$	$4.407 \cdot 10^{-5} M_z(t)$	$4.407 \cdot 10^{-5} M_z(t)$
$\sigma_w(t) =$	$0.000 \cdot M_x(t)$	$0.000 \cdot M_x(t)$
$\tau_{VSF}(t) =$	$16.666 \cdot 10^{-5} Q_z(t)$	$15.833 \cdot 10^{-4} Q_z(t)$
$\tau_s(t) =$	$-6.398 \cdot 10^{-5} M_x(t)$	$-7.875 \cdot 10^{-5} M_x(t)$
$\tau_w(t) =$	$-1.844 \cdot 10^{-5} M_x(t)$	$-1.045 \cdot 10^{-4} M_x(t)$

Sectional forces and moments are calculated using Eqn. (2.45) and their units are kN and kNm, respectively, while the stresses are in N/mm^2.

Time series of individual stresses can be obtain directly from the time series of sectional loads using Table 2.12. The nonlinear von Mises stress can then be calculated using Eqns. (2.58) and (2.59). Figure 2.20 shows the probabilities of exceedance of the von Mises stresses for fifty voyages at two considered points on the S 175 hull. The empirical cumulative distribution functions are fitted with two parameter Weibull distributions.

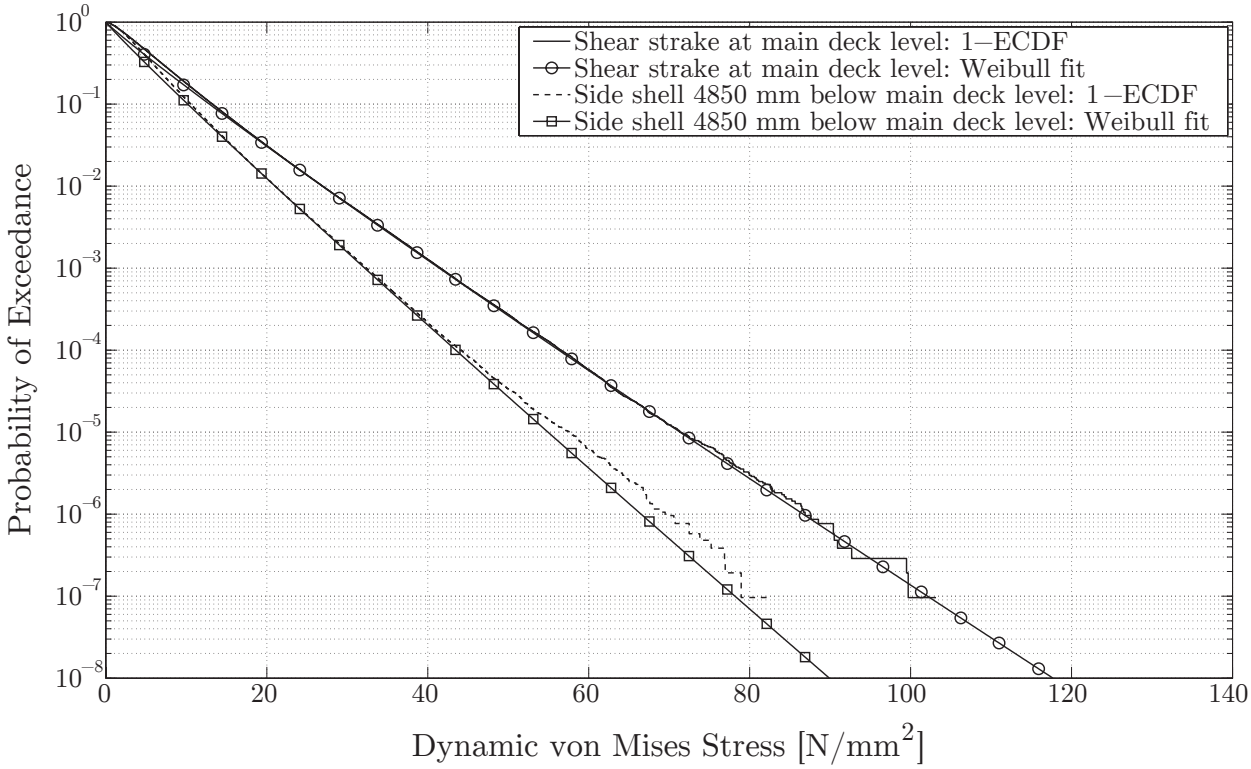

Figure 2.20: Dynamic von Mises stress for S 175 container ship on NA route.

The maximum simulated shear stress, τ_{xy} in shear strake at deck level is around 8 N/mm^2,

while the maximum simulated longitudinal stress, σ_x, is around 103 N/mm^2. Therefore, von Mises stress at that location is dominated by the longitudinal stresses and it is not surprising that the Weibull distribution fits the simulated data very well, especially for larger stress values, as was noted in the previous section. On the other hand, the maximum simulated shear stress in the second location 4850 mm below the deck level is around 38 N/mm^2 and the maximum simulated longitudinal stress is around 66 N/mm^2. The Weibull fit in this case is not as good, leading to the conclusion that it might not be the best statistical model for describing long-term von Misses stresses when two or more stress components have significant contributions.

In the presented case, all the stresses are linear functions of loads. If a more accurate structural analysis, e.g. using FEM, reveals a nonlinear relationship between the stresses and the sectional loads, that too can easily be incorporated in the simulation method. This is done by simply transforming the load time record into the stress time record using previously established nonlinear functions that relate them. The individual stresses are then combined in the same manner as discussed previously.

Other currently available long-term methods that are not based on simulation techniques are not capable of combining the loads in such a nonlinear fashion without first knowing the short-term probability density functions of the nonlinear load combination in each sea state / velocity profile combination. Therefore, no examples of long-term distribution of dynamic von Mises stress peaks could be identified in the literature. Published full-scale measurement results also don't include the von Mises stresses. For the validation of simulation results with respect to nonlinear combination of loads, it is necessary to compare them with full-scale measurements when they become available.

Chapter 3

Nonlinearities in the Vertical Bending Moment and High-Frequency Loads Due to Springing

3.1 Introduction

3.1.1 Linear vs. Nonlinear Analysis of Wave Loads

The wave response analysis may be linear and nonlinear. The former is much easier and has been applied in Chapter 2. However, for severe sea states there are several sources of nonlinearity: the waves themselves, the governing hydrodynamic equations, and the ship geometry. Stress measurements on ships have shown that the VBM can be considerably larger is sagging than in hogging, especially for ships with fine form such as naval vessels and container ships. These ships have significant flare in the bow and stern regions and are not wall-sided at the waterline level. The free surface and the nonlinear characteristics of the incident waves cause these ships to behave nonlinearly.

The linear analysis is based on these principal assumptions:

1. The irregular wave surface of the ocean can be represented as the linear sum of a large number of individual regular wave components of different heights and frequencies;

2. The hydrodynamic forces can be calculated for each transverse section of the ship separately. The total hydrodynamic force acting on the hull is a linear sum of the sectional forces;

3. The hydrodynamic force acting on each transverse section of the ship is proportional to the difference between the local wave height and the ship's still waterplane.

The accuracy of the first two assumptions is generally satisfactory while the third one is valid only for ships that are approximately wall-sided at the waterline level. As already

mentioned, this assumption is not valid for container ships. Therefore, a nonlinear analysis is necessary for these ships, especially with respect to the VBM which is affected by the nonlinearities much more than the other hull girder sectional loads.

Obtaining wave-induced ship motions and loads in irregulars seas with constant forward speed of the ship is a complex hydrodynamic problem. Compressibility effects and cavitation can be ignored reducing the mathematical problem and the number of variables that need to be calculated (three fluid velocity components and the fluid pressure). These four unknowns are determined by solving the continuity equation and the three-component Navier-Stokes equations, both of which are nonlinear. A number of boundary conditions have to be satisfied: the kinematic boundary conditions on the free and hull surface ensure that no fluid passes through the free or hull surface, respectively, the dynamic boundary condition on the free surface ensures a constant atmospheric pressure, and the radiation boundary condition prevents the waves from reflecting in the far field. Both, the kinematic and dynamic boundary conditions on the free surface make a highly nonlinear free surface boundary condition. Additionally, no-slip boundary condition on hull surface and no tangential shear stress on the free surface are needed if the fluid is viscous. For potential flow computations the fluid is assumed inviscid, homogeneous, incompressible, and of constant density. In that case, the Navier-Stokes equations reduce to Euler equations and the continuity equation reduces to the Laplace equation. Euler equation can then be integrated to obtain the Bernoulli equation. Therefore, for an ideal fluid, the coupled system of nonlinear partial differential equations reduces to the linear Laplace equation that yields the three velocity components and the Bernoulli equation that yields the pressure.

Presently available computer codes for calculating wave-induced ship motions and loads can be divided into two main categories: the frequency domain codes and the time domain codes, and they have different levels of approximation, accuracy and computational efficiency. All the codes fall into one of the following categories:

1. FREQUENCY DOMAIN CODES

    - Linear strip theory codes based on two-dimensional potential flow theory. An example of such a code is SEAWAY [53] used in Chapter 2;
    - Linear boundary element (panel) codes based on three-dimensional potential flow theory. An internationally well-known code from this category is SWAN 1 (Ship Wave ANalysis) [94];
    - Quadratic strip theory code based on the perturbation of the two-dimensional fluid potential in which the quadratic terms arise due to nonlinearity of the exciting waves, the nonvertical sides of the ship, and nonlinear hydrodynamic forces. This theory was developed by Jensen and Pedersen [51] and implemented into the computer code SOST (Second-Order Strip Theory);

2. TIME DOMAIN CODES

- Moderately nonlinear strip theory codes based on two-dimensional potential flow theory where the hydrostatic and Froude-Krylov forces are calculated using the instantaneous submerged part of the hull (nonlinear body boundary condition) and the rest of the hydrodynamic forces (due to diffraction and radiation) are calculated using the linearized body boundary condition. The free surface boundary condition is also linearized;
- Linear boundary element (panel) codes based on three-dimensional potential flow theory where the body and free surface boundary conditions are fully linearized;
- Moderately nonlinear boundary element (panel) codes based on three-dimensional potential flow theory where the hydrostatic and Froude-Krylov forces are calculated using the nonlinear body boundary condition, and the hydrodynamic forces due to diffraction and radiation are calculated using the linearized body boundary condition. The free surface boundary condition is also linearized. An example of such a code is SWAN 2 [81] and [93];
- Nonlinear boundary element (panel) codes based on three-dimensional potential flow theory where all hydrostatic and hydrodynamic forces are calculated using the nonlinear body boundary condition. The free surface boundary condition is linearized. An example of such a code is LAMP (Large Amplitude Motions Program) [65];
- Fully nonlinear codes capable of computing the three dimensional average flow in a viscous fluid with fully nonlinear boundary conditions. Reynolds-averaged Navier-Stokes (RANS) equations are typically used in combination with the volume-of-fluid (VOF) interface-capturing technique. Most of these codes are still in the research stage and they are extremely computationally intensive. They are used to solve strongly nonlinear problems and compute complex free-surface shapes associated with breaking waves, sprays, and air trapping.

Frequency domain codes obtain solutions for periodic ship responses in elementary regular waves. They are robust and computationally efficient. However, if the motion of the ship in waves and the associated wave-induced loads are highly nonlinear with respect to the wave amplitude, the ship response should not be investigated in regular waves, because these waves do not appear in nature. In that case, the nonlinear response of the ship in natural seaway cannot be deduced from the response in regular waves. For these strong nonlinear cases, time domain nonlinear codes should be used.

Codes based on simple linear frequency domain strip theory are still widely used by the shipbuilding industry because of their simplicity and efficient computation. Wave loads obtained by these methods (see Chapter 2) are used to develop the "nominal" loads for structural design and strength evaluation. However, the linear strip theory is limited to slender ships with vertical sides in the waterplane region. Useful results can be obtained even for speeds corresponding to a Froude number of 0.4, albeit only for relatively small amplitude waves.

A detailed discussion on calculating wave-induced hydrodynamic forces and associated motion responses of marine vessels can be found in Beck et al. [14].

3.1.2 Springing Analysis

As the ships grow in size (predominantly length, breadth and speed of a vessel) their hull structures become more flexible and the wave-induced vessel vibrations become more important because the resonant condition between the excitation waves and the ship structure becomes more easily satisfied. Depending on the size, type and operational profile of the vessel, additional VBM due to high-frequency springing vibrations might become significant and require consideration in the rational hull strength assessment. This is evident from the full-scale measurements (e.g. Storhaug et al. [105]; Storhaug et al. [103]; Okada [88]; Storhaug and Moe [102]).

In the past, the effects of springing on the VBM have not been properly incorporated into the ship design process. In recent years, however, the research on springing vibrations has undergone a revival. Classification societies are modifying their load criteria in order to account for the ship hydroelasticity. Classification society ABS issued guidance notes on springing assessment for container ships [3]. These ships are much more susceptible to springing then other cargo ships because of their big length, fine form, and high speed. ABS procedure starts with isolating those combinations of sea states, speeds, headings, and loading conditions which have a springing susceptibility indicator grater than one. This indicator can be formulated based on the natural frequency of the 2-node hull girder vibration mode and the zero up-crossing wave period. A more detailed springing analysis is required for those sea states / operational profile combinations that have the springing susceptibility indicator grater than one.

The structural model of the flexible hull must reflect its dynamic properties in the frequency range that is of interest, i.e. the natural frequencies, the associated vibration modes, and damping characteristics. Depending on the desired level of accuracy, the following structural models are used (from simple to more sophisticated):

1. Quasi-static calculations using the dynamic amplification factors;
2. Analytic formulae for impulsive or harmonic excitations of one or two degree of freedom systems;
3. Euler-Bernoulli, Vlasov, or Timoshenko nonuniform dynamic beam models for vertical, horizontal, or torsional vibration modes;
4. 3D FE models of the complete hull with possible mesh refinement for assessing stress concentration effects.

As the level of accuracy of the structural model increases, so does the computational effort. In order to obtain the wave-induced loads and motions of a hydroelastic hull, these

structural models have to be combined with any of the hydrodynamic codes for wave-induced load calculations described in Section 3.1.1. However, more complex structural models are usually integrated with more complex hydrodynamic codes to achieve consistency.

The structural and hydrodynamic models can be coupled and decoupled. Decoupling neglects the influence of hull vibration displacement on the magnitude of the impulsive or harmonic hydrodynamic excitation forces. This enables the use of well established and effective calculation methods, but might compromise the accuracy in some cases. Usually, the modal analysis is used for the sake of computational efficiency. Normally, only a few of the first natural vibration modes of the hull girder are required to describe its dynamic response with sufficient accuracy.

The results of Chapter 2 were obtained using the linear strip theory in combination with the rigid hull. Present chapter extends these results by introducing nonlinearities in the VBM as well as the vibratory response of the hull due to springing. For that purpose, the quadratic strip theory program SOST (see Section 3.1.1) is used to obtain the linear and quadratic transfer functions (LTF and QTF, respectively) for the VBM. SOST is used because it is robust, computationally efficient, and it takes into account the flexibility of the ship using Timoshenko beam theory and modal analysis. LTF and QTF generated by SOST in the frequency domain are very suitable for efficient simulations of long time series of the nonlinear VBM. Nonlinear hydrodynamic time domain codes generate nonlinear VBM directly in the time domain. They are, however, extremely computationally expensive and thus unsuitable for such long-term analysis. Additionally, the results of nonlinear time domain codes are not consistently better than the results of quadratic strip theories (ISSC [47]).

Before presenting the results of the long-term simulation of nonlinear VBM with the effects of springing, a brief introduction into nonlinear systems is given. The basics of the quadratic hydrodyamic theory are given in Appendix B.1.

3.2 A Brief Introduction to Volterra Series

The physical notion of a complex engineering system is usually that of a black box which transforms a time function of an input, $x(t)$, into an output time function, $y(t)$. It can be shown that the output time function of a time invariant nonlinear system, with certain restrictions, can be expressed using the so called *Volterra series* named after Italian mathematician Vito Volterra

$$\begin{aligned} y(t) = &\int_{-\infty}^{\infty} h_1(\tau_1)x(t-\tau_1)d\tau_1 + \int_{-\infty}^{\infty}\int_{-\infty}^{\infty} h_2(\tau_1,\tau_2)x(t-\tau_1)x(t-\tau_2)d\tau_1 d\tau_2 \\ &+ \int_{-\infty}^{\infty}\int_{-\infty}^{\infty}\int_{-\infty}^{\infty} h_3(\tau_1,\tau_2,\tau_3)x(t-\tau_1)x(t-\tau_2)x(t-\tau_3)d\tau_1 d\tau_2 d\tau_3 \\ &\ldots + \int_{-\infty}^{\infty}\ldots\int_{-\infty}^{\infty} h_n(\tau_1,\ldots,\tau_n)x(t-\tau_1)\ldots x(t-\tau_n)d\tau_1\ldots d\tau_n + \ldots \end{aligned} \tag{3.1}$$

in which for $n = 1, 2, \ldots$

$$h_n(\tau_1, \ldots, \tau_n) = 0 \quad \text{for any } \tau_j < 0, \quad j = 1, 2, \ldots, n \tag{3.2}$$

Functions $h_n(\tau_1, \ldots, \tau_n)$ are called the Volterra kernels of the system. Because they are equal to zero for any $\tau < 0$, the lover limits of the integrals in Eqn. (3.1) can be replaced with zeros. Volterra series in Eqn. (3.1) can also be expresses in the following form

$$y(t) = \mathbb{H}_1[x(t)] + \mathbb{H}_2[x(t)] + \mathbb{H}_3[x(t)] + \ldots + \mathbb{H}_n[x(t)] + \ldots \tag{3.3}$$

in which

$$\mathbb{H}_n[x(t)] = \int_{-\infty}^{\infty} \ldots \int_{-\infty}^{\infty} h_n(\tau_1, \ldots, \tau_n) x(t - \tau_1) \ldots x(t - \tau_n) d\tau_1 \ldots d\tau_n \tag{3.4}$$

$\mathbb{H}_n$ is called the nth-order Volterra operator.

Volterra series is a power series. This is seen by changing the input by a gain factor a so that the new input is $ax(t)$. Then, by using equation Eqns. (3.3) and (3.4) the new output is equal to

$$\begin{aligned} y(t) &= \sum_{n=1}^{\infty} \mathbb{H}_n[ax(t)] \\ &= \sum_{n=1}^{\infty} a^n \mathbb{H}_n[x(t)] \end{aligned} \tag{3.5}$$

which is a power series in the amplitude factor a. Volterra series is also a series with memory since the integrals in Eqn. (3.1) are convolutions. A discussion on this topic can be found in Schetzen [92].

3.2.1 First-Order (Linear) Time Invariant Systems

The input-output relationship of a linear time invariant systems, such as the one considered in Chapter 2, can be represented by the first term of the Volterra series

$$y^{(1)}(t) = \int_{-\infty}^{\infty} h_1(\tau_1) x(t - \tau_1) d\tau_1 \tag{3.6}$$

In fact, this first term is almost identical to Eqn. (2.3) in Section 2.1.1.1 used to describe the ship as a liner system. The only difference is that Eqn. (2.3) represents an output to a linear combination of inputs. The kernel $h_1(\tau)$ of the first-order Volterra operator, $\mathbb{H}_1$, is the system's unit impulse response function because it is equal to the output of the system when the input is a unit impulse. In other words, testing a linear time invariant system with a unit impulse completely defines the system. This, however, is not true for second- and

higher-order systems. For example, a unit impulse only defines the second-order Volterra kernel $h_2(\tau_1, \tau_2)$ along the line $\tau_1 = \tau_2$.

An important function for studying linear time invariant systems is the phasor $e^{i\omega t}$ where i is the imaginary unit and ω is the angular frequency of the input signal. Phasors are important because they are characteristic functions of a stable linear time invariant system. An input, $x(t)$ is called a characteristic function of a system if the corresponding output is $y(t) = cx(t)$ where c is a constant. The output of a stable linear time invariant system to a phasor is equal to

$$\begin{aligned} y^{(1)}(t) &= \int_{-\infty}^{\infty} h_1(\tau) e^{i\omega(t-\tau)} d\tau \\ &= e^{i\omega t} \int_{-\infty}^{\infty} h_1(\tau) e^{-i\omega\tau} d\tau \\ &= H_1(\omega) e^{i\omega t} \end{aligned} \tag{3.7}$$

where

$$H_1(\omega) = \int_{-\infty}^{\infty} h_1(\tau) e^{-i\omega\tau} d\tau \tag{3.8}$$

The complex constant $H_1(\omega)$ by which the input phasor is multiplied is called the linear transfer function (LTF). From Eqn. (3.8) it is evident that

$$|H_1(\omega)| \leq \int_{-\infty}^{\infty} |h_1(\tau)| \, d\tau \tag{3.9}$$

Since

$$\int_{-\infty}^{\infty} |h_1(\tau)| \, d\tau < \infty \tag{3.10}$$

is a sufficient condition for a stable system, LTF is bounded (exists) for any stable linear time invariant system with phasor input. This argument can be easily extended for any bounded input. Eqn. (3.8) is observed to be the Fourier transform of the impulse response function, $h_1(\tau)$, which means that the impulse response function can be completely determined from knowledge of the transfer function by using the inverse Fourier transform

$$h_1(\tau) = \frac{1}{2\pi} \int_{-\infty}^{\infty} H_1(\omega) e^{i\omega\tau} d\omega \tag{3.11}$$

For a linear time invariant system, the input-output relationship in the time domain, given by the first term of the Volterra series, is by no means restricted to phasor inputs. It is valid regardless of the nature of the input (periodic, aperiodic, or random). However, if the input signal is periodic, the input-output relationship can be obtained by realizing that any periodic input can be expressed with an infinite Fourier series

$$x(t) = \sum_{n=-\infty}^{\infty} c_n e^{i\omega_n t} \tag{3.12}$$

in which ω_n is a multiple of the fundamental angular frequency of the input waveform such that $\omega_n = n\omega_1$. By using linearity and Eqn. (3.7), the output $y^{(1)}(t)$ can also be expressed as a Fourier series

$$y^{(1)}(t) = \sum_{n=-\infty}^{\infty} c_n H_1(\omega_n) e^{i\omega_n t} \tag{3.13}$$

It is important to note that the response of an linear time invariant system does not contain any frequency components not present in the input. Therefore, there is no interaction between input components at different frequencies and the system threats each of them independently.

For aperiodic transient functions it is often more convenient to conduct the analysis in the frequency domain. Transient functions satisfy the absolute integrability condition

$$\int_{-\infty}^{\infty} |x(t)|\, dt < 0 \tag{3.14}$$

This condition ensure the existence of the Fourier transform pair

$$X(\omega) = \int_{-\infty}^{\infty} x(t) e^{-i\omega t} dt \tag{3.15}$$

$$x(t) = \frac{1}{2\pi} \int_{-\infty}^{\infty} X(\omega) e^{i\omega t} d\omega \tag{3.16}$$

Using Eqn. (3.6), the Fourier transform of the response, $y^{(1)}(t)$, can be obtained as follows

$$\begin{aligned} Y^{(1)}(\omega) &= \int_{-\infty}^{\infty} y^{(1)}(t) e^{-i\omega t} dt \\ &= \int_{-\infty}^{\infty} \int_{-\infty}^{\infty} h_1(\boldsymbol{\tau}) x(t-\boldsymbol{\tau}) e^{-i\omega t} d\boldsymbol{\tau} dt \end{aligned} \tag{3.17}$$

If the change of variable $\sigma = t - \boldsymbol{\tau}$ is introduced, then

$$Y^{(1)}(\omega) = \int_{-\infty}^{\infty} \int_{-\infty}^{\infty} h_1(\boldsymbol{\tau}) x(\sigma) e^{-i\omega(\sigma+\tau)} d\boldsymbol{\tau} d\sigma \tag{3.18}$$

$$= \int_{-\infty}^{\infty} h_1(\boldsymbol{\tau}) e^{-i\omega\tau} d\boldsymbol{\tau} \int_{-\infty}^{\infty} x(\sigma) e^{-i\omega\sigma} d\sigma \tag{3.19}$$

where the first integral is the transfer function $H_1(\omega)$ and the second integral is $X(\omega)$. The final result is

$$Y^{(1)}(\omega) = H_1(\omega) X(\omega) \tag{3.20}$$

Therefore, a convolution in the time domain (Eqn. (3.6)) corresponds to a simple product in the frequency domain.

The foregoing analysis in the frequency domain is not valid if $x(t)$ is a random function like the ocean wave elevations are. The reason is that, in accordance with the Wiener theorem of quadratic variation [92], the Fourier transform of a random function does not exist. However, the random function, $x(t)$ can be put into the autocorrelation form as follows

$$R(\tau) = \mathbb{E}\left[x(t)x(t+\tau)\right] \tag{3.21}$$

According to the well known Wiener-Khintchine theorem, this autocorrelation function of the input has a Fourier transform in the form of a spectral density of the input, i.e.

$$S(\omega) = \int_{-\infty}^{\infty} R(\tau)e^{-i\omega\tau}d\tau \tag{3.22}$$

$$R(\tau) = \frac{1}{2\pi}\int_{-\infty}^{\infty} S(\omega)e^{i\omega\tau}d\omega \tag{3.23}$$

Finally, the relationship between the input and the output in the frequency domain is obtained indirectly through spectral densities

$$S_y(\omega) = \left|H_1(\omega)\right|^2 S_x(\omega) \tag{3.24}$$

3.2.2 Second-Order (Nonlinear) Time Invariant Systems

Nonlinear time invariant systems can be represented using the first n terms of the Volterra series where $n \geq 2$. The quadratic Volterra model has been found very useful for nonlinear analysis of ships in weakly nonlinear random seas. It consists of first two terms of the Volterra series, and they are considered to be uncorrelated. Therefore, the output, $y(t)$, can be thought of as a sum of linear and quadratic parts as follows

$$y^{(1)}(t) = \int_{-\infty}^{\infty} h_1(\tau_1)x(t-\tau_1)d\tau_1 \tag{3.25}$$

$$y^{(2)}(t) = \int_{-\infty}^{\infty}\int_{-\infty}^{\infty} h_2(\tau_1,\tau_2)x(t-\tau_1)x(t-\tau_2)d\tau_1 d\tau_2 \tag{3.26}$$

$$y(t) = y^{(1)}(t) + y^{(2)}(t) \tag{3.27}$$

The first-order response of the system involves convoluting the first-order Volterra kernel, $h_1(\tau_1)$, with the a single input function, while the second-order response involves a double convolution of the second-order Volterra kernel, $h_2(\tau_1,\tau_2)$, with the product of two identical input functions. Thus, a single input function excites the linear component of the system, while the product of two identical input functions excites the nonlinear component.

As it will be seen later in this section, the individual harmonics of the input function are no longer treated independently by the nonlinear system, as was the case with the linear

system. A second-order nonlinear system responds to interactions between any two harmonic components of the input. Thus, the output contains higher-order harmonics that are not present in the input. Another feature of the second-order nonlinear time invariant system is that the output is no longer Gaussian, given a Gaussian input.

It was pointed out in Section 3.2.1 that the second-order Volterra kernel, $h_2(\tau_1, \tau_2)$, is not a second-order response to a unit impulse. In fact, the second-order response to a unit impulse is equal to the second-order kernel along the line $\tau_1 = \tau_2 = \tau$, i.e. equal to $h_2(\tau, \tau)$. In addition, the second-order kernel is not necessarily symmetric. However, any asymmetric kernel can be symmetrized without any loss of generality, so that

$$h_2(\tau_1, \tau_2) = h_2(\tau_2, \tau_1) \tag{3.28}$$

The absolute integrability condition of the second-order Volterra kernel in time domain, $h_2(\tau_1, \tau_2)$, is sufficient for the stability of the second-order Volterra operator.

$$\int_{-\infty}^{\infty} \int_{-\infty}^{\infty} |h_2(\tau_1, \tau_2)| \, d\tau_1 d\tau_2 < \infty \tag{3.29}$$

Then, second-order Volterra kernel can be transformed into the second-order transfer function in frequency domain, $H_2(\omega_1, \omega_2)$, by means of two-dimensional Fourier transform. Therefore, similar to the first-order case, second-order Volterra kernel and the second-order transfer function form a Fourier pair

$$H_2(\omega_1, \omega_2) = \int_{-\infty}^{\infty} \int_{-\infty}^{\infty} h_2(\tau_1, \tau_2) e^{-i(\omega_1 \tau_1 + \omega_2 \tau_2)} d\tau_1 d\tau_2 \tag{3.30}$$

$$h_2(\tau_1, \tau_2) = \frac{1}{(2\pi)^2} \int_{-\infty}^{\infty} \int_{-\infty}^{\infty} H_2(\omega_1, \omega_2) e^{i(\omega_1 \tau_1 + \omega_2 \tau_2)} d\omega_1 d\omega_2 \tag{3.31}$$

Function $H_2(\omega_1, \omega_2)$ is also called the quadratic transfer function (QTF). This terminology is used throughout this dissertation. Since h_2 is symmetric, the following relations hold for H_2

$$H_2(\omega_1, \omega_2) = H_2(\omega_2, \omega_1) \tag{3.32}$$

$$H_2^*(\omega_1, \omega_2) = H_2(-\omega_1, -\omega_2) = H_2(-\omega_2, -\omega_1) \tag{3.33}$$

It was already mentioned in Section 3.2.1, that there are no restrictions on the input function of the Volterra series since it is expressed in time domain. An input function can even be random, e.g. wave elevations. In Chapter 2 the wave elevations were considered to be a zero-mean Gaussian process. As per the spectral representation theorem, such a process can be expressed with a Fourier integral and approximated with a finite sum of harmonic components over a discrete set of frequencies (see Eqn. (2.39) which is repeated below).

$$\eta(t) \approx \sum_{j=1}^{N} a_{\eta,j} \cos\left(\omega_{e,j} t + \phi_j\right) = \Re\left[\sum_{j=1}^{N} a_{\eta,j} e^{i(\omega_{e,j} t + \phi_j)}\right]$$

Eqn. (2.39) describes free surface elevations of the linear, or first-order, or Airy waves, as it is a solution of the linear differential equation describing wave kinematics (Laplace equation for velocity potential) with linearized homogeneous free surface boundary condition. If the ship is represented with a quadratic Volterra model and the linear waves are taken as input, then any of the ship responses (loads, motions, stresses) can be written as

$$
\begin{aligned}
y(t) &= \int_{-\infty}^{\infty} h_1(\tau_1)\Re\left[\sum_{j=1}^{N} a_{\eta,j} e^{i\left[\omega_{e,j}(t-\tau_1)+\phi_j\right]}\right] d\tau_1 \\
&+ \int_{-\infty}^{\infty}\int_{-\infty}^{\infty} h_2(\tau_1,\tau_2)\Re\left[\sum_{j=1}^{N} a_{\eta,j} e^{i\left[\omega_{e,j}(t-\tau_1)+\phi_j\right]}\right]\Re\left[\sum_{k=1}^{N} a_{\eta,k} e^{i\left[\omega_{e,k}(t-\tau_2)+\phi_k\right]}\right] d\tau_1 d\tau_2 \\
&= \Re\sum_{j=1}^{N} a_{\eta,j}\left[\int_{-\infty}^{\infty} h_1(\tau_1) e^{-i\omega_{e,j}\tau_1} d\tau_1\right] e^{i(\omega_{e,j}t+\phi_j)} \\
&+ \frac{1}{2}\Re\sum_{j=1}^{N}\sum_{k=1}^{N} a_{\eta,j}a_{\eta,k}\int_{-\infty}^{\infty}\int_{-\infty}^{\infty} h_2(\tau_1,\tau_2)\Big[e^{i\left[\omega_{e,j}(t-\tau_1)+\phi_j\right]} e^{i\left[\omega_{e,k}(t-\tau_2)+\phi_k\right]} \\
&+ e^{i\left[\omega_{e,j}(t-\tau_1)+\phi_j\right]} e^{-i\left[\omega_{e,k}(t-\tau_2)+\phi_k\right]}\Big] d\tau_1 d\tau_2 \\
&= \Re\sum_{j=1}^{N} a_{\eta,j} H_1\left(\omega_{e,j}\right) e^{i(\omega_{e,j}t+\phi_j)} \\
&+ \frac{1}{2}\Re\sum_{j=1}^{N}\sum_{k=1}^{N} a_{\eta,j}a_{\eta,k}\Bigg\{\left[\int_{-\infty}^{\infty}\int_{-\infty}^{\infty} h_2(\tau_1,\tau_2) e^{-i\left(\omega_{e,j}\tau_1+\omega_{e,k}\tau_2\right)} d\tau_1 d\tau_2\right] e^{i\left[\left(\omega_{e,j}+\omega_{e,k}\right)t+(\phi_j+\phi_k)\right]} \\
&+ \left[\int_{-\infty}^{\infty}\int_{-\infty}^{\infty} h_2(\tau_1,\tau_2) e^{-i\left(\omega_{e,j}\tau_1-\omega_{e,k}\tau_2\right)} d\tau_1 d\tau_2\right] e^{i\left[\left(\omega_{e,j}-\omega_{e,k}\right)t+(\phi_j-\phi_k)\right]}\Bigg\} \\
&= \Re\sum_{j=1}^{N} a_{\eta,j} H_1\left(\omega_{e,j}\right) e^{i(\omega_{e,j}t+\phi_j)} + \frac{1}{2}\Re\sum_{j=1}^{N}\sum_{k=1}^{N} a_{\eta,j}a_{\eta,k}\Big[H_2\left(\omega_{e,j},\omega_{e,k}\right) e^{i\left[\left(\omega_{e,j}+\omega_{e,k}\right)t+(\phi_j+\phi_k)\right]} \\
&+ H_2\left(\omega_{e,j},-\omega_{e,k}\right) e^{i\left[\left(\omega_{e,j}-\omega_{e,k}\right)t+(\phi_j-\phi_k)\right]}\Big]
\end{aligned}
\tag{3.34}
$$

in which $H_2\left(\omega_{e,j},\omega_{e,k}\right)$ and $H_2\left(\omega_{e,j},-\omega_{e,k}\right)$ are the QTFs associated with the sum of frequency terms (superharmonics) and difference of frequency terms (subharmonics), respectively. The

following notation is used in this work

$$H_2\left(\omega_{e,j},\omega_{e,k}\right) \equiv H_2^+\left(\omega_{e,j},\omega_{e,k}\right)$$

$$H_2\left(\omega_{e,j},-\omega_{e,k}\right) \equiv H_2^-\left(\omega_{e,j},\omega_{e,k}\right)$$

Finally, the quadratic Volterra model can be expressed as

$$\begin{aligned} y(t) &= y^{(1)}(t) + y^{(2)}(t) \\ &= \Re\sum_{j=1}^{N} a_{\eta,j} H_1\left(\omega_{e,j}\right) e^{i(\omega_{e,j}t+\phi_j)} + \frac{1}{2}\Re\sum_{j=1}^{N}\sum_{k=1}^{N} a_{\eta,j}a_{\eta,k}\Bigg[H_2^+\left(\omega_{e,j},\omega_{e,k}\right) e^{i\left[\left(\omega_{e,j}+\omega_{e,k}\right)t+\left(\phi_j+\phi_k\right)\right]} \\ &\quad + H_2^-\left(\omega_{e,j},\omega_{e,k}\right) e^{i\left[\left(\omega_{e,j}-\omega_{e,k}\right)t+\left(\phi_j-\phi_k\right)\right]}\Bigg] \end{aligned} \tag{3.35}$$

The super and subharmonics of the output time series are not present in the input and they reflect the system's nonlinear response to a mutual interaction between different input harmonics. Unlike the linear system case, the input harmonics are no longer considered independent in the quadratic Volterra model. Therefore, even if the input is Gaussian, the output is not necessarily Gaussian in the Central Limit sense, because the Central Limit Theorem no longer applies. Additionally, constant terms associated with the difference of equal frequencies, e.g. $(\omega_{e,j},-\omega_{e,k})$ for $j=k$, produce a non zero-mean output, even in the case of zero-mean input.

The quadratic Volterra model in Eqn. (3.35) was developed assuming a first-order Gaussian zero-mean wave input. A statistical analysis of wave elevation time series taken in the ocean in deep water conditions show no evidence to reject this assumption. Usually, the deviation form normality is so small that it does not need to be considered in the calculation of the ship responses. However, in shallow water or in severe sea storms, the deviations become more significant and the energy transfer between different frequency components takes place which means that the wave harmonics are no longer independent. This requires the use of second-order wave theory. Jensen and Pedersen [51] used this theory in the development of the quadratic strip theory (see Appendix B.1). Their final result is the second-order VBM that is calculated using a hydrodynamic analysis of a flexible hull in second-order waves. Although not mentioned in their original work, the final expression for the second-order VBM closely resembles the quadratic Volterra model with first-order wave input, but without the $\frac{1}{2}$ factor in front of the second-order term. This is clarified in Chapter 9 of Kim [57] who showed that the second-order response of a ship in second-order waves can be obtained using a quadratic Volterra model with first-order Gaussian waves, Eqn. (3.35), but without the $\frac{1}{2}$ factor in front of the second-order term of the response. The same thing is also noted by Winterstein et al. [117].

3.3 Second-Order Vertical Bending Moment Simulation

The notation used in this section is consistent with the one used in Chapter 2. Jensen and Pedersen used a slightly different definition of random harmonic components of the wave elevation process in [51]. They used harmonics defined as $\cos(\omega_{e,i}t - \phi_i)$, whereas the ones used in Chapter 2 are of the form $\cos(\omega_{e,i}t + \phi_i)$. Since ϕ_i is a uniformly distributed random variable on the interval $[-\pi, \pi]$, this difference is purely a matter of convention and has no effect on the physical behavior of the system. The expression for the linear part of the VBM from [51] is modified to include the effect of wave energy spreading in short-crested seas, while the nonlinear part is not modified to account for this effect in order to make the simulation more efficient.

The total vertical bending moment amidships can be represented as a sum of first-order (linear) and the second-order (nonlinear) contributions

$$M_y(x,t) = M_y^{(1)}(x,t) + M_y^{(2)}(x,t) \tag{3.36}$$

where x denotes the longitudinal coordinate of the midship section. Since the VBM is calculated only at amidship, the longitudinal coordinate can be omitted for simplicity. According to the quadratic Volterra model, Eqn. (3.35), the linear part of the VBM for a certain relative angle between the ship's heading and the wave direction, α, and the ship speed, V, can be expressed as

$$M_y^{(1)}(t) = \sum_{j=1}^{N} a_{\eta,j}\left[\tilde{H}_1^C(\omega_{e,j})\cos(\omega_{e,j}t + \phi_j) - \tilde{H}_1^S(\omega_{e,j})\sin(\omega_{e,j}t + \phi_j)\right] \tag{3.37}$$

where

$$\tilde{H}_1^C(\omega_{e,j}) = \sqrt{\int_{-\pi/2}^{\pi/2} \frac{2}{\pi}\cos^2(\mu)\left[H_1^C(\omega_{e,j};\alpha-\mu)\right]^2 d\mu} \tag{3.38}$$

$$\tilde{H}_1^S(\omega_{e,j}) = \sqrt{\int_{-\pi/2}^{\pi/2} \frac{2}{\pi}\cos^2(\mu)\left[H_1^S(\omega_{e,j};\alpha-\mu)\right]^2 d\mu} \tag{3.39}$$

and

$$H_1^C(\omega_{e,j}) = \Re\left[H_1(\omega_{e,j})\right] \tag{3.40}$$

$$H_1^S(\omega_{e,j}) = \Im\left[H_1(\omega_{e,j})\right] \tag{3.41}$$

"C" and "S" superscripts denote the real and imaginary parts of the transfer function associated with cosine and sine terms, respectively. $\tilde{H}_1^C(\omega_{e,j})$ and $\tilde{H}_1^S(\omega_{e,j})$ are weighted first-order transfer functions that take into account the directional energy spreading in the short-crested seas. The rest of the notation in Eqn. (3.37) is the same as in Eqn. (2.39). The absolute

value of the first-order transfer function (response amplitude operator - RAO) is then equal to

$$\left|H_1\left(\omega_{e,j}\right)\right| = \sqrt{\left[H_1^C\left(\omega_{e,j}\right)\right]^2 + \left[H_1^S\left(\omega_{e,j}\right)\right]^2} \tag{3.42}$$

Using the trigonometric identities, Eqn. (3.42), and Eqn. (2.37), it can easily be shown that Eqn. (3.37) for the linear VBM is identical to Eqn. (2.45e) from Chapter 2.

The nonlinear part of the VBM, according to the quadratic Volterra model without the $\frac{1}{2}$ factor, can be expressed as

$$\begin{aligned} M_y^{(2)}(t) = \sum_{j=1}^{N}\sum_{k=1}^{N} a_{\eta,j}a_{\eta,k}\Big\{ & H_2^{C+}\left(\omega_{e,j},\omega_{e,k}\right)\cos\left[\left(\omega_{e,j}+\omega_{e,k}\right)t+\left(\phi_j+\phi_k\right)\right] \\ & - H_2^{S+}\left(\omega_{e,j},\omega_{e,k}\right)\sin\left[\left(\omega_{e,j}+\omega_{e,k}\right)t+\left(\phi_j+\phi_k\right)\right] \\ & + H_2^{C-}\left(\omega_{e,j},\omega_{e,k}\right)\cos\left[\left(\omega_{e,j}-\omega_{e,k}\right)t+\left(\phi_j-\phi_k\right)\right] \\ & - H_2^{S-}\left(\omega_{e,j},\omega_{e,k}\right)\sin\left[\left(\omega_{e,j}-\omega_{e,k}\right)t+\left(\phi_j-\phi_k\right)\right]\Big\} \end{aligned} \tag{3.43}$$

and the absolute values of the second-order transfer functions associated with super and subharmonic terms are equal to

$$\left|H_2^{+}\left(\omega_{e,j},\omega_{e,k}\right)\right| = \sqrt{\left[H_2^{C+}\left(\omega_{e,j},\omega_{e,k}\right)\right]^2 + \left[H_2^{S+}\left(\omega_{e,j},\omega_{e,k}\right)\right]^2} \tag{3.44}$$

$$\left|H_2^{-}\left(\omega_{e,j},\omega_{e,k}\right)\right| = \sqrt{\left[H_2^{C-}\left(\omega_{e,j},\omega_{e,k}\right)\right]^2 + \left[H_2^{S-}\left(\omega_{e,j},\omega_{e,k}\right)\right]^2} \tag{3.45}$$

Eqn. (3.43) can be used to simulate the second-order VBM. However, in order to speed up the calculations this equation can be expanded using trigonometric identities. The idea is to separate each super and subharmonic into the time dependent part and the random part as follows

$$\begin{aligned} M_y^{(2)}(t) = \sum_{j=1}^{N}\sum_{k=1}^{N} a_{\eta,j}a_{\eta,k}\Bigg\{ & H_2^{C+}\left(\omega_{e,j},\omega_{e,k}\right)\Big[\cos\left[\left(\omega_{e,j}+\omega_{e,k}\right)t\right]\cos\left(\phi_j+\phi_k\right) \\ & - \sin\left[\left(\omega_{e,j}+\omega_{e,k}\right)t\right]\sin\left(\phi_j+\phi_k\right)\Big] \\ & - H_2^{S+}\left(\omega_{e,j},\omega_{e,k}\right)\Big[\sin\left[\left(\omega_{e,j}+\omega_{e,k}\right)t\right]\cos\left(\phi_j+\phi_k\right) \\ & + \cos\left[\left(\omega_{e,j}+\omega_{e,k}\right)t\right]\sin\left(\phi_j+\phi_k\right)\Big] \end{aligned}$$

$$
\begin{aligned}
&+ H_2^{C-}\left(\omega_{e,j},\omega_{e,k}\right)\Bigg[\cos\left[\left(\omega_{e,j}-\omega_{e,k}\right)t\right]\cos\left(\phi_j-\phi_k\right)\\
&- \sin\left[\left(\omega_{e,j}-\omega_{e,k}\right)t\right]\sin\left(\phi_j-\phi_k\right)\Bigg]\\
&- H_2^{S-}\left(\omega_{e,j},\omega_{e,k}\right)\Bigg[\sin\left[\left(\omega_{e,j}-\omega_{e,k}\right)t\right]\cos\left(\phi_j-\phi_k\right)\\
&+ \cos\left[\left(\omega_{e,j}-\omega_{e,k}\right)t\right]\sin\left(\phi_j-\phi_k\right)\Bigg]\Bigg\} \qquad (3.46)
\end{aligned}
$$

Rearranging the terms, Eqn. (3.46) becomes

$$
\begin{aligned}
M_y^{(2)}(t) = \sum_{j=1}^{N}\sum_{k=1}^{N} a_{\eta,j}a_{\eta,k}\Bigg\{&\cos\left[\left(\omega_{e,j}+\omega_{e,k}\right)t\right]\Bigg[H_2^{C+}\left(\omega_{e,j},\omega_{e,k}\right)\cos\left(\phi_j+\phi_k\right)\\
&- H_2^{S+}\left(\omega_{e,j},\omega_{e,k}\right)\sin\left(\phi_j+\phi_k\right)\Bigg]\\
&- \sin\left[\left(\omega_{e,j}+\omega_{e,k}\right)t\right]\Bigg[H_2^{C+}\left(\omega_{e,j},\omega_{e,k}\right)\sin\left(\phi_j+\phi_k\right)\\
&+ H_2^{S+}\left(\omega_{e,j},\omega_{e,k}\right)\cos\left(\phi_j+\phi_k\right)\Bigg]\\
&+ \cos\left[\left(\omega_{e,j}-\omega_{e,k}\right)t\right]\Bigg[H_2^{C-}\left(\omega_{e,j},\omega_{e,k}\right)\cos\left(\phi_j-\phi_k\right)\\
&- H_2^{S-}\left(\omega_{e,j},\omega_{e,k}\right)\sin\left(\phi_j-\phi_k\right)\Bigg]\\
&- \sin\left[\left(\omega_{e,j}-\omega_{e,k}\right)t\right]\Bigg[H_2^{C-}\left(\omega_{e,j},\omega_{e,k}\right)\sin\left(\phi_j-\phi_k\right)\\
&+ H_2^{S-}\left(\omega_{e,j},\omega_{e,k}\right)\cos\left(\phi_j-\phi_k\right)\Bigg]\Bigg\} \qquad (3.47)
\end{aligned}
$$

or

$$M_y^{(2)}(t) = \sum_{j=1}^{N}\sum_{k=1}^{N} A_{jk}\Big\{\cos\left[\left(\omega_{e,j}+\omega_{e,k}\right)t\right]C_{jk}^{+} - \sin\left[\left(\omega_{e,j}+\omega_{e,k}\right)t\right]S_{jk}^{+}$$

$$+\cos\left[\left(\omega_{e,j}-\omega_{e,k}\right)t\right]C_{jk}^{-} - \sin\left[\left(\omega_{e,j}-\omega_{e,k}\right)t\right]S_{jk}^{-}\Big\} \tag{3.48}$$

where

$$A_{jk} = a_{\eta,j}a_{\eta,k} \tag{3.49}$$

$$C_{jk}^{+} = H_2^{C+}\left(\omega_{e,j},\omega_{e,k}\right)\cos\left(\phi_j+\phi_k\right) - H_2^{S+}\left(\omega_{e,j},\omega_{e,k}\right)\sin\left(\phi_j+\phi_k\right) \tag{3.50}$$

$$S_{jk}^{+} = H_2^{C+}\left(\omega_{e,j},\omega_{e,k}\right)\sin\left(\phi_j+\phi_k\right) + H_2^{S+}\left(\omega_{e,j},\omega_{e,k}\right)\cos\left(\phi_j+\phi_k\right) \tag{3.51}$$

$$C_{jk}^{-} = H_2^{C-}\left(\omega_{e,j},\omega_{e,k}\right)\cos\left(\phi_j-\phi_k\right) - H_2^{S-}\left(\omega_{e,j},\omega_{e,k}\right)\sin\left(\phi_j-\phi_k\right) \tag{3.52}$$

$$S_{jk}^{-} = H_2^{C-}\left(\omega_{e,j},\omega_{e,k}\right)\sin\left(\phi_j-\phi_k\right) + H_2^{S-}\left(\omega_{e,j},\omega_{e,k}\right)\cos\left(\phi_j-\phi_k\right) \tag{3.53}$$

Similarly to the linear VBM simulation, the nonlinear part can also be rewritten in a way that replaces the double sum with matrix-vector multiplication. This way, Mathlab's very efficient algorithm for matrix-vector multiplication can be used to simulate the nonlinear VBM. Let

$$\boldsymbol{M_y^{(2)}} = \left[M_{y,1}^{(2)}, M_{y,2}^{(2)}, \cdots, M_{y,M}^{(2)}\right]^{\mathrm{T}} \tag{3.54}$$

be a column vector of the nonlinear part of the VBM calculated at time instants $\boldsymbol{t} = [t_1, t_2, \cdots, t_M]^{\mathrm{T}}$. If the entire range of encounter frequencies from $\omega_{e,MIN}$ to $\omega_{e,MAX}$ is divided into N frequency intervals, then the matrices of super and subharmonic encounter frequencies are defined as

$$\boldsymbol{\Omega}^{+} = \begin{pmatrix} (\omega_{e,1}+\omega_{e,1}) & (\omega_{e,1}+\omega_{e,2}) & \cdots & (\omega_{e,1}+\omega_{e,N}) \\ (\omega_{e,2}+\omega_{e,1}) & (\omega_{e,2}+\omega_{e,2}) & \cdots & (\omega_{e,2}+\omega_{e,N}) \\ \vdots & \vdots & \ddots & \vdots \\ (\omega_{e,N}+\omega_{e,1}) & (\omega_{e,N}+\omega_{e,2}) & \cdots & (\omega_{e,N}+\omega_{e,N}) \end{pmatrix} \tag{3.55}$$

and

$$\boldsymbol{\Omega}^{-} = \begin{pmatrix} (\omega_{e,1}-\omega_{e,1}) & (\omega_{e,1}-\omega_{e,2}) & \cdots & (\omega_{e,1}-\omega_{e,N}) \\ (\omega_{e,2}-\omega_{e,1}) & (\omega_{e,2}-\omega_{e,2}) & \cdots & (\omega_{e,2}-\omega_{e,N}) \\ \vdots & \vdots & \ddots & \vdots \\ (\omega_{e,N}-\omega_{e,1}) & (\omega_{e,N}-\omega_{e,2}) & \cdots & (\omega_{e,N}-\omega_{e,N}) \end{pmatrix} \tag{3.56}$$

Now, using Eqn. (3.48) the nonlinear part of the VBM can be simulated using

$$\boldsymbol{M_y^{(2)}} = \begin{pmatrix} M_{y,1}^{(2)} \\ M_{y,2}^{(2)} \\ \vdots \\ M_{y,M}^{(2)} \end{pmatrix} =$$

$$\cos \begin{pmatrix} t_1\Omega_{11}^+ & t_1\Omega_{12}^+ & \cdots & t_1\Omega_{1N}^+ & t_1\Omega_{21}^+ & t_1\Omega_{22}^+ & \cdots & t_1\Omega_{2N}^+ & \cdots & t_1\Omega_{NN}^+ \\ t_2\Omega_{11}^+ & t_2\Omega_{12}^+ & \cdots & t_2\Omega_{1N}^+ & t_2\Omega_{21}^+ & t_2\Omega_{22}^+ & \cdots & t_2\Omega_{2N}^+ & \cdots & t_2\Omega_{NN}^+ \\ \vdots & \vdots & \ddots & \vdots & \vdots & \vdots & \ddots & \vdots & \ddots & \vdots \\ t_M\Omega_{11}^+ & t_M\Omega_{12}^+ & \cdots & t_M\Omega_{1N}^+ & t_M\Omega_{21}^+ & t_M\Omega_{22}^+ & \cdots & t_M\Omega_{2N}^+ & \cdots & t_M\Omega_{NN}^+ \end{pmatrix} \cdot \begin{pmatrix} A_{11}C_{11}^+ \\ A_{12}C_{12}^+ \\ \vdots \\ A_{NN}C_{NN}^+ \end{pmatrix}$$

$$-\sin \begin{pmatrix} t_1\Omega_{11}^+ & t_1\Omega_{12}^+ & \cdots & t_1\Omega_{1N}^+ & t_1\Omega_{21}^+ & t_1\Omega_{22}^+ & \cdots & t_1\Omega_{2N}^+ & \cdots & t_1\Omega_{NN}^+ \\ t_2\Omega_{11}^+ & t_2\Omega_{12}^+ & \cdots & t_2\Omega_{1N}^+ & t_2\Omega_{21}^+ & t_2\Omega_{22}^+ & \cdots & t_2\Omega_{2N}^+ & \cdots & t_2\Omega_{NN}^+ \\ \vdots & \vdots & \ddots & \vdots & \vdots & \vdots & \ddots & \vdots & \ddots & \vdots \\ t_M\Omega_{11}^+ & t_M\Omega_{12}^+ & \cdots & t_M\Omega_{1N}^+ & t_M\Omega_{21}^+ & t_M\Omega_{22}^+ & \cdots & t_M\Omega_{2N}^+ & \cdots & t_M\Omega_{NN}^+ \end{pmatrix} \cdot \begin{pmatrix} A_{11}S_{11}^+ \\ A_{12}S_{12}^+ \\ \vdots \\ A_{NN}S_{NN}^+ \end{pmatrix}$$

$$+\cos \begin{pmatrix} t_1\Omega_{11}^- & t_1\Omega_{12}^- & \cdots & t_1\Omega_{1N}^- & t_1\Omega_{21}^- & t_1\Omega_{22}^- & \cdots & t_1\Omega_{2N}^- & \cdots & t_1\Omega_{NN}^- \\ t_2\Omega_{11}^- & t_2\Omega_{12}^- & \cdots & t_2\Omega_{1N}^- & t_2\Omega_{21}^- & t_2\Omega_{22}^- & \cdots & t_2\Omega_{2N}^- & \cdots & t_2\Omega_{NN}^- \\ \vdots & \vdots & \ddots & \vdots & \vdots & \vdots & \ddots & \vdots & \ddots & \vdots \\ t_M\Omega_{11}^- & t_M\Omega_{12}^- & \cdots & t_M\Omega_{1N}^- & t_M\Omega_{21}^- & t_M\Omega_{22}^- & \cdots & t_M\Omega_{2N}^- & \cdots & t_M\Omega_{NN}^- \end{pmatrix} \cdot \begin{pmatrix} A_{11}C_{11}^- \\ A_{12}C_{12}^- \\ \vdots \\ A_{NN}C_{NN}^- \end{pmatrix}$$

$$-\sin \begin{pmatrix} t_1\Omega_{11}^- & t_1\Omega_{12}^- & \cdots & t_1\Omega_{1N}^- & t_1\Omega_{21}^- & t_1\Omega_{22}^- & \cdots & t_1\Omega_{2N}^- & \cdots & t_1\Omega_{NN}^- \\ t_2\Omega_{11}^- & t_2\Omega_{12}^- & \cdots & t_2\Omega_{1N}^- & t_2\Omega_{21}^- & t_2\Omega_{22}^- & \cdots & t_2\Omega_{2N}^- & \cdots & t_2\Omega_{NN}^- \\ \vdots & \vdots & \ddots & \vdots & \vdots & \vdots & \ddots & \vdots & \ddots & \vdots \\ t_M\Omega_{11}^- & t_M\Omega_{12}^- & \cdots & t_M\Omega_{1N}^- & t_M\Omega_{21}^- & t_M\Omega_{22}^- & \cdots & t_M\Omega_{2N}^- & \cdots & t_M\Omega_{NN}^- \end{pmatrix} \cdot \begin{pmatrix} A_{11}S_{11}^- \\ A_{12}S_{12}^- \\ \vdots \\ A_{NN}S_{NN}^- \end{pmatrix} \tag{3.57}$$

Since the LTFs are vectors of size N and the QTFs are $N \times N$ matrices, the number of operations needed to calculate $M_y^{(1)}$ at a single instant of time is of the order N, while the number of operations needed for calculating $M_y^{(2)}$ is of the order N^2. From this it is clear that, by far, the highest computational cost will be associated with the nonlinear part of the VBM, $M_y^{(2)}$. However, as it will be explained in Section 3.4.4.3, a lot of QTF matrix elements are equal, or very close to zero. Therefore, it is theoretically possible to significantly

reduce the number of operations needed for simulating the nonlinear VBM. The results of such analysis will be presented in the next section.

3.4 Results of the Long-Term VBM Simulation with Nonlinearities and Springing

Results of the long-term simulation of the VBM with nonlinearities and springing are presented for two ships - C 319 container ship and T 306 tanker. Both, the nonlinearities and the springing effects are expected to be more significant for the container ship because of its fine form and much higher design speed compared to the tanker. Structural properties that are needed for the springing assessment are given in Vidić-Perunović [109] for T 306 and in Senjanović et al. [96] for C 319. Added mass of C 319 container ship, which is not given in Senjanović et al., is calculated using the procedure of Šimanskij described in [100]. Detailed plots of structural and mass properties of C 319 container ship are also given in Appendix C.1. Same operational profiles as those described in Section 2.2.2.2 are used in this chapter.

3.4.1 Damping Considerations

The total damping of the hull that is vibrating in water is composed of hydrodynamic damping, structural damping and damping due to friction between the hull structure and the cargo it caries. Hydrodynamic part of the damping is usually close to zero at springing frequencies because the ship vibratory motions are small and there is very little wave radiation. Damping due to cargo is also very small. Therefore, the structural damping is the dominant part of the total damping at springing frequencies. Total damping coefficient, n, depends on many factors including ship structural properties, hull geometry, loading condition, mode and frequency of vibration. In practice, it is very difficult to quantify the damping coefficient. Exact mechanism of damping cannot be theoretically modeled today for a complex structure such as the ship hull. Full-scale measurements suggest that the damping ratio ξ, given by

$$\xi = \frac{n}{n_0} \tag{3.58}$$

is of the order of 10^{-3} to 10^{-2}. n_0 is the critical damping of an equivalent single degree of freedom system and is given by

$$n_0 = 2m\omega_1 \tag{3.59}$$

where m is the total mass of the ship, including the added mass, and ω_1 is the natural frequency of the springing two-node vibration mode. It is assumed that the damping coefficient, n, does not change over the length of the beam. This assumption is reasonable since it is not possible to measure the damping per section, only the overall damping (Jensen [48]). ABS [3] suggests the use of $\xi = 0.03$ and $\xi = 0.015$ for container ships in full load and

ballast conditions, respectively. The vale of $\xi = 0.03$ is used for both ships considered in this chapter (C 319 and T 306). However, in order to cover the spread in suggested values found in the literature, the long-term simulations are also performed with damping ratios equal to 0.001 and 0.01 for C 319 on NA route (see Section 3.4.4.4).

3.4.2 Linear and Quadratic Transfer Functions

Linear and quadratic transfer functions for VBM, both accounting for the hydroelastic response of the ship, have been calculated using the quadratic strip theory program SOST for each speed and loading condition from the operational profile, each damping ration, and each relative heading, α, in ten degree increments. Figure 3.1 shows linear RAOs for C 319 container ship with forward speed $V = 6.35$ knots and relative damping $\xi = 0.03$. For comparison, the RAOs from linear strip theory program SEAWAY are given as well (dashed lines). SEAWAY does not take hydroelasticity into account. Therefore, RAOs from SEAWAY do not have a pronounced second peak at the natural frequency corresponding to the two-node vibration mode of the hull.

This resonant springing frequency is found to be around $\omega_e = 2.95$ rad/s ($\omega = 1.8$ rad/s at $V = 6.35$ knots and $\alpha = 0°$) for C 319 in full load condition and around $\omega_e = 2.90$ rad/s and $\omega_e = 2.35$ rad/s for T 306 in ballast and full load conditions, respectively. These frequencies are slightly affected by the value of damping ratio. However, the magnitude of the response of the hull at the resonant springing frequency varies significantly with damping ratio, especially for T 306 in ballast. This can be seen in Figure 3.2 which shows the VBM RAOs from SOST for C 319 and T 306 ships traveling at their design speeds in head seas with $\xi = 0.001$, 0.01, and 0.03. The abscissa is the encounter frequency, ω_e, as opposed to the absolute frequency, ω, in Figure 3.1.

Both wave-induced (fundamental) and springing peaks of the VBM response amplitude operator are higher in the case of T 306 in ballast compared to T 306 in full load condition. This is caused by the increase in hydrodynamic force on the hull when the draft decreases. The hydrodynamic pressure is equal to the difference between the total pressure in the fluid and the hydrostatic pressure. This difference, represented by the Smith correction factor (see Appendix B.1), decays with the depth level in the fluid, i.e. with the draft of the ship.

Moduli of the VBM QTFs for superharmonics, H_2^+, and subharmoniscs, H_2^-, in the bi-encounter frequency domain are shown in Figure 3.3 for the C 319 container ship in full load condition with speed $V = 25.4$ knots in head seas and damping ratio $\xi = 0.03$. It can be seen that for C 319 container ship superharmonics play a more dominant role in the second-order VBM compared to the subharmonics. Second-order springing seems to be the dominant factor in the second-order response since the maximum values of $\left|H_2^+\right|$ lie on the line representing superharmonics with the encounter frequency equal to the springing frequency, i.e., $\omega_{e,i} + \omega_{e,j} \approx 2.95$ rad/s. This can be seen more easily in Figure 3.4 which shows a contour plot of the same $\left|H_2^+\right|$ as in Figure 3.3a.

It should be noted that the program SOST only considers superharmonics whose frequency does not exceed the maximum encounter frequency of all single harmonics, i.e,

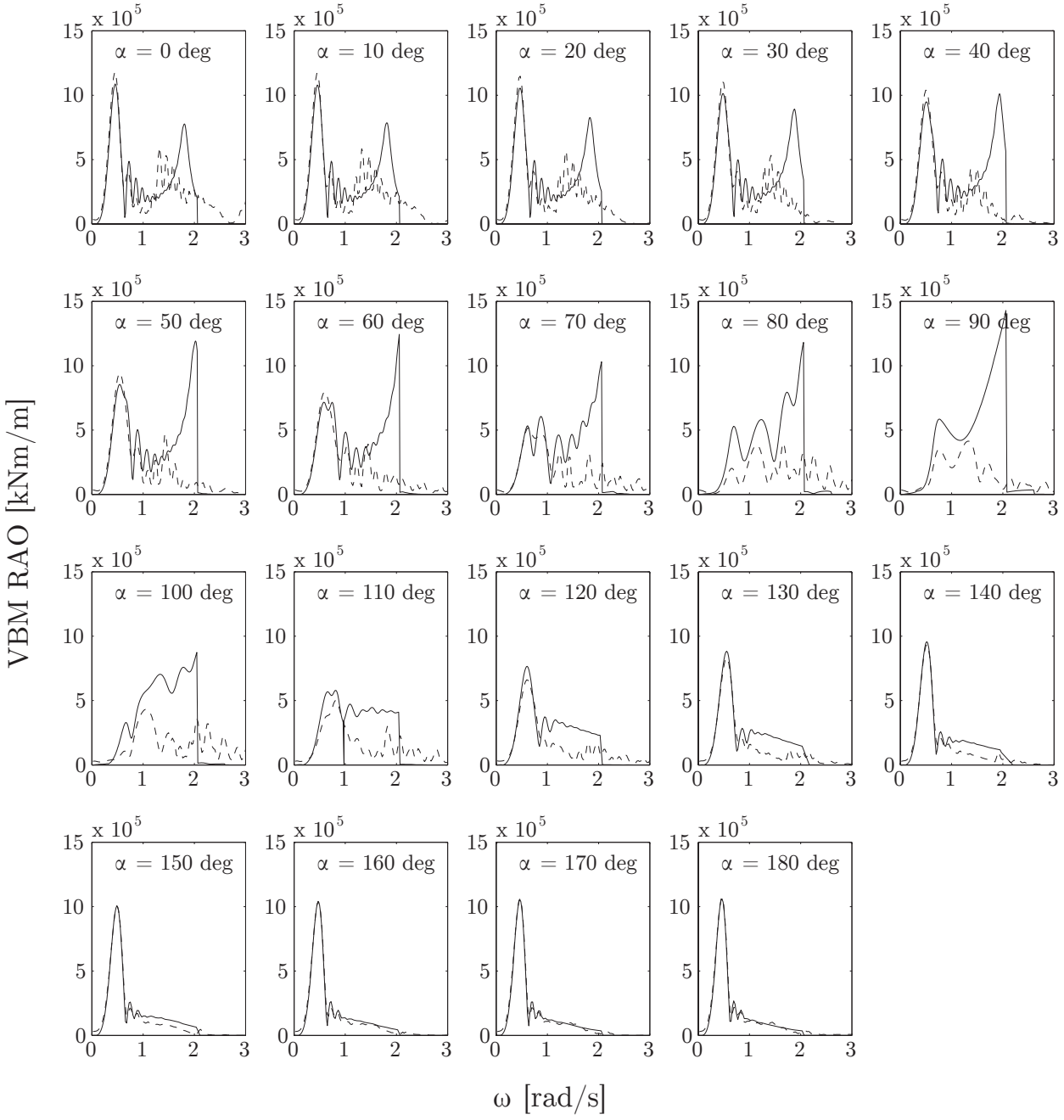

Figure 3.1: Linear VBM RAOs for fully loaded C 319 container ship with forward speed of $V = 6.35$ knots and relative damping $\xi = 0.03$; Solid lines are from SOST and they include the high-frequency springing response; Dashed lines are from SEAWAY without any springing effects.

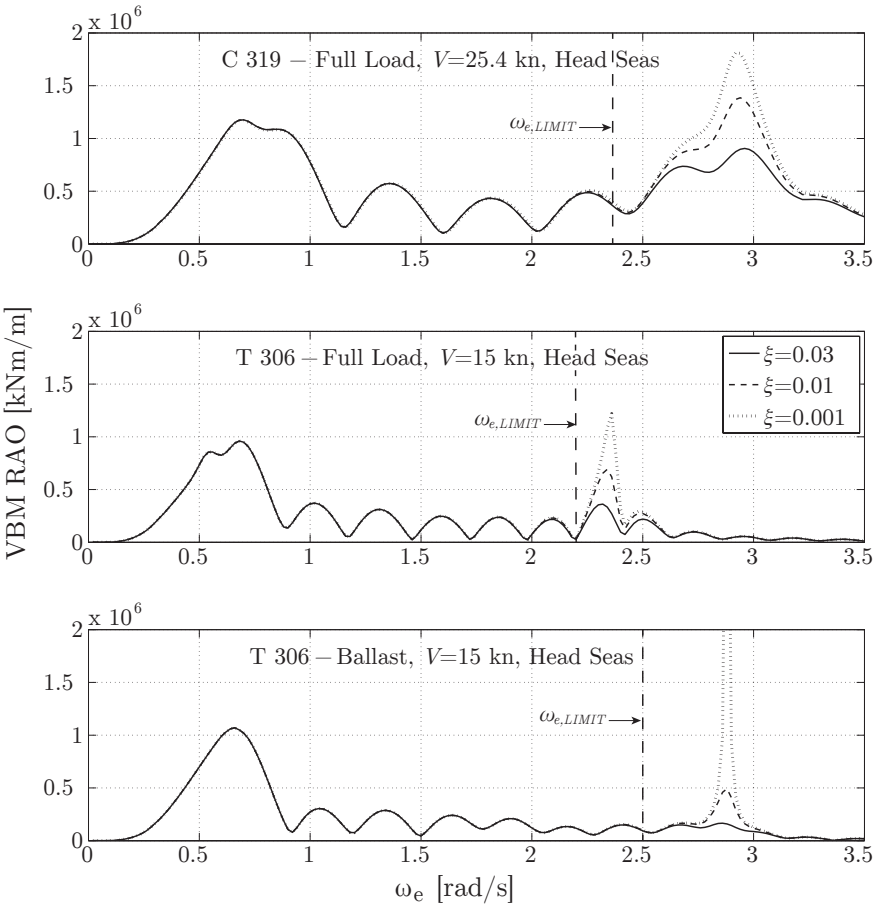

Figure 3.2: Linear VBM RAOs for C 319 container ship and T 306 tanker at their respective design speeds and head seas.

$\omega_{e,i} + \omega_{e,j} \leq \omega_{e,MAX}$. This is because the second-order response of the ship to superharmonics with such high encounter frequencies is usually negligible in realistic sea conditions. This is also observed in this work. All simulated harmonics, superharmonics and subharmonics carrying any appreciable amount of energy had encounter frequencies of less than 3.5 rad/s. Therefore, the Nyquist frequency for the second-order simulation is equal to 7 rad/s. In this work, both the first-order and the second-order VBM are generated with a frequency equal to 8 rad/s (1.27 Hz) which is sufficient since it exceeds the Nyquist frequency. The number of frequency intervals is the same as for the first-order analysis, i.e., $N = 200$.

Figure 3.5 shows plots of $\left|H_2^+\right|$ for T 306 tanker with speed $V = 15$ knots in head seas for ballast and full load conditions, respectively. The damping ratio is $\xi = 0.03$ for both loading conditions. As in the case of container ship, second-order response of tanker also peaks along the line in the bi-encounter frequency domain which represents springing (2.35 rad/s for ballast and 2.90 rad/s for full load). The second-order response is significantly larger for the tanker in ballast compared to the full load condition. The reason is the same

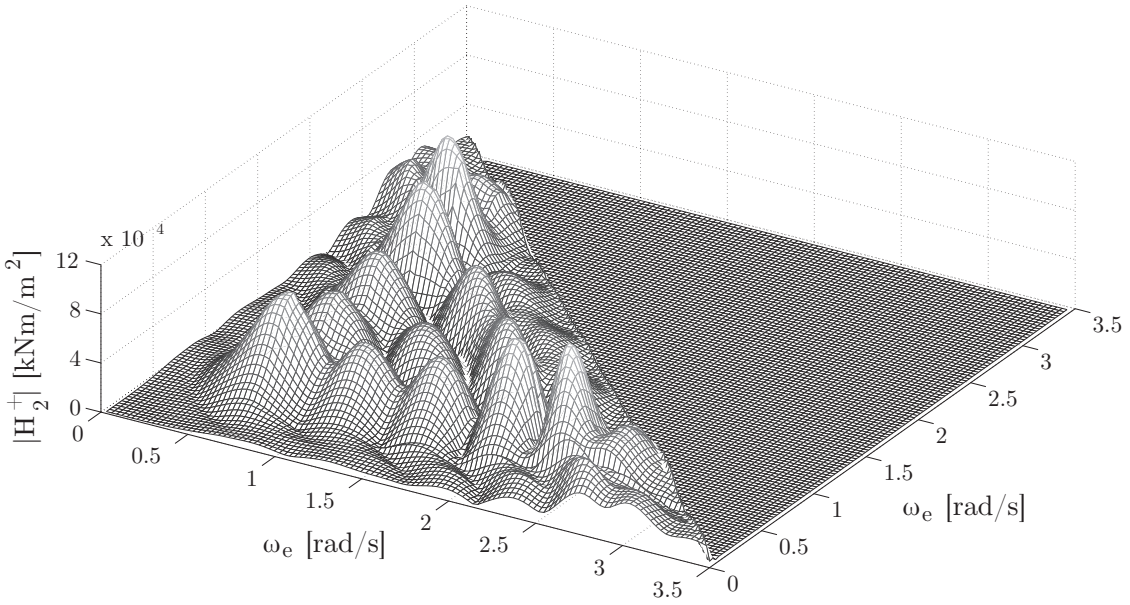

(a) Superharmonics.

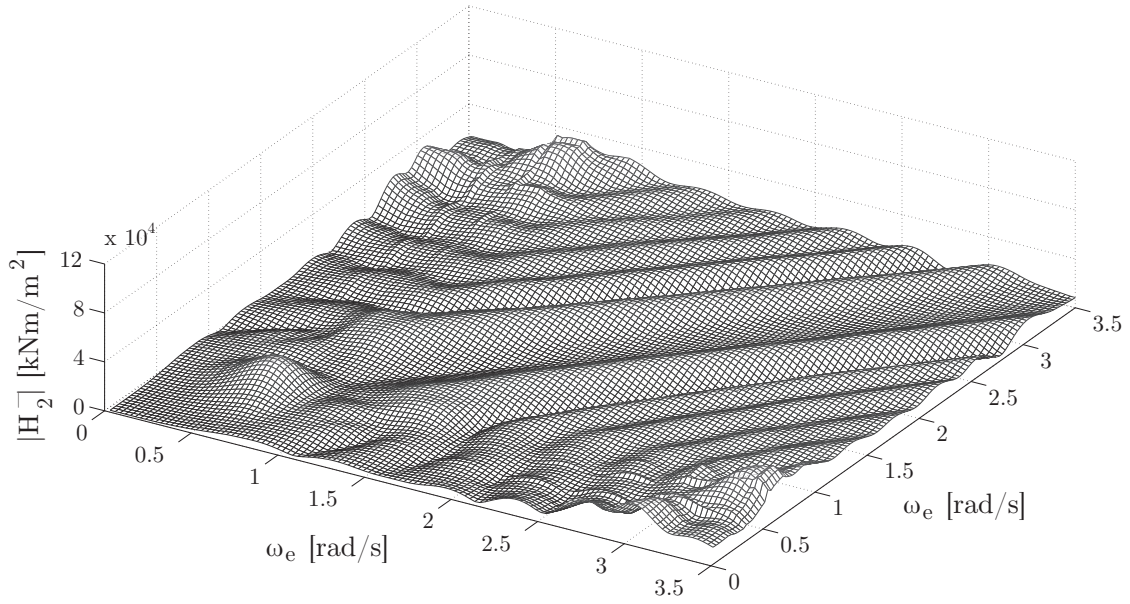

(b) Subharmonisc.

Figure 3.3: Moduli of QTFs associated with super and subharmonic second-order VBM terms for C 319 container ship; $V = 25.4$ knots, $\alpha = 0$ degrees, $\xi = 0.03$.

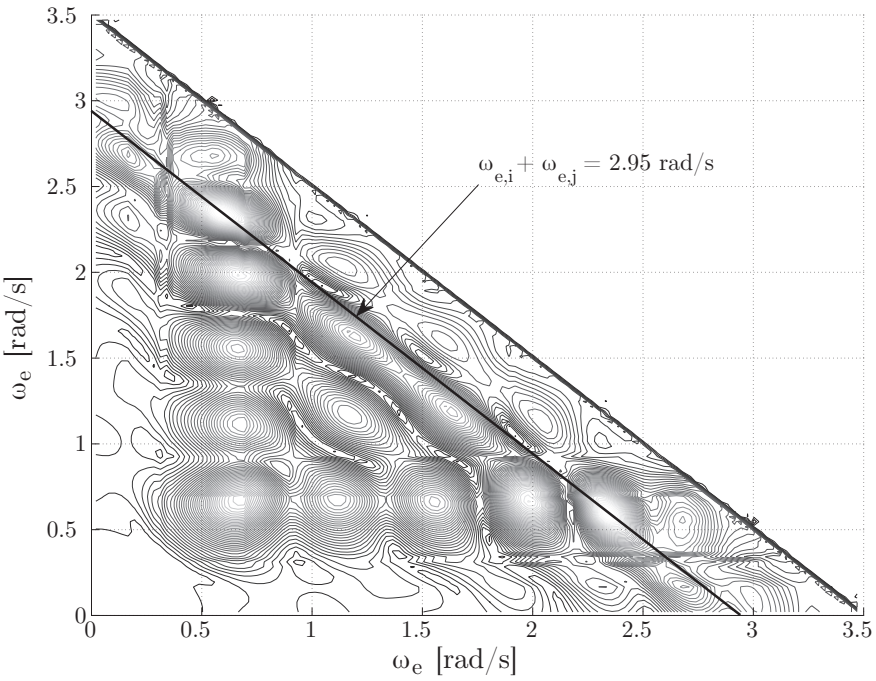

Figure 3.4: Contour plot of $\left|H_2^+\right|$ from Figure 3.3a.

as in the first-order case: the hydrodynamic forces are larger when the vessel is at a lower draft.

3.4.3 Short-Term Simulations

The simulated total VBM (first- and second-order) in larger sea states can no longer be assumed Gaussian. The Central Limit Theorem no longer applies in the second-order case since each superharmonic and subharmonic involves two uniformly distributed random variables, ϕ_j and ϕ_k (see Eqn (3.43)) and are, therefore, not independent of each other. The influence of the second-order VBM on the total VBM becomes larger in moderate to high sea states. Therefore, it is expected that the resulting VBM will deviate more from normality in higher sea states than in low ones. Figure 3.6 shows the q–q plots of the total VBM in two sea states / operational profile combinations for C 319 container ship. The first one is relatively benign and is characterized by $H_S = 4$ meters, $T_0 = 5.52$ seconds, $\alpha = 0°$, and $V = 25.4$ knots. The second sea state and the associated operational profile of the ship are much more severe and are characterized by $H_S = 13.7$ meters, $T_0 = 11.07$ seconds, $\alpha = 0°$, and $V = 6.35$ knots. From Figure 3.6b it is evident that the assumption of normality of the VBM no longer holds in high sea states. For low sea states (Figure 3.6a) there is no reason to reject the assumption of normality as the total VBM is dominated by the first-order term. It was shown in Section 2.2.2.3, Figure 2.7, that there is no evidence to reject the assumption of normality of this term.

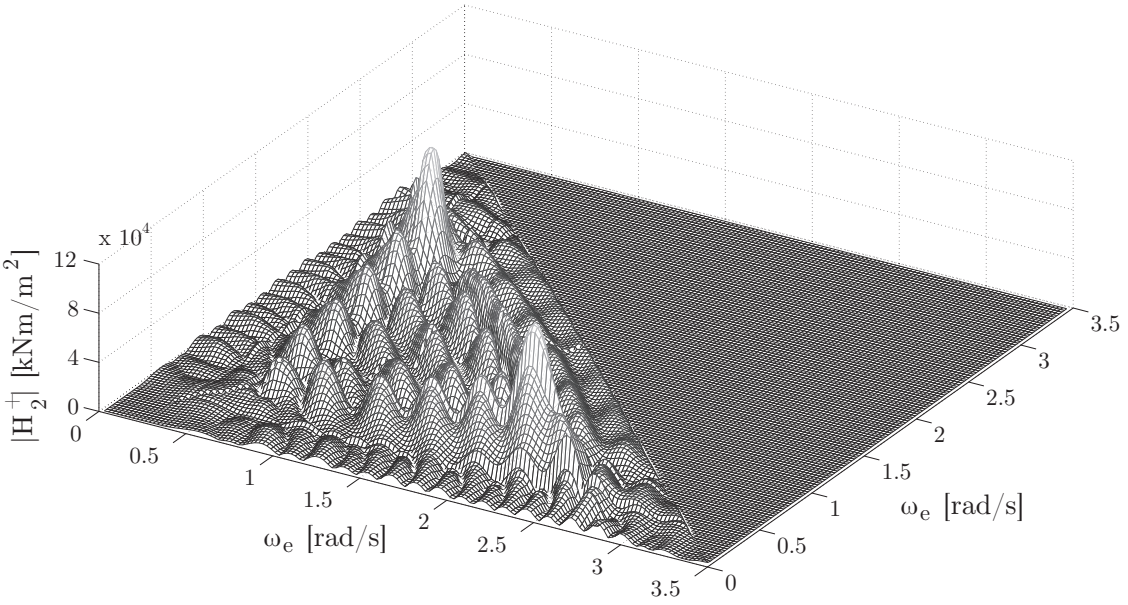

(a) Superharmonics; ballast condition.

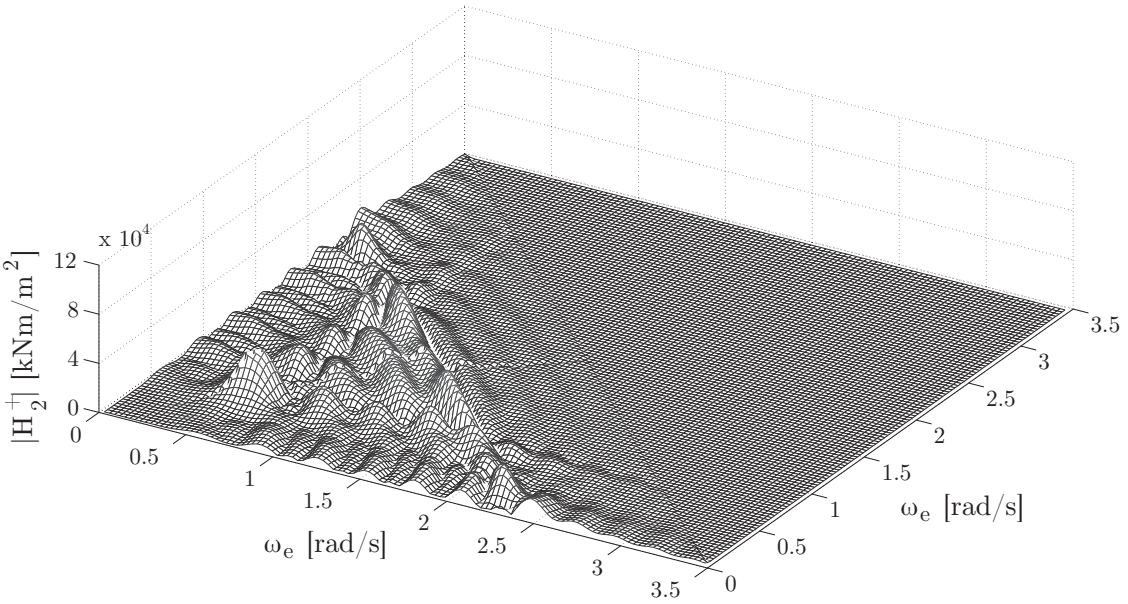

(b) Superharmonics; full load condition.

Figure 3.5: Moduli of QTFs associated with superharmonic second-order VBM terms for T 306 tanker in different loading conditions; $V = 15$ kn, $\alpha = 0°$, $\xi = 0.03$.

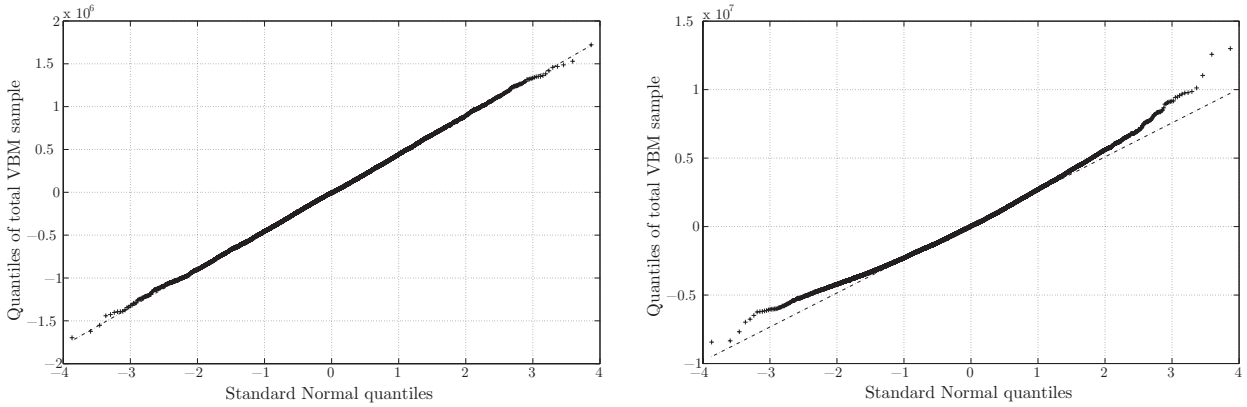

(a) Low sea state; $H_S = 4$ m, $T_0 = 5.52$ s, $\alpha = 0°$, $V = 25.4$ kn.

(b) High sea state; $H_S = 13.7$ m, $T_0 = 11.07$ s, $\alpha = 0°$, $V = 6.35$ kn.

Figure 3.6: q–q plot of the simulated total VBM in low and high sea states for C 319 container ship; $\xi = 0.03$.

In order to study the effects of high-frequency linear terms, as well as the effects of second-order super and subharmonic terms on the VBM, the total value of the VBM is decomposed as follows

$$M_y^{(1)+(2)^{\pm}} = M_{y,LF}^{(1)} + M_{y,HF}^{(1)} + M_y^{(2)^+} + M_y^{(2)^-} \tag{3.60}$$

where $M_y^{(1)+(2)^{\pm}}$ is the total VBM, $M_{y,LF}^{(1)}$ is the low-frequency first-order (linear) VBM, $M_{y,HF}^{(1)}$ is the high-frequency (springing) first-order VBM, $M_y^{(2)^+}$ is the second-order (nonlinear) superharmonic VBM, and $M_y^{(2)^-}$ is the second-order subharmonic VBM. The second-order terms encompass the whole range of frequencies between $\omega_e = 0$ and $\omega_e = 2\omega_{e,MAX}$, and the distinction between low- and high-frequency ones is not needed. Also

$$M_{y,LF+HF}^{(1)} = M_{y,LF}^{(1)} + M_{y,HF}^{(1)} \tag{3.61}$$

is the total first-order VBM obtained by using the same principles already described in Chapter 2, but with LTFs from program SOST which include the high-frequency hydroelastic response of the ship. The low-frequency part, $M_{y,LF}^{(1)}$, can be simulated by considering only the encounter frequencies up to the limit marking the onset of springing. This limiting encounter frequency (see Figure 3.1) is set to $\omega_{e,LIMIT} = 2.36$ rad/s for the C319 container ship in full load, $\omega_{e,LIMIT} = 2.50$ for the T 306 tanker in ballast, and $\omega_{e,LIMIT} = 2.20$ for tanker in full load.

Figures 3.7 and 3.8 show hundred seconds long time series of each of these terms for C 319 container ship navigating in aforementioned low and high sea states, respectively.

In the low sea state (Figure 3.7), first-order high-frequency VBM, $M_{y,HF}^{(1)}$, is very significant and is of the same order of magnitude as the first-order low-frequency VBM. This

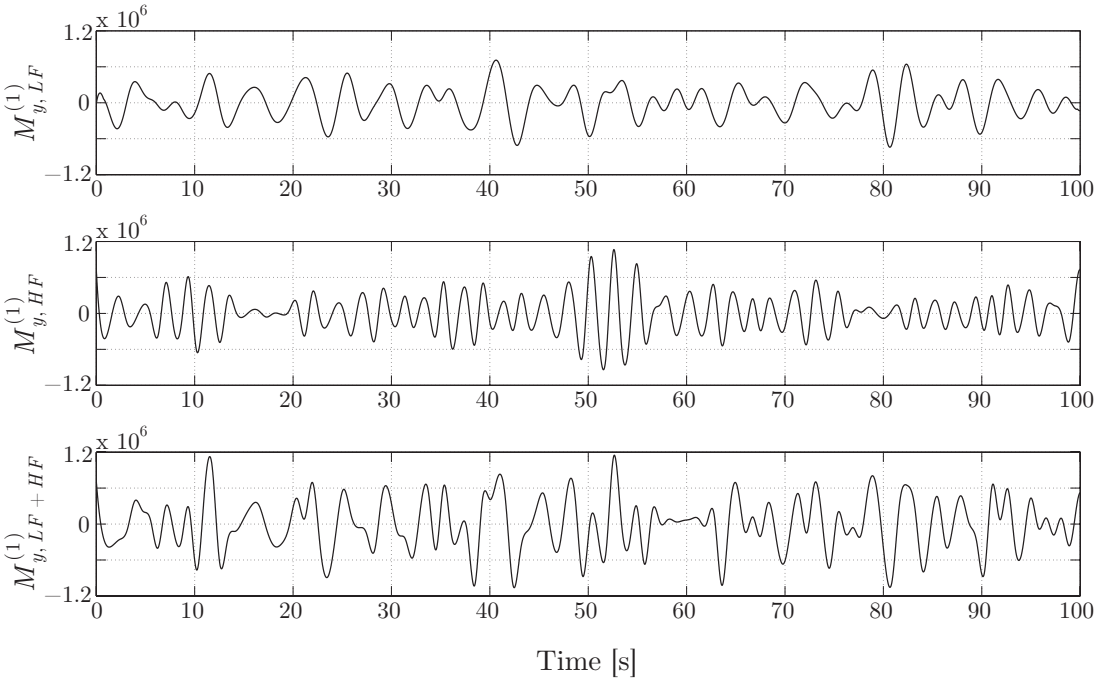

(a) First-order terms.

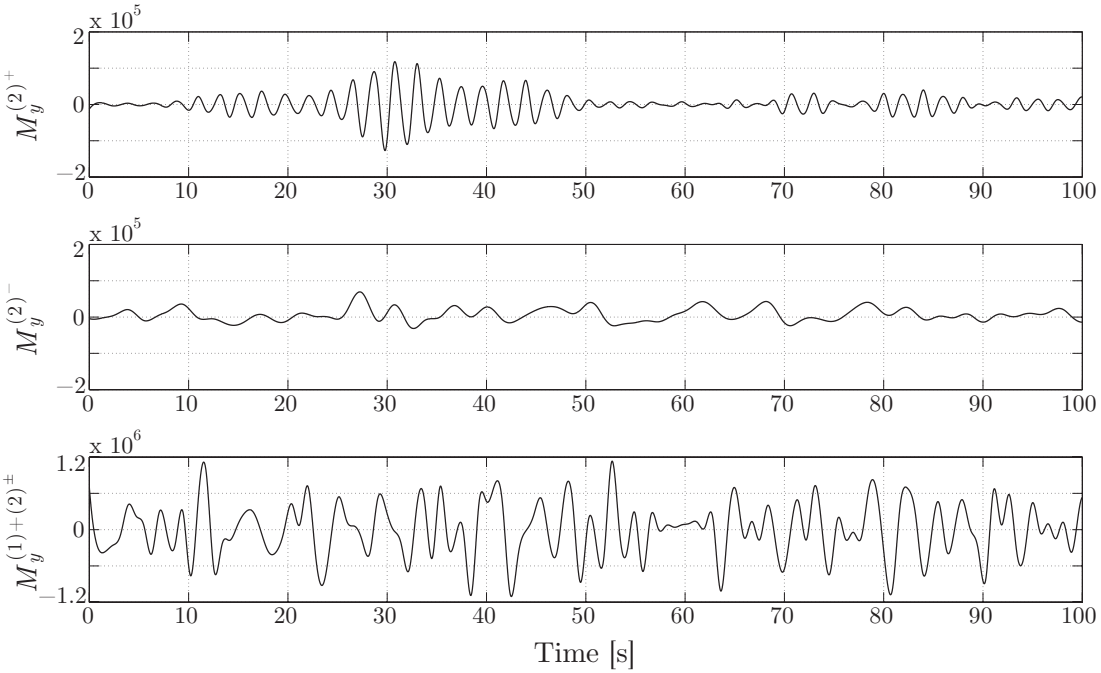

(b) Second-order terms and total VBM.

Figure 3.7: First- and second-order VBM terms for C 319 container ship in low sea state; $H_S = 4$ m, $T_0 = 5.52$ s, $\alpha = 0°$, $V = 25.4$ kn, $\xi = 0.03$.

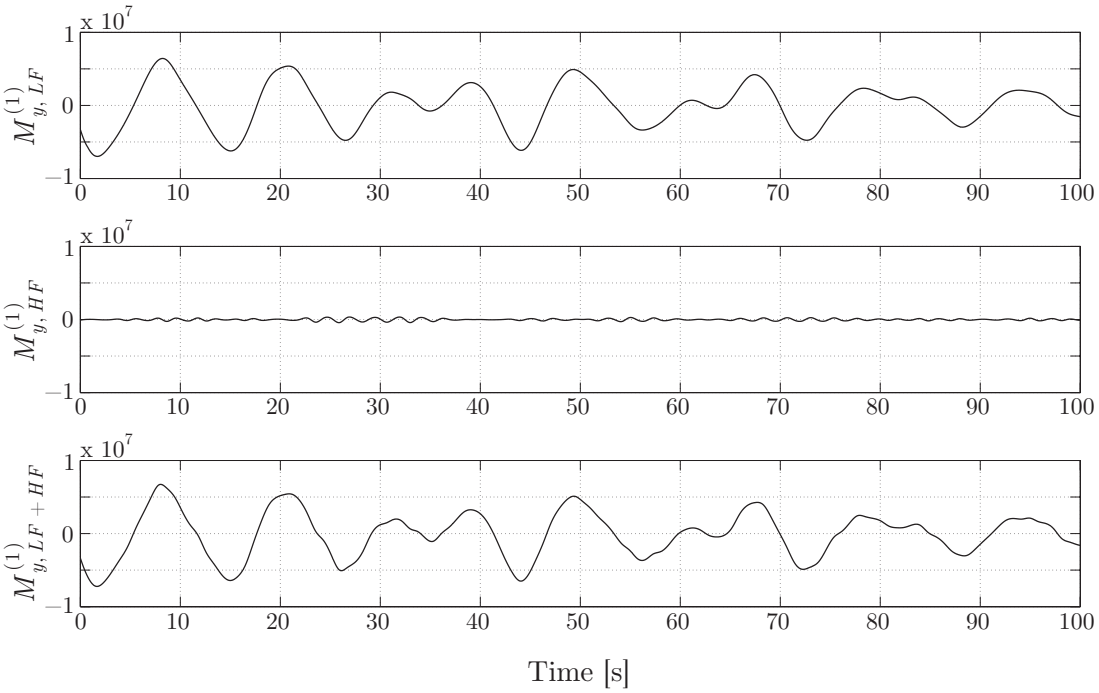

(a) First-order terms.

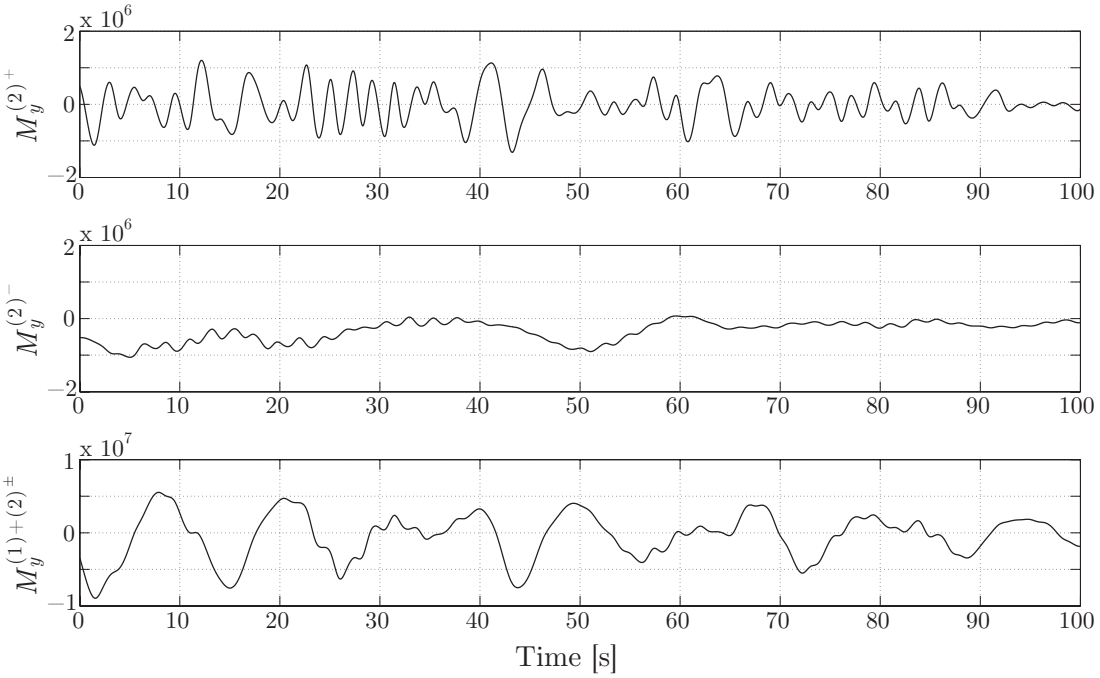

(b) Second-order terms and total VBM.

Figure 3.8: First- and second-order VBM terms for C 319 container ship in high sea state; $H_S = 13.7$ m, $T_0 = 11.07$ s, $\alpha = 0^circ$, $V = 6.35$ kn, $\xi = 0.03$.

is expected since the average zero crossing period in that sea state is equal to 5.52 seconds, corresponding to encounter frequency of 2.86 rad/s which is close to the springing frequency of 2.95 rad/s. On the other hand, the second-order parts of the VBM are one order of magnitude smaller than the first order VBM. The basic frequency of oscillations of the second-order superharmonic VBM is very close to the springing frequency. This is called the second-order springing and it is caused by the bi-harmonic wave components whose combined encounter frequency approximately equals the frequency of the two node vibration mode of the hull, i.e., $\omega_{e,j} + \omega_{e,k} \approx 2.95$ rad/s.

In the high sea state the situation is quite different. Apart from the total VBM being much larger, there is very little first-order springing since the average encounter frequency of the incoming waves is well outside the springing frequency range. On the other hand, second-order VBM is quite significant, both the superharmonic and the subharmonic parts. Looking at the frequency of oscillations of the superharmonic VBM reveals the presence of second-order springing which is now mixed with other lower frequency superharmonics. The slowly-varying subharmonic VBM has a nonzero mean value due to subharmonic terms with zero frequency. These constant terms arise when $\omega_{e,j} = \omega_{e,k}$.

The maximum second-order response of the C 319 container ship in two hundred voyages occurs while the ship is in a moderate sea state with very steep waves close to the wave breaking limit ($H_S = 7.4$ m, $T_0 = 6.86$ s). Larger sea states carry energy at lower frequencies (longer periods) which are outside the nonlinear springing region in which the second-order response is dominant. Also, the speed of the ship reduces in heavy seas which further shifts the encounter wave spectrum towards lower frequencies. On the other hand, lower sea states with periods closer to the nonlinear springing region don't have enough energy to excite significant second-order response. Therefore, largest nonlinear responses of the C 319 container ship will not coincide with the largest linear responses because the latter occur in the highest sea states.

It is interesting to compare directly the first-order VBM ($M^{(1)}_{y,LF+HF}$) with the total VBM in the high sea state. This is done in Figure 3.9 for the same hundred seconds time interval as in Figure 3.8b. First-order short-term VBM is assumed Gaussian and symmetrically distributed around the zero mean value. Second-order terms have the effect of increasing the negative (sagging) and decreasing the positive (hogging) VBM peaks. This asymmetry between the sagging and hogging VBMs is caused mainly by the nonvertical sides of the ship, and the effect is more pronounced for ships with large flaring of the sides, such as container ships. This will have an effect on the long-term probabilities of exceedance of the total VBM as is shown later in Section 3.4.4.2.

3.4.4 Long-Term Simulations

Of particular importance to every ship designer is the long-term distribution of the total VBM. If the first- and second-order VBM time series, expressed by Eqns. (3.37) and (3.43), are simulated using the same random waves, then their proper correlation is ensured and the resulting total VBM time series can be obtained by a simple addition of corresponding

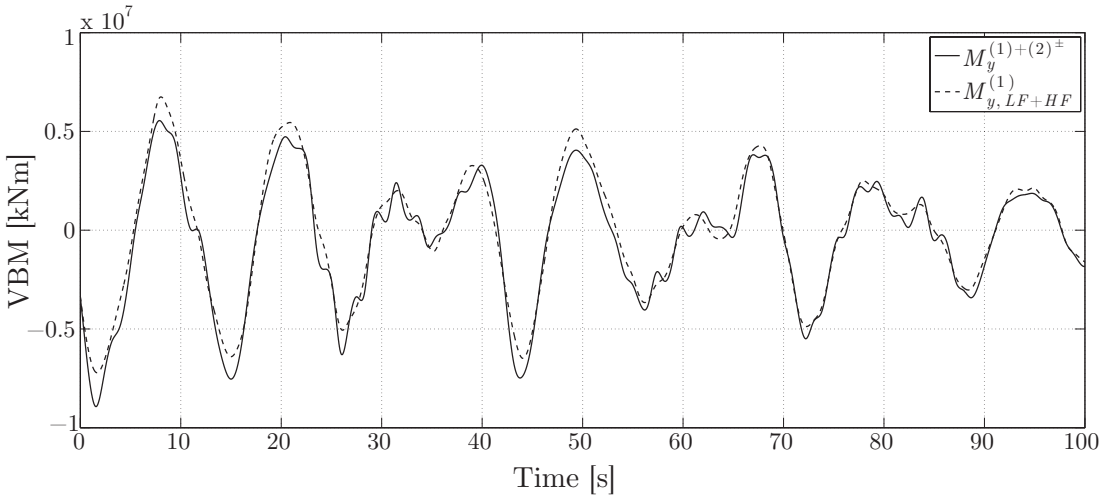

Figure 3.9: The effect of second-order VBM; C 319, $H_S = 13.7$ m, $T_0 = 11.07$ s, $\alpha = 0°$, $V = 6.35$ kn, $\xi = 0.03$.

point-in-time values. Empirical long-term probabilities of exceedance (1-ECDF) of the total VBM are then obtained using the procedure described in Section 2.3.3.

Figure 3.10 shows the empirical probability of exceedance of sagging VBM peaks for C 319 container ship on NA route with the damping ratio $\xi = 0.03$. 95% confidence intervals and two parameter Weibull distribution fit are shown as well. This distribution fits the simulated long-term VBM data very well, even when the nonlinearities are taken into account. This is consistent with the observation of many authors including: Lewis [61], Fukuda [26], and Hoffman and Lewis [37]. It was found in these studies that the Weibull distribution is general enough to fit the VBM data measured on ships. Similarly to the case of linear VBM, the empirical probabilities of exceedance converge for time series of fifty voyages or longer.

3.4.4.1 Long-Term Effects of Nonlinearities and Hull Flexibility on VBM

The effects of nonlinearities and high-frequency VBM due to springing can be seen in Figure 3.11 where the fitted probabilities of exceedance of sagging peaks are shown for the individual VBM components from Eqns. (3.60) and (3.61). The second-order terms have a significant effect on the long-term exceedance probability of VBM peaks. Nonlinearities account for the 24.7% increase in the extreme VBM value at 10^{-8} probability level compared to the linear rigid body (low-frequency) VBM. If only the superharmonic second-order terms are considered, then the increase is 16.0% at the same probability level. Therefore, superharmonic terms seem to be more significant than subharmonics.

The first-order VBM for flexible hull, $M_{y,LF+HF}^{(1)}$, has a slightly lower probabilities of exceedance and lower extreme VBM value at 10^{-8} probability level than the first-order VBM for rigid hull, $M_{y,LF}^{(1)}$. This is counterintuitive and requires further explanation. The second (springing) peak in the high-frequency region of the LTF for a flexible hull increases the

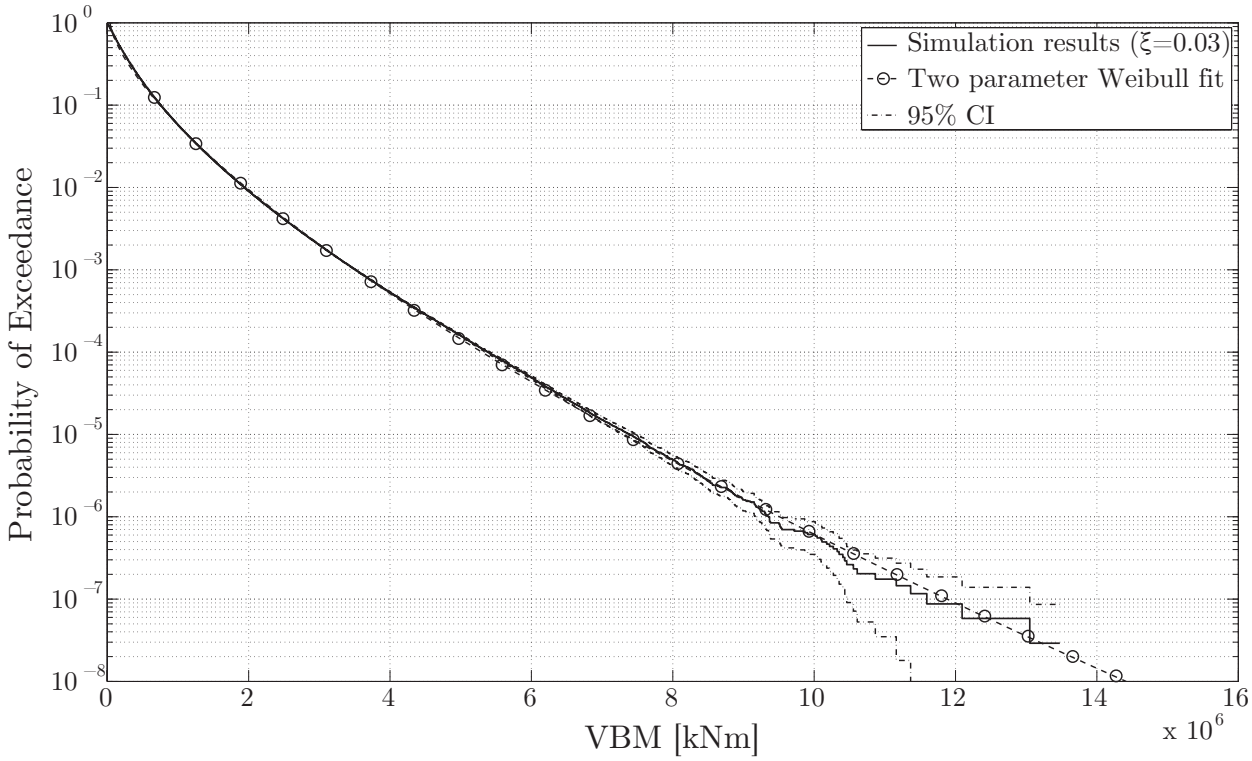

Figure 3.10: Probability of exceedance of nonlinear sagging VBM peaks based on two hundred voyages of C 319 container ship on NA route with $\xi = 0.03$.

total area underneath the VBM spectrum. Therefore, the total variance of the VBM which includes the response to springing is larger than the variance of the rigid hull VBM. However, first-order springing affects only smaller VBM peaks since it occurs in relatively short and low amplitude waves with encounter frequencies in the springing range. Also, the damping ratio of 0.03 does not allow for large dynamic amplification. Yet, springing increases the total number of peaks which reduces the empirical probabilities of exceedance of the larger VBM peaks that are unaffected by the springing. All the fitted probabilities of exceedance in Figure 3.11 are based on two hundred voyages, i.e., same time interval. However, the number of peaks in the long-term time series representing individual parts of the total VBM is different. Therefore, the meaning of the exceedance probabilities will be different. For example, the total VBM time series, which is the most realistic representation of the true VBM, will have the largest number of peaks compared to other time series representing only parts of the total VBM. The largest value of the total VBM can be taught of as "once in two hundred voyages". In this context, the largest value of the first-order rigid hull VBM cannot be taught of as "once in two hundred voyages" since the total number of peaks of its long-term time series does not have the required number of peaks which the total VBM time series has in the same time interval. In order to plot the probabilities of exceedance

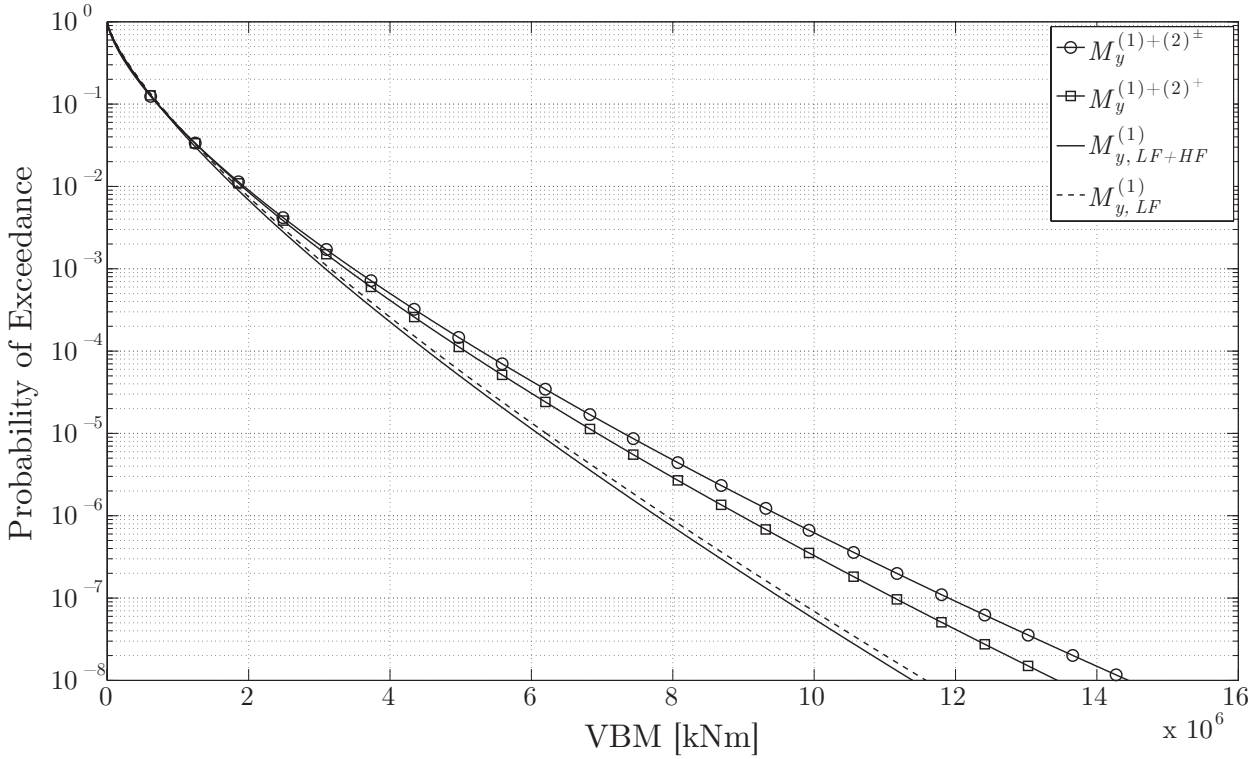

Figure 3.11: Probability of exceedance of linear and nonlinear sagging VBM peaks based on two hundred voyages of C 319 container ship on NA route with $\xi = 0.03$.

of the total VBM and its parts on the same graph it is, therefore, necessary to normalize each ECDF with the number of peaks of the total VBM time series. The total number of VBM peaks for C 319 container ship in two hundred voyages is $N_{LF}^{(1)} = 27,653,397$ for the first-order rigid hull VBM, $N_{LF+HF}^{(1)} = 33,558,534$ for the first-order flexible hull VBM, and $N_{(1)+(2)^{\pm}} = 34,367,647$ for the total VBM. The normalization of the exceedance probabilities is then performed as follows

$$\tilde{PE}_{LF}^{(1)} = PE_{LF}^{(1)} \frac{N_{LF}^{(1)}}{N_{(1)+(2)^{\pm}} \left(1 - PE_{LF}^{(1)}\right) + PE_{LF}^{(1)} N_{LF}^{(1)}} \tag{3.62}$$

$$\tilde{PE}_{LF+HF}^{(1)} = PE_{LF+HF}^{(1)} \frac{N_{LF+HF}^{(1)}}{N_{(1)+(2)^{\pm}} \left(1 - PE_{LF+HF}^{(1)}\right) + PE_{LF+HF}^{(1)} N_{LF+HF}^{(1)}} \tag{3.63}$$

where $PE_{LF}^{(1)}$ and $PE_{LF+HF}^{(1)}$ are the probabilities of exceedance of the first-order rigid and flexible hulls, respectively. Tilde denotes the normalization. When $PE_{LF}^{(1)}$ or $PE_{LF+HF}^{(1)}$ approach one, the fractions in Eqns. (3.62) and (3.63) approach one, and when $PE_{LF}^{(1)}$ or

$PE^{(1)}_{LF+HF}$ approach zero, the fractions approach $\frac{N^{(1)}_{LF}}{N_{(1)+(2)^{\pm}}}$ and $\frac{N^{(1)}_{LF+HF}}{N_{(1)+(2)^{\pm}}}$, respectively.

Figure 3.12 shows normalized probabilities of exceedance for the first-order VBM of rigid and flexible hull, together with the probability of exceedance of the total VBM. As expected, the normalized first-order rigid hull VBM has now slightly lower probabilities of exceedance in the midrange of VBM values compared to the first order VBM for flexible hull. Since larger values of the VBM are unaffected by springing, as explained earlier, both probabilities of exceedance converge for larger VBM values yielding almost the same value of the extreme VBM at 10^{-8} probability level. Figure 3.12 also shows the ABS Rule value for the sagging

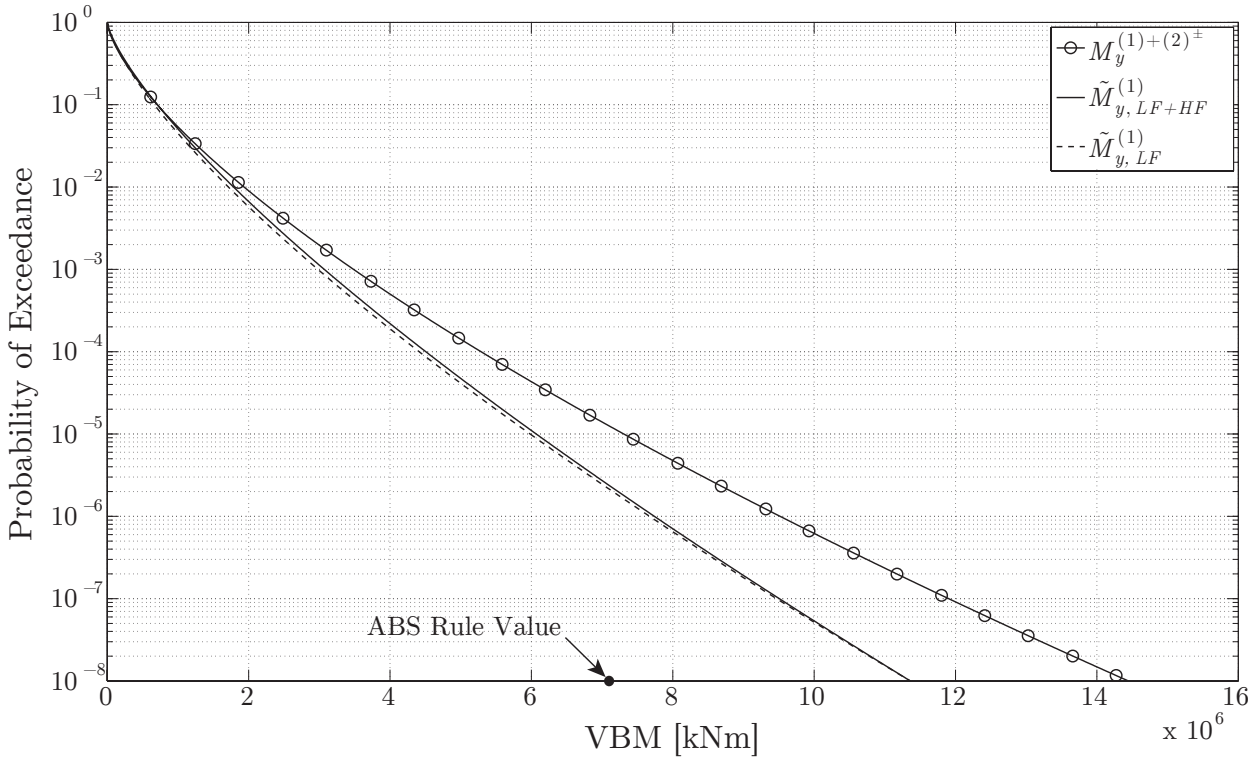

Figure 3.12: Normaized probability of exceedance of linear and nonlinear sagging VBM peaks based on two hundred voyages of C 319 container ship on NA route with $\xi = 0.03$.

VBM. Its value of 7.107E+06 kNm is 50.8% lower than the extreme value of the nonlinear VBM calculated in this work. Similar results were observed by Hughes and Paik [42] and Baarholm and Jensen [9] who found that the Rule value is between 38.7% and 59.2% lower than the extreme value of the nonlinear VBM that they calculated for S 175 container ship. The scatter was caused by the application of different long-term methods at various forward speeds. Baarholm and Jensen argued that the discrepancy was probably caused by the lack of weather routing in their approach. On the other hand, Hughes and Paik argued that the rule-based values are nominal loads used to specify ship scantlings. Therefore, extreme values, such as the nonlinear VBM value at 10^{-8} probability level, must exceed the rule-based

values. Because of this, they point out that a direct comparison of extreme values with the rule-based value is not appropriate.

Table 3.1 gives the parameters of the two parameter Weibull distribution fits and the extreme VBM values at 10^{-8} probability level for the total VBM and its constitutive parts form Figures 3.11 and 3.12.

Table 3.1: Weibull parameters and VBM at Pr = 10^{-8}; C 319, 200 voyages, NA route, $\xi = 0.03$.

VBM	$\widehat{\lambda}$ [kNm]	$\widehat{k}$	VBM at Pr = 10^{-8} [kNm]	% change from $M^{(1)}_{y,LF}$	% change from $\tilde{M}^{(1)}_{y,LF}$
$M_y^{(1)+(2)^{\pm}}$	2.11E+05	0.690	1.445E+07	24.7	27.2
$M_y^{(1)+(2)^{+}}$	2.22E+05	0.710	1.344E+07	16.0	18.3
$M^{(1)}_{y,LF+HF}$	2.35E+05	0.751	1.139E+07	-1.6	0.3
$M^{(1)}_{y,LF}$	2.43E+05	0.754	1.158E+07	–	2.0
$\tilde{M}^{(1)}_{y,LF+HF}$	2.33E+05	0.749	1.136E+07	-1.9	0.0
$\tilde{M}^{(1)}_{y,LF}$	2.13E+05	0.733	1.136E+07	-1.9	–

$M_y^{(1)+(2)^{\pm}}$ = total VBM
$M_y^{(1)+(2)^{+}}$ = total VBM without the subharmonic terms
$M^{(1)}_{y,LF+HF}$ = first-order VBM for flexible hull
$M^{(1)}_{y,LF}$ = first-order VBM for rigid hull
$\tilde{M}^{(1)}_{y,LF+HF}$ = normalized first-order VBM for flexible hull
$\tilde{M}^{(1)}_{y,LF}$ = normalized first-order VBM for rigid hull

Nonlinearities and ship flexibility cause a 27.2% increase in the extreme sagging VBM over the normalized linear case. This value matches closely with the 26.5% increase published by Hughes and Paik in [42] for the post Panamax container ship with main particulars very similar to C 319 ($L = 316.9$ m, $B = 45.6$ m, $T = 15$ m, $D = 27.2$ m, $C_b = 0.64$, $GM = 2.93$ m, and $V = 26.9$ kn). Their method is based on the All Sea States Method utilizing pseudo nonlinear transfer functions. Final comparison with measurements and simplified method of Jensen et al. [52] is deferred to Chapter 4 after the addition of the whipping VBM to the total VBM.

It should be pointed out that the probability of exceedance of the linear VBM for the rigid hull in Figure 3.11 is slightly different than the one calculated in Chapter 2 for the same ship, route, and number of voyages (see Figure 2.14). The reason for this discrepancy is that the LTFs from program SEAWAY are used in Chapter 2, while the LTFs from program SOST are used in the current chapter for consistency with the QTFs. Using SEAWAY gives a 5.6% larger value of the extreme linear VBM at 10^{-8} probability level. The differences between various hydrodynamic codes with respect to the long-term probabilities

of exceedance are very well known and documented, e.g., Guedes Soares and Moan [31] and Guedes Soares [30]. Therefore, validation against model tests and full-scale long-term measurements is very important.

3.4.4.2 Asymmetry Between Sagging and Hogging VBM

As mentioned in Section 3.4.3, nonlinearities cause asymmetry between the sagging and hogging VBM. The long-term effects of this can be seen in Figure 3.13 which shows the probabilities of exceedance of both sagging and hogging VBM peaks. It was already pointed out in Section 3.4.4.1 that the linear VBM significantly underestimates the total sagging VBM. However, it overestimates the total hogging VBM.

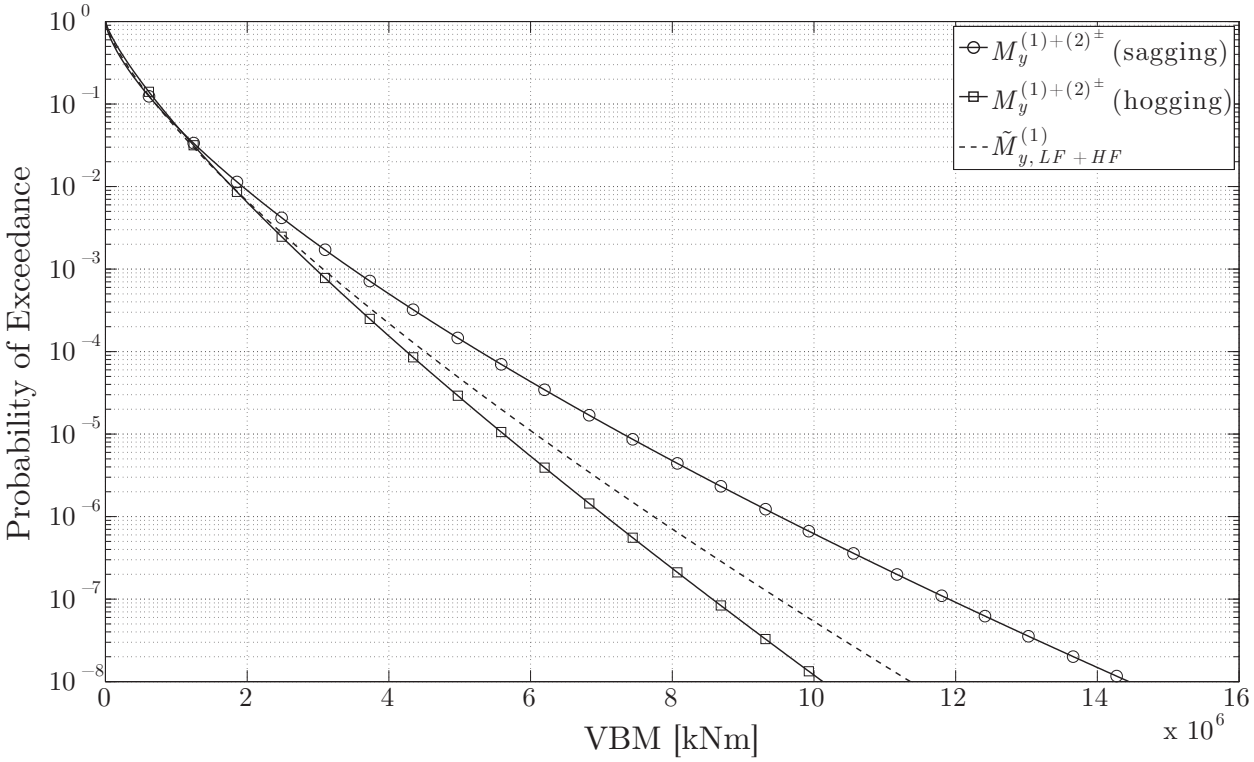

Figure 3.13: Probability of exceedance of linear (sagging or hogging), nonlinear sagging, and nonlinear hogging VBM peaks based on two hundred voyages of C 319 container ship on NA route with $\xi = 0.03$.

Table 3.2 gives the parameters of the Weibull distribution fits and the extreme VBM values at 10^{-8} probability level for linear, nonlinear sagging, and nonlinear hogging VBM peaks. Extreme value of the nonlinear hogging VBM at 10^{-8} probability level is 10.9% smaller than the extreme linear VBM.

Table 3.2: Weibull parameters and VBM at Pr = 10^{-8}; C 319, 200 voyages, NA route, $\xi = 0.03$.

VBM	$\widehat{\lambda}$ [kNm]	$\widehat{k}$	VBM at Pr = 10^{-8} [kNm]	% change from $M_{y,LF+HF}^{(1)}$
$M_y^{(1)+(2)^{\pm}}$ (sagging)	2.11E+05	0.690	1.445E+07	27.2
$M_y^{(1)+(2)^{\pm}}$ (hogging)	2.63E+05	0.798	1.013E+07	-10.9
$\tilde{M}_{y,LF+HF}^{(1)}$	2.33E+05	0.749	1.136E+07	–

3.4.4.3 Reduction of Simulation Time

Simulating nonlinear second-order part of the VBM theoretically requires $2N$ times more computations compared to the first-order simulation (see Section 3.3), where N is the number of frequency intervals chosen to discretize the encounter frequency domain. The factor of two takes into account super and subharmonic parts of the second-order VBM. Even though the CPU time needed for simulating time series of linear VBM for one whole voyage takes only a couple of seconds on an ordinary personal computer, simulation of 50 or more voyages of the second-order VBM could take tens of hours. Fortunately, QTF matrices have a lot of elements equal to, or close to zero due to the fact that the response of a typical ship to very high frequency bi-harmonics is negligible. This situation becomes even more favorable when QTF matrices are multiplied with the product of wave spectra. Therefore, depending on the particular sea state–operational profile combination, a great number of elements from vectors on the right hand side of Eqn. (3.57) can be omitted which reduces the number of computations by one order of magnitude without any loss in accuracy. Further reductions in the CPU time can be achieved by discarding all super and subharmonics whose amplitudes do not exceed a certain threshold level. However, these savings in CPU time are achieved at the expense of accuracy. Figure 3.14 shows long-term probabilities of exceedance of nonlinear sagging VBM peaks for C 319 container ship on NA route for different amounts of neglected super and subharmonics. For example, 90% case represents the probabilities of exceedance of the nonlinear VBM where the super and subharmonics not exceeding 10% of their maximum amplitudes were neglected. It is seen that 90% case offers virtually the same level of accuracy as the 100% case. 75% case causes only a 1.4% reduction in the extreme VBM value at 10^{-8} probability level, while the 50% case causes an 8.9% reduction.

Table 3.3 gives the parameters of the two parameter Weibull distribution fits, extreme VBM values at 10^{-8} probability level, and CPU time for these reduced second-order simulations. The 90% case reduces the CPU time by more than three times compared to the complete second-order simulation, while retaining the same level of accuracy. With these reductions, the necessary CPU time is brought to levels that are acceptable even for the initial ship design stage.

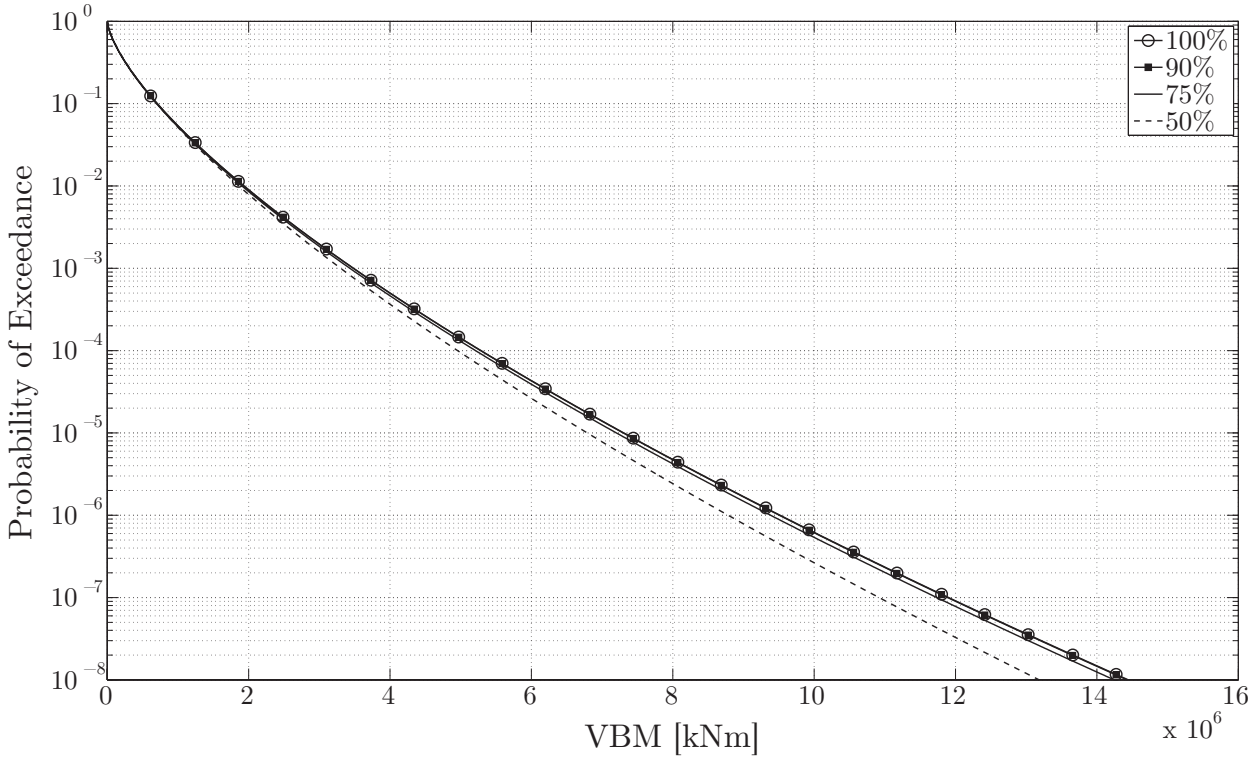

Figure 3.14: Probability of exceedance of nonlinear sagging VBM peaks for various cases of reduced second-order simulation; C 319, 200 voyages, NA route, $\xi = 0.03$.

Table 3.3: Weibull parameters, total extreme VBM at $\Pr = 10^{-8}$, and CPU time for various cases of reduced second-order simulation; C 319, 200 voyages, NA route, $\xi = 0.03$.

VBM	$\widehat{\lambda}$ [kNm]	$\widehat{k}$	VBM at $\Pr = 10^{-8}$ [kNm]	% change from (100%)	CPU time [min]
$M_y^{(1)+(2)^{\pm}}$ (100%)	2.11E+05	0.690	1.445E+07	–	190
$M_y^{(1)+(2)^{\pm}}$ (90%)	2.11E+05	0.690	1.443E+07	0.1	61
$M_y^{(1)+(2)^{\pm}}$ (75%)	2.08E+05	0.689	1.425E+07	1.4	33
$M_y^{(1)+(2)^{\pm}}$ (50%)	2.16E+05	0.708	1.318E+07	8.7	10

Note: CPU time is for a 50 voyage simulation on a workstation with two Intel® Xeon® processors with a total of twelve cores.

3.4.4.4 Long-Term Effects of Damping

All the results presented in this chapter, thus far, are based on the damping ratio $\xi = 0.03$. In order to investigate the effect of damping on the long-term probabilities of exceedance of $M_y^{(1)+(2)^{\pm}}$, long-term simulation is performed for two additional damping ratios: $\xi = 0.01$ and $\xi = 0.001$. These three values of the damping ratio cover a range of values found in the literature.

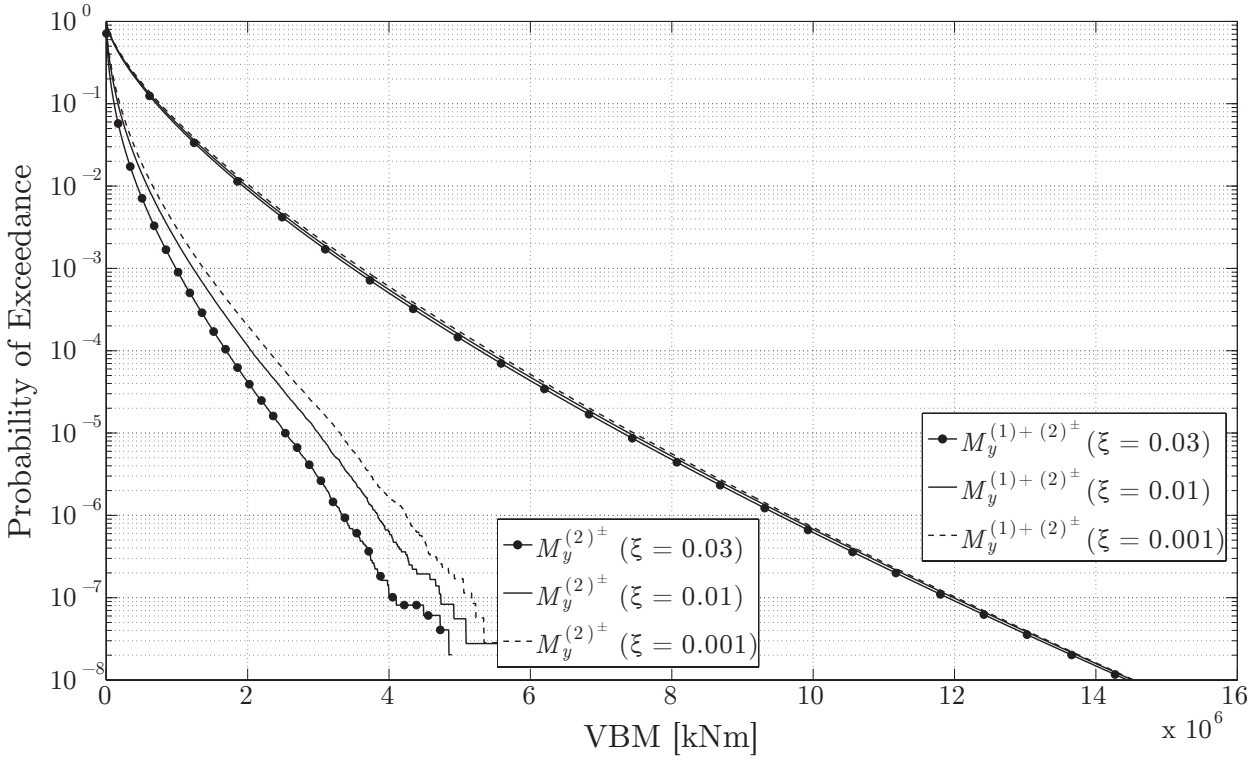

Figure 3.15: The effects of damping on long-term probabilities of exceedance of the nonlinear part of the VBM ($M_y^{(2)^{\pm}}$) and the total VBM ($M_y^{(1)+(2)^{\pm}}$); C 319, 200 voyages, NA route.

Figure 3.15 shows two sets of curves. First three on the left are the long-term probabilities of exceedance of the nonlinear part of the total VBM, $M_y^{(2)^{\pm}}$, and the three on the right are Weibull fits of the total VBM, $M_y^{(1)+(2)^{\pm}}$, each for a separate value of the damping ratio and each normalized by the same number of peaks. As the figure shows, damping has a significant impact on the nonlinear component of the total VBM. However, the effect of damping on the total VBM is much less pronounced, especially for very small and very large values of the VBM. This happens because the largest nonlinear responses, where the effect of damping is pronounced, don't occur in the same sea states in which the largest linear responses occur (see Section 3.4.3). QTFs for various values of damping ratio differ only in the nonlinear springing region which is defined with $\omega_{e,j} + \omega_{e,k} \approx 2.95$ rad/s. These

superharmonics are significantly excited only in moderate sea states with steep waves for which the linear responses are not significant. Therefore, the long-term probabilities of exceedance of $M_y^{(1)+(2)^{\pm}}$ for various values of ξ differ more significantly only in the midrange of $M_y^{(1)+(2)^{\pm}}$ values.

For similar reasons, damping has a negligible effect on the linear part of the VBM, $M_{y,LF+HF}^{(1)}$. As Figure 3.2 shows, damping only affects RAO values in the linear springing region that cannot be excited by high sea states with longer periods.

Table 3.4 summarizes the results shown in Figure 3.15. It is seen that the lowest damping ratio of 0.001 results in only 0.6% larger extreme value of total VBM at 10^{-8} probability level compared to the case of largest damping ratio of 0.03. There is almost no difference between $\xi = 0.01$ and $\xi = 0.001$ cases.

Table 3.4: Weibull parameters and total extreme VBM at $\Pr = 10^{-8}$ for all three values of damping ratio; C 319, 200 voyages, NA route.

VBM	$\widehat{\lambda}$ [kNm]	$\widehat{k}$	VBM at $\Pr = 10^{-8}$ [kNm]	% change from $\xi = 0.03$
$M_y^{(1)+(2)^{\pm}}$ ($\xi = 0.03$)	2.11E+05	0.690	1.445E+07	–
$M_y^{(1)+(2)^{\pm}}$ ($\xi = 0.01$)	2.22E+05	0.697	1.452E+07	0.5
$M_y^{(1)+(2)^{\pm}}$ ($\xi = 0.001$)	2.33E+05	0.705	1.454E+07	0.6

3.4.4.5 Long-Term Effects of Ship Route

Similarly as in the linear VBM case (see Chapter 2), nonlinear long-term analysis with C 319 container ship is performed on all three routes considered in this work (NA, NP, EA), as well as on the composite "Worldwide" route that consists of fifty voyages on NA route together with equivalent time periods on NP and EA routes. The results of this analysis for hogging and sagging are given in Figure 3.16 with numerical summary in Table 3.5. The effect of nonlinearities is most pronounced on the NA route with total sagging VBM being 27% larger than the linear value and with total hogging VBM being 11% lower than the linear value. NA route is followed by the NP route and EA route, just as in the linear case. "Worldwide" route seems to be dominated by the NP route for small values of VBM, and by the NA route for larger values of VBM. This is the same trend as in the linear case. A careful comparison of the linear results presented in this section with the ones presented in Section 2.3.3.2 in Chapter 2 reveals small discrepancies both in Weibull parameters and in the values of the extreme VBM at 10^{-8} probability level. This is because LTFs from program SOST are used throughout the present chapter as opposed to the LTFs from program SEAWAY used in Chapter 2. Program SOST is used here for consistency with QTFs.

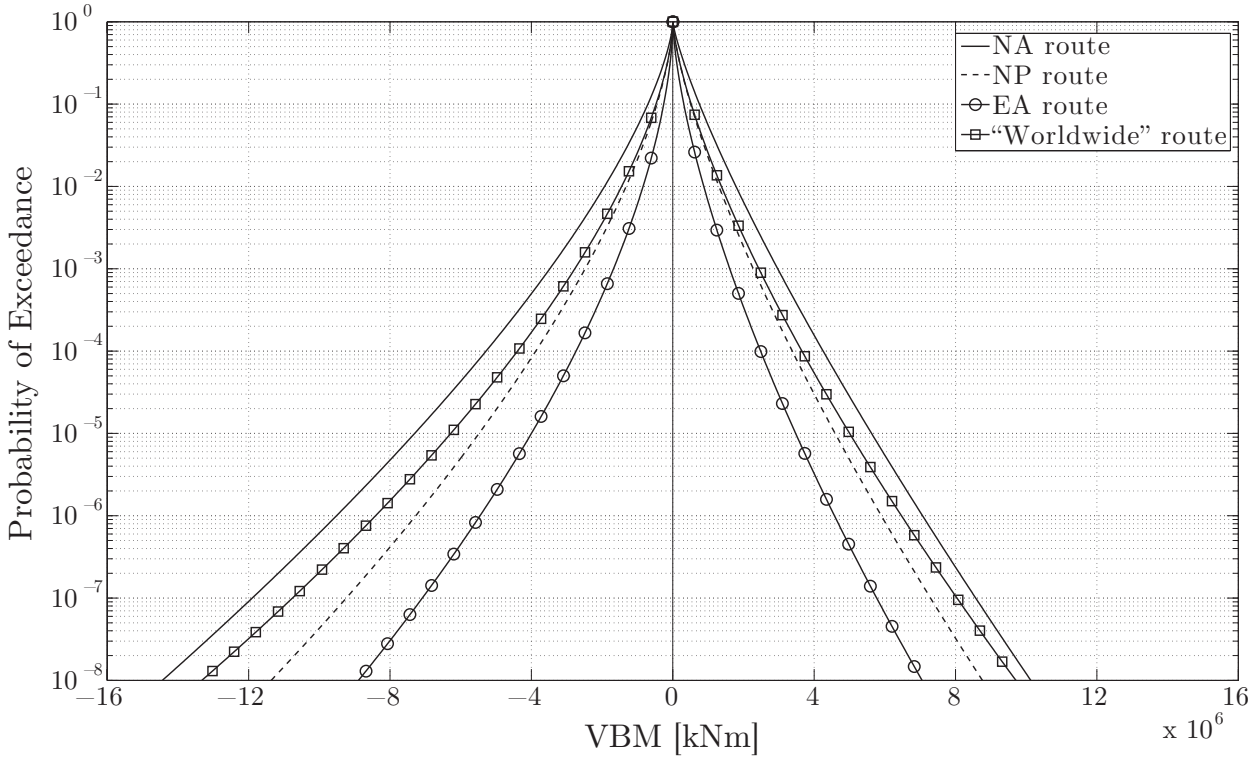

Figure 3.16: The effect of ship route on long-term probabilities of exceedance of total VBM ($M_y^{(1)+(2)^{\pm}}$); sagging–negative, hogging–positive; C 319, $\xi = 0.03$.

3.4.4.6 Long-Term Effects of Ship Type

This section presents the nonlinear long-term analysis performed on tanker T 306 in order to assess the effects of nonlinearities on a different ship type with larger block coefficient and lower design speed. Figure 3.17 shows the long-term probabilities of exceedance of the linear and nonlinear parts of the VBM for T 306 tanker on NA route in the case of $\xi = 0.03$. Due to lack of QTFs for the subharmonic terms, only the superharmonic nonlinear contribution to the total VBM is considered.

The superharmonic nonlinear terms increase the total extreme sagging VBM at 10^{-8} probability level by 10.6% and decrease the corresponding hogging value by 5.5%. These percentages should be compared with the 16.0% increase that the superharmonics caused for extreme sagging VBM in the case of C 319 container ship, and 11% decrease in corresponding hogging value (see Table 3.1). Hence, nonlinearities seem to be a less important factor for tankers, but as in the case of C 319 container ship, they are more pronounced in sagging than in hogging.

As the nonlinear effects are expected to be primarily caused by the nonlinear hydrostatic component of the total hydrodynamic force, ships of fine form and without much flare, such as tankers, are expected to be less prone to these effects. Nevertheless, a number of authors

Table 3.5: Comparison of linear and nonlinear Weibull parameters and extreme VBM at $\Pr = 10^{-8}$ for different routes; C 319, $\xi = 0.03$.

Route	VBM	$\widehat{\lambda}$ [kNm]	$\widehat{k}$	VBM at $\Pr = 10^{-8}$ [kNm]	% change from $M^{(1)}_{y,LF+HF}$
NA	NLS	2.11E+05	0.690	1.445E+07	27
	NLH	2.63E+05	0.798	1.013E+07	-11
	LIN	2.33E+05	0.749	1.136E+07	–
NP	NLS	1.24E+05	0.645	1.137E+07	25
	NLH	1.60E+05	0.727	8.756E+06	-4
	LIN	1.45E+05	0.705	9.080E+06	–
EA	NLS	6.30E+04	0.589	8.897E+06	21
	NLH	8.73E+04	0.664	7.050E+06	-4
	LIN	7.27E+04	0.631	7.374E+06	–
Worldwide	NLS	1.26E+05	0.625	1.333E+07	23
	NLH	1.59E+05	0.709	9.703E+06	-11
	LIN	1.39E+05	0.668	1.086E+07	–

NLS = nonlinear sagging ($M_y^{(1)+(2)^{\pm}}$ in sagging)
NLH = nonlinear hogging ($M_y^{(1)+(2)^{\pm}}$ in hogging)
LIN = linear ($M^{(1)}_{y,LF+HF}$)

have reported significant nonlinearities in the VBM of tankers. Baarholm and Moan [12] reported a 17.8% difference between 100-year nonlinear VBM values in sagging and hogging for a 272.8 m long tanker. Guedes Soares and Schellin [32] investigated 174 m long tanker and found significant nonlinearities which they attributed to the combination of the ship's short length and bulbous bow which emerges from the water in high sea states causing nonlinearities in the hydrostatic component of the total force. They found that both sagging and hogging extreme VBMs were larger than the liner values by 27% and 15%, respectively. Similar results were reported by Jensen et al. [49] who analyzed 233 m long tanker and found that the linear extreme VBM underestimates both nonlinear extreme sagging and hogging VBMs by 14% and 12%, respectively.

The results of this work indicate that nonlinearities play an important role for T 306 tanker. Contrary to the results of Guedes Soares and Schellin [32] and Jensen et al. [49], nonlinear sagging and hogging VBMs for T 306 tanker are on the "opposite" sides of the linear VBM. Since T 306 is a full form large tanker with very little flare, nonlinearities in the VBM are not likely to be caused by the nonlinearities in the hydrostatic component of the force. Rather, they probably come from the nonlinearities in the hydrodynamic Froude-Krylov force (see Appendix B.1 and Section 3.4.2), especially when the vessel is on a shallow draft in ballast. This can be seen by looking at the moduli of the QTF for superharmonics

in Figure 3.5. It is evident that the QTFs are much more significant for the ballast condition compared to the full load condition. Since T 306 spends half of its life in ballast, nonlinear effects will be noticeable. Guedes Soares and Schellin [32] and Jensen et al. [49] considered only the full load condition. Therefore, the effect of shallow draft on the hydrodynamic nonlinearities were not considered in their studies.

It is important to note that further analysis is required for T 306 tanker in terms of adding the effect of subharmonics to get a more clear picture of the nonlinear VBM behavior. The adequacy of the quadratic strip theory for vessels on shallow draft should also be investigated since the bottom of the ship may emerge from the water in high sea states and this effect is not accounted for by the theory.

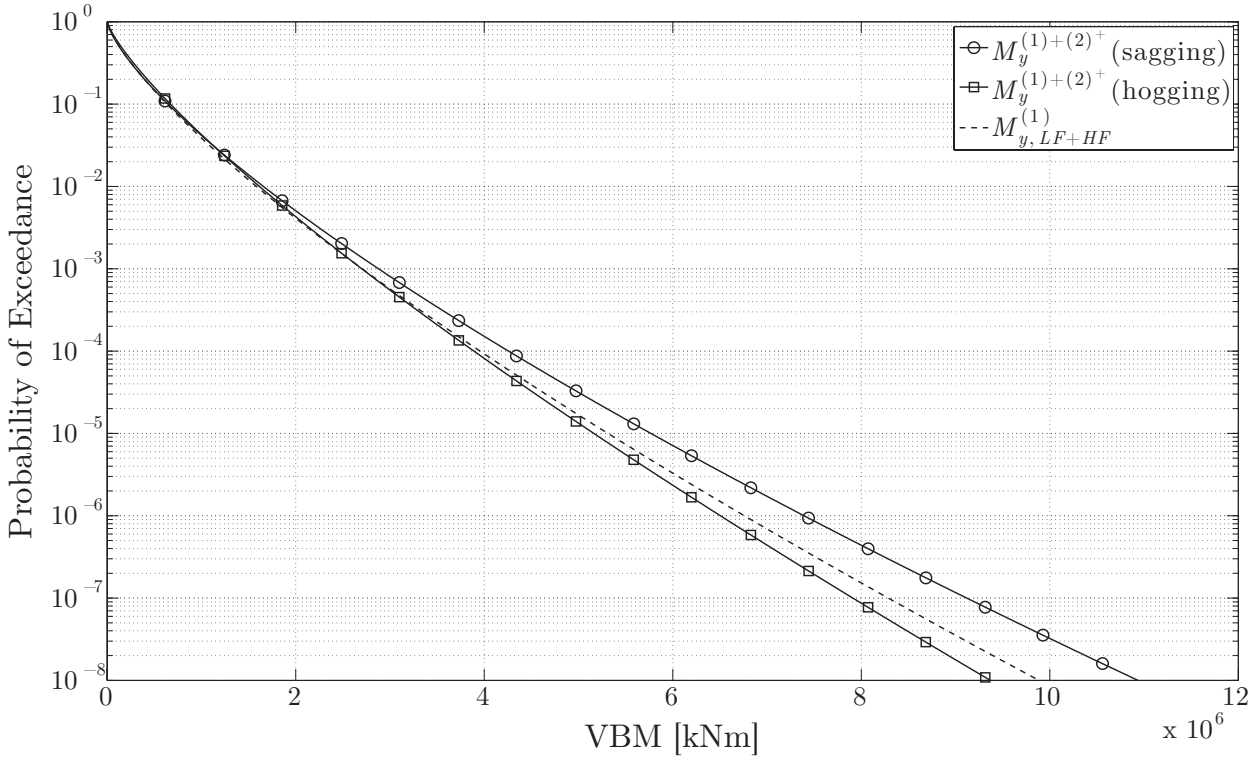

Figure 3.17: Probability of exceedance of linear (sagging or hogging), nonlinear sagging, and nonlinear hogging VBM peaks based on fifty voyages of T 306 tanker on NA route with $\xi = 0.03$.

Table 3.6 summarizes the results shown in Figure 3.17.

Table 3.6: Weibull parameters and extreme VBM at Pr = 10^{-8} for T 306 tanker on NA route with $\xi = 0.03$.

VBM	$\widehat{\lambda}$ [kNm]	$\widehat{k}$	VBM at Pr = 10^{-8} [kNm]	% change from $M^{(1)}_{y,LF+HF}$
$M_y^{(1)+(2)^+}$ (sagging)	2.07E+05	0.735	1.094E+07	10.6
$M_y^{(1)+(2)^+}$ (hogging)	2.33E+05	0.788	0.937E+07	-5.3
$M^{(1)}_{y,LF+HF}$	2.10E+05	0.757	0.989E+07	–

Chapter 4

High-Frequency Loads Due to Bow Flare Slamming and Fatigue Analysis

4.1 Introduction

Chapters 2 only considered the linear loads. Nonlinearities in the VBM, as well as the high-frequency VBM fluctuations due to springing of the hull girder were introduced in Chapter 3. Current chapter introduces yet another addition to the VBM in the form of a high-frequency transient fluctuations due to slamming of the ship's bow into the free surface of the water.

Slamming can occur in three locations: forward part of the bottom, especially if it is flat, the bow if it is flared outwards, and the stern if it has a large overhanging, as on many container ships. The methods developed in this chapter can theoretically be applied to the analysis of all types of slamming. However, in the case of stern slamming, additional difficulties arise due to the fact that the incident wave profile that comes in contact with the overhanging stern is usually disturbed by the presence of the moving ship.

In this work, the impact of the bow flare slamming on the VBM is analyzed for the C 319 container ship. This ship is purposely used in all the chapters of this dissertation in order to demonstrate how the long-term probabilities of exceedance of the VBM peaks change when nonlinearities and flexibility of the hull are accounted for in the analysis. Analyzing only the effect of the bow flare slamming on the VBM is justified in the following. Since container ships have fine form in the forward region with very small flat bottom portion, bottom slamming can usually be neglected for these ships. Also, stern slamming usually happens at very low speeds (lower then 5 knots). Since this speed range is outside the operational profile of the considered container ship, stern slamming can also be neglected with regard to its influence on the long-term VBM exceedance probabilities. The classification society ABS also emphasizes the dominance of the bow flare slamming for container ships compared to the other two types of slamming. ABS considers only the bow flare slamming in their simplified procedure for whipping assessment of container ships [4].

Bow flare slamming is the plunging of the upper flared portion of the bow deeper into

the waves. It imparts a relatively sudden and intensive force to the forward part of the ship which is caused by a sudden change in the breadth of the immersed cross sections of the ship as it moves downward. The sudden growth of the submerged body rapidly changes the momentum of the surrounding water by changing its velocity and mass (amount of water involved), and this in turn causes a large reaction force on the forward part of the ship acting for a very short period of time. The consequence of this large force is a sudden deflection of the bow that excites flexural vibrations of the hull girder, mainly in the fundamental two-node mode. These vibrations are called whipping. Unlike the springing vibrations that are also mainly in the two-node mode, whipping is a transient phenomena as it is not excited by the periodic wave forces and it is damped by the combined dissipative mechanism of the structure and the surrounding water. It is very difficult to separate the whipping from springing in the measured time series of the VBM. However, these two phenomena have a completely different physical origins and can easily be separated during simulation.

4.1.1 Hydrodynamic Models for Slamming

Slamming is a strongly nonlinear phenomenon and a random process that is sensitive to relative motion and contact angle between hull and free surface of the waves. From the 1930's to present day, there has been a great number of publications dealing with the slamming problem on theoretical, as well as experimental levels. Classical theories treat the slamming problem analytically in the framework of potential theory. Von Karman [54] was the first to theoretically study the water impact of a two-dimensional wedge using momentum conservation. It neglects the water surface elevation upon impact which leads to underestimation of the impact loads.

Wagner [110] improved on the von Karman's model by including the local jet flow analysis. As long as the deadrise angle of the wedge is large enough not to trap air, Wagner's theory can be applied to arbitrarily shaped bodies. It is simple and gives accurate peak pressure estimates compared to the measurements. However, it introduces a singularity at the edge of the wedge, causing an infinite negative pressure at that point. This was remedied by Watanabe [112] by taking spray into account. He asymptotically matched the inner solution for the wedge with the outer solution for the spray region.

Zhao and Faltinsen [119] used a different local jet flow approximation with matched asymptotic solutions to develop a two-dimensional nonlinear boundary element method (BEM) for water impact problems. Arai and Matsunga [8] used the volume-of-fluid (VOF) method to predict the water impact on an arbitrary two-dimensional section. Zhao et al. [120] improved on the original two-dimensional BEM by Zhao and Faltinsen and made it more robust and efficient. The vertical pressures and forces obtained with these two-dimensional methods agree quite well with the measurements from drop tests with two-dimensional ship-shape sections. However, two-dimensional methods can sometimes significantly overestimate the slamming loads for real ship forms with forward speed. This indicates that the three-dimensional effects are important and they should be taken into account.

In recent years, a real progress has been made in the development and application of computational fluid dynamics (CFD) to solving the water impact problems. Many of the newly developed codes use the interface capturing technique of the VOF type to solve this highly nonlinear three-dimensional problem in time domain. Computer code COMET is a Reynolds-averaged Navier-Stokes solver based on VOF technique. Schellin and el Moctar [91] used it to find the spatial mean slamming pressure that can be considered as equivalent static design load and applied to the ship structure to analyze its structural adequacy.

More recently, Seng, Jensen and Pedersen conducted a numerical slamming analysis of a 270 meters long Panamax container ship using CFD open source program openFOAM. This code uses the finite-volume method in combination with the VOF technique. The flow was assumed to be incompressible and the structure was modeled as rigid. Because of the short duration of the impact it was assumed that there is no need for a turbulence model. The 2-D CFD model was first compared with the measurements of the 2-D drop test in calm water and the agreement was found to be satisfactory. Then, the 2-D and 3-D CFD models were compared for the container ship impacting a calm water at a negative trim angle of 10°. Both methods yielded comparable results. Finally, a fully nonlinear 3-D CFD analysis of slamming was performed on the same container ship sailing in head sea at half service speed in a critical wave episode which is conditioned on a predefined value of the wave-induced VBM. However, no comparison was made with the 2-D model in waves. The computational effort for conducting this type of analysis was found to be massive. CPU time needed in order to simulate 3 seconds of physical time using a fine mesh with 19.8×10^6 cells was approximately 180 hours on 40 cores of Intel® Xeon® X5550 cluster. The authors concluded that, at present, the 3-D analysis procedure is best suited to derive or calibrate more approximate but faster methods.

4.1.2 Structural Models for Slamming

The response of a flexible ship structure can be looked at two different structural levels:

1. *Hull girder level* - at this level only the global whipping of the structure is of interest. The flexural vibrations of the hull give rise to vibratory hull girder bending stresses which are of much higher frequency than the wave-induced stresses and are effectively superimposed on them. The period of the fundamental vibration mode excited by slamming is usually in the range from 0.5 to 2 seconds.

2. *Principal member level* - the structural analysis of shall plating and its supporting structure is of interest at this level. High pressure forces accelerate and deflect these structural members and may induce local vibrations, especially of the plating. Damage may occur in the form of plastic deformation or fatigue cracks. Detailed information about the local pressure filed is required at this level.

Since this work considers only the global hull girder sectional loads, the whipping response of the structure will only be considered in this chapter. Full-scale measurements of slamming

for monohull vessels, see e.g. Ochi and Motter [86], have shown that the whipping VBM amidships can be of the same order of magnitude as the wave-induced VBM. Figure 4.13 shows a typical time record of VBM consisting of wave-induced and slamming parts where the decaying whipping high-frequency part is superimposed on the low-frequency wave-induced part.

Two factors greatly simplify the treatment of slamming. First, the structural response to the impact occurs at much higher frequency than wave-induced responses. Second, large and medium-sized ships have sufficiently large mass and damping that the slamming forces acting over a very short period of time (milliseconds) cannot appreciably affect the motion of the ship. This means that the ship motions and all other wave-induced responses can be analyzed completely separately from impact-related slamming and green water effects. Slamming can be investigated by first performing the rigid body seakeeping analysis of the relative velocity between the ship and the water surface to identify the slamming events. Then, the dynamic analysis of the flexible ship structure is performed to yield the whipping response which is simply superimposed on the wave-induced response. Various experimental and theoretical studies (e.g., Yamamoto et al. [118]) confirmed the validity of this approach. A similar procedure is also used in this work.

In principle, all the methods and tools developed for the analysis of structural response to springing (see Section 3.1.2) can also be used for structural analysis of whipping. As for the springing, the structural model can be coupled with, or decoupled from the hydrodynamic model. Usually, it is sufficient to perform a one-way coupling where the influence of the hydrodynamic pressure on the hull deformation is taken into account, and to neglect the effect of hull deformation on the hydrodynamic pressure as this latter effect is usually very small [42].

Mansour and d'Oliveira [71] presented a classical work on predicting the VBM due to ship bottom slamming in regular waves. They used the rate of change of momentum of the added mass to estimate the slamming loads. The authors also used dynamic Timoshenko beam, but without the rotary inertia term (see Section 4.3), in which case the dynamic behavior of the beam can be treated in terms of series of responses in each of the normal orthogonal vibration modes. The system of partial differential equations of the Timoshenko dynamic beam model can then be condensed into a simple constant-coefficient second-order linear differential equation that has a closed form solution. The method does, however, require the knowledge of the normal vibration modes of the beam and their associated frequencies which have to be obtained using, e.g, FEM. Mansour and d'Oliveira finally developed a computer code that does a one-way coupling of their hydrodynamic and structural models.

Many other variations of the foregoing slamming analysis exist in the literature. More recently the focus has shifted towards coupling fully nonlinear CFD codes with full ship FEM models. One such application was by el Moctar et al. [78] where a one-way coupling of the RANS solver COMET and FE code ANSYS was done for a large 13,000 TEU generic container ship. This procedure is very computationally intensive since, at each time step, two complex numerical calculations have to be performed: one for the hydrodynamic forces and one for the structural response.

Any long-term simulation procedure requires very efficient methods for load and response prediction. Methods described thus far are usually computationally too intensive to be used for long-term load predictions. Therefore, some simplifications have to be made. In this work the bow of the ship is assumed to be a uniform wedge impacting the water surface without any trim. The boundary value method by Zhao and Faltinsen [119] is used to obtain the time dependent vertical hydrodynamic impact forces by integrating the pressure field on the wedge. This procedure is suggested by ABS [4] as a method that provides a good compromise between accuracy and efficiency at the initial ship design level. As such, it is applicable to long-term simulations of the slamming impact loads. The Timoshenko dynamic nonuniform beam model, without any simplifications, is used to model the response of the elastic hull girder. A 1-D FE solution in the space domain and the implicit trapezoidal method in the time domain are used to solve the system of partial differential equations resulting from the structural model.

4.1.3 Combination of Wave-Induced and Whipping VBM

Even though there is a positive correlation between the average intensities of the wave-induced and whipping VBMs, the individual whipping maxima do not occur simultaneously with the wave-induced maxima. For example, bow flare slamming has been observed to take place during the transition of the wave-induced VBM from hogging to sagging. Therefore, it is very important to properly describe the slamming events in the statistical sense, and to properly account for their correlation with the wave-induced loads.

One of the first statistical analysis of slamming was conducted by Tick [106] who calculated the mean slamming rate in a given sea state. Later Ochi [85] proposed the truncated exponential distribution for the impact pressure and a truncated Poisson distribution for the slamming interarrival times by fitting the experimental data. Ochi and Motter [86] assumed slamming to be a Poisson process and suggested the short-term combination of extreme slamming and wave-induced VBMs using a suitable phase angle.

Mansour and Lozow [73] proposed a more rigorous mathematical approach to obtaining the short-term statistical properties of slamming. They represented slamming with a Poisson pulse process with independent intensities and interarrival times and developed the probability density functions, spectral densities, autocorrelation functions, and other statistical properties of both the input slams and the output vessel responses, focusing on the VBM.

Ferro and Mansour [24] further developed the mathematical model of Mansour and Lozow by accounting for the dependency between the slamming pulse intensities and interarrival times. They investigated the combination of wave-induced VBM with the whipping VBM using stationary linear Gaussian waves as an input. The ship was considered as a linear system with respect to the hydrodynamic forces and structural response. It was further assumed that whipping VBM is statistically independent from the wave-induced VBM. Consequently, Ferro and Mansour obtained the short-term extreme-value probability distribution of the combined response using Turkstra's Rule (see Section 2.1.1.4).

However, it has been observed that the slamming events do not appear at random times. Rather, slam impacts tend to be clustered. Hansen [34] developed a method for statistical analysis of whipping and its combination with the wave-induced loads by taking clustering into account.

Jensen and Mansour [50] developed a simplified closed-form expressions for calculating the transfer functions and standard deviations of the vertical bending moment for mono-hull ships at amidships. These expressions are based on the quadratic strip theory by Jensen and Pedersen [51]. Therefore, they include the effect of nonlinearities and springing on the VBM. The effect of whipping is also included by assuming that whipping and wave-induced responses are independent in any given sea state.

Baarholm and Jensen [9] used a nonlinear time domain simulation of VBM to investigate the influence of whipping on the VBM. They estimated the short-term probabilities of exceedance of the combined whipping and wave-induced VBM peaks, and then used the Contour Line Method (see Section 2.1.2.2) to find the extreme long-term values of the VBM. Only head sea cases were considered. The whipping VBM was filtered out from the total VBM with the Buttrerworth filter. This procedure cannot distinguish between springing, nonlinear superharmonic terms, or whipping. Correlation of whipping and wave-induced VBM peaks in time was not examined. Wave-induced peak and the largest whipping peak in a horizontal time window, with origin determined by the wave-induced peak, were simply added together. However, no mention of the size of this time window was given. Although not explicitly indicated by the authors, this procedure ensures the independence of individual maxima, as will be explained in Section 4.4.4. Baarholm and Jensen found whipping and wave-induced VBM to be strongly correlated in magnitude for the sea states considered in their analysis. The conclusion of their work was that if the correlation is accounted for, whipping will have larger effect on the VBM than if the independence is assumed for both sagging and hogging.

Jensen et al. [52] used the findings of Baarholm and Jensen [9] to account for the correlation between whipping and wave-induced VBMs and to improve on the simplified closed-form expressions for the VBM transfer functions developed by Jensen and Mansour [50]. They incorporated these transfer functions into a simple spreadsheet program that uses the All Sea States Method to find the long-term probabilities of exceedance of the total VBM. The procedure is very efficient and requires knowledge of only the basic particulars of the ship. As such, it can be applied at the initial design phase. Different weather routing schemes and different longitudinal extents of slamming can also be investigated using this approach. Nonlinearities are included only in sagging by using an analytical formula for skewness together with a Hermite transformation of the response. The effect of green water on deck can also be investigated, assuming that green water contribution is statistically independent from bottom slamming.

All the foregoing methods for combining whipping and wave-induced VBMs are essentially short-term methods that require the use of simplified long-term methods (Contour Line Method or All Sea States Method) to obtain the long-term probability of exceedance, or just the long-term extreme value of the total VBM, as in the case of the Contour Line Method.

Before the Contour Line or the All Sea States Methods can be applied, short-term CFDs of the total VBM have to be known either by performing very lengthy time domain simulations (Baarholm and Jensen [9]), or by using mathematically fairly involved theoretical approach (Ferro and Mansour [24]).

Following sections describe the long-term simulation approach to including the whipping to the total VBM. It uses simplified hydrodynamic and structural models to predict whipping and then properly correlates it with the wave-induced VBM and the nonlinear VBM with the effects of springing. Proper correlation is achieved by taking into account the precise phase difference between all the loads and motions of the vessel at all times.

4.2 Simplified Hydrodynamic Model for Slamming

The two-dimensional boundary element method developed by Zhao and Faltinsen [119] is used in this work to predict the slamming pressure as suggested by Jensen et al. [52] and adopted by the ABS [4]. The biggest simplification that is made here is to model the impact of the ship's bow section with a uniform wedge impacting the water surface without any trim. Therefore, one bow section has to be taken as being representative of the entire wedge. This section is called the slamming section (see Figure 4.1).

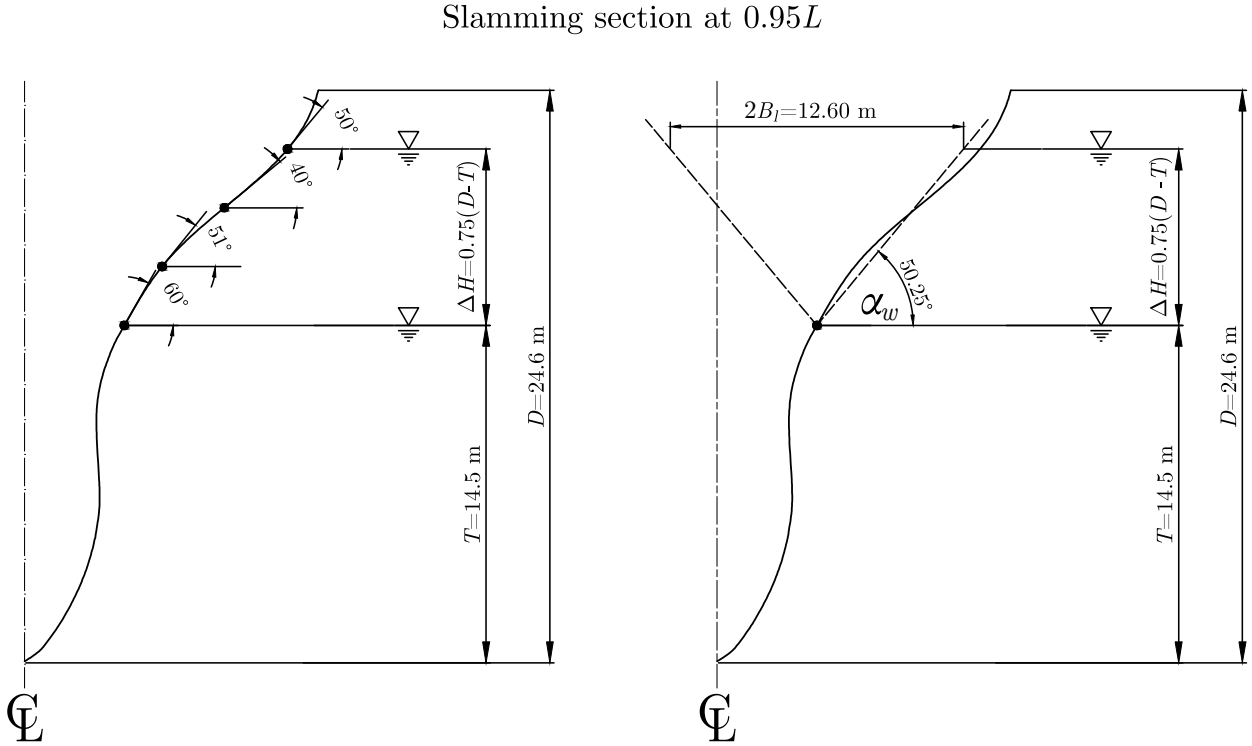

Figure 4.1: Slamming section for C 319 container ship.

Since the slamming pressure is very sensitive to actual hull geometry and the relative velocity between the hull and water, determining the position and geometric characteristics of the slamming section might require calibration with the more precise three-dimensional numerical methods or with model tests and full-scale measurements. Based on such calibration, ABS recommends that this section is selected at $0.95L$ for container ships, where L is the length of the vessel. The deadrise angle, α_w, is the average of deadrise angles calculated at four different points on the slamming section separated by equal vertical distances between T and $\Delta H = 0.75(D - T)$, where T is the design draft of the vessel and D is its depth (see Figure 4.1). Then, the local breadth of the slamming section, B_l, can be calculated using simple geometry

$$B_l = \frac{\Delta H}{\tan \alpha_w} \tag{4.1}$$

The instantaneous impact force per unit length of the wedge, $q(t)$, can be calculated by integrating the pressure field and it is equal to

$$q(t) = 3C_p \rho g \dot{z}_{rel}^3 t \tag{4.2}$$

where

$$C_p = \frac{\pi^2}{4 \tan^2 \alpha_w} \tag{4.3}$$

and where ρ is the density of water, g is the acceleration of gravity, $\dot{z}_{rel}$ is the relative vertical velocity at the slamming location, and t is the time measured from the wedge apex hitting the water.

Duration of the slamming event measured from the time the wedge apex hits the water to the time of maximum immersion, taking into account the water rise-up, is given by

$$t_S = \frac{2}{3} \frac{B_l \tan \alpha_w}{2 \dot{z}_{rel}} \tag{4.4}$$

The foregoing expression takes into account that the water rise-up is about half of the total immersion of the slamming section, as shown by Zhao and Faltinsen [119].

According to this simplified model, the vertical slamming force depends linearly on the duration of slamming. Based on the model tests conducted by Ochi and Motter [86], time behavior of the vertical slamming force on a section can be modeled with an isosceles triangle. Therefore, after reaching its maximum value at $t_S/2$, the vertical slamming force starts to decrease linearly with time until it reaches zero at t_S. This is shown in Figure 4.2.

Since Eqn. (4.2) represents the vertical force per unit length, the extent of slamming, Δx_{slam}, also needs to be determined. Based on full-scale measurements, ABS recommends applying the slamming force over 4% of the ship length around the slamming section. This slamming extent is used in this work as well, see Figure 4.3.

The impact force due to slamming is very sensitive to the vertical relative velocity between the hull and the water, as pointed out earlier. The magnitude of the vertical slamming force is proportional to the cube of the relative velocity. However, one of the necessary conditions

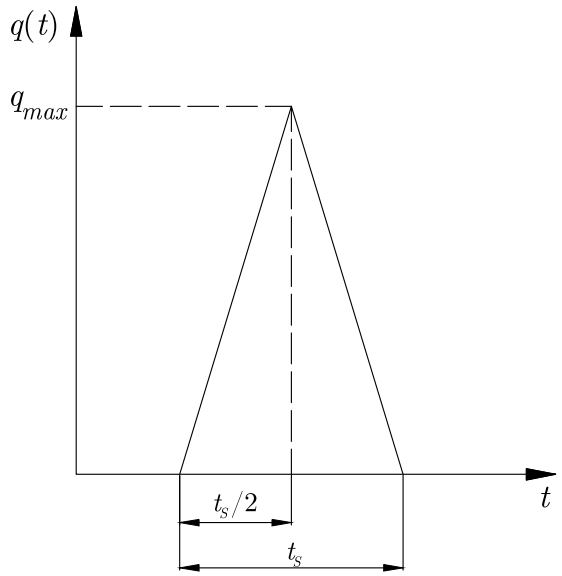

Figure 4.2: Time profile of the vertical slamming force.

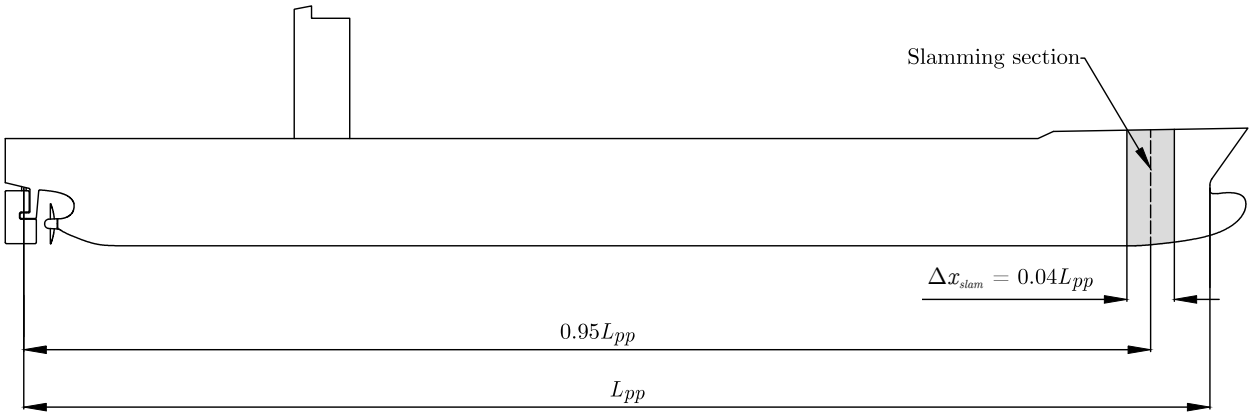

Figure 4.3: The extent of slamming.

for the slamming to occur is that this vertical velocity exceeds a certain threshold. One of the first researchers to point this out was Ochi [85]. He established the following widely used threshold value for relative speed

$$\dot{z}_{rel,cr} = 0.093\sqrt{gL} \tag{4.5}$$

where g is the acceleration of gravity and L is the length of the ship.

Unlike the bottom slamming, which requires bow emergence, bow flare slamming only requires that the assumed wedge apex at the slamming section (see Figure 4.1) enters the water surface as it is moving downwards while, at the same time, exceeding the threshold relative velocity.

4.2.1 Relative Motion Analysis

In order to identify the slamming events, an accurate record of ship motions and wave surface elevations at the slamming section must be obtained. To do this, linear ship motion analysis can be performed where the waves are simulated as long-crested and Gaussian. This procedure is similar to the one used in Chapter 2 to simulate the sectional forces and moments where short crested waves were used. Hence, it is very efficient and it keeps a precise phase relationship between waves, motions, and sectional loads. Linear ship motion analysis is frequently used as a first step in the analysis of slamming, e.g. Schellin and el Moctar [91] and ABS [4]. Motion analysis in long-crested waves gives conservative motions compared to the analysis in short-crested waves. This partially compensates for the lack of additional motion caused by nonlinearities in the waves and the system.

The same linear strip theory program SEAWAY used in Chapter 2 is used here to obtain the transfer functions of all six degrees of ship motion (surge, sway, heave, roll, pitch, and yaw). The motion reference point is the ship's center of gravity (CG), while the reference plane for the VBM is the midship section. Although close, the longitudinal center of gravity (LCG) does not coincide with the midship section. Further difficulty arises due to the fact that the relative motion analysis needs to be performed at the slamming section which is $0.45L$ forward of the midship section. In order to properly correlate the relative vertical motion of the slamming section with the simulated VBM at the midship section, the common random wave input needs to be propagated in space from the midship section to the LCG and also to the slamming section. Figure 4.4 shows this for C 319 container ship.

Random wave elevation time record at the midship section, used to simulate the VBM, can be approximated using Eqn. (2.39) from Chapter 2

$$\eta_{MS}(t) \approx \sum_{i=1}^{N} a_{\eta,i} \cos\left(\omega_{e,i} t + \phi_i\right) \tag{4.6}$$

The corresponding wave elevations at the slamming section can then be obtained as follows

$$\eta_{SS}(t) \approx \sum_{i=1}^{N} a_{\eta,i} \cos\left[-k_i(x_{SS} - x_{MS})\cos\alpha + \omega_{e,i} t + \phi_i\right] \tag{4.7}$$

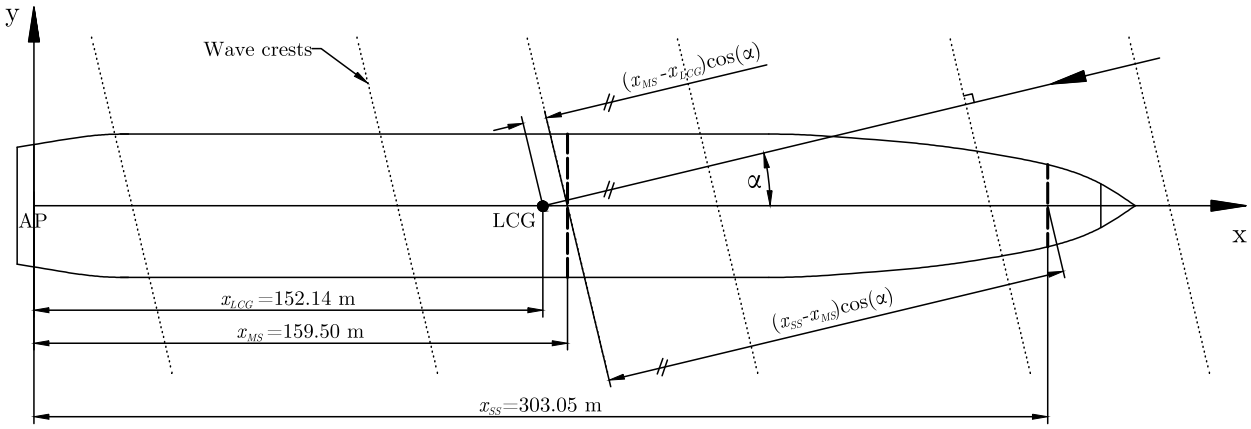

Figure 4.4: Propagation of long-crested waves and associated notation: MS = midship section, SS = slamming section, LCG = longitudinal center of gravity, α = relative angle between the ship heading and the wave direction, x-y = coordinate system fixed to the ship.

where $k_i = \omega_{e,i}^2/g$ is the wave number for deep water waves. Finally, the wave elevations at the motion reference point can be expressed as

$$\eta_{LCG}(t) \approx \sum_{i=1}^{N} a_{\eta,i} \cos\left[k_i(x_{MS} - x_{LCG})\cos\alpha + \omega_{e,i}t + \phi_i\right] \tag{4.8}$$

Simulation of the relative vertical motion between the hull and the waves starts with simulating all six degrees of ship motion at the motion reference point, CG, using $\eta_{LCG}(t)$ as random input. Motion of the apparent wedge apex, which is located on the side shell plating at the intersection of the slamming section and design draft, is obtained from the motion of CG using simple geometry. Vertical motion of the wedge apex is influenced by heave, pitch, and roll motions. The effects of forward speed and heading of the ship are taken into account by using encounter frequencies instead of absolute frequencies. Ship's oscillatory motions in the horizontal plane (surge, sway and yaw) have very small effect on the relative vertical speed and are, therefore, neglected. At the end, the relative vertical speed is obtained by differentiating the relative vertical motion between the wedge apex and the waves.

4.3 Symplified Structural Model of a Flexible Hull

In Section 4.1.2 it was pointed out that the response of the hull structure to slamming can be analyzed separately from the low-frequency wave-induced and high-frequency springing responses, and then simply superimposed on them. In this work, the ship hull is represented with a nonuniform dynamic beam model loaded only with the vertical impact force during a very short period of time. The weight and inertial forces acting on the beam are continuously balanced by the hydrostatic and hydrodynamic forces and they can be omitted from

the slamming analysis. Since the ship hull is a free-free beam with no end supports, the unbalanced impact force will set the hull of the ship into permanent motion. This is of no significance in the calculation of whipping VBM and VSF, because these loads depend on the derivatives of the underlying vertical deflections of the beam which will be shown later. Figure 4.5, redrawn from Senjanović [95], shows a differential beam element under lateral load. The notation in Figure 4.5 is as follows; z is the total vertical deflection of the beam

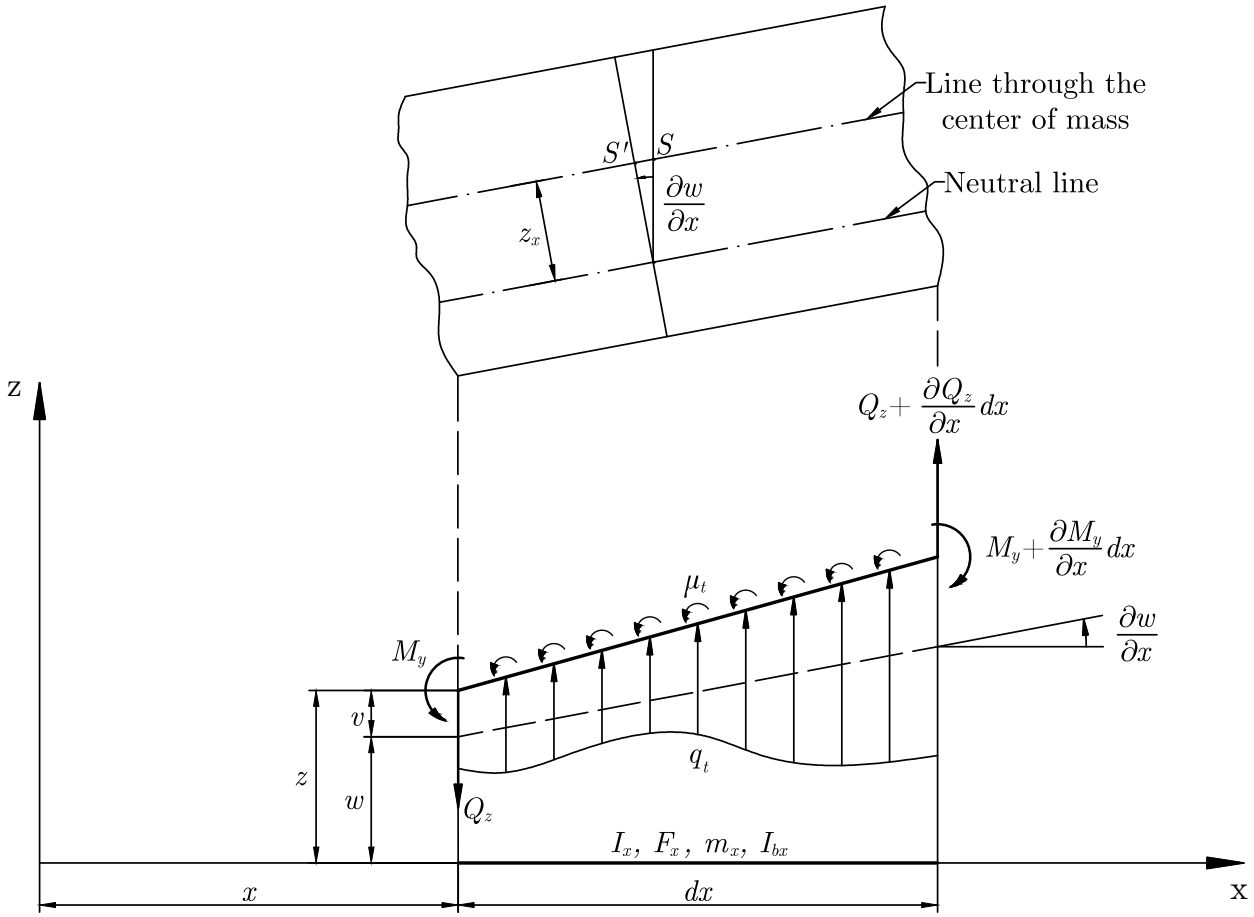

Figure 4.5: Laterally loaded beam element.

that consists of a part due to pure bending, w, and a part due to shear deflection, v, such that

$$z = w + v \tag{4.9}$$

z_x is the distance between the neutral line and the line through the center of mass. The separation between these two lines gives rise to the rotary inertial terms. The effect of rotating masses can be quite significant, especially at higher frequencies. I_x is the vertical moment of inertia of the cross section of the beam, F_x is the vertical shear area, m_x is the mass per unit length, including the added mass of water, and I_{bx} is the mass moment of

inertia per unit length about the center of mass. Finally, q_t is the total lateral load on the beam per unit length and μ_t is the total distributed moment per unit length. Both, q_t and μ_t, consist of parts due to external loads as well as inertial loads due to vibrating masses. The following constitutive equations from theory of elasticity relate the VBM and VSF with the appropriate derivatives of beam deflection

$$M_y = -EI_x \frac{\partial^2 w}{\partial x^2} \tag{4.10a}$$

$$Q_z = GF_x \frac{\partial v}{\partial x} \tag{4.10b}$$

where E and G are Young's and shear moduli, respectively.

The equilibrium equations can be established by considering the equilibrium of forces and moments acting on the differential element

$$\frac{\partial M_y}{\partial x} = Q_z + \mu_t \tag{4.11a}$$

$$\frac{\partial Q_z}{\partial x} = -q_t \tag{4.11b}$$

where q_t and μ_t are given by the following expressions

$$q_t = q_x + q_i + q_d \tag{4.12}$$

$$\mu_t = \cancel{\mu_x}^{0} + \mu_i = \mu_i \tag{4.13}$$

where q_x is the external impact force due to slamming, q_i is the inertial force due to vibration of masses, and q_d is the damping force. μ_x is the external distributed moment per unit length, and μ_i is the inertial distributed moment. In the case of slamming, $\mu_x = 0$. The inertial and damping forces are given by

$$q_i = -m_x \frac{\partial^2 z}{\partial t^2} \tag{4.14}$$

$$q_d = -n_x \frac{\partial z}{\partial t} \tag{4.15}$$

where n_x is the damping coefficient per unit length. The inertial moment per unit length is given by

$$\begin{aligned} \mu_i &= -I_{bx} \frac{\partial^2}{\partial t^2} \left(\frac{\partial w}{\partial x} \right) - m_{bx} z_x^2 \frac{\partial^2}{\partial t^2} \left(\frac{\partial w}{\partial x} \right) \\ &= -I_{bx}^* \frac{\partial^3 w}{\partial x \partial t^2} \end{aligned} \tag{4.16}$$

where $I^*_{bx} = I_{bx} + m_{bx} z_x^2$ is the mass moment of inertia per unit length with respect to the neutral line and m_{bx} is the mass of the ship per unit length, but without the added mass. The first term of Eqn. (4.16) is the moment due to the rotation of the cross section, while the second term arises due to longitudinal acceleration of the center of mass with respect to the neutral line. Since the added mass associated with the rotation and longitudinal movement of the cross section is negligible, both terms in Eqn. (4.16) contain mass parameters associated with the ship without the added mass.

Inserting Eqns. (4.10a), (4.10b), and (4.16) into Eqn. (4.11a), the following is obtained

$$\frac{\partial}{\partial x}\left(EI_x \frac{\partial^2 w}{\partial x^2}\right) + GF_x \frac{\partial v}{\partial x} = I^*_{bx} \frac{\partial^3 w}{\partial x \partial t^2} \tag{4.17}$$

Also, inserting Eqns. (4.10b), (4.14), and (4.15) into Eqn. (4.11b), one gets

$$\frac{\partial}{\partial x}\left(GF_x \frac{\partial v}{\partial x}\right) - m_x \frac{\partial^2 z}{\partial t^2} - n_x \frac{\partial z}{\partial t} = -q_x \tag{4.18}$$

Using Eqn. (4.9) and substitution $\gamma = \frac{\partial w}{\partial x}$, Eqns. (4.17) and (4.18) can be rewritten as follows

$$\frac{\partial}{\partial x}\left(EI_x \frac{\partial \gamma}{\partial x}\right) + GF_x \left(\frac{\partial z}{\partial x} - \gamma\right) = I^*_{bx} \frac{\partial^2 \gamma}{\partial t^2} \tag{4.19a}$$

$$\frac{\partial}{\partial x}\left[GF_x \left(\frac{\partial z}{\partial x} - \gamma\right)\right] - m_x \frac{\partial^2 z}{\partial t^2} - n_x \frac{\partial z}{\partial t} = -q_x \tag{4.19b}$$

Eqns (4.19a) and (4.19b) form a system of two linear coupled hyperbolic partial differential equations with two unknowns: z and γ. The free-free beam is characterized by the absence of bending moment and shear force at the beam ends at all times. Therefore, the boundary conditions are

$$M_y(0,t) = M_y(L,t) = 0 \quad \Rightarrow \quad \left.\frac{\partial \gamma}{\partial x}\right|_{0,L} = 0 \tag{4.20a}$$

$$Q_z(0,t) = Q_z(L,t) = 0 \quad \Rightarrow \quad \left.\left(\frac{\partial z}{\partial x} - \gamma\right)\right|_{0,L} = 0 \tag{4.20b}$$

Initially, the beam is at rest with no excitation with the following initial conditions

$$z(x, t=0) = 0 \tag{4.21a}$$

$$\frac{\partial z}{\partial t}(x, t=0) = 0 \tag{4.21b}$$

$$\gamma(x, t=0) = 0 \tag{4.21c}$$

$$\frac{\partial \gamma}{\partial t}(x, t=0) = 0 \tag{4.21d}$$

The system of PDEs in Eqn. (4.19) is usually refereed to in the literature as the Timoshenko dynamic beam model. Using modal analysis to obtain the closed form solution to this system (like in Mansour and d'Oliveira [71]) is not possible due to presence of the rotary inertia term $I^*_{bx}(\partial^3 w)/(\partial x \partial t^2)$. Therefore, a numerical solution is sought for. Finite difference method is frequently used in space and time domains, but in this work a direct numerical solution to the Timoshenko dynamic beam model is achieved using the FEM in the space domain and the trapezoidal method for propagating the solution in time. The numerical solution is furnished without making any simplifications to the model and without relying on the modal analysis.

4.3.1 Direct Numerical Solution of the Timoshenko Dynamic Beam Model

The Timoshenko dynamic beam model in Eqn. (4.19) is a one-dimensional time dependent boundary value problem (BVP) called initial-boundary value problem (IBVP). It can be solved by using FEM to solve the BVP at each time step and using temporal discretization to propagate the solution in time from the initial conditions. The basic idea of FEM is to use a finite dimensional sub-spatial approximation of the true solution. This method has three main advantages over other numerical methods for solving BVPs (Zohdi [121]): (1) it is computationally systematic and efficient, (2) it is based on reformulation of differential equations that removes the problems of differentiability of the true solution, and (3) it is based on Galerkin method that forces orthogonality between the approximate solution and the error. This ensures that the error is minimized. Since the true solution is usually unknown, error cannot be found. However, the residual from applying the approximate solution to the BVP can always be found. Enforcing orthogonality between the approximate solution and the residual ensures that the error is minimized, albeit only when the error and the residual are from the same space of functions. It can be shown (e.g., Zohdi [121]) that if the accuracy of the finite element solution is measured in the energy norm, and if such norm exists, then the finite element solution is the best possible solution given the space from which the sub-spatial approximation functions are chosen.

The first step in developing the FE solution is to find the weak form of the governing partial differential equations of the BVP. The weak form relaxes (weakens) the differentiability conditions on the true solution and enforces the Galerkin principle provided that the testing function is chosen from the same space from which the sub-spatial approximation functions are chosen. If the true solution exists and if it is smooth enough, the weak form is equivalent to the strong form. The weak form of both equations in (4.19) is obtained by testing each equation with arbitrary scalar functions $\mathcal{V}_1(x)$ and $\mathcal{V}_2(x)$, respectively, and integrating them over the entire domain $\Omega \equiv x \in [0, L]$ as follows

$$\int_0^L \left[\frac{\partial}{\partial x}\left(EI_x \frac{\partial \gamma}{\partial x} \right) + GF_x \left(\frac{\partial z}{\partial x} - \gamma \right) - I^*_{bx} \frac{\partial^2 \gamma}{\partial t^2} \right] \mathcal{V}_1 dx = 0 \tag{4.22a}$$

$$\int_0^L \left\{ \frac{\partial}{\partial x}\left[GF_x \left(\frac{\partial z}{\partial x} - \gamma \right) \right] - m_x \frac{\partial^2 z}{\partial t^2} - n_x \frac{\partial z}{\partial t} + q_x \right\} \mathcal{V}_2 dx = 0 \tag{4.22b}$$

Using chain rule, this can be rewritten as

$$\int_0^L \left[\frac{\partial}{\partial x}\left(EI_x \frac{\partial \gamma}{\partial x} \mathcal{V}_1 \right) - EI_x \frac{\partial \gamma}{\partial x}\frac{\partial \mathcal{V}_1}{\partial x} + GF_x \left(\frac{\partial z}{\partial x} - \gamma \right) \mathcal{V}_1 - I^*_{bx} \frac{\partial^2 \gamma}{\partial t^2} \mathcal{V}_1 \right] dx = 0 \tag{4.23a}$$

$$\int_0^L \left\{ \frac{\partial}{\partial x}\left[GF_x \left(\frac{\partial z}{\partial x} - \gamma \right) \mathcal{V}_2 \right] - GF_x \left(\frac{\partial z}{\partial x} - \gamma \right) \frac{\partial \mathcal{V}_2}{\partial x} - m_x \frac{\partial^2 z}{\partial t^2} \mathcal{V}_2 - n_x \frac{\partial z}{\partial t} \mathcal{V}_2 + q_x \mathcal{V}_2 \right\} dx = 0 \tag{4.23b}$$

Taking into account the boundary conditions at $x = 0$ and $x = L$, the foregoing expressions simplify to

$$\int_0^L \left[-\frac{\partial \gamma}{\partial x} EI_x \frac{\partial \mathcal{V}_1}{\partial x} + \left(\frac{\partial z}{\partial x} - \gamma \right) GF_x \mathcal{V}_1 - I^*_{bx} \frac{\partial^2 \gamma}{\partial t^2} \mathcal{V}_1 \right] dx + \cancelto{0}{\frac{\partial \gamma}{\partial x}} EI_x \mathcal{V}_1 \Bigg|_0^L = 0 \tag{4.24a}$$

$$\int_0^L \left[-\left(\frac{\partial z}{\partial x} - \gamma \right) GF_x \frac{\partial \mathcal{V}_2}{\partial x} - m_x \frac{\partial^2 z}{\partial t^2} \mathcal{V}_2 - n_x \frac{\partial z}{\partial t} \mathcal{V}_2 + q_x \mathcal{V}_2 \right] dx + \cancelto{0}{\left(\frac{\partial z}{\partial x} - \gamma \right)} GF_x \mathcal{V}_2 \Bigg|_0^L = 0 \tag{4.24b}$$

The finite element approximations for the unknowns z and γ, as well as the testing functions $\mathcal{V}_1$ and $\mathcal{V}_2$ must be selected such that the integrals in Eqn. (4.19) remain finite. Mathematically, this is achieved by requiring that all these functions be members of the Hilbert-Sobolev space, $H^1(\Omega)$, that contains only scalar functions which generalized partial derivatives of order ≤ 1 are square integrable, i.e.

$$u \in H^1(\Omega) \quad \text{if} \quad \|u\|^2_{H^1(\Omega)} \overset{\text{def}}{=} \int_\Omega \frac{\partial u}{\partial x}\frac{\partial u}{\partial x} dx + \int_\Omega uu \; dx < \infty \tag{4.25}$$

This yields the FE weak formulation of the BVP

$$\begin{aligned}
&\text{find } z^h \in H^1_z(\Omega) \subset H^1(\Omega) \text{ and } \gamma^h \in H^1_\gamma(\Omega) \subset H^1(\Omega) \text{ such that} \\
&\int_0^L \left[-\frac{\partial \gamma^h}{\partial x} EI_x \frac{\partial \mathcal{V}^h_1}{\partial x} + \left(\frac{\partial z^h}{\partial x} - \gamma^h \right) GF_x \mathcal{V}^h_1 - I^*_{bx} \frac{\partial^2 \gamma^h}{\partial t^2} \mathcal{V}^h_1 \right] dx = 0, \\
&\int_0^L \left[-\left(\frac{\partial z^h}{\partial x} - \gamma^h \right) GF_x \frac{\partial \mathcal{V}^h_2}{\partial x} - m_x \frac{\partial^2 z^h}{\partial t^2} \mathcal{V}^h_2 - n_x \frac{\partial z^h}{\partial t} \mathcal{V}^h_2 + q_x \mathcal{V}^h_2 \right] dx = 0, \\
&\forall \mathcal{V}^h_1 \in H^1_{\mathcal{V}_1}(\Omega) \subset H^1(\Omega) \text{ and } \forall \mathcal{V}^h_2 \in H^1_{\mathcal{V}_2}(\Omega) \subset H^1(\Omega)
\end{aligned} \tag{4.26}$$

If subspaces $H^1_z(\Omega)$, $H^1_\gamma(\Omega)$, $H^1_{\mathcal{V}_1}(\Omega)$, and $H^1_{\mathcal{V}_2}(\Omega)$ coincide, that is, if the test functions $\mathcal{V}_1^h$ and $\mathcal{V}_2^h$ come from the same space as the approximate solutions z^h and γ^h, then the Galerkin's principle is enforced.

In this work, linear finite elements are used. Therefore, functions z^h, γ^h, $\mathcal{V}_1^h$ and $\mathcal{V}_2^h$ can be expressed as a sum of N linear shape functions, ϕ_i, where N is the number of nodes chosen to partition the one-dimensional space domain Ω.

$$\gamma^h(x,t) = \sum_{i=1}^{N} a_i(t)\phi_i(x) \tag{4.27}$$

$$z^h(x,t) = \sum_{j=1}^{N} b_j(t)\phi_j(x) \tag{4.28}$$

$$\mathcal{V}_1^h(x,t) = \sum_{k=1}^{N} c_k(t)\phi_k(x) \tag{4.29}$$

$$\mathcal{V}_2^h(x,t) = \sum_{l=1}^{N} d_l(t)\phi_l(x) \tag{4.30}$$

The foregoing functions depend on space and time arguments which will be omitted when possible. Each linear shape function, ϕ_i, has a unit value at node i, and vanishes at all other nodes. This can be seen in Figure 4.6.

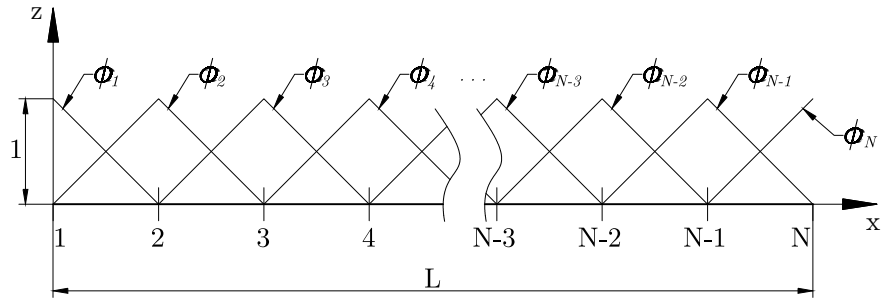

Figure 4.6: Linear shape functions.

Time derivatives appearing in Eqn. (4.26) can be discretized using the implicit trapezoidal method. This method is second-order accurate, it is very simple and has larger region of stability than the explicit forward Euler method. In fact, trapezoidal method is said to be A-stable method with the smallest truncation error, see, e.g., LeVeque [60]. However, its region of stability is smaller than the region of stability of the implicit backward Euler method which is also L-stable. Since the solution of the Timoshenko dynamic beam model contains rapid transients (higher-order vibration modes) that have to be resolved, trapezoidal method

will perform better than the backward Euler method which tends to numerically damp these higher order transients. As a drawback, all implicit methods require solving a nonlinear equation implicitly at each time step given that the underlying partial differential equations contain nonlinear time derivatives. This is not the case, however, with the Timoshenko dynamic beam model which consists of two liner PDEs.

The following set of equations is obtained by substituting Eqns. (4.28), (4.27), (4.29) and (4.30) into Eqns. (4.26) and using the trapezoidal time discretization scheme.

$$\begin{aligned}\sum_{i=1}^{N} c_i(t+\Delta t)\Bigg\{ &-\frac{1}{2}\sum_{j=1}^{N}\left[a_j(t+\Delta t)+a_j(t)\right]\int_0^L \phi_i^{'} EI_x \phi_j^{'} dx \\ &+\frac{1}{2}\sum_{j=1}^{N}\left[b_j(t+\Delta t)+b_j(t)\right]\int_0^L \phi_i GF_x \phi_j^{'} dx \\ &-\frac{1}{2}\sum_{j=1}^{N}\left[a_j(t+\Delta t)+a_j(t)\right]\int_0^L \phi_i GF_x \phi_j dx \\ &-\sum_{j=1}^{N}\frac{a_j(t+\Delta t)-2a_j(t)+a_j(t-\Delta t)}{(\Delta t)^2}\int_0^L \phi_i I_{bx}^{*} \phi_j dx\Bigg\} = 0 \end{aligned} \tag{4.31}$$

$$\begin{aligned}\sum_{i=1}^{N} d_i(t+\Delta t)\Bigg\{ &-\frac{1}{2}\sum_{j=1}^{N}\left[b_j(t+\Delta t)+b_j(t)\right]\int_0^L \phi_i^{'} GF_x \phi_j^{'} dx \\ &+\frac{1}{2}\sum_{j=1}^{N}\left[a_j(t+\Delta t)+a_j(t)\right]\int_0^L \phi_i^{'} GF_x \phi_j dx \\ &-\sum_{j=1}^{N}\frac{b_j(t+\Delta t)-2b_j(t)+b_j(t-\Delta t)}{(\Delta t)^2}\int_0^L \phi_i m_x \phi_j dx \\ &-\sum_{j=1}^{N}\frac{b_j(t+\Delta t)-b_j(t)}{\Delta t}\int_0^L \phi_i n_x \phi_j dx+\frac{1}{2}\int_0^L \left[q_x(t+\Delta t)+q_x(t)\right]\phi_i dx\Bigg\} = 0 \end{aligned} \tag{4.32}$$

The integrals in Eqns. (4.31) and (4.32) can be expressed in matrix notation

$$\left[\mathbf{K_b}\right]_{i,j} = \int_0^L \phi_i^{'} EI_x \phi_j^{'} dx \tag{4.33a}$$

$$\left[\mathbf{K_{s,z}}\right]_{i,j} = \int_0^L \phi_i GF_x \phi_j^{'} dx \tag{4.33b}$$

$$\left[\tilde{\mathbf{K}}_{\mathbf{s,z}}\right]_{i,j} = \int_0^L \phi_i' G F_x \phi_j' dx \tag{4.33c}$$

$$\left[\mathbf{K}_{\mathbf{s},\gamma}\right]_{i,j} = \int_0^L \phi_i G F_x \phi_j dx \tag{4.33d}$$

$$\left[\mathbf{M}_{\mathbf{I}}\right]_{i,j} = \int_0^L \phi_i I_{bx}^* \phi_j dx \tag{4.33e}$$

$$\left[\mathbf{M}\right]_{i,j} = \int_0^L \phi_i m \phi_j dx \tag{4.33f}$$

$$\left[\mathbf{N}\right]_{i,j} = \int_0^L \phi_i n \phi_j dx \tag{4.33g}$$

$$\left\{\mathbf{f}\right\}_{i,j} = \int_0^L q_x \phi_i dx \tag{4.33h}$$

where in this work $[\mathbf{K_b}]$ is called the bending stiffness matrix, $[\mathbf{K_{s,z}}]$ is the shear stiffness matrix due to derivative of the total deflection, $\frac{\partial z}{\partial x}$, $\left[\tilde{\mathbf{K}}_{\mathbf{s,z}}\right]$ is similar to $[\mathbf{K_{s,z}}]$ and tilde distinguishes them apart, $[\mathbf{K}_{\mathbf{s},\gamma}]$ is the stiffness matrix due to derivative of the bending deflection, $\gamma = \frac{\partial w}{\partial x}$, $[\mathbf{M_I}]$ is the mass moment of inertia matrix, $[\mathbf{M}]$ is the mass matrix, $[\mathbf{N}]$ is the damping matrix, and $\{\mathbf{f}\}$ is the vector of external loads.

Since functions $\mathcal{V}_1^h$ and $\mathcal{V}_2^h$ are arbitrary, Eqns. (4.31) and (4.32) must be valid for any c_i or d_i. Therefore, Eqns. (4.31) and (4.32) can now be rewritten as follows

$$\begin{aligned}
&\frac{1}{2}\left[-\left[\mathbf{K_b}\right]\left(\left\{\mathbf{a}\right\}^{t+\Delta t}+\left\{\mathbf{a}\right\}^{t}\right)+\left[\mathbf{K_{s,z}}\right]\left(\left\{\mathbf{b}\right\}^{t+\Delta t}+\left\{\mathbf{b}\right\}^{t}\right)-\left[\mathbf{K}_{\mathbf{s},\gamma}\right]\left(\left\{\mathbf{a}\right\}^{t+\Delta t}+\left\{\mathbf{a}\right\}^{t}\right)\right] \\
&-\frac{\left[\mathbf{M_I}\right]}{(\Delta t)^2}\left[\left\{\mathbf{a}\right\}^{t+\Delta t}-2\left\{\mathbf{a}\right\}^{t}+\left\{\mathbf{a}\right\}^{t-\Delta t}\right]=0
\end{aligned} \tag{4.34}$$

$$\begin{aligned}
&\frac{1}{2}\left[-\left[\tilde{\mathbf{K}}_{\mathbf{s,z}}\right]\left(\left\{\mathbf{b}\right\}^{t+\Delta t}+\left\{\mathbf{b}\right\}^{t}\right)+\left[\mathbf{K_{s,z}}\right]^{\mathrm{T}}\left(\left\{\mathbf{a}\right\}^{t+\Delta t}+\left\{\mathbf{a}\right\}^{t}\right)\right] \\
&-\frac{\left[\mathbf{M}\right]}{(\Delta t)^2}\left[\left\{\mathbf{b}\right\}^{t+\Delta t}-2\left\{\mathbf{b}\right\}^{t}+\left\{\mathbf{b}\right\}^{t-\Delta t}\right]-\frac{\left[\mathbf{N}\right]}{\Delta t}\left[\left\{\mathbf{b}\right\}^{t+\Delta t}-\left\{\mathbf{b}\right\}^{t}\right]+\frac{1}{2}\left[\left\{\mathbf{f}\right\}^{t+\Delta t}+\left\{\mathbf{f}\right\}^{t}\right]=0
\end{aligned} \tag{4.35}$$

Eqns. (4.34) and (4.35) present the finite element solution to the Timoshenko dynamic beam model with trapezoidal time integration scheme. When the solution vectors $\{\mathbf{a}\}$ and $\{\mathbf{b}\}$ of both unknowns are known at two previous time steps $t-\Delta t$ and t, then the solution vectors $\{\mathbf{a}\}^{t+\Delta t}$ and $\{\mathbf{b}\}^{t+\Delta t}$ at the next time step can be easily found using Eqns. (4.34)

and (4.35) which are two linear matrix equations with two unknowns $\left(\{\mathbf{a}\}^{t+\Delta t}\right.$ and $\left.\{\mathbf{b}\}^{t+\Delta t}\right)$. Solution vectors $\{\mathbf{a}\}$ and $\{\mathbf{b}\}$ at $t = 0$ and $t = \Delta t$ can be obtained from the initial conditions (see Eqn. (4.21)). From there, the solution can be propagated in time using Eqns. (4.34) and (4.35) to obtain $\left(\{\mathbf{a}\}^{2\Delta t}, \{\mathbf{b}\}^{2\Delta t}\right)$, $\left(\{\mathbf{a}\}^{3\Delta t}, \{\mathbf{b}\}^{3\Delta t}\right)$, etc.

All the matrices in Eqns. (4.34) and (4.35) don't change with time since they represent material, mass, and geometric characteristics of the beam which are assumed to be time independent. The only vector that depends on time, apart from the solution vectors, is the vector of external loads, $\{\mathbf{f}\}$. Therefore, all the matrices have to be calculated only once using element-by-element assembly to preserve sparsity and to make the computations more efficient. The calculation of all the integrals in Eqns. (4.33) can be greatly simplified by breaking the original domain, Ω, into finite number of element domains and then mapping each element domain into the so called "Master element" domain spanning from $\zeta = -1$ to $\zeta = 1$. All the integrals over the Master element domain can be efficiently calculated using the Gaussian quadrature. The entire numerical solution of the Timoshenko dynamic beam model is implemented in a computer program using Matlab.

4.4 Results

4.4.1 Accuracy of the Numerical Model

4.4.1.1 Considerations of the Time Step

The accuracy of a numerical method in time domain is often check by testing it on a simplified system. This is usually a single degree of freedom (SDOF) free oscillating spring-mass system with no damping for which the analytical solution is available. Typical errors are wrong period of oscillation, or numerically introduced damping. Since slamming phenomena is analyzed independently from other wave-induced loads, there is no restoring force which brings the hull girder into equilibrium. Therefore, a mass-damper system is used in this work to check for consistency. Figure 4.7 shows a response (vertical displacement z) of a SDOF mass-damper system with equivalent mass and damping coefficient to that of the C 319 container ship. The initial conditions are: $z(t = 0) = 0$ m, and $\dot{z}(t = 0) = 1$ m/s. As the time step decreases, numerical solutions converge to the analytical one. There is no numerically introduced damping, even for relatively large time steps which is a property of the trapezoidal method.

The foregoing analysis is not sufficient for determining a proper time step of integration since the hull girder is a flexible body and will have flexural vibrations. According to Økland [89], maximum time step should be:

- less than 0.1 times the lowest natural period of interest and;
- small enough to capture the sudden rise of the slamming force.

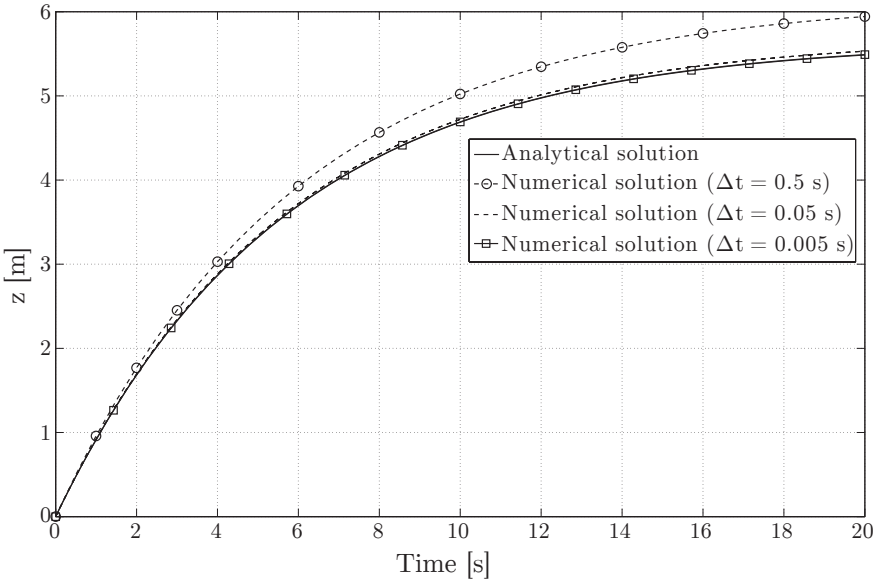

Figure 4.7: Validation of the numerical method using SDOF mass-damper system.

The lowest natural period of interest in slamming analysis is the one associated with the two-node vibration mode of the hull girder. In the case of C 319 container ship, this period is equal to $1/(2\pi \times 2.95) = 0.054$ seconds. Therefore, a time step $\Delta t = 0.005$ seconds should be sufficient to properly resolve the system's response at the basic two-node vibration mode frequency. Smaller time steps are required if the response at higher vibration modes is sought for. Since the duration of slamming force, Eqn. (4.4), is inversely proportional to relative speed between the ship and the waves, and since the largest relative speeds observed in this work are around 15 m/s, the shortest duration of slamming force is around 0.168 seconds. Therefore, a time step $\Delta t = 0.005$ s is sufficiently small to capture the behavior of the slamming force for all relative speeds.

Figure 4.8 shows the whipping VBM response of a C 319 container ship slamming into water with relative vertical velocity $\dot{z}_{rel} = 15$ m/s, damping ratio $\xi = 0.03$, and for three different time steps. The extent of slamming is $\Delta x_{slam} = 0.04L$. Clearly, $\Delta t = 0.05$ s (solid line with circles) is not sufficient to completely resolve the response, even at the two-node mode frequency. It is seen that the basic frequency of oscillation of the whipping VBM is very close to the two-node frequency of the hull girder ($\omega_{2-node} \approx 2.95$) rad/s. $\Delta t = 0.005$ s (solid line) completely resolves the two-node mode response, and the onset of the three-node mode response can also be observed. Decreasing the time step to $\Delta t = 0.0005$ s (dashed line) resolves the three-node mode response which is seen to be much less significant than the two-node mode response. Decreasing the time step even further (not shown here) adds high-frequency small-amplitude components corresponding to higher modes of vibration.

Given a ship geometry, the whipping response of the hull girder in the simplified hydrodynamic model depends only on the relative vertical speed between the ship and the waves,

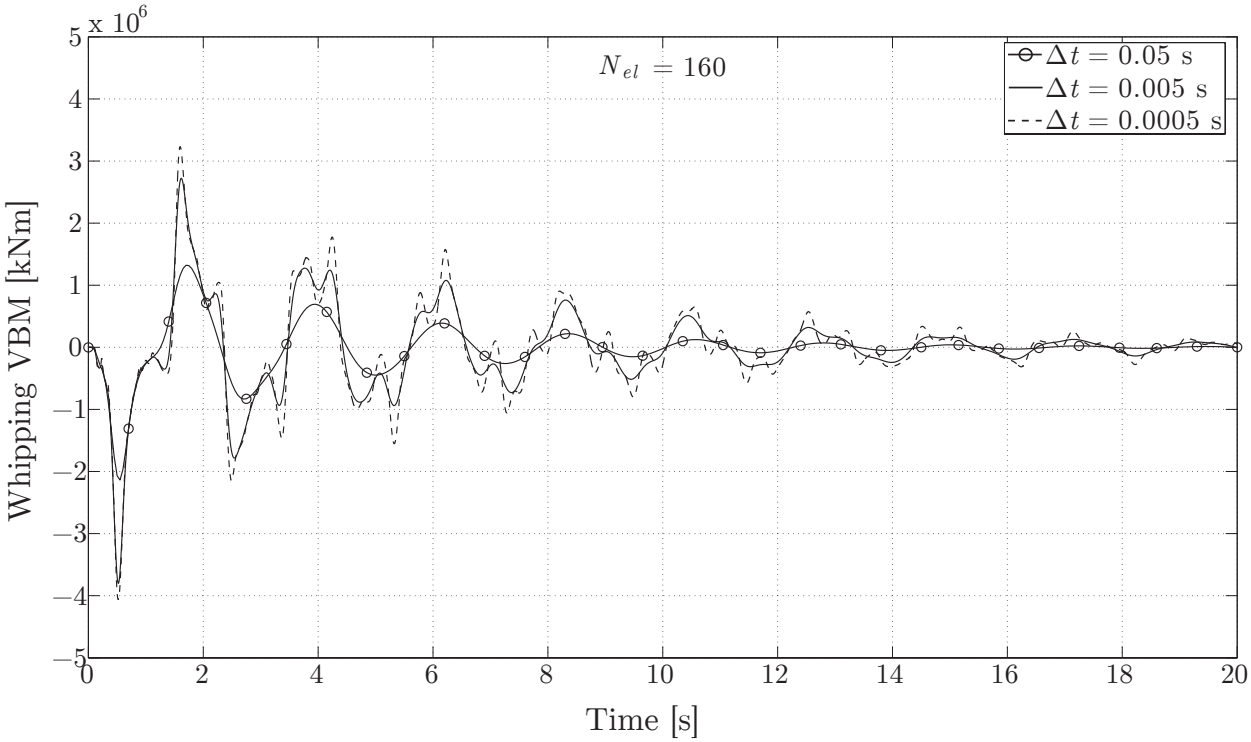

Figure 4.8: Whipping VBM response at amidship of C 319 container ship with $\xi = 0.03$ for various time steps; $\Delta x_{slam} = 0.04L$.

and the extent of slamming. Whipping response can be pre calculated for a range of relative speeds and the response surface of the whipping response time series can be obtained. Then, for all slamming instants, defined using the long-term ship motion analysis, an appropriate time series of the whipping VBM is superimposed onto other components of the VBM. Relative velocity of the slamming event determines, of course, which whipping response time series will be inserted. Therefore, it is not necessary to run the numerical model for simulation of the whipping response for each slamming event. Obtaining the whipping response surface is the only computational effort in whipping analysis. The length of the long-term time series of the VBM, and the associated number of slams, have no effect on the CPU time needed for whipping analysis. Figure 4.9 shows a plot of the whipping response of C 319 container ship at the midship section for various values of relative impact velocity $\dot{z}_{rel}$. The time step is equal to $\Delta t = 0.0005$ s which is sufficiently small to reveal the three-node mode vibrations of the hull girder. The range of relative speeds shown in the figure (5 to 15 m/s) captures all the simulated relative speeds associated with slamming impacts during a simulation of two hundred voyages. The whipping response increases steadily as the relative speed increases. Although the increase in the VBM whipping amplitudes seems to be linear, that is not quite the case since the "crests" and "throughs" in Figure 4.9 are not parallel to y-axis (i.e. there is a positive time shift for first couple of whipping peaks as the relative

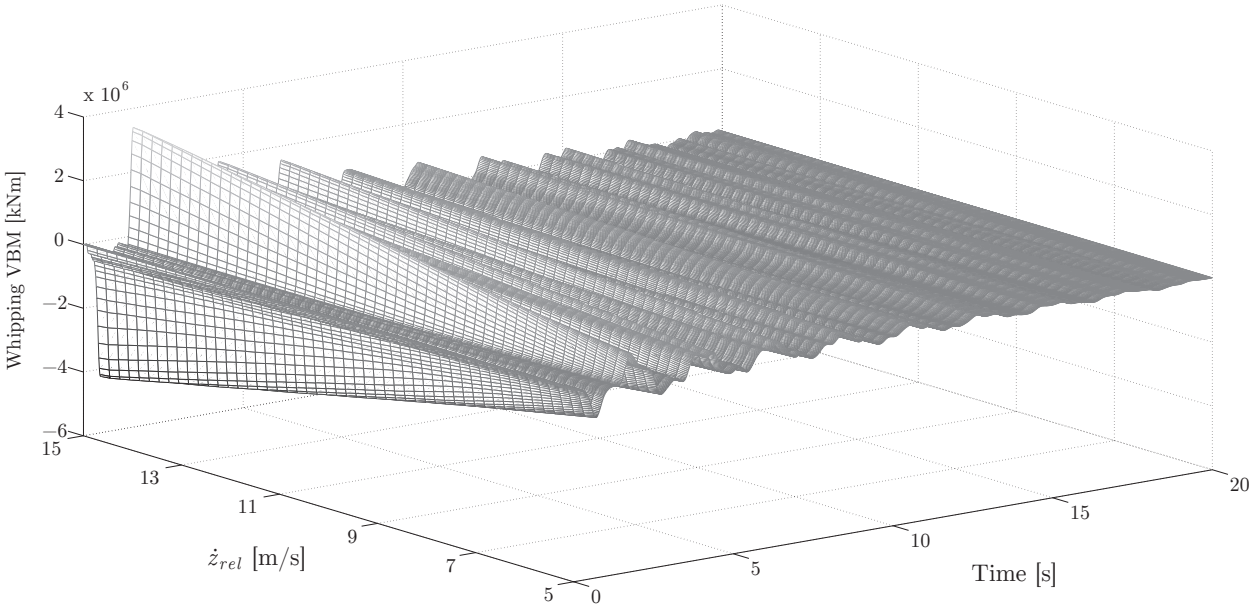

Figure 4.9: Whipping VBM at amidship of C 319 container ship with $\xi = 0.03$ for various values of relative velocity $\dot{z}_{rel}$; $\Delta x_{slam} = 0.04L$, $\Delta t = 0.0005$ s.

velocity increases). Nevertheless, there are no abrupt changes in the whipping response with changes in relative velocity. The response surface is quite smooth in the direction of $\dot{z}_{rel}$ which means that it can be obtained by considering only a limited number of relative impact speeds.

To save on CPU time, three-node and higher modes of vibration can be neglected. The significance of the higher modes of vibration is investigated in Section 4.4.4.

4.4.1.2 Considerations of the Number of Finite Elements

Error estimates of the FE solutions in the spatial coordinate for a fixed time t can be obtained using the L^2 norm measure as follows

$$e^{N_{el}} \stackrel{\text{def}}{=} \frac{\|M_{y,whip} - M_{y,whip}^{N_{el}}\|}{\|M_{y,whip}\|} \tag{4.36}$$

$$\|M_{y,whip}\| \stackrel{\text{def}}{=} \sqrt{\int_{\Omega} M_{y,whip}^2 dx} \tag{4.37}$$

where $M_{y,whip}$ is the true solution of the whipping VBM, $M_{y,whip}^{N_{el}}$ is the numerical solution, and $\Omega \equiv x \in [0, L]$ is the space domain. Since the true solution of the Timoshenko dynamic non-prismatic beam model is not known, a numerical solution for a very high number of finite elements ($N_{el} = 1280$) is taken as the true solution. In order to determine the number

of equal-sized finite elements needed to achieve satisfactory accuracy, the number of elements is doubled at each iteration, starting from $N_{el} = 20$, until the error estimate falls below the tolerance level set at $e^{N_{el}} \leq TOL = 0.05$. Figure 4.10 shows the whipping VBM response for the entire hull girder at time $t = 0.475$, corresponding to the instant when the whipping VBM at midship section ($L/2 = 159.5$ m) reaches maximum in sagging (largest negative peak - see Figure 4.8). The solution converges to the "true" solution as the number of

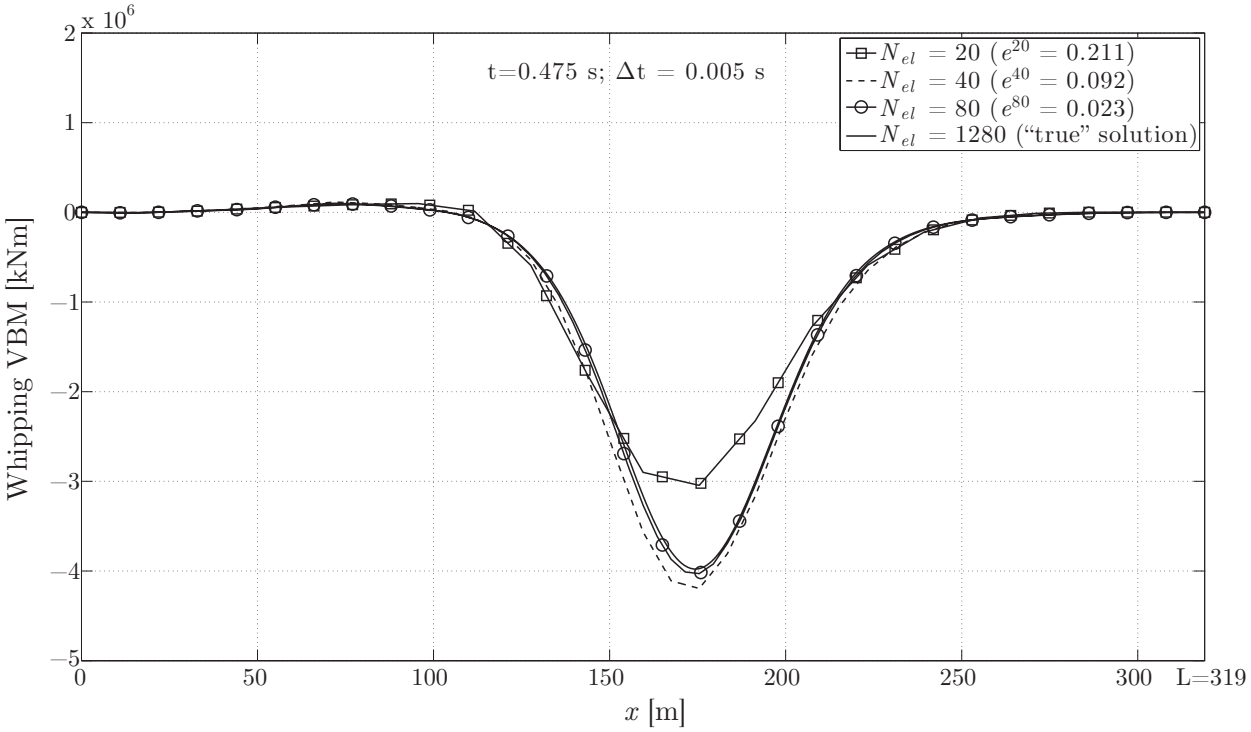

Figure 4.10: Whipping VBM response at time $t = 0.475$ s for varying number of finite elements; C 319, $x = L/2$, $\Delta x_{slam} = 0.04L$, $\xi = 0.03$.

elements increases and the error estimate decreases such that $e^{20} = 0.210$, $e^{40} = 0.093$, and $e^{80} = 0.023$. Therefore, $N_{el} = 80$ is chosen as sufficient throughout this work. It should be noted that the whipping bending moment reaches its maximum, not at midship section, but at a section approximately ten meters forward of amidship.

4.4.2 Whipping VBM in Space-Time Domain

Numerical model for solving Timoshenko dynamic beam enables the examination of the behavior of the whipping VBM in both space and time domains. Figure 4.11a shows whipping VBM for C 319 container ship at all longitudinal sections propagating in time. Figure 4.11b shows a contour plot of the same whipping VBM. Immediately after the slamming excitation in the bow region, a wave of VBM starts to propagate backwards and forwards across the

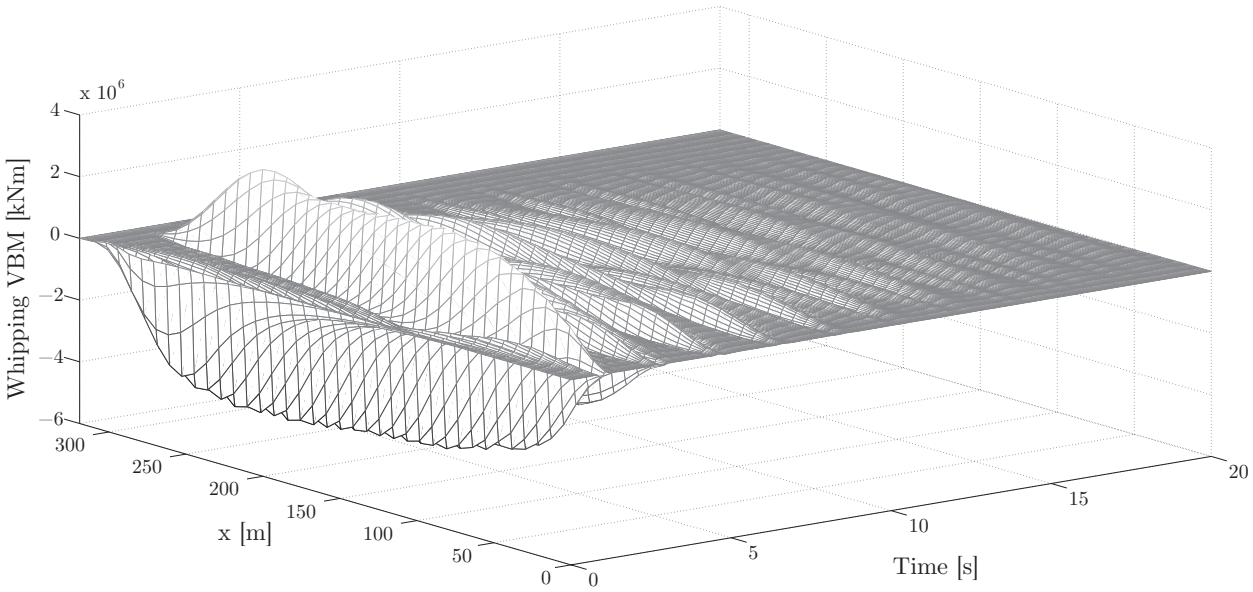

(a) Surface plot of the whipping VBM.

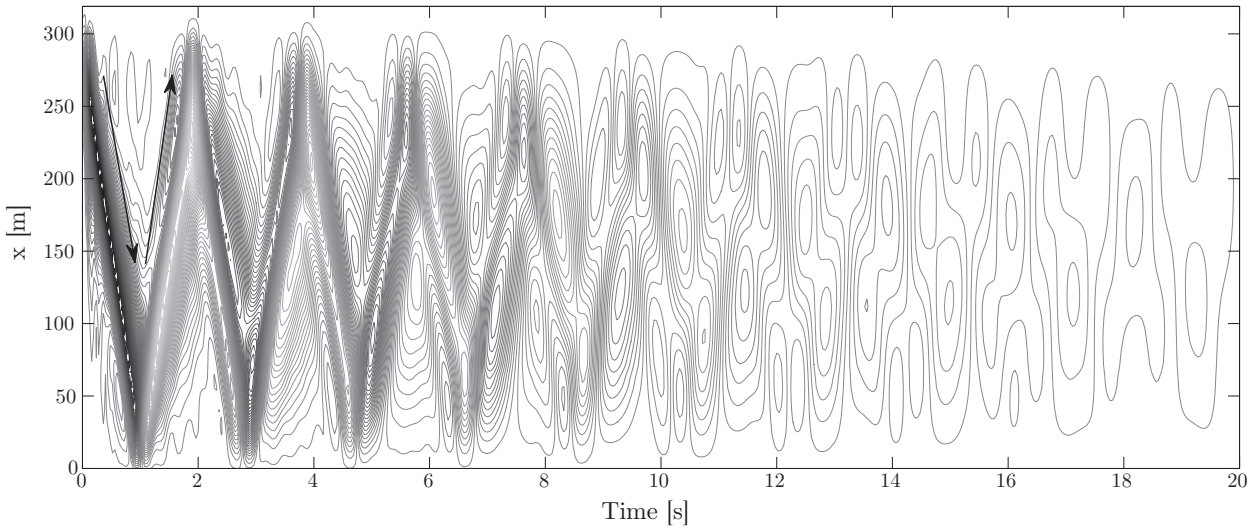

(b) Contour plot of the whipping VBM.

Figure 4.11: Space-time behavior of the whipping VBM; C 319, $\xi = 0.03$, $\Delta x_{slam} = 0.04L$, $\Delta t = 0.005$ s, $N_{el} = 80$.

hull. This behavior is clearly seen on the contour plot. It should also be noted that the largest overall whipping VBM occurs in sagging close to the impact zone at the bow, shortly after the impact. But, since the wave-induced VBM is small in that region, the whipping VBM is of no practical importance at that location. Wave-induced shear forces reach their maximum at one quarter and three quarters of the ship's length. Therefore, large slamming shear force in the bow region will potentially significantly increase the total maximum shear force. Since slamming-induced shear forces can easily be simulated using the same numerical model (shear forces are proportional to the derivative of the shear deflection), this effect can also be investigated. However, this is not done in the present study.

4.4.3 Analysis of Slamming Events

The slamming events are identified using linear ship motion analysis and the criteria described in Section 4.2. During two hundred simulated voyages of C 319 container ship on NA route, a little more than fourteen thousand slamming events are identified. Figure 4.12 shows plots which facilitate the analysis of these slamming events. Plot in Figure 4.12a shows sea states in which slamming occurred. No slamming events are identified in sea states with significant wave height of less than three meters with the majority of slams occurring in sea states with significant wave height of more than four meters.

Figure 4.12b shows a histogram of ship relative headings in which slamming occurred. Expectedly, the largest number of slams is observed in head seas due to largest pitch amplitudes at that heading. Only a small number of slams occurred at relative headings greater than or equal to 90 degrees, i.e. in beam, oblique following, and following seas. This is a well known fact for bow flare slamming. The classification society ABS requires only the considerations of headings between the head and the beam seas for slamming analysis. This assumptions is found to be quite reasonable considering the results of this work.

Figure 4.12c shows a scatter plot of relative impact velocities, $\dot{z}_{rel}$, and the associated significant wave heights. There is clearly a linear relationship between the maximum value of relative impact velocity and the significant wave height. This is a logical consequence of applying the linear ship motion analysis. The relative velocities in the extreme sea state of $H_S = 18$ meters don't seem to follow the overall linear trend. The reason for this is that only one such high sea state is sampled in two hundred voyages, and as it happens, the relative heading of the ship in that sea state is 160 degrees. This is almost following seas where the ship "rides" on the waves much more gently than in head seas.

Finally, Figure 4.12d shows a histogram of relative impact speeds with the truncated exponential distribution fit with mean value $\mu = \frac{1}{\lambda} = 0.806$. Truncated exponential model is used because the relative velocities are left truncated at $\dot{z}_{rel,cr} = 0.093\sqrt{gL} = 5.20$ m/s.

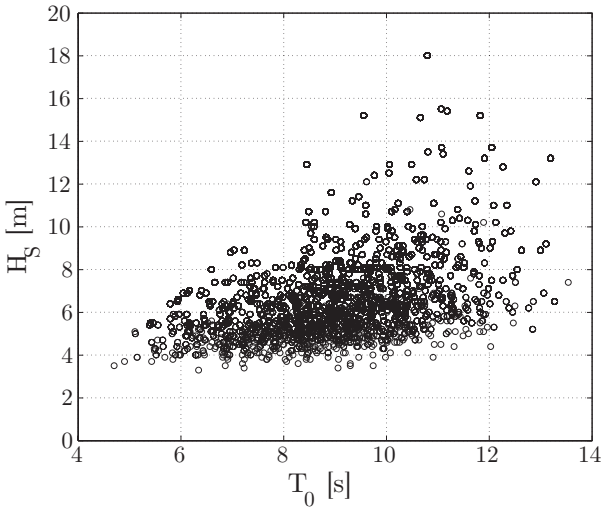

(a) Sea states where slamming is observed.

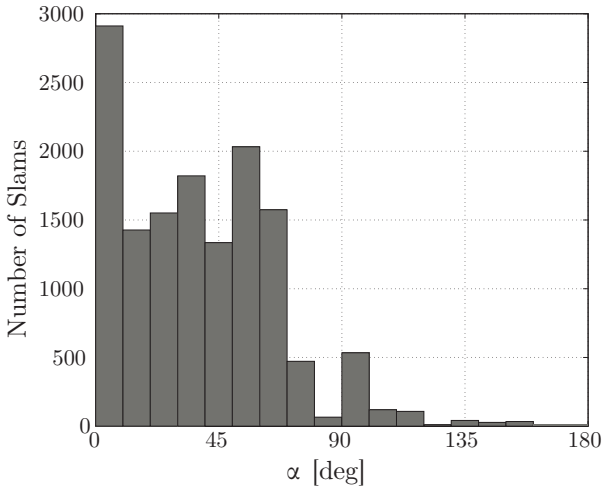

(b) Number of impacts versus relative heading.

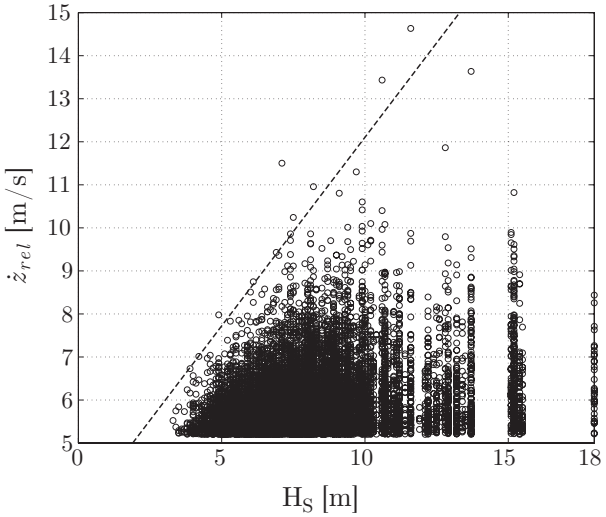

(c) Relative impact velocities versus significant wave height.

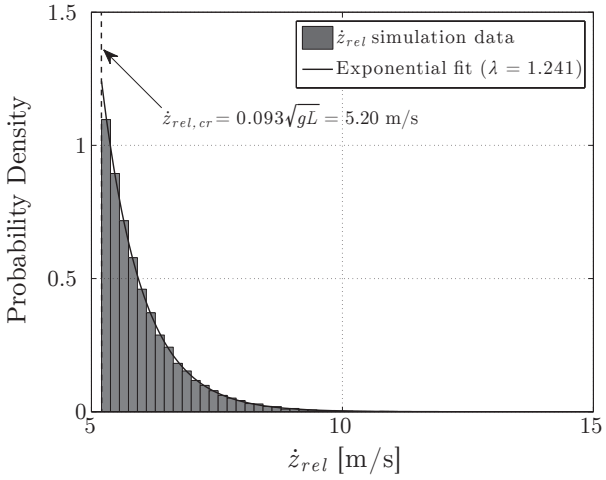

(d) Long-term distribution of the relative impact velocity.

Figure 4.12: Statistics of slamming events; C 319, NA.

4.4.4 Long-Term Probabilities of Exceedance of the Total VBM Including Whipping

A time series of whipping response creates a cluster of maxima due to damped vibrations. In the statistical sense, this means that the peaks of the whipping response, M_y^{whip}, and also of the total VBM response, $M_y^{(1)+(2)^{\pm}} + M_y^{whip}$, subsequent to a slam are strongly correlated. Therefore, in order to obtain a sample of independent response maxima, the literature suggests using only the largest whipping response peak subsequent to each slam, see Davison and Smith [20]. However, the largest whipping VBM subsequent to a certain slam event does not necessarily produce the largest total VBM, depending on the underlying time series of VBM onto which the whipping is being added. Therefore, after each impact, only one slamming peak is considered, not necessarily the largest one, but the one that produces the largest total VBM when combined with the underlying VBM time series. This is illustrated in Figure 4.13 which shows a whipping VBM from two slam events superimposed onto other VBM components. The events are separated by less than the duration of the first whipping response, so both responses are superimposed during the overlapping time interval. First slamming event occurs while the ship is in sagging condition from other VBM contributions. In this case, the counted peak, marked with a solid circle, corresponds to the first (and largest) whipping peak in sagging because it produces the largest total VBM in sagging. The second slamming event occurs while the ship is in hogging condition. Here, the counted peak corresponds to the fifth whipping peak in sagging since it produces the largest total VBM for that slamming event.

At damping ratio of 0.03, the whipping vibrations are damped within twenty seconds at all relative impact speeds. However, some slams are less than twenty seconds apart which means that the whipping response from one impact may overlap with the whipping response from another one. In some instances, even three whipping responses will overlap. It is assumed that the structure responds independently to each impact, without any effect of one whipping response on another one. With this assumption, all the individual whipping responses can be superimposed at time instants where they overlap and added to other VBM components ($M_y^{(1)+(2)^{\pm}}$).

The effect of whipping on the long-term probability of exceedance of the total VBM, $M_y^{(1)+(2)^{\pm}} + M_y^{whip}$, can be seen in Figure 4.14. The largest simulated whipping sagging VBM in two hundred voyages is $M_y^{whip} = 4.1 \times 10^6$ kNm which is 28% of extreme $M_y^{(1)+(2)^{\pm}}$ in sagging at 10^{-8} probability level. However, when added together, whipping increases $M_y^{(1)+(2)^{\pm}}$ in sagging at 10^{-8} probability level by only 3%. Similar result is obtained for the hogging condition. The reason is that slamming events occur, most often, at times when $M_y^{(1)+(2)^{\pm}}$ is relatively small. This is also noted in Økland [89] based on observations of bow flare slamming and short-term time domain simulations. Figure 4.15 shows a histogram of simulated $M_y^{(1)+(2)^{\pm}}$ values at slamming instants. The distribution is slightly right-tailed with the average value of 6.264×10^4 kNm and the standard deviation of 1.298×10^6 kNm. Almost no slamming events occur when $M_y^{(1)+(2)^{\pm}}$ is larger than $\pm 4 \times 10^6$ kNm.

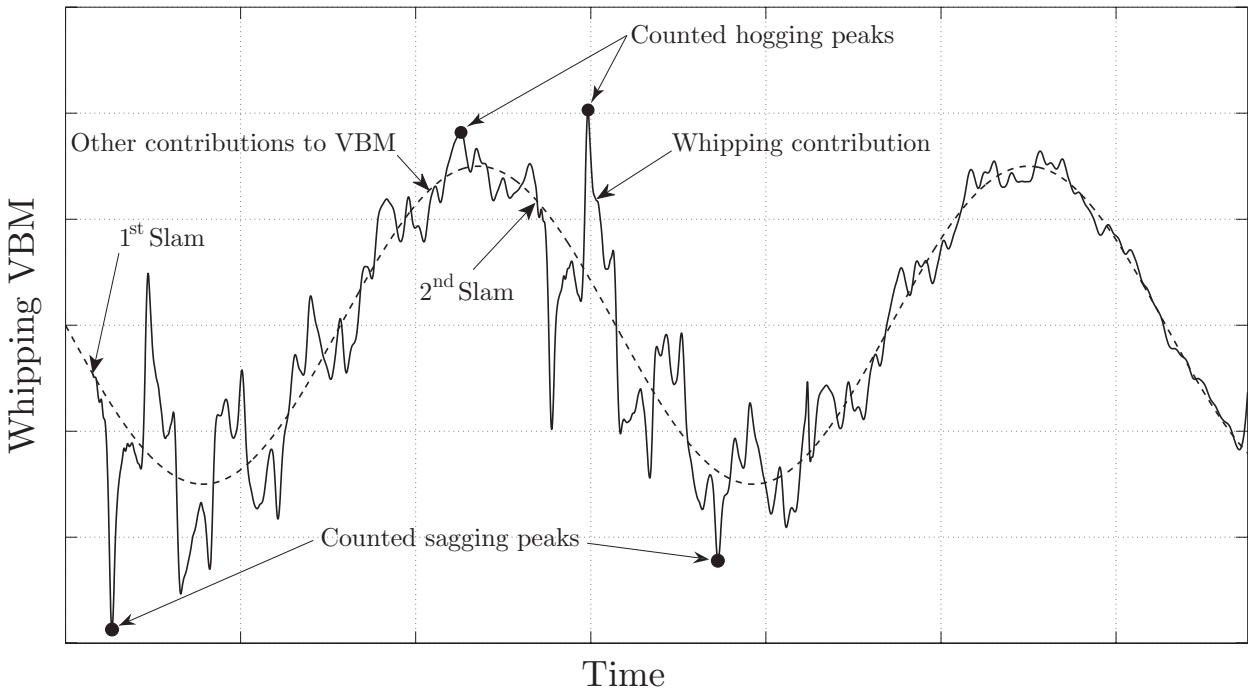

Figure 4.13: Peak counting for slamming events.

Baarholm and Jensen [9], in their study of whipping influence on the total VBM, found a strong correlation between magnitudes of low-frequency wave-induced responses and the whipping responses, i.e., that the large whipping responses occur at times of larger wave-induced responses. The correlation coefficients between magnitudes of wave-induced and whipping peaks that they obtained in a single sea state (short-term) varied between 0.655 and 0.759 for sagging and between 0.195 and 0.441 for hogging, depending on the forward speed. Although a simplified long-term analysis has been performed by Baarholm and Jensen, using only one forward speed and head seas, the long term correlation coefficients between peak magnitudes were not calculated. Long-term simulation procedure used in this work enables the calculation of long-term correlation coefficients between $M_y^{(1)+(2)^{\pm}}$ and M_y^{whip} peaks which are found to be 0.294 for sagging and 0.291 for hogging. Understandably, they are smaller than the short-term correlation coefficients in head sea condition. It should also be noted that Baarholm and Jensen considered the total high-frequency response of the ship as the whipping response. However, their high-frequency signal also contained other two node mode vibrations, such as linear and nonlinear springing which could not be separated from whipping.

Perhaps even more important than the correlation of $M_y^{(1)+(2)^{\pm}}$ and M_y^{whip} peak magnitudes is their correlation in time, or phase relationship. An accurate prediction of the long-term properties of the total VBM, $M_y^{(1)+(2)^{\pm}} + M_y^{whip}$, can only be established when the time of impact and the subsequent whipping response, M_y^{whip}, are correctly related to

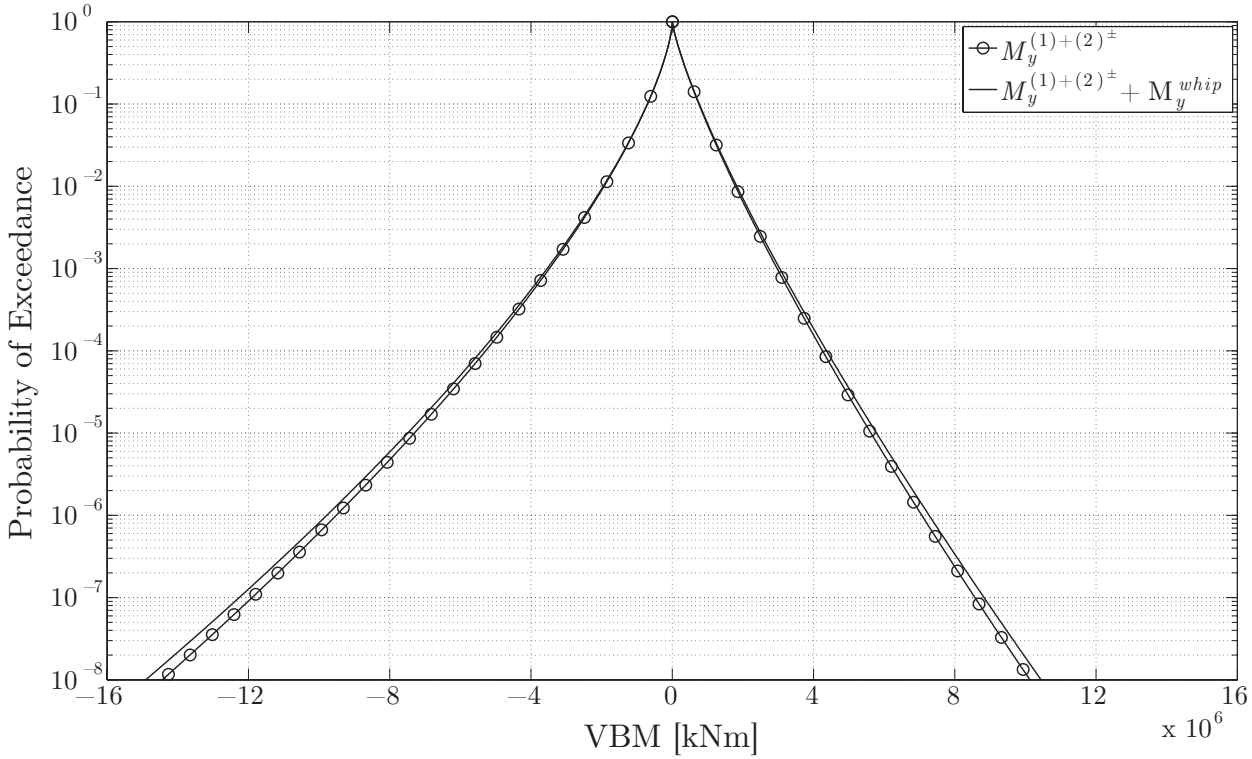

Figure 4.14: Weibull fits of the VBM sagging (negative) and hogging (positive) peaks with and without whipping; C 319, NA, $\xi = 0.03$, $\Delta x_{slam} = 0.04L$.

$M_y^{(1)+(2)^{\pm}}$. As seen in this work, the fact that the slams occur mostly when $M_y^{(1)+(2)^{\pm}}$ is close to zero has a significant effect on the long-term probabilities of exceedance of the total VBM. For example, if the sagging peaks of $M_y^{(1)+(2)^{\pm}}$ are perfectly correlated in time with the maximum sagging peaks of M_y^{whip}, then the extreme value of $M_y^{(1)+(2)^{\pm}} + M_y^{whip}$in sagging at 10^{-8} probability level will be approximately 28% larger than the same extreme value of $M_y^{(1)+(2)^{\pm}}$. The fact that it is only 3% larger is a direct consequence of the lack of strong positive correlation in time between largest M_y^{whip} peaks and $M_y^{(1)+(2)^{\pm}}$ peaks for C 319 container ship on NA route. In fact, out of all 14030 slamming events simulated in two hundred voyages, in only 1072 of them (7.6%) the first (and largest) whipping peak in sagging produced the largest total sagging VBM response. In 3507 slamming events (25%), the largest whipping peak in hogging produced the largest overall VBM peak in hogging. These percentages partially explain why slamming extent affects hogging peaks more than sagging, as it will be shown later in Section 4.4.4.2.

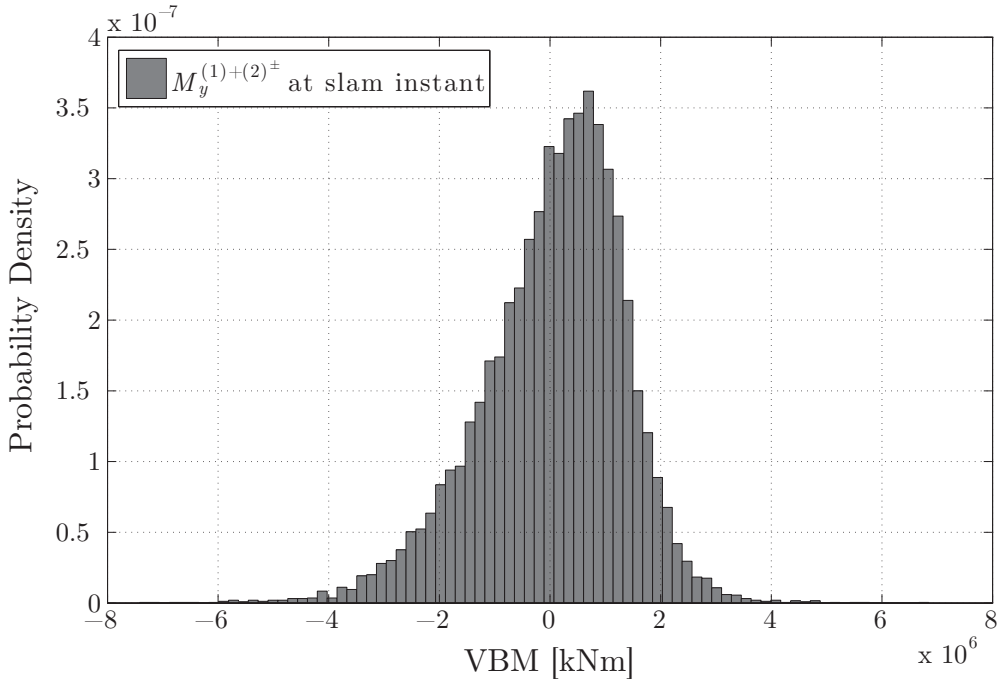

Figure 4.15: Histogram of values of the total VBM without whipping ($M_y^{(1)+(2)^{\pm}}$) at times of impact; C 319, NA, $\xi = 0.03$, $\Delta x_{slam} = 0.04L$.

4.4.4.1 The Effect of the Time Step on the Long-Term Probabilities of Exceedance

It was mentioned in Section 4.4.1.1 that the CPU time needed for calculating the whipping response surface can be reduced by increasing the time step of integration. Increasing the time step from $\Delta t = 0.0005$ s to $\Delta t = 0.005$ s eliminates three-node modes of vibration from the whipping time series. However, since the three-node mode vibrations are much less significant than the two-node mode vibrations (see Figure 4.8), and since only one whipping peak is counted per slam, simplifying the whipping response analysis by increasing the time step to $\Delta t = 0.005$ s has a negligible effect on the resulting long-term probabilities of exceedance of sagging total VBM peaks, as shown in Figure 4.16. Weibull fits representing these two time step cases overlap over the entire VBM domain.

With the time step of $\Delta t = 0.005$ s and $N_{el} = 80$, time needed to calculate M_y^{whip} for one speed is less than a minute on an ordinary personal computer. Since the whipping response surface is very smooth in the relative impact velocity variable, only a limited number of whipping response calculations is need for selected impact velocities. Then, the complete response surface can be found using interpolation. For these reasons, the entire slamming analysis takes a very short amount of time, meaning that it can be applied at the ship initial design stage to test different slamming parameters such as the extent of slamming.

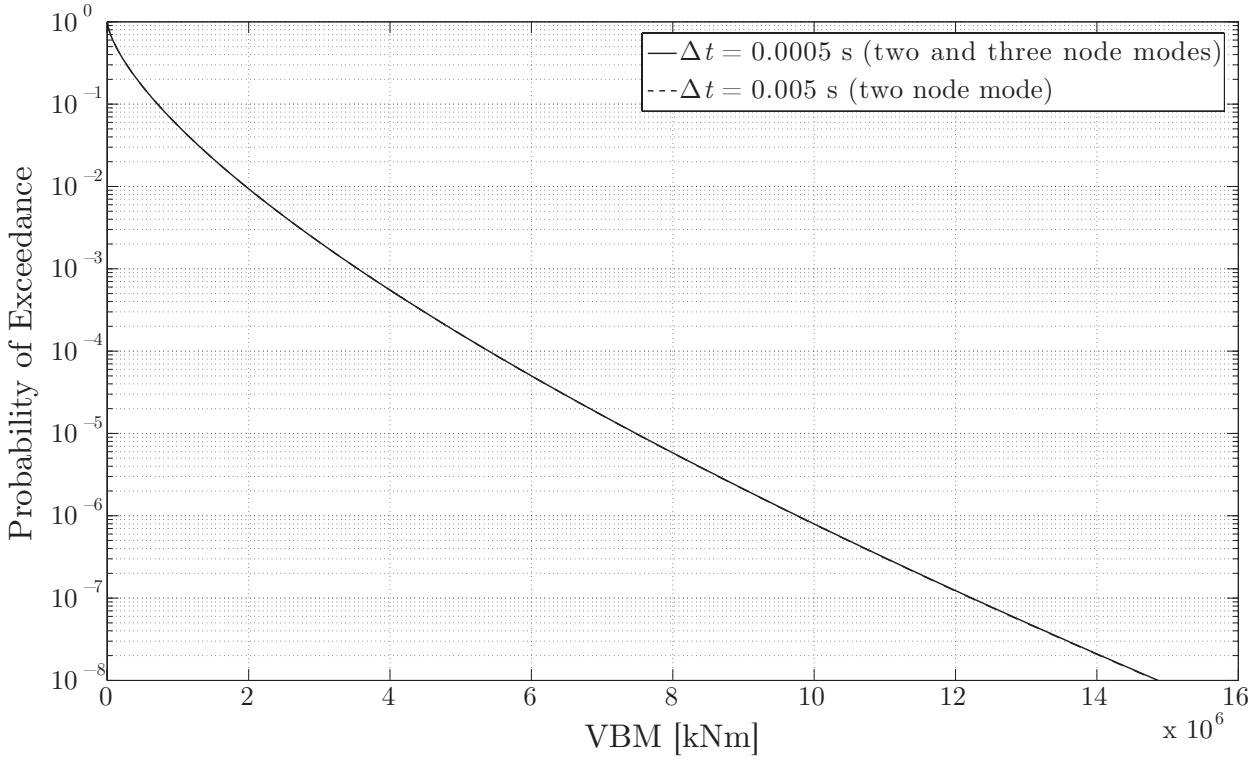

Figure 4.16: Weibull fits of the total VBM ($M_y^{(1)+(2)^{\pm}} + M_y^{whip}$), where the whipping part (M_y^{whip}) is calculated using two different time steps; C 319, NA, $\xi = 0.03$, $\Delta x_{slam} = 0.04L$.

4.4.4.2 The Effect of Slamming Extent on the Long-Term Probabilities of Exceedance

Slamming extent, Δx_{slam}, has a significant effect on the whipping response of the hull girder. This can be seen in Figure 4.17 which shows whipping responses of C 319 container ship with $\dot{z}_{rel} = 15$ m/s for three different extents of slamming: $\Delta x_{slam} = 0.02L$, $\Delta x_{slam} = 0.04L$ (default), and $\Delta x_{slam} = 0.06L$.

On the other hand, the effect of slamming extent on the long term probabilities of exceedance is rather small due to the fact that $M_y^{(1)+(2)^{\pm}}$ and M_y^{whip} peaks are not strongly correlated in time. This is seen in Figure 4.18 which shows the effects of slamming extent on the long-term probabilities of exceedance of the total VBM in both hogging and sagging. Although the overall effect of slamming extent is small, hogging peaks are more affected than the slamming peaks, for which this effect can barely be noticed. This is, of course, related to the phase lag between $M_y^{(1)+(2)^{\pm}}$ and M_y^{whip} time series. Since container ships are usually in hogging condition in still water, dynamic hogging VBM is generally more important than dynamic sagging VBM. Therefore, any increase in the dynamic hogging VBM is very important from ship design point of view.

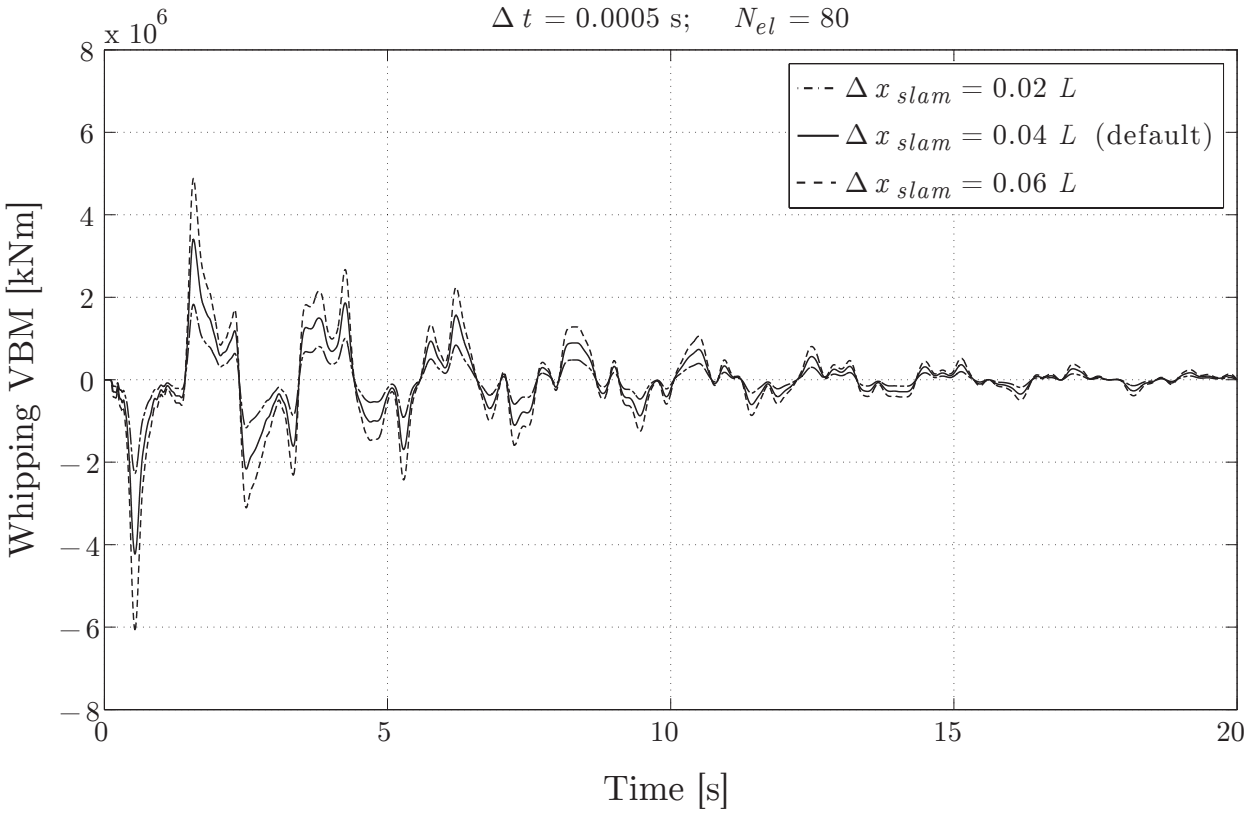

Figure 4.17: Whipping VBM for various extents of slamming; C 319, $\xi = 0.03$.

4.4.4.3 Comparison With Full-Scale Measurements and Jensen's Simplified Method for Container Ships

A comparison of total VBM including linear, nonlinear, springing, and whipping contributions between full-scale measurements, Jensen's long term method [52] for container ships, and the simulation method is presented in this section. Very few studies have been identified in the literature that report on the long-term probabilities of exceedance of the VBM with sufficient information about the vessel and its operational profile to enable proper comparison (see also Section 2.3.3.3). Only one study by Okada et al. [88] satisfied these conditions and presented measurements for a vessel with similar particulars as the C 319 container ship. The same study is used in Section 2.3.3.3 to compare the long-term probabilities of exceedance of the low-frequency part of the total VBM obtained by simulation and full-scale measurements.

Vessel on which the full scale measurements have been performed in [88] and the C 319 container ship for which the linear, springing, nonlinear, and whipping analysis are performed throughout this work are both post-Panamax container ships with the same breadth ($B =$ 42.8 m), and very similar depths (24.4 m and 24 m), drafts (14 m and 14.5 m) and service speeds (24.5 kn and 25.4 kn). Also, they have a very similar operational profile on the EA

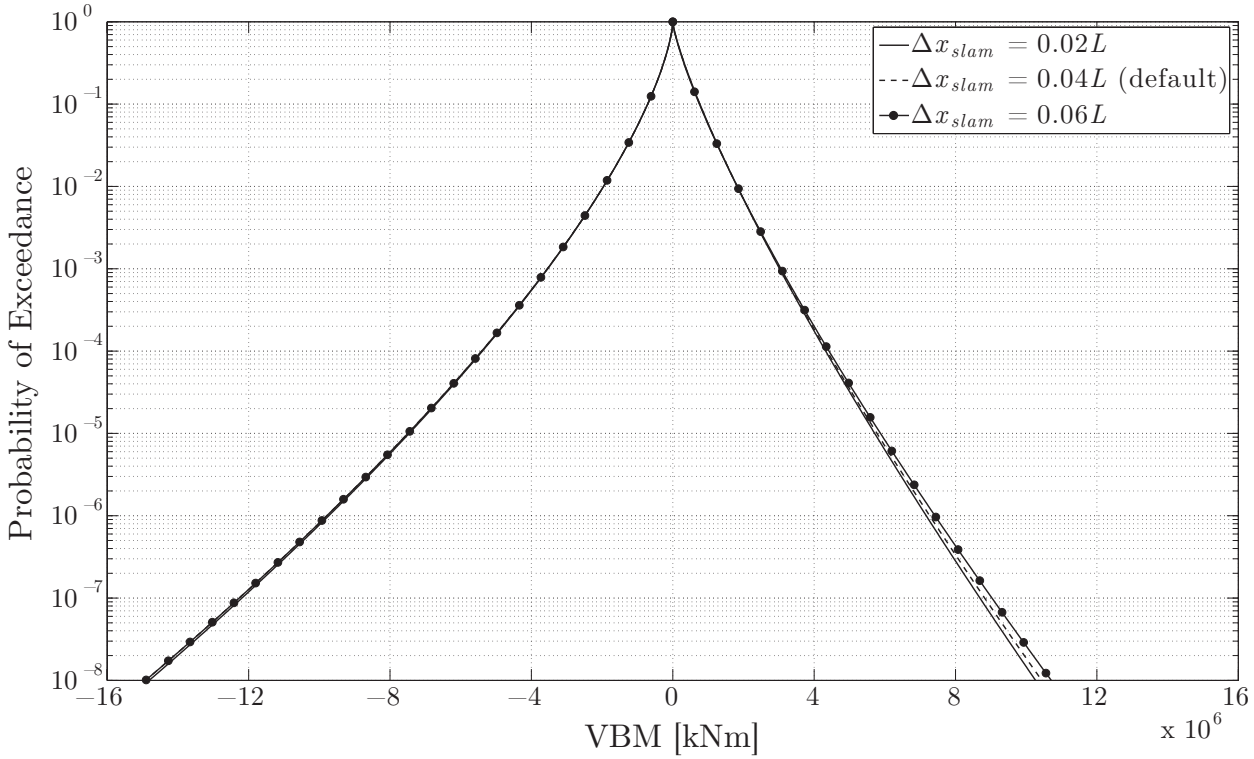

Figure 4.18: Weibull fits of the total VBM, $M_y^{(1)+(2)^{\pm}} + M_y^{whip}$, where M_y^{whip} is calculated using various slamming extents; C 319, NA, $\xi = 0.03$.

route. However, C 319 container ship is 35 meters longer than the container ship form [88]. Therefore, only stresses caused by VBM can be compared under the assumption that both vessels are designed to experience similar longitudinal bending stresses in the hull girder, i.e. vessels that have similar factors of safety against yielding of principal longitudinal members.

A short description of Jensen's method (see Jensen et al. [52]) is given in Section 4.1.3. It is a very efficient numerical procedure, based on the All Sea States Method, and capable of calculating long-term probabilities of exceedance of the total VBM including springing, nonlinear and whipping effects. It only requires knowledge of the basic ship particulars.

Okada et al. [88] measured the average vertical bending stress amplitude between hogging and sagging peaks. In order to account for this, Jensen et al. [52] proposed taking the average of the sagging peak and 80% of the hogging peak at each probability of exceedance level. This accounts for the correlation between sagging and hogging peaks for non-narrow-banded signals. This percentage is chosen based on the autocorrelation function of the bending moment. The aforementioned procedure is also used in this work to facilitate the comparison.

Values of the longitudinal extent of slamming and the damping ratio are selected based on ABS recommendations: $\Delta x_{slam} = 0.04L$ and $\xi = 0.03$, respectively. Deadrise angle, $\alpha_w = 50.25°$, local breadth at slamming section, $B_l = 6.3$ m, and local draft at slamming

section, $T = 14.5m$, are selected to match the bow geometry of C 319 container ship. Operational profile for the Jensen's method is derived from the operational profile used in the simulation method for the EA route. No weather routing is applied. Okada et al. have not measured wave heights higher than ten meters during their full-scale measurement campaign that lasted for three years. Similarly, in 50 voyage simulations on EA route, which is equivalent to 3.3 years of non-stop navigation, the largest simulated wave height is 10.1 m without any weather routing.

Figure 4.19 shows the comparison of the full scale measurements with the Jensen's simplified method and the simulation method. Simulation results agree very well with the full-scale measurements over the entire range of vertical bending stress amplitudes. The agreement is good even for large stress amplitudes which is very important from the ship design point of view. Jensen's simplified method also agrees quite well with the measurements at low stress amplitude levels. For larger amplitudes, the agreement is not as good, especially for the largest amplitudes where this method underestimates stress exceedance probabilities. However, Jensen's method does have an advantage over the simulation method in terms of computer efficiency. While approximately thirty minutes of CPU time is needed for the entire linear and nonlinear simulation analysis, only a couple of minutes are needed for Jensen's method.

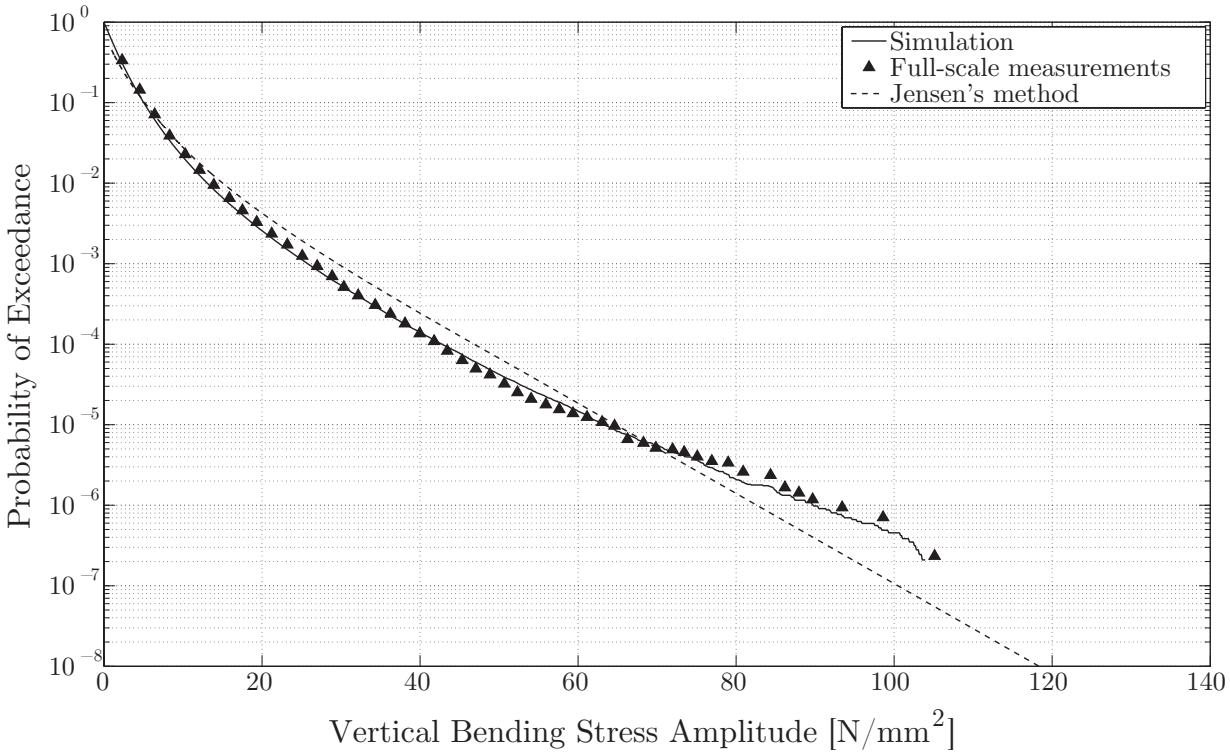

Figure 4.19: Comparison of simulation results with full-scale measurements and Jensen's method for container ship on EA route.

Jensen's method is intended to be used at the initial ship design stage when only the basic ship particulars are known and a large number of design alternatives have to be analyzed. The method can provide reasonable results, and as shown in [52], it can easily be calibrated to yield results very similar to the full scale measurements.

Simulation method provides a more rational and accurate framework for analyzing long-term properties of the VBM at the expense of CPU time. It can also be used to analyze various design alternatives, but only after their number has been reduced by Jensen's or similar methods and when more detailed information on vessel hull geometry, mass, and structural properties is know.

The importance of further validation of the simulation method with full-scale measurements, as they become available, must be emphasized again. Most valuable are the full-scale measurements in harsh sea environments, like the North Atlantic, where nonlinearities and whipping effects will be pronounced the most.

4.4.5 Long-Term Fatigue Analysis

The focus of this section is on demonstrating the use of the simulation method in long-term fatigue analysis and also on its further validation by comparison with full-scale measurements. A cumulative damage principle for variable cycle loading is used. This well know principle was first stated by Palmgren and Miner as follows: if the damage contributed by one cycle of stress range S_i is $1/N_f i$, where N_{fi} is the characteristic fatigue life under a constant amplitude stress range S_i, then, by superposition, the cumulative damage D caused by n stress ranges $S_1, S_2, \ldots, S_n$ applied $N_1, N_2, \ldots, N_n$ cycles is equal to

$$D = \sum_{i=1}^{n} \frac{N_i}{N_{fi}} \tag{4.38}$$

According to this definition, the structure is considered to have failed when the cumulative damage ratio D reaches one. Fatigue life for each stress range S_i is determined from the characteristic S–N curve for the structural detail considered. In order to directly compare the simulation method with the full-scale measurements from Okada et al. [88], the same structural detail in the deck of the C 319 container ship is considered. Okada et al. used U.K. Health and Safety Executive (HSE) [41] S–N D curve for transverse butt weld joint and the same curve is used in this work. HSE S–N curve is "characteristic" curve since it gives the characteristic fatigue life defined as the mean fatigue life minus the two standard deviations. HSE S–N curve also accounts for the Haibach effect [33] regarding the decreasing fatigue limit for low stress range random loading. The curve is given as $S^m N = K$, where S is the stress range, N is the number of cycles to failure, m is the inverse slope of the curve in a log–log plot, and K is the intercept of the curve on N axis. Constants m and K are equal to 3 and 1.519×10^{12} N/mm^2, respectively, for the high stress ranges (above 53.37 N/mm^2), and 5 and 4.239×10^{15} N/mm^2, respectively, for low stress ranges (below 53.37 N/mm^2).

HSE curves include the geometric stress concentration factor and the stress concentration factor associated with the weld detail. Although, HSE procedure for fatigue assessment does

not account for the effect of mean stress, in this work the mean stress effect is accounted for through the use of equivalent completely reversed stress amplitude, σ_{ar} which is calculated using the Goodman line modified by J. Morrow (see e.g. Dowling [22]) as follows

$$\sigma_{ar} = \frac{\sigma_a}{1 - \dfrac{\sigma_m}{2K^{1/m}}} \tag{4.39}$$

where σ_a is the stress amplitude, and σ_m is the mean stress. The effect of this correction, for the structural detail analyzed in this work, is found to be negligible due to low values of mean stresses found in the stress time series.

Fatigue damage of a certain structural detail can be calculated using the closed-form spectral-based fatigue analysis, see ABS [2]. This analysis is based on calculating the short-term fatigue damage in each sea state assuming narrow-banded Gaussian stress, and then finding the total long-term damage by linear summation of the weighted short-term damages in a manner similar to the All Sea States Method. Spectral-based methods require a correction factor, called the *Wirsching' rainflow correction factor*, to account for non-narrow-banded stress spectra. Fatigue damage can also be calculated in closed-form using fitted or estimated long-term distributions of stress amplitudes. This approach was used by Okada et al. [88] in their fatigue analysis of measured stresses, and by Jensen et. al [52] in their simplified method for long-term analysis of VBM loads on container ships. A difficulty arises in defining stress amplitudes in highly irregular stress signals.

Since the simulation method generates realistic long-term time series of vertical bending stress, a direct *rainflow cycle counting technique* (RFC) can be applied to determine the exact number of stress cycles with corresponding stress amplitudes σ_a and mean stresses σ_m. RFC is considered to be the most accurate cycle counting algorithm and it is widely used in fatigue analysis when irregular random loads are present. Figure 4.20 shows a rainflow cycle counting matrix for C 319 container ship on EA route containing the number of counted low-frequency linear bending stress cycles divided into σ_a and σ_m bins.

When calculating the fatigue damage, individual values of σ_a and σ_m, i.e., not the bin means, are used. Each stress cycle amplitude is first corrected for the effect of its corresponding mean value, according to Eqn. (4.39), and the cumulative fatigue damage is calculated using Eqn. (4.38) and S–N curve with $S = 2\sigma_{ar}$. In order to assess the effect that high-frequency and nonlinear VBM components have on the total fatigue damage in twenty years, a separate fatigue analysis is performed on vertical bending stress time series resulting from:

1. $M^{(1)}_{y,LF}$ = linear low-frequency (LLF) VBM;
2. $M^{(1)}_{y,LF+HF}$ = linear low- and high-frequency (LLHF) VBM;
3. $M^{(1)+(2)^{\pm}}_{y}$ = nonlinear (NL) VBM;

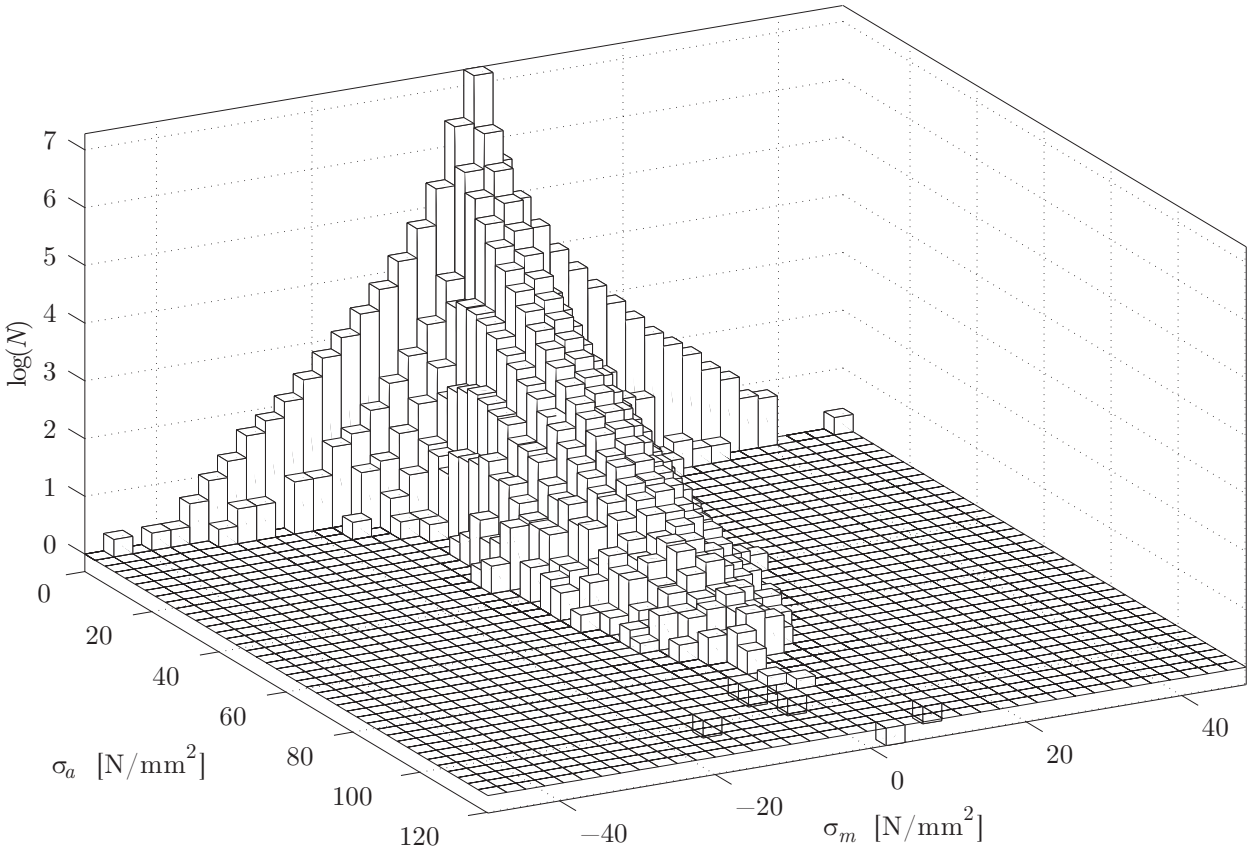

Figure 4.20: RFC matrix of low-frequency linear vertical bending stresses; C 319, EA, $\xi = 0.03$, $\Delta x_{slam} = 0.04L$.

4. $M_y^{(1)+(2)^{\pm}} + M_y^{whip}$ = nonlinear VBM with whipping (NLW).

Each subsequent VBM time series in the list above presents a more complete description of the total VBM. Table 4.1 contains fatigue damage and fatigue life calculated for the vessel on all three routes (NA, NP, EA) for stresses arising from VBMs in the aforementioned list. Numbers in brackets indicate the length of simulated time series used to calculate the fatigue damage. Simulated time series present a continuous signal of VBM data generated while the ship is navigating at sea. In order to correctly estimate the fatigue life, time spent in port, with very little dynamic loading, must be taken into account. Ship analyzed in [88] completes a full voyage between Japan and Europe (both legs) in two months, as stated by Okada et al. The total length of that voyage is $2 \times 11,286$ nautical miles for which the vessel needs 42.74 days, assuming an average speed of 22 knots. This means that the ship spends approximately 28% of time in various ports along its route. The same percentage is used in this work for C 319 container ship on all three routes to transform the time length of simulated series into the real ship time.

Table 4.1: Fatigue damage and fatigue life for a structural detail in the deck of C 319 container ship for all three routes; $\xi = 0.03$, $\Delta x_{slam} = 0.04L$.

	NA (7.79 yrs)			NP (4.99 yrs)			EA (4.59 yrs)		
VBM	D	% D_{NLW}	F. L. [yrs]	D	% D_{NLW}	F. L. [yrs]	D	% D_{NLW}	F. L. [yrs]
LLF	0.272	79	28.6	0.059	72	84.9	0.013	61	340.5
LLHF	0.300	87	26.0	0.069	85	72.5	0.018	79	260.5
NL	0.340	99	22.9	0.081	99	61.9	0.022	99	208.1
NLW	0.344	100	22.7	0.081	100	61.4	0.022	100	206.4

LLF = linear low-frequency VBM
LLHF = linear low- and high-frequency VBM
NL = nonlinear VBM
NLW = nonlinear VBM with whipping
F. L. = fatigue life

The largest fatigue damage, by far, is accumulated on the NA route, followed by the NP route and then EA route. Fatigue life on the NA route, when all the VBM components are considered, is just little over twenty years which is usually considered as the life time of a ship structure. No weather routing is applied on any of the routes. A total of seven sea states with significant wave height larger than 15 meters is sampled on NA route, while the largest sea states sampled on NP and EA routes are 10.1 and 13.4 meters, respectively. Vessel encounters many more moderate to severe sea states on the NA route than on the other two routes which results in much lower fatigue life.

Many researchers have reported on fatigue problems found on ships operating in the North Atlantic. Moe et al. [79] reported on the full scale measurement campaign conducted on board 220,000 dwt bulk carrier that experienced extensive fatigue damage. As a result, the section modulus of the vessel had to be increased by up to 47%.

Storhaug et al. [104] performed full-scale measurement on a midsize 2,800 TEU container ship operating in the North Atlantic. The vessel was selected for monitoring based on the presence of fatigue cracks after only eight years of operation.

Storhaug and Moe [102] conducted full-scale monitoring of a large 4,400 TEU container ship operating in the North Atlantic between Europe and Canada and concluded that the fatigue damage for a monitored winter season roundtrip was 4.8 times worse than the assumed design value. The authors also found that the fatigue damage accumulated during the most severe day corresponded to two months of average fatigue loading.

Storhaug and Heggelund [101] reported on the full-scale measurement campaign on the sister ship of the 2,800 TEU container ship monitored in Storhaug et al. [104]. The vessel was operated in the North Atlantic. The authors defined the "fatigue damage rate" as the ratio between the actually measured fatigue damage in a half hour period and the average half hour fatigue damage corresponding to a 20-year design life time. During the worst half hour

record the fatigue damage rate reached approximately 60. During the measurement period from August 2007 to May 2008 the average fatigue damage rate was 1.6. Storhaug and Heggelund also reported on measurements on board the 4,400 TEU container ship operated in the North Atlantic between November 2007 and May 2008. The average fatigue rate during this period was 2.2 and the accumulated fatigue damage for a side shell longitudinal stiffener was 0.35. However, since the vessel had already operated in the North Atlantic for five previous winter seasons without any observable cracks, the authors doubted the applied method for superposition of the global and local stresses.

Measured dynamic stresses caused by the VBM are usually decomposed into low-frequency (LF) and high-frequency (HF) components in the literature. HF components correspond to the two-node mode vibrations of the hull girder. When the measured signal is considered, there is no reliable way to separate linear from nonlinear contributions or to distinguish between different HF components such as linear springing, nonlinear springing, and whipping, as is the case with the simulation method. The contribution of the HF VBM components to the total fatigue damage can be obtained by subtracting the LF fatigue damage from the total fatigue damage ($D_{NLW} - D_{LLF}$).

The focus of the recent full-scale measurements was on the fatigue performance of the container ships, mainly in the North Atlantic. A few measurement campaigns have been conducted on the EA route. The study by Okada et al. [88], that was previously used for comparison of the full-scale measurements with the simulation results regarding the long-term exceedance probabilities of the VBM, also reported on the measured fatigue damage for the same 6,700 TEU post-Panamax vessel. The estimated fatigue life for the same structural detail in the deck as the one considered in this work was 190.5 years when all VBM frequencies are included. This value is only 7.7% lower than the fatigue life estimated using the simulation method (206.4 years). Okada et al. found that the HF contribution was 52% while the simulation results suggest that this contribution is 39% (100% - 61%, see Table 4.1). The difference probably occurs because of different definitions of the limiting frequency marking the onset of HF response. In this work, the discriminating frequency is 20% lower than the two-node mode frequency, while Okada et al. placed it 30% below the two-node mode frequency which extended their HF range compared to the HF range used in this work.

The contribution of the HF components to the total fatigue damage is largest for the EA route (39%) followed by the NP route (28%) and NA route (21%). It is evident that HF fatigue damage becomes less important in more severe sea states. This is explained using the fact that fatigue life decreases exponentially with the increase of stress amplitudes. Therefore, large stress amplitudes in extreme sea states will dominate the fatigue damage accumulation. Such extreme sea states are more likely to be encountered on the NA route than on the other two routes, and since there is comparatively less HF VBM in these sea states, HF contribution becomes less significant. This is also in accordance with observations and measurements taken on board ships in service. Mathiesen et al. [75] utilized the measurements on two ore carriers to conclude that the HF components of the VBM are more important in moderate than in high sea states. A similar conclusion was obtained by Aalberts and Nieuwenhuijs [1]

for a 130 meter long general cargo/container vessel operating in the North Atlantic and the Baltic Sea. Storhaug and Moe [102] reported that the HF part increased the fatigue damage by 23% for the 4,400 TEU container ship on NA route. This is very similar to the value of 21% obtained in this work for the same route, though for a longer and wider container ship. Storhaug and Heggelund [101] reported that the HF contribution to the fatigue damage for a 2,800 TEU and 4,400 TEU container ships on the NA route was 25% for both of them.

None of the authors cited in this section have reported on significant horizontal and torsional vibrations of the hull girder that would give rise to additional longitudinal HF stresses.

Linear springing accounts for 55% of the fatigue damage caused by all HF components on EA route, 45% on the NP route, and 39% on the NA route (see Table 4.1). The rest of the HF fatigue damage is caused by nonlinearities and whipping. The latter seems to cause very little fatigue damage in the case of C 319 container ship. Two-node mode vibrations caused by slamming are not significant source of fatigue damage compared to other HF components, regardless of the route. Some authors erroneously use the term whipping for all the HF VBM components. Moreover, the decaying two-node mode vibrations, that are found in the measured VBM time series, can sometimes be mistakenly treated as whipping. Decaying vibrations could be originating from linear or nonlinear springing for which the periodic wave excitation no longer exists. Since the total VBM response is very sensitive to the correlation between whipping and wave-induced VBMs, both in time and magnitude, whipping can have a significant effect on the extreme value of the VBM as well as on the fatigue behavior. Results of the simulation method, by no means, suggest that whipping should be ignored. More research is needed to properly assess the long-term effects of whipping on a wide range of ship types, sizes and routes.

Chapter 5

Conclusions, Recommendations for Future Work, and Possible Improvements

5.1 Conclusions

A novel simulation-based method for statistical analysis of hull girder sectional loads and their linear and nonlinear combinations has been presented in this work. The method provides a rational framework for simulating realistic, properly correlated, multi-voyage time series of ship responses using a comprehensive statistical model to simulate and sample a total of nine variables affecting ship responses: significant wave height, zero crossing wave period, prevailing wind and wave direction, ship's relative heading with respect to waves, ship's location, season of the year, ship's speed, voluntary and involuntary speed reductions in severe sea states, and the ship's loading condition.

Main advantages of the simulation approach over existing long-term methods are the following:

- It does not require the knowledge of the joint probability density function of all nine aforementioned variables affecting ship responses. Consequently, no simplifications or assumptions regarding these distributions are needed;
- It does not require a priori knowledge of the short term probability density functions of ship responses in each possible sea state–operational profile combination. Therefore, no assumptions are needed regarding the bandwidths of the responses or their probability distributions;
- It enables nonlinear load combinations (e.g., von Mises stress) of linear and nonlinear loads. Short-term probability density functions of combined loads are not needed;
- It establishes proper correlation between each linear load, between linear and nonlinear parts of each load, and between slamming events and other VBM components;

- Having multi-voyage time series of individual loads or of their combination enables the use of rainflow cycle counting method for fatigue life predictions;
- Weather routing can easily be applied without rescaling and reshaping the joint probability density functions of random variables describing sea states and operational profiles;
- Simulation method provides a more rational, more flexible, and more accurate framework for global hull girder load analysis than the most commonly used All Sea States Method.

Some limitations of the simulation method are:

- A simulation time of approximately half an hour on a workstation computer might be too long for analyzing a large number of design alternatives at the beginning of ship design process. Instead, the simulation method should be used after another more computationally efficient method has reduced the number of potential design alternatives;
- Hydrodynamic model used to calculate the impact loads on the ship is quite simple and does not account for the three-dimensional effects and the specific shape of the free surface. Also, the linear motion analysis might not be completely adequate for determining the slamming instants in very harsh sea states;
- Quadratic strip theory, which has been used in this work, is based on the second-order wave theory and might be too conservative in the extreme or phenomenal sea states with $H_S > 14$ m;
- Very long time series of loads are needed in order to achieve small confidence intervals of empirical cumulative distribution functions at very small exceedance probabilities.

Correlation structure of all six sectional loads has been examined for six ships on three different routes. Where possible, the correlation coefficient values have been compared with the ones found in the literature and the agreement has been found satisfactory, especially between the VBM and HBM.

Probabilities of exceedance of simulated linear vertical bending stress amplitudes for C 319 container ship on Euro-Asia route match closely the ones measured on board a similar container ship on Euro-Asia route. A very good agreement has also been found in the case of total vertical bending stress amplitudes which include nonlinear and hydroelastic effects. Two parameter Weibull distribution has been found to satisfactorily fit the simulated data in both linear and nonlinear cases.

Simulation method has been used to show how long-term linear and nonlinear combinations of sectional loads can be obtained by simple superposition of properly correlated load time series.

Nonlinearities in the VBM caused by the nonlinear waves, nonlinear hydrodynamic forces and geometric nonlinearities of the ship form have been taken into account in the simulation method through the use of sophisticated quadratic strip theory program SOST. This software also takes into account the hydroelastic springing response of the ship and uses Timoshenko dynamic beam model to obtain the response of the structure in the frequency domain.

Whipping has also been taken into account by coupling a simplified hydrodynamic model based on two-dimensional boundary element method and a structural model based on Timoshenko dynamic beam. The whipping response of the ship has been solved in space and time domain using a combination of the finite element and trapezoidal methods. This numerical approach has been validated using simple SDOF mass damper system. It has been shown that the two-node vibration mode dominates the whipping response. Decreasing the solution time step below $\Delta t = 0.005$ s to resolve higher modes of whipping response has been found unnecessary since they do not have an effect on the long-term VBM exceedance probabilities.

Fatigue analysis has been performed for the C 319 container ship trading on all three routes. Linear damage accumulation principle, stated by Palmgren and Miner, has been used in combination with the rainflow cycle counting method.

The following main conclusions can be made regarding nonlinear and hydroelastic VBM responses:

- Linear springing does not have a significant effect on the long-term exceedance probabilities of the VBM, but has a significant effect on the fatigue life of the structure;
- Nonlinearities, including the nonlinear springing, have a significant effect on the long-term VBM exceedance probabilities and on the fatigue life of the vessel;
- Largest nonlinear effects are observed in moderate sea states ($H_S \approx 7.4$ m, $T_0 \approx 6.9$ s) with very steep waves that are close to the wave breaking limit. Since the ratio of moderate to low sea states is largest on the North Atlantic route, nonlinearities will have the largest effect on this route;
- Nonlinearities increase the extreme sagging VBM at 10^{-8} probability level by 27% and decrease the hogging extreme VBM by 11% for C 319 container ship on the North Atlantic route. Lower discrepancies between sagging and hogging have been found on other routes;
- Damping ratio has a relatively significant effect on the nonlinear component of the VBM for C 319 container ship, but does not significantly affect the long-term exceedance probabilities of the total VBM, especially at high bending moment values. This is attributed to the fact that the maximum linear VBM occurs in highest sea states, while the second-order response reaches maximum in moderate sea states with steep waves. No general conclusions could be made regarding damping effects since preliminary results for C 283 container ship indicate that damping might have a more significant effect on the long-term VBM exceedance probabilities due to its large nonlinear springing response for small damping ratios.

- Superharmonic second-order terms are more important than the slowly varying subharmonic terms. However, subharmonic terms cannot be neglected;

- Second-order superharmonic terms have a significant effect on the VBM of full form ships such as tankers, especially when the vessel is in ballast condition;

- Neglecting super and subharmonic terms with the smallest amplitudes can drastically reduce the simulation time while retaining reasonable accuracy. For example, neglecting all super and subharmonics with amplitudes smaller than 25% of their largest amplitudes decreases the computation time by 5.8 times, while reducing the extreme VBM at 10^{-8} probability level by only 1.4%. In this case, the total simulation time for first- and second-order terms on a workstation computer with two Intel® Xeon® processors is approximately half an hour;

- Slamming occurs most frequently in head seas, and rarely in beam, oblique following or following seas. For C 319 container ship, slamming usually occurs when the underlying VBM (VBM without whipping) has a small positive value (small hogging).

- Whipping alone has a relatively small effect on the exceedance probabilities of the VBM for C 319 container ship. This effect is around 3% in both sagging and hogging for North Atlantic route. Also, the effect of whipping on the fatigue life is relatively small, around 1% regardless of the route. This can be attributed to the lack of strong positive correlation in time between whipping peaks and the peaks of the underlying VBM for this particular ship;

- Contribution of the high-frequency (HF) stresses to the total fatigue life is very significant. Significance of the HF stresses is largest on the Euro-Asia route (39%) followed by the North Pacific route (28%) and the North Atlantic route (21%). These percentages are in accordance with the full-scale measurements and can be explained using the fact that fatigue life decreases exponentially with the increase of stress amplitudes. Therefore, large stress amplitudes in extreme sea states will dominate the fatigue damage accumulation. Such extreme sea states are more likely to be encountered on the North Atlantic route than on the other two routes, and since there is comparatively less HF VBM in these sea states, HF contribution becomes less significant;

- Predicted fatigue life of a typical butt weld joint in the deck of C 319 container ship on Euro-Asia route based on simulated stresses is in a very good agreement with the predicted fatigue life of the same structural element based on full-scale measurement of stresses on a similar post-Panamax container ship also trading between Europe and Asia. The difference in predicted fatigue life is 7.7%.

5.2 Recommendations for Future Work and Improvements

In order to achieve greater confidence in the simulation results and to get a better understanding of various factors affecting ship design, future work should be focused on:

- Developing a more sophisticated hydrodynamic model for slamming that will be just as efficient as the one used in this work, but will have correction factors to account for the three-dimensional effects and local shape of the free surface. The model should also include correction factors for different heading angles and short-crested seas;
- Prediction of slamming instants should be improved by accounting for the nonlinear short-crested waves and nonlinear ship motions;
- Phase relation between whipping and wave-induced VBM peaks should be further investigated for various ship types, sizes, and routes;
- Stern slamming model should be added for ships with large overhanging stern and relatively low forward speed;
- Bottom slamming model should be added for ships with large flat bottom forward;
- The effect of damping ratio on the long-term VBM exceedance probabilities should be investigated in more detail, as preliminary results on C 283 container ship show that it can be more significant than in the case of C 319 container ship;
- Damping ratio might also have a significant effect on the fatigue damage and more investigation is needed in that respect;
- A more sophisticated model for weather routing should be developed that takes into account route modifications based on predicted sea states;
- Wave energy spreading (short-crested waves) should also be accounted for in the calculation of second-order VBM;
- Subharmonics should also be added to the total second-order VBM of the T 306 tanker in order to obtain a more complete picture about the nonlinearities in the VBM for such full form ships;
- The accuracy of the quadratic strip theory should be investigated in cases when the ship is in ballast with shallow draft since the bottom of the ship could emerge from water in rough seas. This effect cannot be captured with the quadratic strip theory;

- Simulation method seems well suited for reliability analysis since the estimate of the joint probability density function of the combined load effect can be obtained directly from the corresponding time series. If the probability density function of the structure's capacity is known, and is independent of the loads, then the joint probability density function of all the random variables involved in the limit state function of a certain structural member can be obtained. This joint probability density function can then be numerically integrated over the part of the domain where the limit state function is less then zero to yield the probability of failure;

- More comparisons with the full-scale measurements should be performed as they become available;

- Finally, a simplified procedure for long-term load combination analysis, that is based on the simulation method presented herein, might be obtained for use in the preliminary ship design stages.

Bibliography

[1] P. J. Aalberts and M. W. Nieuwenhuijs. “Full Scale Wave and Whipping Induced Hull Girder Loads”. In: *4th. International Conference on Hydroelasticity in Marine Technology*. Wuxi, China, 2006.

[2] ABS. *Guidance Notes On Spectral-Based Fatigue Analysis for Vessels*. Houston, TX: American Bureau of Shipping, Feb. 2012.

[3] ABS. *Guidance Notes on Springing Assessment for Container Carriers*. Houston, TX: American Bureau of Shipping, Dec. 2010.

[4] ABS. *Guidance Notes on Whipping Assessment for Container Carriers*. Houston, TX: American Bureau of Shipping, Dec. 2010.

[5] ABS. *Guide for "SafeHull-Dynamic Loading Approach" for Vessels*. Houston, TX: American Bureau of Shipping, Dec. 2006.

[6] ABS. *Rules for Building and Classing Steel Vessels*. Houston, TX: American Bureau of Shipping, 2012.

[7] K. S. Andrews, N. M. C. Dacunha, and N. Hogben. *Wave Climate Synthesis*. Tech. rep. R149. London, UK: NMI Ltd., Jan. 1983.

[8] M. Arai and K. Matsunaga. “A Numerical Study of Water Entry of Two-Dimensional Ship-Shaped Bodies”. In: *Proceedings of the 4th International Symposium on Practical Design of Ships and Mobile Units*. Varna, Bulgaria: Bulgarian Ship Hydrodynamics Centre, Oct. 1989.

[9] G. S. Baarholm and J. J. Jensen. “Influence of Whipping on Long-Term Vertical Bending Moment”. In: *Journal of Ship Research* 48.4 (2004), pp. 261–272.

[10] G. S. Baarholm and T. Moan. “Application of Contour Line Method to Estimate Extreme Ship Hull Loads Considering Operational Restrictions”. In: *Journal of Ship Research* 45.3 (Sept. 2001), pp. 228–240.

[11] G. S. Baarholm and T. Moan. “Efficient Estimation of Extreme Long-Term Stresses by Considering a Combination of Longitudinal Bending Stresses”. In: *Journal of Marine Science and Technology* 6.3 (2002), pp. 122–134.

[12] G. S. Baarholm and T. Moan. “Estimation of Nonlinear Long-Term Extremes of Hull Girder Loads in Ships”. In: *Marine Structures* 13.6 (2000), pp. 495–516.

[13] T. T. Baber and Y. K. Wen. "Random Vibration of Hysteretic Degrading Systems". In: *Journal of the Engineering Mechanics Division* 107.6 (Dec. 1981), pp. 1069–1087.

[14] R. S. Beck et al. *Motion in Waves*. Ed. by J. R. Paulling. The Principles of Naval Architecture Series. Jersey City, NJ: Society of Naval Architects and Marine Engineers, 2009.

[15] R. E. D. Bishop and W. G. Price. *Hydroelasticity of Ships*. Cambridge, UK: Cambridge Univ Press, 1979.

[16] BMT. *Global Wave Statistics Online*. 2012. URL: `www . globalwavestatisticsonline.com`.

[17] D. R. Brillinger. *Time Series: Data Analysis and Theory*. Vol. 36. Classics in Applied Mathematics. Philadelphia, PA: Society for Industrial and Applied Mathematics, 2001.

[18] N. M. C. Dacunha, N. Hogben, and K. S. Andrews. "Wave Climate Synthesis World-Wide". In: *Proceedings of the International Symposium on Wave and Wind Climate World-Wide*. RINA. London, UK, Apr. 1984.

[19] A. C. Davison. *Statistical Models*. Cambridge Series in Statistical and Probabilistic Mathematics. Cambridge, UK: Cambridge University Press, 2003.

[20] A. C. Davison and R. L. Smith. "Models for Exceedances Over High Thresholds". In: *Journal of the Royal Statistical Society. Series B* (1990), pp. 393–442.

[21] DNV. *Fatigue Assessment of Ship Structures*. Tech. rep. Classification Notes No. 30.7. Høvik, Norway: Det Norske Veritas, June 2010.

[22] N. E. Dowling. *Mechanical Behavior of Materials: Engineering Methods for Deformation, Fracture, and Fatigue*. 3rd ed. Upper Saddle River, NJ: Pearson Prentice Hall, 2007.

[23] R. A. Fain and E. T. Booth. *Results of The First Five "Data Years" of Extreme Stress Scratch Gauge Data Collected Aboard Sea-Land's SL-7's*. Tech. rep. SSC-286. Washington, DC: Ship Structure Committee, Mar. 1979.

[24] G. Ferro and A. E. Mansour. "Probabilistic Analysis of the Combined Slamming and Wave-Induced Responses". In: *Journal of Ship Research* 29.3 (Sept. 1985), pp. 170–188.

[25] P. A. Frieze et al. "Report of ISSC Committee V. 1. Applied Design". In: *Proceedings of the 11th International Ship and Offshore Structures Congress (ISSC)*. Wuxi, China, 1991.

[26] J. Fukuda. "Long-Term Predictions of Wave Bending Moment". In: *Journal of the Society of Naval Architects of Japan, Selected Papers* 5 (1968), pp. 33–55.

[27] J. Fukuda. "Statistical Prediction of Ship Response". In: *The 1st Symposium of Seakeeping, The Society of Naval Architect of Japan*. 1969, pp. 99–120.

[28] T. Funaki et al. "A Note on the Correlation Coefficient Between Wave-Induced Stress (in Japanese)". In: *Journal of the Society of Naval Architects of Japan* 180 (Dec. 1996), pp. 575–589.

[29] GL. *Rules for Classification and Construction*. Hamburg, Germany: Germanischer Lloyd SE, 2011.

[30] C. Guedes Soares. "On the Uncertainty in Long-Term Predictions of Wave Induced Loads on Ships". In: *Marine Structures* 12.3 (1999), pp. 171–182.

[31] C. Guedes Soares and T. Moan. "Uncertainty Analysis and Code Calibration of the Primary Load Effects in Ship Structures". In: *Proceedings of the 4th International Conference on Structural Safety and Reliability*. Vol. 3. Kobe, Japan, 1985, pp. 501–512.

[32] C. Guedes Soares and T. E. Schellin. "Nonlinear Effects on Long-Term Distributions of Wave-Induced Loads for Tankers". In: *Journal of Offshore Mechanics and Arctic Engineering* 120.2 (May 1998), pp. 65–70.

[33] E. Haibach. *Modified Linear Damage Accumulation Hypothesis Considering the Decline of the Fatigue Limit Due to Progressive Damage*. Tech. rep. 50. Darmstadt, Germany: Laboratorium für Betriebsfestigkeit, 1970.

[34] P. F. Hansen. "On Combination of Slamming- and Wave-Induced Responses". In: *Journal of Ship Research* 38.2 (1994), pp. 104–114.

[35] S. E. Heggelund, G. Storhaug, and B. K. Choi. "Full Scale Measurements of Fatigue and Extreme Loading Including Whipping on an 8600TEU Post Panamax Container Vessel in the Asia to Europe Trade". In: *Proceedings of the ASME 2011 30th International Conference on Ocean, Offshore and Arctic Engineering*. ASME. Rotterdam, The Netherlands, June 2011.

[36] P. G. Hoel, S. C. Port, and C. J. Stone. *Introduction to Probability Theory*. The Houghton Mifflin Series in Statistics. Boston, MA: Houghton Mifflin Boston, 1971. Chap. 8, p. 212.

[37] D. Hoffman and E. V. Lewis. *Analysis and Interpretation of Full-Scale Data on Midship Bending Stresses of Dry Cargo Ships*. Tech. rep. SSC-169. Washington, DC: Ship Structure Committee, June 1969.

[38] N. Hogben and N. M. C. Dacunha. "Wave Climate Synthesis: Some Recent Advances". In: *Proceedings of the Offshore Technology Conference*. Paper No. OTC 4938. OTC. Houston, TX, May 1985.

[39] N. Hogben, N. M. C. Dacunha, and K. S. Andrews. "Assessment of a New Global Capability for Wave Climate Synthesis". In: *Proceedings of OCEANS '83, San Francisco*. IEEE. New York, NY, 1983.

[40] L. Hovem. *Loads and Load Combinations for Fatigue Calculations-Background for the Wave Load Section for the DNVC Classification Note: Fatigue Assessment of Ships*. Tech. rep. No. 93-0314. Høvik, Norway: DNVC Report, 1993.

[41] HSE. *Offshore Technology Report*. Tech. rep. OTO/2001/015. U.K. Health & Safety Executive, 2001.

[42] O. F. Hughes and J. K. Paik. *Ship Structural Analysis and Design*. Jersey City, NJ: The Society of Naval Architects and Marine Engineers, 2010.

[43] IACS. *Common Structural Rules for Bulk Carriers*. London, UK: International Association of Classification Societies, Ltd., July 2012.

[44] IACS. *Common Structural Rules for Double Hull Oil Tankers*. London, UK: International Association of Classification Societies, Ltd., July 2012.

[45] Y. Ikeda, Y. Himeno, and N. Tanaka. *A Prediction Method for Ship Rolling*. Tech. rep. 00405. Osaka, Japan: Department of Naval Architecture, University of Osaka Prefecture, 1978.

[46] ISSC. "Report of Committees 3 and 10". In: *Proceedings of the Fifth International Ship Structures Congress*. Hamburg, Germany, 1973.

[47] ISSC. "Report of Special Task Committee VI.1: Extreme Hull Girder Loads". In: *Proceedings of the 14th International Ship and Offshore Structures Congress*. Nagasaki, Japan, 2000, pp. 263–320.

[48] J. J. Jensen. *Load and Global Response of Ships*. Vol. 4. Elsevier Ocean Engineering Book Series. Kidlington, UK: Elsevier Science, 2001.

[49] J. J. Jensen, L. Banke, and M. Dogliani. "Long-Term Predictions of Wave-Induced Loads Using a Quadratic Strip Theory". In: *Proceedings of the International Conference on Ship and Marine Research*. Vol. 1. Rome, Italy, 1994, pp. 1–14.

[50] J. J. Jensen and A. E. Mansour. "Estimation of Ship Long-Term Wave-Induced Bending Moment Using Closed-Form Expressions". In: *Transactions of the Royal Institution of Naval Architects, Part A* (2002), pp. 41–55.

[51] J. J. Jensen and P. T. Pedersen. "Wave-Induced Bending Moments in Ships-a Quadratic Theory". In: *Transactions of RINA* 121 (1979), pp. 151–165.

[52] J. J. Jensen et al. "Wave Induced Extreme Hull Girder Loads on Containerships". In: *Proceedings of SNAME Annual Meeting*. Houston, TX, Oct. 2008, pp. 128–152.

[53] J. M. J. Journee and L. J. M. Adegeest. *Theoretical Manual of Strip Theory Program SEAWAY for Windows*. Tech. rep. 1370. Delft University of Technology, Sept. 2003.

[54] T. von Karman. *The Impact on Seaplane Floats During Landing*. Tech. rep. TN-321. Washington, DC: National Advisory Committee for Aeronautics, 1929.

[55] H. Kawabe and K. Shibazaki. "Combination of the Fatigue Damage Produced by Several Wave-Induced Loads Based on the Correlation Coefficient Method". In: *Proceedings of the 8th International Symposium on Practical Design of Ships and Other Floating Structures*. Ed. by Y. S. et al. Wu. Vol. 2. Shanghai, China: Elsevier, Sept. 2001, pp. 1089–1095.

[56] H. Kikuiri and J. Mathisen. *Some Correlation Coefficients for Wave Induced Loads in Series 60 Ships*. Tech. rep. 73-2-S. Det Norske Veritas Research Department, 1973.

[57] C. H. Kim. *Nonlinear Waves and Offshore Structures*. Vol. 27. Advanced Series on Ocean Engineering. World Scientific, 2008.

[58] J. B. Koo et al. "Fatigue Damage Assessment Based on Full Scale Measurement Data for a Large Container Carrier". In: *Proceedings of the Twenty-first (2011) International Offshore and Polar Engineering Conference*. ISOPE. Maui, Hawaii, USA, June 2011.

[59] S. J. Lee et al. "Analysis of Full-Scale Hull Girder Loads of a Container Carrier and Its Simulation Using a Nonlinear Seakeeping Program". In: *Proceedings of the ASME 2010 29th International Conference on Ocean, Offshore and Arctic Engineering*. ASME. Shanghai, China, June 2010.

[60] R. J. LeVeque. *Finite Difference Methods for Ordinary and Partial Differential Equations*. Philadelphia, PA: Society for Industrial and Applied Mathematics Philadelphia, 2007.

[61] E. V. Lewis. "Predicting Long-Term Distributions of Wave-Induced Bending Moment on Ship Hulls". In: *Proceedings of the Spring Meeting, SNAME*. 1967.

[62] E. V. Lewis and R. B. Zubaly. *Dynamic Loadings Due to Waves and Ship Motions*. Tech. rep. STAR Symposium, SNAME, 1975.

[63] Z. Li and J. W. Ringsberg. "Fatigue Routing of Container Ships–Assessment of Contributions to Fatigue Damage from Wave-Induced Torsion and Horizontal and Vertical Bending". In: *Ships and Offshore Structures* 7.2 (2012), pp. 119–131.

[64] Z. Li, J. W. Ringsberg, and W. Mao. "Fatigue Damage Assessment of Container Ships Concerning Wave-Induced Torsion". In: *Proceedings of the ASME 2010 29th International Conference on Ocean, Offshore and Arctic Engineering*. ASME. Shanghai, China, June 2010.

[65] W. M. Lin and D. Yue. "Numerical Solutions for Large-Amplitude Ship Motions in the Time Domain". In: *Proceedings of 18th Symposium on Naval Hydrodynamics*. Washington, DC: National Academic Press, 1991, pp. 41–46.

[66] R. S. Little, E. V. Lewis, and F. C. Bailey. "A Statistical Study of Wave-Induced Bending Moments on Large Oceangoing Tankers and Bulk Carriers". In: *Transactions of SNAME* 79 (1971), pp. 117–168.

[67] P. L. Liu and A. Der Kiureghian. "Multivariate Distribution Models With Prescribed Marginals and Covariances". In: *Probabilistic Engineering Mechanics* 1.2 (1986), pp. 105–112.

[68] H. Madsen. *Time Series Analysis*. Texts in Statistical Science Series. Boca Raton, FL: Chapman & Hall/CRC, 2008. Chap. 4, p. 80.

[69] A. E. Mansour. *An Introduction to Structural Reliability Theory*. Tech. rep. SSC-351. Washington, DC: Ship Structure Committee, Jan. 1989.

[70] A. E. Mansour. "Extreme Loads and Load Combinations". In: *Journal of Ship Research* 39.1 (Mar. 1995), pp. 53–61.

[71] A. E. Mansour and J. M. d'Oliveira. "Hull Bending Moment Due to Ship Bottom Slamming in Regular Waves". In: *Journal of Ship Research* 19.2 (June 1975), pp. 80–92.

[72] A. E. Mansour and D. Liu. *Strength of Ships and Ocean Structures*. Ed. by J. R. Paulling. The Principles of Naval Architecture Series. Jersey City, NJ: Society of Naval Architects and Marine Engineers, 2008.

[73] A. E. Mansour and J. Lozow. "Stochastic Theory of the Slamming Response of Marine Vehicles in Random Seas". In: *Journal of Ship Research* 26.4 (Dec. 1982), pp. 276–285.

[74] W. Mao et al. "Assessment of Full-Scale Measurements with Regard to Extreme Hogging and Sagging Condition of Container Ships". In: *Proceedings of the ASME 2011 30th International Conference on Ocean, Offshore and Arctic Engineering*. Rotterdam, The Netherlands, June 2011.

[75] J. Mathiesen et al. "Hull Girder Vibration Effects in Bending Stresses Measured under Harsh, Stationary Conditions". In: *Proceedings of the International Symposium on Ship Design and Construction*. Shanghai, China, 2007, pp. 171–185.

[76] MATLAB. *version 2010a*. Natick, MA: The MathWorks Inc., 2010.

[77] R. K. Mattu. *Methodology for Combining Dynamic Responses*. Vol. 88. 10–484. Division of Safety Technology, Office of Nuclear Reactor Regulation, US Nuclear Regulatory Commission, 1980.

[78] O. el Moctar, T. E. Schellin, and T. Priebe. "CFD and FE Methods to Predict Wave Loads and Ship Structural Response". In: *Proceedings of the 26th Symposium on Naval Hydrodynamics, Rome, Italy*. Washington, DC: National Academic Press, 2006.

[79] E. Moe, G. Holtsmark, and G. Storhaug. "Full Scale Measurements of The Wave Induced Hull Girder Vibrations of an Ore Carrier Trading in the North Atlantic". In: *Proceedings of the International Conference on Design and Operation of Bulk Carriers*. RINA. London, UK, 2005, pp. 57–85.

[80] S. Naito et al. "Long-Term Prediction Method Based on Ship Operation Criteria". In: *International Shipbuilding Progress* 53.3 (2006), pp. 229–252.

[81] D. E. Nakos, D. Kring, and P. D. Sclavounos. "Rankine Panel Methods for Transient Free-Surface Flows". In: *Proceedings of 6th International Conference on Numerical Ship Hydrodynamics*. Iowa City, IA, 1993, pp. 613–634.

[82] Netpas. *Netpas Distance Software*. 2009. URL: `www.netpas.net`.

[83] N. Nordenström. *A Method to Predict Long-Term Distributions of Waves and Wave-Induced Motions and Loads on Ships and Other Floating Structures*. Tech. rep. 81. Det Norske Veritas, 1973.

[84] M. K. Ochi. *Ocean Waves: The Stochastic Approach*. Vol. 6. Cambridge Ocean Technology Series. Cambridge, UK: Cambridge University Press, 1998. Chap. 5, p. 132.

[85] M. K. Ochi. "Prediction of Occurrence and Severity of Ship Slamming at Sea". In: *Proceedings of the 5th Symposium on Naval Hydrodynamics, Bergen, Norway*. Washington, DC: Office of Naval Research, 1964.

[86] M. K. Ochi and L. E. Motter. "Prediction of Slamming Characteristics and Hull Responses for Ship Design". In: *Transactions of SNAME* 81 (1973), pp. 144–176.

[87] M. K. Ochi and C. H. Tsai. "Prediction of Occurrence of Breaking Waves in Deep Water". In: *Journal of Physical Oceanography* 13.11 (1983), pp. 2008–2019.

[88] T. Okada, Y. Takeda, and T. Maeda. "On Board Measurement of Stresses and Deflections of a Post-Panamax Containership and its Feedback to Rational Design". In: *Marine Structures* 19.2 (2006), pp. 141–172.

[89] O. D. Økland. "Numerical and Experimental Investigation of Whipping in Twin Hull Vessels Exposed to Serve Wet Deck Slamming". PhD thesis. Trondheim, Norway: Norwegian University of Science and Technology, Aug. 2002.

[90] M. Petričić and A.E. Mansour. "Long-Term Correlation Structure of Wave Loads Using Simulation". In: *Marine Structures* 24.2 (June 2011), pp. 97–116.

[91] T. E. Schellin and O. el Moctar. "Numerical Prediction of Impact-Related Wave Loads on Ships". In: *Journal of Offshore Mechanics and Arctic Engineering* 129 (2007), pp. 39–47.

[92] M. Schetzen. *The Volterra and Wiener Theories of Nonlinear Systems*. John Wiley & Sons, 1980.

[93] P. D. Sclavounos. "Computation of Wave Ship Interactions". In: *Advances in Marine Hydrodynamics* 5 (1996), pp. 233–278.

[94] P. D. Sclavounos, D. E. Nakos, and Y. Huang. "Seakeeping and Wave Induced Loads on Ships with Flare by a Rankine Panel Method". In: *Proceedings of 6th International Conference on Numerical Ship Hydrodynamics*. Iowa City, IA, 1993, pp. 57–78.

[95] I. Senjanović. *Vibracije Broda: II dio (in Croatian)*. II izdanje. Zagreb, Hrvatska: Sveučilište u Zagrebu, Fakultet Strojarstva i Brodogradnje, 1980.

[96] I. Senjanović, S. Tomašević, and R. Grubišić. "Coupled Horizontal and Torsional Vibrations of Container Ships". In: *Brodogradnja* 58.4 (2007), pp. 365–379.

[97] M. Shama. *Torsion and Shear Stresses in Ships*. Springer Verlag, 2010.

[98] Y. S. Shin, B. Kim, and A. J. Fyfe. "Stress Combination for Fatigue Analysis of Ship Structures". In: *Journal of Offshore Mechanics and Arctic Engineering* 127 (May 2005), pp. 175–181.

[99] R. H. Shumway and D. S. Stoffer. *Time Series Analysis and Its Applications*. 2nd ed. Springer Texts in Statistics. New York, NY: Springer, 2006. Chap. Appendix C, pp. 534–554.

[100] Ju. A. Šimanskij. "Dinamičeskij Rasčet Sudoyh Konstrukcij". In: *Sudpromgiz*. Leningrad, 1963.

[101] G. Storhaug and S. E. Heggelund. "Measurements of Wave Induced Vibrations and Fatigue Loading Onboard Two Container Vessels Operating in Harsh Wave Environment". In: *Proceedings of the International Conference on Design and Operation of Container Ships*. London, UK, 2008, pp. 81–100.

[102] G. Storhaug and E. Moe. "Measurements of Wave Induced Vibrations Onboard a Large Container Vessel Operating in Harsh Environment". In: *Proceedings of the 10th International Symposium on Practical Design of Ships and Other Floating Structures*. Houston, TX, 2007, pp. 419–427.

[103] G. Storhaug, E. Moe, and G. Holtsmark. "Measurements of Wave Induced Hull Girder Vibrations of an Ore Carrier in Different Trades". In: *Proceedings of the 25th International Conference on Offshore Mechanics and Arctic Engineering*. Hamburg, Germany, 2006.

[104] G. Storhaug, E. Moe, and T. A. Piedras Lopes. "Whipping Measurements Onboard a Midsize Container Vessel Operating in the North Atlantic". In: *Proceedings of the International Symposium on Ship Design and Construction*. Shanghai, China, 2007, pp. 55–70.

[105] G. Storhaug et al. "Springing/Whipping Response of a Large Ocean Going Vessel-A Comparison Between Numerical Simulations and Full-Scale Measurements". In: *Proceedings of 3rd International Conference on Hydroelasticity in Marine Technology*. Ed. by R. E. Taylor. Oxford, UK, 2003, pp. 117–131.

[106] L. J. Tick. "Certain Probabilities Associated with Bow Submergence and Ship Slamming in Irregular Seas". In: *Journal of Ship Research* 2.1 (1958), pp. 30–36.

[107] C. J. Turkstra. "Theory of Structural Safety". In: *SM Study* 2 (1970).

[108] T. C. Ude and S. R. Winterstein. *IFORM: An Inverse-FORM Routine to Estimate Response Levels With Specified Return Periods*. Tech. rep. TN-3. Paolo Alto, CA: Stanford University, Department of Civil Engineering, June 1996.

[109] J. Vidić-Perunović. "Towards the Prediction of Hull Springing Response". In: *Proceedings of the ASME 2010 29th International Conference on Ocean, Offshore and Arctic Engineering*. ASME. Shanghai, China, June 2010.

[110] H. Wagner. *Landing of Sea Planes*. Tech. rep. TN-622. Washington, DC: National Advisory Committee for Aeronautics, May 1931.

[111] X. Wang and T. Moan. "Stochastic and Deterministic Combinations of Still Water and Wave Bending Moments in Ships". In: *Marine Structures* 9.8 (1996), pp. 787–810.

[112] I. Watanabe. "Analytical Expression of Hydrodynamic Impact Pressure by Matched Asymptotic Expansion Technique". In: *Transactions of the West-Japan Society Of Naval Architects* 71 (Mar. 1986), pp. 77–85.

[113] Y. K. Wen. "Clustering Model for Correlated Load Processes". In: *Journal of the Structural Division* 107.5 (May 1981), pp. 965–983.

[114] Y. K. Wen. "Statistical Combination of Extreme Loads". In: *Journal of the Structural Division* 103.5 (May 1977), pp. 1079–1093.

[115] Y. K. Wen and H. T. Pearce. "Combined Dynamic Effects of Correlated Load Processes". In: *Nuclear Engineering and Design* 75.2 (1983), pp. 179–189.

[116] Y. K. Wen and H. T. Pearce. *Stochastic Models for Dependent Load Processes*. Tech. rep. 489, UILUENG-81-2002. Urbana, IL: Civil Engineering Studies, Univeristy of Illinois, Mar. 1981.

[117] S. R. Winterstein, T. C. Ude, and G. Kleiven. "Springing and Slow-Drift Responses: Predicted Extremes and Fatigue vs. Simulation". In: *Proceedings of BOSS-94*. Vol. 3. Cambridge, UK, July 1994.

[118] Y. Yamamoto, M. Fujino, and T. Fukasawa. "Motion and Longitudinal Strength of a Ship in Head Sea and the Effects of Nonlinearities". In: *Naval Architecture and Ocean Engineering* 18 (1980), pp. 91–100.

[119] R. Zhao and O. Faltinsen. "Water Entry of Two-Dimensional Bodies". In: *Journal of Fluid Mechanics* 246.1 (1993), pp. 593–612.

[120] R. Zhao, O. Faltinsen, and J. Aarsnes. "Water Entry of Arbitrary Two-Dimensional Sections With and Without Flow Separation". In: *Proceedings of the 21st Symposium on Naval Hydrodynamics, Trondheim, Norway*. Washington, DC: National Academic Press, 1996, pp. 408–423.

[121] T. I. Zohdi. *Reading Materials for: ME 280A - Finite Element Methods*. Copy Central. Berkeley, 2007.

Appendix A

A.1 A Short Proof of the Stationarity of R

The estimate of the correlation coefficient between loads X_1 and X_2, calculated from two voyages long time series, is given as

$$\begin{aligned} R_{2voy} &= \frac{\sum_{i=1}^{2n}\left(x_{1,i}-\bar{x}_1\right)\left(x_{2,i}-\bar{x}_2\right)}{\left[\sum_{j=1}^{2n}\left(x_{1,j}-\bar{x}_1\right)^2\sum_{k=1}^{2n}\left(x_{2,k}-\bar{x}_2\right)^2\right]^{1/2}} \\ &= \left[\frac{1}{n}\sum_{i=1}^{n}\left(x_{1,i}x_{2,i}-\bar{x}_1\bar{x}_2\right)+\frac{1}{n}\sum_{i=n+1}^{2n}\left(x_{1,i}x_{2,i}-\bar{x}_1\bar{x}_2\right)\right]\div \\ &\left\{\frac{1}{n}\left[\sum_{j=1}^{n}\left(x_{1,j}-\bar{x}_1\right)^2+\sum_{j=n+1}^{2n}\left(x_{1,j}-\bar{x}_1\right)^2\right]\right. \\ &\left.\cdot\,\frac{1}{n}\left[\sum_{k=1}^{n}\left(x_{2,k}-\bar{x}_2\right)^2+\sum_{k=n+1}^{2n}\left(x_{2,k}-\bar{x}_2\right)^2\right]\right\}^{1/2} \end{aligned} \tag{A.1}$$

where n is the number of load values in one voyage. It is assumed that each simulated voyage time series contains all known randomness including the seasonality effects. If the randomization of both portions ($i = 1, 2, \ldots, n$ and $i = n+1, n+2, \ldots, 2n$) of the time series for each load is performed (preserving the value of R as explained in Chapter 2), then the load values from both voyages can be taught of as realizations of $2n$ independent and identically distributed random variables $X_{1,1}, X_{1,2}, \ldots, X_{1,2n}$ and $X_{2,1}, X_{2,2}, \ldots, X_{2,2n}$. Also, changing $2n$ to n, $3n$, $4n, \ldots$ will not alter these distributions. Therefore, the weak low of large numbers (WLLN) can be applied to each term of Eqn. (A.1). WLLN, together with Slutsky's lemma and the convergence in probability ($\xrightarrow{\mathrm{P}}$) and convergence in distribution ($\xrightarrow{\mathrm{D}}$) rules yield, as $n \to \infty$

$$\bar{x}_1 \xrightarrow{\mathrm{P}} \mathbb{E}\left[X_1\right] \Rightarrow \bar{x}_1 \xrightarrow{\mathrm{D}} \mathbb{E}\left[X_1\right] = \mu_{X_1} \tag{A.2}$$

$$\bar{x}_2 \xrightarrow{\text{P}} \mathbb{E}[X_2] \Rightarrow \bar{x}_2 \xrightarrow{\text{D}} \mathbb{E}[X_2] = \mu_{X_2} \tag{A.3}$$

$$\bar{x}_1^2 \xrightarrow{\text{P}} \{\mathbb{E}[X_1]\}^2 \Rightarrow \bar{x}_1^2 \xrightarrow{\text{D}} \{\mathbb{E}[X_1]\}^2 = \mu_{X_1^2} \tag{A.4}$$

$$\bar{x}_2^2 \xrightarrow{\text{P}} \{\mathbb{E}[X_2]\}^2 \Rightarrow \bar{x}_2^2 \xrightarrow{\text{D}} \{\mathbb{E}[X_2]\}^2 = \mu_{X_2^2} \tag{A.5}$$

$$\frac{1}{n}\sum_{i=1}^{n}(x_{1,i}x_{2,i} - \bar{x}_1\bar{x}_2) \xrightarrow{\text{D,P}} \mathbb{E}[X_1X_2] - \mathbb{E}[X_1]\mathbb{E}[X_2] \tag{A.6}$$

$$\frac{1}{n}\sum_{i=n+1}^{2n}(x_{1,i}x_{2,i} - \bar{x}_1\bar{x}_2) \xrightarrow{\text{D,P}} \mathbb{E}[X_1X_2] - \mathbb{E}[X_1]\mathbb{E}[X_2] \tag{A.7}$$

$$\frac{1}{n}\sum_{j=1}^{n}(x_{1,j} - \bar{x}_1)^2 \xrightarrow{\text{D,P}} \text{Var}[X_1] \tag{A.8}$$

$$\frac{1}{n}\sum_{j=n+1}^{2n}(x_{1,j} - \bar{x}_1)^2 \xrightarrow{\text{D,P}} \text{Var}[X_1] \tag{A.9}$$

$$\frac{1}{n}\sum_{k=1}^{n}(x_{2,k} - \bar{x}_2)^2 \xrightarrow{\text{D,P}} \text{Var}[X_2] \tag{A.10}$$

$$\frac{1}{n}\sum_{k=n+1}^{2n}(x_{2,k} - \bar{x}_2)^2 \xrightarrow{\text{D,P}} \text{Var}[X_2] \tag{A.11}$$

Finally, using Slutsky's lemma [19] again

$$\begin{aligned} R_{2voy} &\xrightarrow{\text{D}} \frac{\mathbb{E}[X_1X_2] - \mathbb{E}[X_1]\mathbb{E}[X_2] + \mathbb{E}[X_1X_2] - \mathbb{E}[X_1]\mathbb{E}[X_2]}{\sqrt{(2\text{Var}[X_1])\,(2\text{Var}[X_2])}} \\ &= \frac{\mathbb{E}[X_1X_2] - \mathbb{E}[X_1]\mathbb{E}[X_2]}{\sqrt{(\text{Var}[X_1]\text{Var}[X_2])}} = \rho \end{aligned} \tag{A.12}$$

But, since ρ is a constant, it is also true that

$$R_{2voy} \xrightarrow{\text{P}} \rho \tag{A.13}$$

This can easily be extended to R_{3voy}, $R_{4voy}, \ldots$ and, of course, R_{1voy}, thus proving the stationarity of the correlation coefficient estimate when considering multiple voyages.

A.2 Rejection Sampling Algorithm

The rejection sampling algorithm, that is presented here, and its mathematical background have been taken from [19], chapter 3.

The goal of rejection sampling method is to generate samples from an awkward multivariable density f. Samples from a uniform distribution can easily be generated using, for example, *rand* command in Matlab. To use this algorithm, one also needs to be able to sample from a "nicer looking" density, g, for which $\sup_y f(y)/g(y) = b < \infty;\ b > 1$. Then, the rejection sampling algorithm is as follows

1 generate X from g and U from the uniform distribution on (0,1), independently;

2 set $Y = X$ if $Ubg(X) \leq f(X)$, and otherwise go to 1; finally

3 return Y.

Since $\Pr(X \leq a)$ is the area under g to the left of a, then $(X, Ubg(X))$ is uniformly distributed on the set $\{(x, w) : 0 \leq w \leq bg(x)\}$, and the value Y is returned only if $Ubg(X) \leq f(X)$. For a single pair (X, U), the probability a value Y is returned and is less than y is

$$\begin{aligned}\Pr\{Ubg(X) \leq f(X) \text{ and } X \leq y\} &= \int_{-\infty}^{y} \Pr\left\{ U \leq \frac{f(X)}{bg(X)} \middle| X = x \right\} g(x)dx \\ &= \int_{-\infty}^{y} \frac{f(x)}{bg(x)} g(x)dx \\ &= b^{-1} \int_{-\infty}^{y} f(x)dx \end{aligned} \tag{A.14}$$

because U is uniform, independent of X. Hence

$$\begin{aligned}\Pr\{Y \leq y| \text{ value returned }\} &= \frac{\Pr\{Ubg(X) \leq f(X) \text{ and } X \leq y\}}{\Pr\{Ubg(X) \leq f(X) \text{ and } X \leq \infty\}} \\ &= \int_{-\infty}^{y} f(x)dx \end{aligned} \tag{A.15}$$

the density of Y is indeed f. The probability that a value is returned is b^{-1}, so the algorithm is most efficient when b is as small as possible. The envelope function, $bg(x)$, should ensure this. In this work, the envelope function has been conveniently selected as the uniform distribution on (0, max[f]). The upper bound of this interval is in fact the value of b and it enables the most efficient sample generation when using the uniform distribution for g.

A.3 The Flowchart of the Simulation Procedure (Basic Module)

Please see the next page.

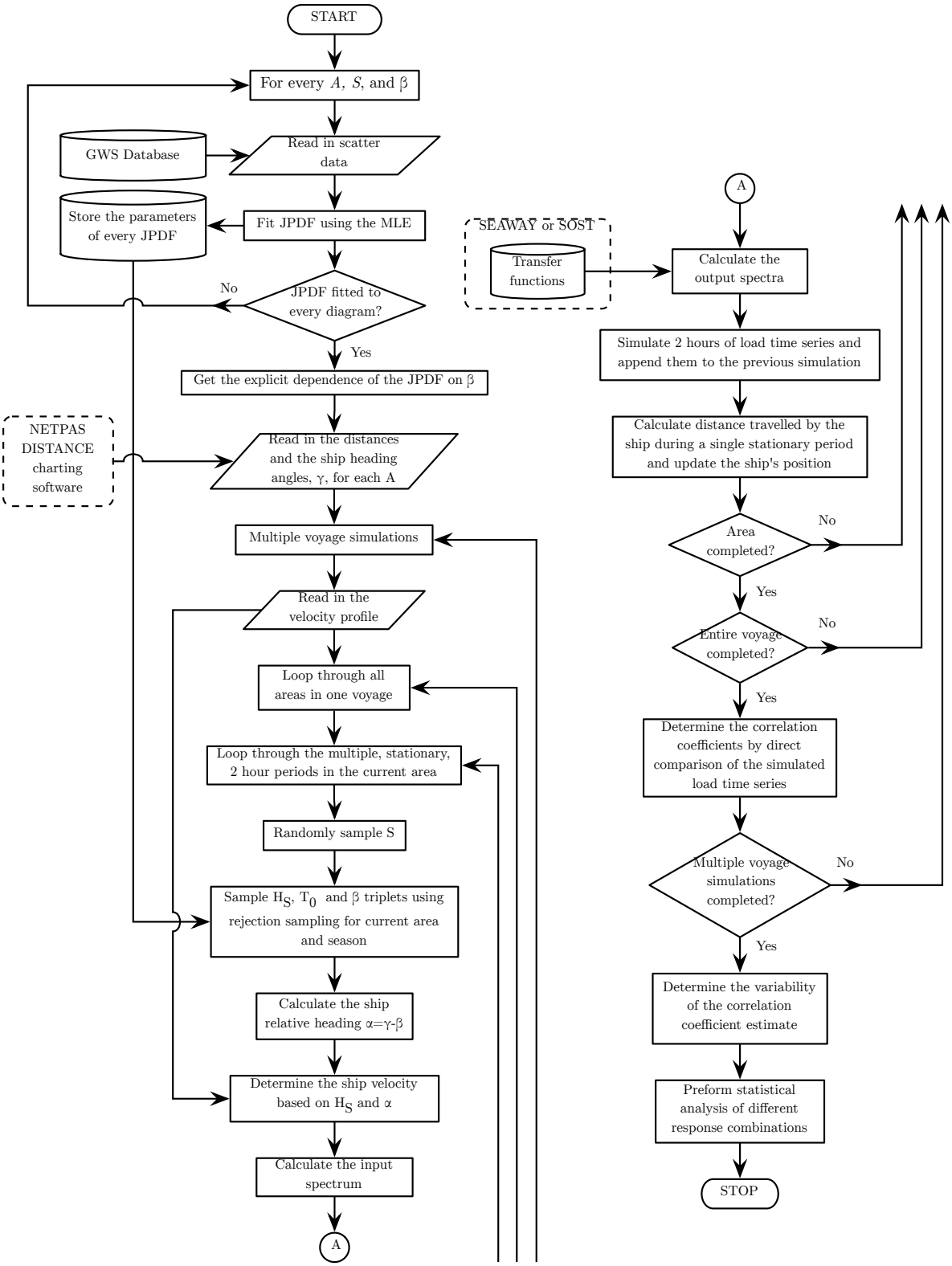

Figure A.1: Flowchart of the simulation procedure.

A.4 Long-Term Correlation Coefficient Estimates

Table A.1: C 319 (C.O.V. < 0.05)

(a) NA

	Q_x	Q_y	Q_z	M_x	M_y	M_z
Q_x	1.00	-0.16	0.28	0.21	0.58	0.19
Q_y	-0.16	1.00	-0.17	-0.72	-0.07	0.11
Q_z	0.28	-0.17	1.00	0.10	0.08	-0.03
M_x	0.21	-0.72	0.10	1.00	0.18	0.00
M_y	0.58	-0.07	0.08	0.18	1.00	0.42
M_z	0.19	0.11	-0.03	0.00	0.42	1.00

(b) NP

	Q_x	Q_y	Q_z	M_x	M_y	M_z
Q_x	1.00	-0.15	0.24	0.20	0.52	0.18
Q_y	-0.15	1.00	-0.16	-0.71	-0.07	0.07
Q_z	0.24	-0.16	1.00	0.09	0.09	-0.04
M_x	0.20	-0.71	0.09	1.00	0.18	0.05
M_y	0.52	-0.07	0.09	0.18	1.00	0.39
M_z	0.18	0.07	-0.04	0.05	0.39	1.00

(c) EA

	Q_x	Q_y	Q_z	M_x	M_y	M_z
Q_x	1.00	-0.15	0.20	0.20	0.39	0.15
Q_y	-0.15	1.00	-0.10	-0.72	-0.08	0.05
Q_z	0.20	-0.10	1.00	0.01	0.09	-0.03
M_x	0.20	-0.72	0.01	1.00	0.19	0.08
M_y	0.39	-0.08	0.09	0.19	1.00	0.35
M_z	0.15	0.05	-0.03	0.08	0.35	1.00

Table A.2: C 283 (C.O.V. < 0.05)

(a) NA

	Q_x	Q_y	Q_z	M_x	M_y	M_z
Q_x	1.00	-0.18	0.31	0.21	0.65	0.20
Q_y	-0.18	1.00	-0.17	-0.75	-0.09	0.09
Q_z	0.31	-0.17	1.00	0.14	0.14	0.02
M_x	0.21	-0.75	0.14	1.00	0.17	-0.04
M_y	0.65	-0.09	0.14	0.17	1.00	0.49
M_z	0.20	0.09	0.02	-0.04	0.49	1.00

(b) NP

	Q_x	Q_y	Q_z	M_x	M_y	M_z
Q_x	1.00	-0.16	0.28	0.19	0.61	0.20
Q_y	-0.16	1.00	-0.16	-0.74	-0.10	0.05
Q_z	0.28	-0.16	1.00	0.16	0.14	0.01
M_x	0.19	-0.74	0.16	1.00	0.16	0.00
M_y	0.61	-0.10	0.14	0.16	1.00	0.47
M_z	0.20	0.05	0.01	0.00	0.47	1.00

(c) EA

	Q_x	Q_y	Q_z	M_x	M_y	M_z
Q_x	1.00	-0.15	0.27	0.19	0.48	0.15
Q_y	-0.15	1.00	-0.14	-0.75	-0.09	0.05
Q_z	0.27	-0.14	1.00	0.13	0.13	-0.02
M_x	0.19	-0.75	0.13	1.00	0.16	0.02
M_y	0.48	-0.09	0.13	0.16	1.00	0.43
M_z	0.15	0.05	-0.02	0.02	0.43	1.00

Table A.3: S 175 (C.O.V. < 0.05)

(a) NA

	Q_x	Q_y	Q_z	M_x	M_y	M_z
Q_x	1.00	-0.29	0.31	0.34	0.54	0.18
Q_y	-0.29	1.00	-0.06	-0.85	-0.20	0.17
Q_z	0.31	-0.06	1.00	0.00	0.04	-0.03
M_x	0.34	-0.85	0.00	1.00	0.24	-0.23
M_y	0.54	-0.20	0.04	0.24	1.00	0.42
M_z	0.18	0.17	-0.03	-0.23	0.42	1.00

(b) NP

	Q_x	Q_y	Q_z	M_x	M_y	M_z
Q_x	1.00	-0.26	0.27	0.32	0.54	0.18
Q_y	-0.26	1.00	-0.06	-0.85	-0.20	0.16
Q_z	0.27	-0.06	1.00	0.03	0.00	-0.10
M_x	0.32	-0.85	0.03	1.00	0.23	-0.19
M_y	0.54	-0.20	0.00	0.23	1.00	0.41
M_z	0.18	0.16	-0.10	-0.19	0.41	1.00

(c) EA

	Q_x	Q_y	Q_z	M_x	M_y	M_z
Q_x	1.00	-0.23	0.22	0.30	0.43	0.12
Q_y	-0.23	1.00	-0.05	-0.84	-0.19	0.17
Q_z	0.22	-0.05	1.00	0.07	-0.09	-0.18
M_x	0.30	-0.84	0.07	1.00	0.21	-0.21
M_y	0.43	-0.19	-0.09	0.21	1.00	0.37
M_z	0.12	0.17	-0.18	-0.21	0.37	1.00

Table A.4: T 306 (C.O.V. < 0.05)

(a) NA

	Q_x	Q_y	Q_z	M_x	M_y	M_z
Q_x	1.00	0.02	0.31	0.04	0.56	0.07
Q_y	0.02	1.00	-0.27	-0.66	-0.05	-0.17
Q_z	0.31	-0.27	1.00	0.25	0.15	0.14
M_x	0.04	-0.66	0.25	1.00	0.17	0.02
M_y	0.56	-0.05	0.15	0.17	1.00	0.32
M_z	0.07	-0.17	0.14	0.02	0.32	1.00

(b) NP

	Q_x	Q_y	Q_z	M_x	M_y	M_z
Q_x	1.00	-0.07	0.31	0.07	0.48	0.08
Q_y	-0.07	1.00	-0.28	-0.71	-0.05	-0.15
Q_z	0.31	-0.28	1.00	0.26	0.12	0.14
M_x	0.07	-0.71	0.26	1.00	0.13	0.05
M_y	0.48	-0.05	0.12	0.13	1.00	0.34
M_z	0.08	-0.15	0.14	0.05	0.34	1.00

(c) EA

	Q_x	Q_y	Q_z	M_x	M_y	M_z
Q_x	1.00	0.01	0.25	0.04	0.35	0.03
Q_y	0.01	1.00	-0.20	-0.65	-0.02	-0.13
Q_z	0.25	-0.20	1.00	0.23	0.06	0.10
M_x	0.04	-0.65	0.23	1.00	0.16	0.04
M_y	0.35	-0.02	0.06	0.16	1.00	0.25
M_z	0.03	-0.13	0.10	0.04	0.25	1.00

Table A.5: T 283 (C.O.V. < 0.05)

(a) NA

	Q_x	Q_y	Q_z	M_x	M_y	M_z
Q_x	1.00	0.09	0.25	-0.06	0.56	0.08
Q_y	0.09	1.00	-0.23	-0.72	0.00	-0.03
Q_z	0.25	-0.23	1.00	0.24	0.38	0.20
M_x	-0.06	-0.72	0.24	1.00	0.06	-0.06
M_y	0.56	0.00	0.38	0.06	1.00	0.34
M_z	0.08	-0.03	0.20	-0.06	0.34	1.00

(b) NP

	Q_x	Q_y	Q_z	M_x	M_y	M_z
Q_x	1.00	-0.04	0.21	0.02	0.48	0.02
Q_y	-0.04	1.00	-0.26	-0.75	0.00	-0.05
Q_z	0.21	-0.26	1.00	0.24	0.36	0.25
M_x	0.02	-0.75	0.24	1.00	0.04	-0.02
M_y	0.48	0.00	0.36	0.04	1.00	0.36
M_z	0.02	-0.05	0.25	-0.02	0.36	1.00

(c) EA

	Q_x	Q_y	Q_z	M_x	M_y	M_z
Q_x	1.00	0.07	0.18	-0.04	0.37	0.00
Q_y	0.07	1.00	-0.18	-0.72	0.03	0.00
Q_z	0.18	-0.18	1.00	0.20	0.30	0.20
M_x	-0.04	-0.72	0.20	1.00	0.04	-0.05
M_y	0.37	0.03	0.30	0.04	1.00	0.29
M_z	0.00	0.00	0.20	-0.05	0.29	1.00

Table A.6: BC 283 (C.O.V. < 0.05)

(a) NA

	Q_x	Q_y	Q_z	M_x	M_y	M_z
Q_x	1.00	-0.05	0.35	0.05	0.55	0.17
Q_y	-0.05	1.00	-0.26	-0.71	-0.04	0.09
Q_z	0.35	-0.26	1.00	0.32	0.22	0.07
M_x	0.05	-0.71	0.32	1.00	0.14	-0.08
M_y	0.55	-0.04	0.22	0.14	1.00	0.36
M_z	0.17	0.09	0.07	-0.08	0.36	1.00

(b) NP

	Q_x	Q_y	Q_z	M_x	M_y	M_z
Q_x	1.00	-0.19	0.33	0.15	0.49	0.17
Q_y	-0.19	1.00	-0.31	-0.75	-0.04	0.06
Q_z	0.33	-0.31	1.00	0.32	0.21	0.06
M_x	0.15	-0.75	0.32	1.00	0.10	-0.03
M_y	0.49	-0.04	0.21	0.10	1.00	0.41
M_z	0.17	0.06	0.06	-0.03	0.41	1.00

(c) EA

	Q_x	Q_y	Q_z	M_x	M_y	M_z
Q_x	1.00	-0.06	0.31	0.06	0.37	0.13
Q_y	-0.06	1.00	-0.23	-0.69	0.00	0.12
Q_z	0.31	-0.23	1.00	0.28	0.12	0.02
M_x	0.06	-0.69	0.28	1.00	0.10	-0.06
M_y	0.37	0.00	0.12	0.10	1.00	0.31
M_z	0.13	0.12	0.02	-0.06	0.31	1.00

A.5 Hull Forms

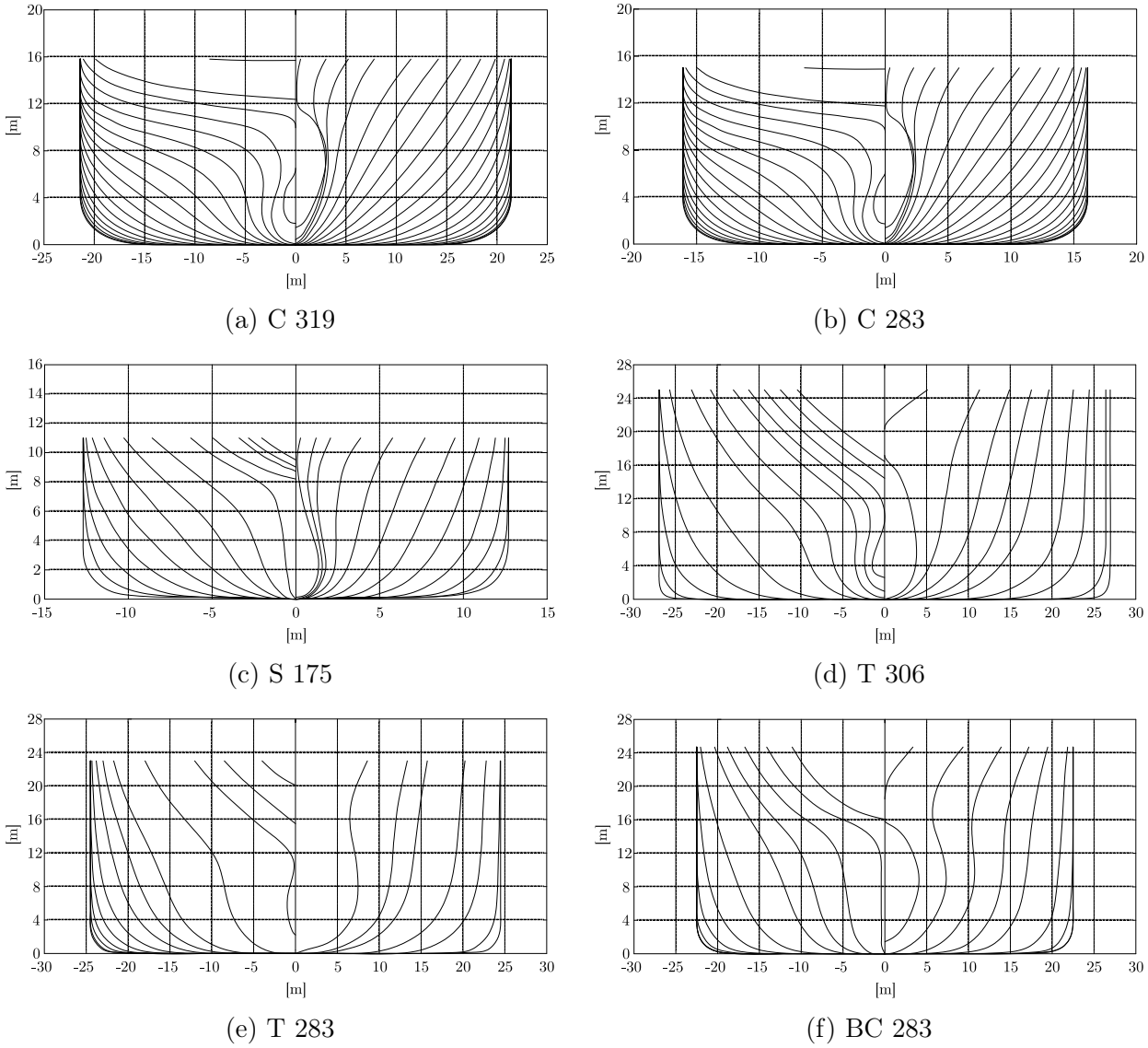

(a) C 319

(b) C 283

(c) S 175

(d) T 306

(e) T 283

(f) BC 283

Figure A.2: Hull forms.

Appendix B

B.1 Calculation of Nonlinear Wave-Induced Forces in the Vertical Plane: Quadratic Theory

The quadratic theory for the calculation of vertical nonlinear hydrodynamic forces acting on the hull of the ship is presented in the following. Figure B.1 shows the coordinate systems and some of the notation used in this derivation. The global X-Y-Z axes are fixed in space, with the X-axis at the still water level. The ship is moving forward with speed V in the X direction. The x-y-z axes are attached to the ship. The origin is at the intersection of the aft perpendicular, ship's centerline plane, and the the still water plane (SWP). $\eta(x,t)$ is the instantaneous height of the ships's SWP above the local free surface. Therefore, η is the "emergence" at location x.

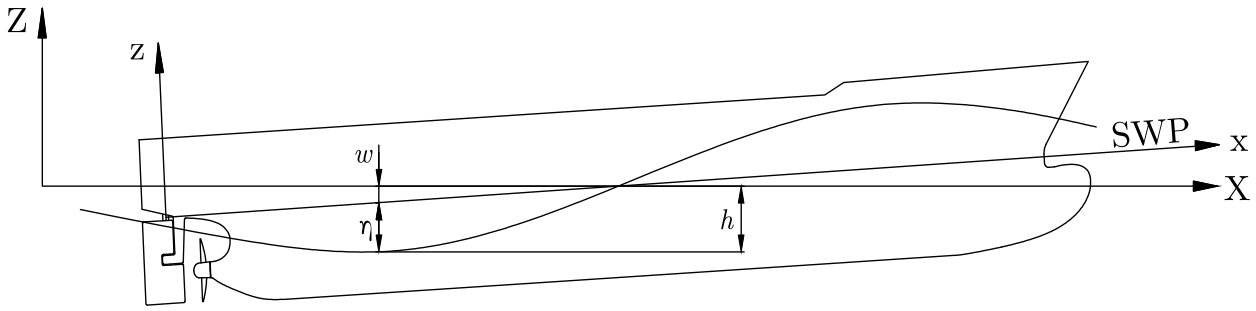

Figure B.1: Coordinate system for ship response.

In order to allow for steep waves whose amplitude is not small compared to their length, the second-order wave theory can be used. In this approach the wave velocity potential (ϕ), as well as the free surface elevations in the global coordinate system (h), can be represented as the sum of first-order and second-order terms as follows

$$h \simeq h_1 + h_2 \quad = \sum_{i=1}^{N} a_i \cos\psi_i + \frac{1}{4}\sum_{i=1}^{N}\sum_{j=1}^{N} a_i a_j \left[(k_i + k_j)\cos(\psi_i + \psi_j) - |k_i - k_j|\cos(\psi_i - \psi_j)\right] \tag{B.1}$$

where $\psi_i = -k_i X - \omega_i t + \theta_i$, k is the wave number and for deep water waves it is equal to $k_i = \omega_i^2/g$. g is the acceleration of gravity. The velocity potential is equal to

$$\phi \simeq \phi_1 + \phi_2 \quad = \sum_{i=1}^{N} \frac{a_i \omega_i}{k_i} e^{k_i Z} \sin\psi_i + \frac{1}{2} \sum_{i=1}^{N} \sum_{j=1}^{N} a_i a_j \max(-\omega_i, \omega_j) e^{|k_i - k_j| Z} \sin(\psi_i - \psi_j) \quad \text{(B.2)}$$

in which

$$\max(-\omega_i, \omega_j) \equiv \begin{cases} -\omega_i & \text{if } \omega_i > \omega_j \\ \omega_j & \text{if } \omega_i < \omega_j \end{cases} \quad \text{(B.3)}$$

The total external vertical hydrodynamic force acting on the ship hull per unit length is equal to

$$F(x,t) = -\left\{ \frac{D}{Dt}\left[m(x,\eta) \frac{D\eta}{Dt} \right] + N(x,\eta) \frac{D\eta}{Dt} + \int_{-T}^{-\eta} B(x,z) \left(\frac{\partial p}{\partial Z} \right)_{z+w} dz \right\} \quad \text{(B.4)}$$

where m is the added mass of fluid per unit length, N is the damping coefficient per unit length, B is the local water line breadth of the ship, p is the Froude-Krylov fluid pressure, T is the still water draft, and w is the instantaneous displacement of the hull at location x. The operator D/Dt is the total derivative with respect to time, that is

$$\frac{D}{Dt} \equiv \frac{\partial}{\partial t} - V \frac{\partial}{\partial x} \quad \text{(B.5)}$$

The first two terms in Eqn. (B.4) represent the hydrodynamic inertia and damping forces due to diffraction of the incident wave and the radiation of waves caused by the ship's motion, while the last term represents the Froude-Krylov force due to the action of the undisturbed incident wave on the ship. All three terms are nonlinear: the added mass and the damping coefficient are nonlinear functions of η, and the pressure distribution within the fluid is a nonlinear function of depth and fluid velocity.

The instantaneous height of the local free surface above the x–axis, $\eta(x,t)$, can be expressed as

$$\eta(x,t) = w(x,t) - h(x,t) \quad \text{(B.6)}$$

$F(x,t)$ can be evaluated by a perturbation method in which the linear and quadratic terms in η and w are taken into account. For that purpose, m, N, and B have to be linearized as follows

$$m(x,\eta) \simeq m(x,0) + \eta \left(\frac{\partial m}{\partial \eta} \right)_{\eta=0} \equiv m_0(x) + \eta(x,t) m_1(x) \quad \text{(B.7)}$$

$$N(x,\eta) \simeq N(x,0) + \eta \left(\frac{\partial N}{\partial \eta} \right)_{\eta=0} \equiv N_0(x) + \eta(x,t) N_1(x) \quad \text{(B.8)}$$

$$B(x,\eta) \simeq B(x,0) + z \left(\frac{\partial B}{\partial z} \right)_{z=0} \equiv B_0(x) + z B_1(x) \quad \text{(B.9)}$$

where m and N are linearized around $\eta = 0$, and B is linearized around $z = 0$.

B.1.1 Froude-Krylov Part of the Hydrodynamic Force

The Froude-Krylov part of the total hydrodynamic force is equal to

$$F_{F-K}(x,t) = -\int_{-T}^{-\eta} B(x,z)\left(\frac{\partial p}{\partial Z}\right)_{z+w} dz \tag{B.10}$$

where the pressure, p, is given by the Bernoulli's equation

$$p(Z,x,t) = -\rho\left[\frac{\partial \phi}{\partial t} + gZ + \frac{1}{2}\left(\nabla\phi\right)^2\right] \tag{B.11}$$

in which ρ is the fluid density, ϕ is the velocity potential of the wave as expressed in Eqn. (B.2), and g is the acceleration of gravity. Pressure can be expressed in terms of the two components of ϕ

$$p \simeq p_0 + p_1 + p_2 \tag{B.12}$$

where

$$p_0 = -\rho g Z \tag{B.13a}$$

$$p_1 = -\rho\frac{\partial \phi_1}{\partial t} \tag{B.13b}$$

$$p_2 = -\rho\left[\frac{\partial \phi_2}{\partial t} + \frac{1}{2}\left(\nabla\phi_1\right)^2\right] \tag{B.13c}$$

in which the contribution of $\nabla\phi_2$ in the third term is neglected. Substituting the components of ϕ into the expressions for the first- and second-order pressure gives

$$p_1 = \rho g \sum_{i=1}^{N} a_i e^{k_i Z}\cos\psi_i \tag{B.14}$$

$$p_2 = -\frac{1}{2}\rho\sum_{i=1}^{N}\sum_{j=1}^{N} a_i a_j\left[\max(\omega_i,\omega_j)\left|\omega_i-\omega_j\right| e^{|k_i-k_j|Z} + \omega_i\omega_j e^{(k_i+k_j)Z}\right]\cos\left(\psi_i-\psi_j\right) \tag{B.15}$$

The Froude-Krylov force in Eqn. (B.10) consists of contributions from the hydrostatic buoyancy term, p_0, and the hydrodynamic contributions from p_1 and p_2. The hydrostatic contribution can further be subdivided into the portion from the keel to the still water plane (SWP) and the portion from the SWP to the local fluid surface.

$$\begin{aligned} F_{F-K}(x,t) = &-\int_{-T}^{0} B(x,z)\left(\frac{\partial p_0}{\partial Z}\right)dz - \int_{0}^{-\eta} B(x,z)\left(\frac{\partial p_0}{\partial Z}\right)dz \\ &-\int_{-T}^{-\eta} B(x,z)\left[\frac{\partial\left(p_1+p_2\right)}{\partial Z}\right]_{z+w} dz \end{aligned} \tag{B.16}$$

The first term in the foregoing equation is the hydrostatic buoyancy force on a ship in still water. When it is integrated over the ship's length it has to be equal and opposite to the total weight of the ship. These two forces eventually cancel constituting the still water loads which can be analyzed separately from the wave-induced loads. Therefore, from this point on, the first term of Eqn. (B.16) can be omitted. The inertia effects associated with the motion of the ship have to be included when writing the equations of motion.

By substituting for the three components of the pressure from Eqn. (B.13), the Froude-Krylov force becomes

$$F_{F-K}(x,t) = \rho g \int_0^{-\eta} B(x,z)dz - \rho g \sum_{i=1}^{N} a_i k_i \cos\psi_i \int_{-T}^{-\eta} B(x,z) e^{k_i(z+w)} dz$$

$$+ \frac{1}{2}\rho g \sum_{i=1}^{N}\sum_{j=1}^{N} a_i a_j \cos(\psi_i - \psi_j) \int_{-T}^{-\eta} B(x,z) \Big[\max\left(\sqrt{k_i}, \sqrt{k_j}\right)$$

$$\times \left(\sqrt{k_i} - \sqrt{k_j}\right)(k_i - k_j)\, e^{|k_i - k_j|Z} + \sqrt{k_i k_j}\,(k_i + k_j)\, e^{(k_i+k_j)Z} \Big] dz \tag{B.17}$$

Second-order approximation of w can also be done using

$$w \simeq w_1 + w_2 \tag{B.18}$$

so that η can also be substituted with

$$\eta \simeq w_1 - h_1 + w_2 - h_2 \tag{B.19}$$

Eqn. (B.17) can be expanded even further by using substitutions from Eqns. (B.9), (B.18) and (B.19). If only the second-order terms are kept, that is terms in $w_1,\ w_1^2,\ w_2,\ h_1,\ h_1^2,$ and h_2, then the final expression for the Froude-Krylov force becomes

$$F_{F-K} \simeq F_{F-K}^{(1)} + F_{F-K}^{(2)} \tag{B.20}$$

where

$$F_{F-K}^{(1)}(x,t) = -\rho g B_0 \left[w_1 - \sum_{i=1}^{N} a_i \kappa_i \cos\psi_i \right] \tag{B.21}$$

and

$$F_{F-K}^{(2)}(x,t) = -\rho g B_0 w_2 + \frac{1}{2}\rho g B_1 w_1^2 - \rho g w_1 \sum_{i=1}^{N} a_i \cos\psi_i \,(B_1 - B_0 k_i \kappa_i)$$

$$+ \frac{1}{4}\rho g \sum_{i=1}^{N}\sum_{j=1}^{N} a_i a_j \Bigg\{ \cos(\psi_i + \psi_j)\, B_1 + \cos(\psi_i - \psi_j)$$

$$\times \left[B_1 + 2B_0 \Big[\Big(\sqrt{k_i k_j} - \max(k_i, k_j) \Big) \kappa_{|i-j|} - \sqrt{k_i k_j}\, \kappa_{|i+j|} \Big] \right] \Bigg\} \tag{B.22}$$

in which κ_i and $\kappa_{|i\pm j|}$ are the Smith correction factors, defined as

$$\kappa_i(x) = 1 - \frac{k_i}{B_0(x)} \int_{-T}^{0} B(x,t) e^{k_i z} dz \tag{B.23}$$

$$\kappa_{|i\pm j|}(x) = 1 - \frac{|k_i \pm k_j|}{B_0(x)} \int_{-T}^{0} B(x,t) e^{|k_i \pm k_j| z} dz \tag{B.24}$$

B.1.2 Hydrodynamic Forces Due to Diffraction and Radiation

The hydrodynamic force due to diffraction and radiation of the waves is modeled with the first two terms of Eqn. (B.4), that is

$$F_H(x,t) = -\frac{D}{Dt}\left(m(x,\eta)\frac{D\eta}{Dt}\right) - N(x,\eta)\frac{D\eta}{Dt} \tag{B.25}$$

Substitution of the linearized expression for m and N, together with the second-order representation of the emergence, $\eta \simeq \eta_1 + \eta_2$, gives the following second-order expression for F_H

$$F_H(x,t) \simeq F_H^{(1)} + F_H^{(2)} \tag{B.26}$$

where

$$F_H^{(1)} = -m_0 \frac{D^2\eta_1}{Dt^2} - n_0 \frac{D\eta_1}{Dt} \tag{B.27}$$

$$F_H^{(2)} = -m_0 \frac{D^2\eta_2}{Dt^2} - n_0 \frac{D\eta_2}{Dt} - \eta_1 \left(m_1 \frac{D^2\eta_1}{Dt^2} + n_1 \frac{D\eta_1}{Dt}\right) - m_1 \left(\frac{D\eta_1}{Dt}\right)^2 \tag{B.28}$$

and where

$$n_0 = n_0(x) = N_0 - V\frac{\partial m_0}{\partial x} \tag{B.29}$$

$$n_1 = n_1(x) = N_1 - V\frac{\partial m_1}{\partial x} \tag{B.30}$$

The final expressions for F_H can be obtained by introducing $\eta = w - h^*$ into Eqns. (B.27) and (B.28), where h^* is the wave elevation including the second-order terms corrected by the

Smith factor

$$F_H^{(1)} = -m_0\frac{D^2w_1}{Dt^2} - n_0\frac{Dw_1}{Dt} - \sum_{i=1}^{N} a_i\omega_i\kappa_i\left(m_0\omega_i\cos\psi_i - n_0\sin\psi_i\right) \tag{B.31}$$

$$\begin{aligned}
F_H^{(2)} = &-m_0\frac{D^2w_2}{Dt^2} - n_0\frac{Dw_2}{Dt} - w_1\left(m_1\frac{D^2w_1}{Dt^2} + n_1\frac{Dw_1}{Dt}\right) - m_1\left(\frac{Dw_1}{Dt}\right)^2 \\
&+ \sum_{i=1}^{N} a_i\kappa_i\left[\cos\psi_i\left(m_1\frac{D^2w_1}{Dt^2} + n_1\frac{Dw_1}{Dt} - \omega_i^2 m_1 w_1\right)\right. \\
&\left. + \sin\psi_i\left(n_1\omega_i w_1 + 2m_1\omega_i\frac{Dw_1}{Dt}\right)\right] \\
&+ \frac{1}{4}\sum_{i=1}^{N}\sum_{j=1}^{N} a_i\kappa_i a_j\kappa_j\Big[\cos(\psi_i+\psi_j)(\omega_i+\omega_j)^2(m_1 - (k_i+k_j)m_0) \\
&+ \cos(\psi_i-\psi_j)(\omega_i-\omega_j)^2(m_1 + |k_i-k_j|\,m_0) \\
&+ \sin(\psi_i+\psi_j)(\omega_i+\omega_j)(-n_1 + (k_i+k_j)n_0) \\
&+ \sin(\psi_i-\psi_j)(\omega_i-\omega_j)(-n_1 - |k_i-k_j|\,n_0)\Big]
\end{aligned} \tag{B.32}$$

Eqns. (B.21), (B.22), (B.31) and (B.32) form a set of first- and second-order contributions to the external vertical force per unit length acting on the hull of the ship in an irregular sea. The ship's hull is usually modeled as a flexible body using the Timoshenko free-free beam. In that case, the total vertical deflection (first- and second-order) of the hull girder, w, can be obtained and used to calculate the nonlinear vertical bending moment. Another way of calculating the vertical bending moment is to integrate the nonlinear vertical forces along the hull. The details of both methods can be found in [51].

Appendix C

C.1 Structural and Mass Properties of C 319 Ship

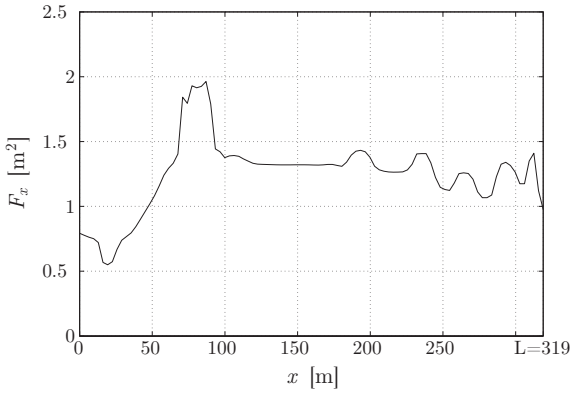

(a) Vertical Shear Area.

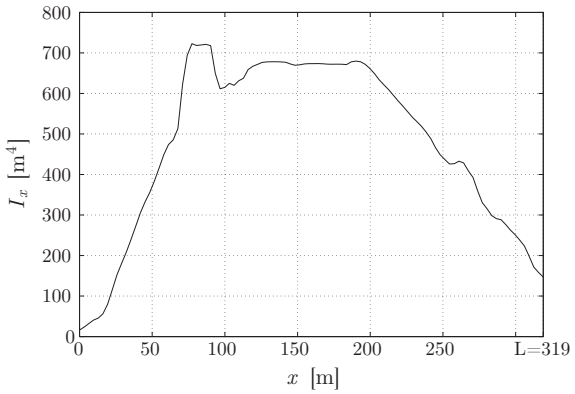

(b) Vertical Moment of Inertia.

Figure C.1: Structural properties of C 319 container ship.

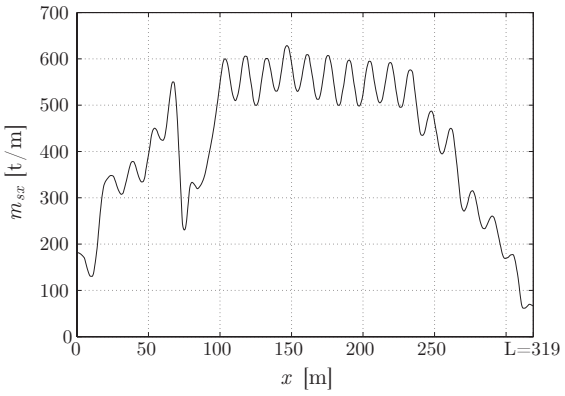

(a) Mass distribution at full load.

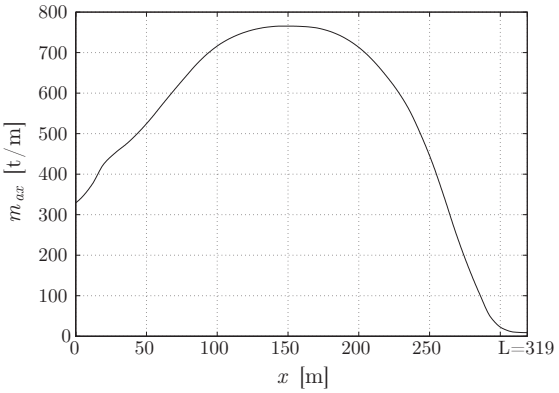

(b) Added mass of water per unit length.

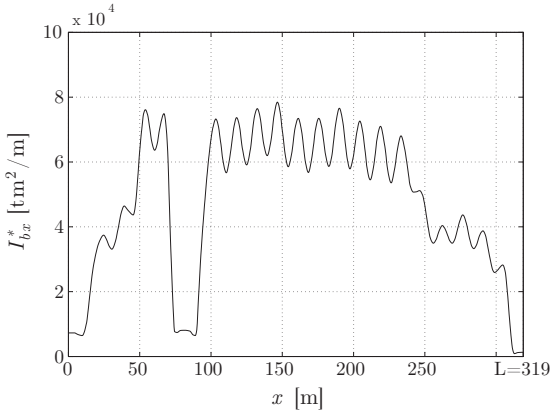

(c) Mass moment of inertia per unit length with respect to the neutral line.

Figure C.2: Mass properties of C 319 container ship.